Multiscale modeling of charge transport and excited-state properties in organic functional materials

Dissertation
zur
Erlangung des Doktorgrades
der
Mathematisch-Naturwissenschaftlichen Fakultät
der
Universität zu Köln

vorgelegt von
Robert Herzhoff
aus
Bonn

Köln, 2025

1. Referee:	Prof. Dr. Klaus Meerholz
2. Referee:	Prof. Dr. Wolfgang Wenzel

Acknowledgements

At first, I would like to thank Prof. Dr. Klaus Meerholz, who gave me the opportunity to write my dissertation within his research group. This was a fantastic chance to learn and work within an incredible team of people that allowed me to grow as a scientist and as a human being and to perform interesting scientific work in an interdisciplinary group.

I would also like to express my gratitude towards Prof. Dr. Daniele Fazzi for the excellent supervision and for providing thoughtful and intelligent guidance throughout my PhD journey.

To both of my supervisors I would like to express my gratitude for their mentorship, scientific and otherwise, that will undoubtedly be highly valuable in the future.

Furthermore, I would like to thank Prof. Dr. Wolfgang Wenzel for taking up the role of the second referee.

I would also like to acknowledge Prof. Dr. Alessandro Troisi and his research group, who hosted me during my research residence at the University of Liverpool.

Additionally I would like to acknowledge Prof. Dr. Stefan Grimme and Dr. Andreas Hansen for the collaboration on constrained xTB.

I would like to extend a special thank you to the people that have not only been my closest collaborators, fellow theoreticians and office colleagues, but with whom I have spent countless hours talking and discussing everything from science to sports, Nora Gildemeister and Sven Geller.

A special thank you also to Laura Plein for providing the experimental data and to Christopher Wallerius for the great collaborative work.

I would also like to acknowledge the entire research group Meerholz for a fantastic time during my PhD. It was great to discuss science but also to spend time and drink coffee in the kitchen, to go on canoe trips or to go for a round of bowling after work. I would also like to acknowledge Agustín López Cabrera and Antonio di Maria.

A special thank you also goes out to the the members of the TIDE research training group not only for the scientific discussions and the collaborations but also for the nice atmosphere during retreats, lecture series and other events.

I would like to acknowledge André Colliard Granero, Fabian Tipp and Kevin Schuller, with whom I have sat side by side in lectures, exercises and exams. I would also like to thank Tim Lippold for a great time at the Organic Chemistry department. Furthermore I would like to thank all members of the Theoretical Chemistry department.

I would also like to thank my family and friends for the support during my studies and my PhD.

Finally, I would like to thank my wife, Lisanne, who walked every step of the way with me.

Abstract

This thesis is based on the multiscale modeling of organic functional materials for Organic Electronic applications, considering both charge transfer as well as photophysical properties and processes. Additionally, related work concerning method development for the evaluation of charge transport parameters is reported.

The first part of the thesis focuses on structure-property relationships with regard to the hole (hopping) transport in triphenylamine derivatives, considering the limit cases of crystalline and amorphous bulk structures. Excellent agreement of the simulated hole mobilities with the available experimental data was achieved, validating the modeling approach. A complex interdependency of molecular and bulk structure was found, where the molecular structure is reflected in the bulk morphology, influencing charge transport parameters, -anisotropy and hole mobility. The energetic disorder resulting from the inclusion of electrostatic effects on the site energies reflects the degree of morphological order, showing discrete distributions in the crystalline case and Gaussian-like distributions in the amorphous case. The same pattern was found for the electronic couplings.

In the second part of the thesis, the electronic and ionic transport in oxetane-functionalized and polymerized triphenylamine derivatives for electrochemical applications was investigated. As main findings, it could be shown that a) charge transport is possible in the presence of high static energetic disorder due to simultaneously high dynamic disorder, and b) that this charge transport can not be described by the standard approach of kinetic Monte Carlo using a fixed set of rates. Therefore, a new descriptor for the charge transport, the effective Marcus residence time, which encompasses the dynamic disorder, was devised. Furthermore, slow ion transport was found compared to the timescales of hole transport, indicating the ion diffusion as the rate limiting step in electrochemical applications. The generally slow ion diffusion can be related to the low average void radii found in the bulk morphologies.

In the third part, an implementation of a charge- and spin-constraining methodology in the framework of the density functional extended tight-binding based method called GFN2-xTB is reported and tested, aiming at the rapid evaluation of energy, gradients (i.e. geometry optimizations) and generally charge transport parameters, requiring charge or spin constraints.

Finally, the excited state characterization of novel emitter compounds at a DFT based quantum chemical level is reported. Unraveling the relationship of molecular design and photophysical properties, the influence of a spiro[acridine-9,9'-fluorene] group as donor unit was found to increase the reverse intersystem crossing rate by lowering the adiabatic singlet triplet gap and the excited state reorganization energy.

Kurzzusammenfassung

Diese Dissertation befasst sich mit der Multiskalenmodellierung von organischen funktionellen Materialien für Anwendungen im Bereich der organischen Elektronik und untersucht sowohl Ladungstransport- als auch photophysikalische Eigenschaften und Prozesse. Zusätzlich werden Ergebnisse im Bereich der Methodenentwicklung für die Auswertung von Ladungstransportparametern dargestellt und diskutiert.

Der erste Teil der Dissertation konzentriert sich auf die Struktur-Eigenschafts-Beziehungen im Bezug auf den Lochtransport in Triphenylaminderivaten und untersucht hierbei die Grenzfälle von einkristallinen und amorphen Systemen. Exzellente Übereinstimmung der simulierten und experimentellen Lochmobilitäten konnte erreicht werden, was den Modellierungsansatz validiert. Ein komplexes Zusammenspiel der molekularen und der Festkörperstruktur wurde gefunden, in dem die molekulare Struktur in der Festkörperstruktur reflektiert wird, was Ladungstransportparameter, -anisotropie und Lochmobilität beeinflusst. Die energetische Unordnung, die von der Miteinbeziehung von elektrostatischen Effekten auf die Energien herrührt, spiegelt den Grad an morphologischer Unordnung wider und zeigt diskrete Verteilungen im kristallinen Fall und Gauss-Verteilungen im amorphen Fall. Das gleiche Muster wurde für die Transferintegrale gefunden.

Im zweiten Teil der Dissertation wird der gekoppelte Ladungs- und Ionentransport in oxetanfunktionalisierten und polymerisierten Triphenylaminderivaten für elektrochemische Anwendungen untersucht. Als Hauptergebnisse konnte gezeigt werden, dass a) Ladungstransport in der Gegenwart hoher statischer energetischer Unordnung durch die gleichzeitige Gegenwart hoher dynamischer Unordnung möglich ist und dass b) dieser Ladungstransport nicht durch den typischen Ansatz von kinetischen Monte Carlo Simulationen und einem festen Satz an Raten beschrieben werden kann. Aus diesem Grund wurde ein neuer Deskriptor für den Ladungstransport entworfen, die effektive Marcus-Residenzzeit, welche die dynamische Unordnung miteinbezieht. Darüberhinaus wurde im Vergleich zum Lochtransport eher langsamer Ionentransport gefunden, was den Ionentransport zum zeitlich limitierenden Faktor für elektrochemische Anwendungen macht. Dieser Umstand hängt mit den geringen Leerstellenradii in den Festkörperstrukturen zusammen.

Im dritten Teil wird eine Implementierung einer Ladungs- und Spin-Beschränkungsmethodologie im Rahmen der dichtefunktionalbasierten tight-binding Methode GFN2-xTB vorgestellt und getestet, welche auf die schnelle Auswertung von Energien und nuklearen Gradienten sowie Ladungstransportparametern in Rechnungen mit Ladungs- und/oder Spinbeschränkungen abzielt.

Zuletzt wird die Charakterisierung angeregter Zustände von neuartigen Emitterverbindungen auf einem DFT-basierten quantenchemischen Level dargestellt. Die Beziehung zwischen molekularem Design und daraus resultierenden photophysikalischen Eigenschaften wurde aufgeschlüsselt wobei sich insbesondere der Einfluss einer Spiro[Acridin-9,9'-Fluoren] Donorgruppe als zuträglich für die rückläufige Interkombination herausgestellt hat, da diese die adiabatische Energiedifferenz sowie die Reorganisationsenergie zwischen angeregten Singulett- und Triplettzuständen verringert.

Contents

1 Introduction 1

1.1 Organic Electronics 1
1.2 Triphenylamines for Organic Electronics 3
1.3 Donor-Acceptor substituted compounds for organic light emitting diodes 6
1.4 Method development for multiscale modeling approaches 6

2 Scope of thesis 7

3 Theory 9

3.1 Charge transport 9
  3.1.1 Classical physics 9
  3.1.2 Ion transport 10
  3.1.3 Quantum mechanical charge transport 11
3.2 Charge transport parameters 13
  3.2.1 Site energy 13
  3.2.2 Electronic coupling 15
  3.2.3 Reorganization energy 17
3.3 Static and dynamic disorder 17
3.4 Thermally activated delayed fluorescence 18
3.5 Methods 19
  3.5.1 Electronic structure theory 19
  3.5.2 Density functional theory 20
  3.5.3 Excited state methods 22
  3.5.4 GFN2-xTB 26
  3.5.5 Molecular dynamics 26
  3.5.6 Kinetic Monte Carlo 28
3.6 Computational procedures 29
  3.6.1 Software 29
  3.6.2 Force field parametrization 29
  3.6.3 Charge transport simulations 30

4 Charge transport in TPA derivatives 33

4.1 Structure-property relationships 33
4.2 Bulk morphologies: crystalline vs amorphous phases 34

4.3 Charge transport parameters 35
  4.3.1 Hole reorganization energy 35
  4.3.2 Site energy differences and electronic coupling 37
4.4 Hole mobility 39
4.5 Conclusion 40
4.6 Publication I 40

5 Mixed hole and ion transport in cross-linkable TPAs **53**
5.1 Mixed hole and ion transport 53
5.2 Polymer systems 54
5.3 Ion transport 55
5.4 Static and dynamic site energy landscapes 56
5.5 Effective Marcus residence times 56
5.6 Conclusion 59
5.7 Publication II 60
5.8 Outlook and continuation of research into TPA-based OMIEC materials 75
  5.8.1 Glass transition temperature 75
  5.8.2 Ion diffusion and swelling 76

6 Constrained GFN2-xTB **79**
6.1 Constrained DFT 79
6.2 Implementation 79
6.3 Test calculations 81
6.4 Conclusion 82
6.5 Manuscript I 82

7 Excited state characterization of TADF emitters **95**
7.1 Computational approach 96
7.2 Excited state characterization and photophysical properties 97
7.3 Conclusion 101

8 Conclusion and outlook **103**

9 Publications and conferences **107**

A Appendix **109**
A.1 Supporting Information Publication I 109
A.2 Supporting Information Publication II 127

Bibliography **153**

CHAPTER 1

Introduction

1.1 Organic Electronics

Electronic devices such as batteries, light-emitting diodes, transistors and solar cells are a vital part of modern life. They enable the use of computers, energy storage, communication, lighting and other key technologies that contemporary science and societies are unquestionably dependent upon. [1] Without exaggeration, it can also be stated that they have become so intertwined with technological progress that they have become essentially indispensable. Perhaps most striking in this context is the case of transistor research, which has developed a self-perpetuating nature within the validity of Moores Law, [2] stating that the number of transistors on a computer chip doubles every one to two years: Computers, which rely on transistors, are central to the generation of scientific insight. Such insight is then used in turn to build better transistors, which are then again used to obtain new insight and so on and so forth in a cycle of innovation. As such a deeply integrated feature of modern life and technology, electronic device research constitutes a broad and ever-evolving scientific field, both as object and tool of research. Owing to its inherently diverse and multiscale nature, the field of electronics encompasses multiple disciplines from chemical synthesis, device physics and manufacturing, quantum chemistry, spectroscopy and many more.

A large part of such research efforts consists of investigation into the materials used to fabricate the devices. Traditionally, inorganic materials such as metals or metal oxides as well as silicon are used for various electronic and semiconducting applications. However, since the discovery of their conductivity by Heeger, Shirakawa and MacDiarmid in 1977, [3, 4] organic, i.e. hydrocarbon-based materials were emerging as a new class of (semi-)conductors, creating the field of Organic Electronics. The first application of an organic material as a core component of an electronic application was fabricated already ten years later in Xerox machines by Tang and Van Slyke. [5] More than the pure pursuit of scientific knowledge, the field of Organic Electronics, branching into e.g. light emission [6], electrochemical energy storage [7] or neuromorphic devices, [8] also holds the promise for solutions to the energy crisis, [9, 10] medicinal progress [9] or an environmentally sustainable future. [11] While the blessings of modern technological progress are certainly undeniable, critical assessment of the ever-growing technological sector must not be foregone, since it can also be detrimental and destabilizing to society, e.g. via mass surveillance, [12] especially due to its self-reinforcing nature as described above.

Various compound classes have emerged and are continuosly being researched and improved. They can be categorized e.g. by their function, i.e. hole- or electron transport materials, emitters, absorbers etc., or by their structure, i.e. small molecules or polymers in an amorphous or (semi-)crystalline state. Generally, the great advantage of organic functional materials compared to inorganic materials is the control over the molecular design, which is very promising for adapting the material to specific application requirements. Chemical engineering can be used to alter the electronic structure at the molecular level, i.e. for example orbital energies, ionization potentials, redox potentials or spectroscopic properties, as well as bulk properties such as crystallization or film formation affinity, solubility or glass transition temperatures. Similar well-known molecular structures are thus continuously being reused and applied in different ways, e.g. as hole- or electron transport layers (HTL or ETL), donor- or acceptor moieties in emitter or absorber layers or as OMIECs (Organic Mixed Ionic Electronic Conductors). [13–15]

Triphenylamines (**TPA**s) are a well-known material class for device applications and have found application in multiple areas of Organic Electronics. Their electron-rich character make them a good candidate for hole-transport layers in organic solar cells or organic light-emitting diodes. They have also been successfully used as active material in organic battery applications due to their high redox potential vs Li/Li^+ (> 3.5 V). Additionally, triphenylamine moieties are present in many organic functional materials such as donor-acceptor substituted TADF (thermally activated delayed fluorescence) emitters for light-emission applications. [16–18]

At the core of (Organic) Electronic applications lie the (semi-)conducting properties of the materials, enabling charge transport. Charge transport is a complex phenomenon related to composition and morphology of the materials as well as to structural properties. It is extremely complicated to predict the performance of any material solely from the molecular structure, since not only the aforementioned bulk properties are of equal importance, but also dynamical properties of the system over multiple time scales (e.g. thermal vibrations or coupling of electronic and ionic charge transport) are crucial to consider. Data-driven device engineering and rational design as well as scientific understanding of the processes at the core of electronic applications therefore require careful cooperation of experimental and theoretical research. [13, 19, 20]

The microscopic theoretical description of charge transport requires detailed knowledge about the electronic structure as well as the morphology of the material and the dynamical properties. [21–27] Such circumstances make the theoretical modeling of charge transport a daunting task. In principle, bottom-up multiscale approaches based on nonadiabatic molecular dynamics (NAMD) are able to describe both static and dynamic bulk properties and include the electronic structure as well as nuclear motion, however due to the enormous computational cost, they are limited to small system sizes and short simulation times. [28–30] More efficiently but perhaps less accurate, especially in complex cases of intermediate charge transport regimes, the morphology can be modeled atomistically or in a coarse-grained fashion on the basis of classical force fields, while the molecular properties relevant to charge transport are described at the quantum chemical level. Such simulations can then be coupled with charge-transport simulations to gain the necessary insight into properties such as the charge mobility. [21, 24] Alternatively, in a top-down approach, phenomenological fitting of various models to numerical results from simulation data can be performed. [31] Analytical methods for the charge mobility such as the extended Gaussian disorder model (EGDM) [32] or the appropriately parametrized analytical equation (APAE) [33] approach also exist. In all cases, the goal of such theoretical investigations is to obtain knowledge and understanding of electronic devices through careful modeling.

1.2 Triphenylamines for Organic Electronics

In this thesis, a bottom-up multiscale modeling approach for triphenylamines (**TPA**s) in organic electronic applications is presented. They are investigated both as hole-transport materials (HTM) and as cathode materials for organic batteries. In order to elucidate structure-property relationships, aspects of molecular structure and polymer chemistry are correlated to micro- and bulk structural properties as well as charge transport processes, also comparing the results to available experimental data. Therefore, the compound class is introduced here in detail.

TPAs are versatile and well-researched compounds that can be used for various applications. They appear for example as hole-transporting materials in OLEDs or OSCs [16, 34–36] or as active materials in Organic Batteries. [37, 38] The general structure of **TPA** is shown in Fig. 1.1.

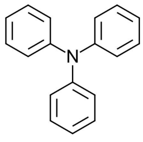

TPA

Figure 1.1: Molecular structure of **TPA**.

The geometry of **TPA** and many of its derivatives is generally governed by the equilibrium between resonance stabilization of the π-electron system requiring flat dihedral angles and the steric repulsion of the protons of neighbouring phenyl rings requiring a more twisted conformation. These opposing forces result in a propeller-like geometry. [17, 35] In terms of electronic behaviour, **TPA** derivatives are known for their electron-rich character, making them ideal HTM candidates. [17] Finally, **TPA** derivatives can easily be modified synthetically, which enables fine-tuning of e.g. their redox- and spectroscopic properties. [17]

The electrochemical behaviour of **TPA**s is well-known. Upon oxidation, the **TPA** radical cation undergoes quick and irreversible dimerization in the *para*-position relative to the nitrogen atom. The dimer is even more easily oxidizable, leading to a quick formation of the dication, which reverts to its charge-neutral form through loss of two protons. [39–41] The possibility of electrochemical oxidation followed by dimerization enables use of **TPA**s as redox-active cross-linking units for the formation of conductive polymers, while the electron-donating character of **TPA**s can be exploited for designing donor-acceptor type molecules for organic electronic applications. [17]

Design and modification of **TPA**s can follow multiple strategies. Substitution influences electrochemical coupling and can modify e.g. the ionization potential [16, 17, 39], while increase of the conjugated system stabilizes the radical cation, in analogy to conjugated polymers. [42] The **TPA** derivatives investigated in this work are shown in Fig. 1.2. While the **TPA**, **TPD**, **FTPD** and ***spiro*-OMeTAD** can be used as monomeric hole transporters, oxetane-functionalized **TPAs** can be employed as cross-linkable hole-transport layers or OMIECs, with the main advantage of enabling solution processability. [36, 43–45] Once deposited, cross-linking makes the material insoluble, preventing degradation of the film. [36] Moreover, cross-linking of oxetanes only leads to low volume-shrinkage compared to other cross-linking modalities. [46]

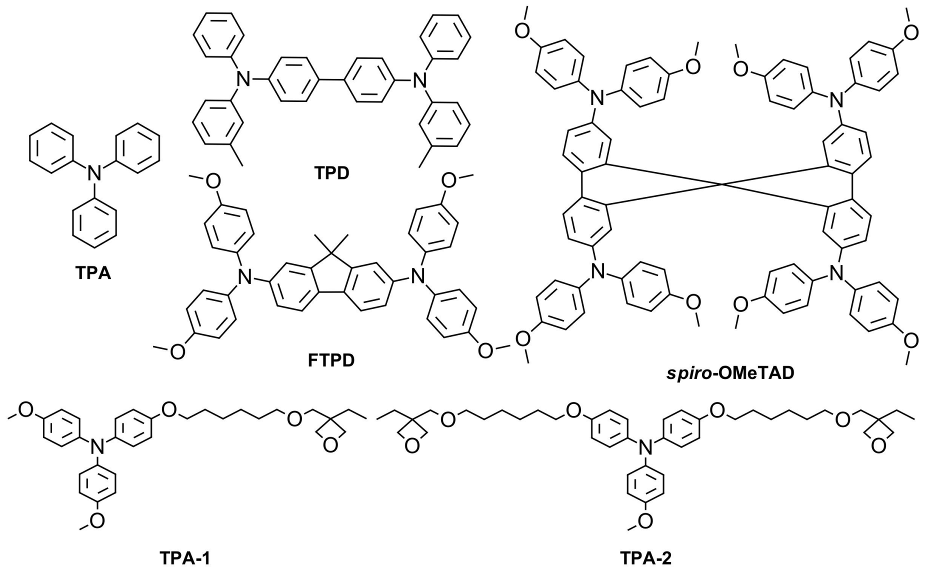

Figure 1.2: **TPA** derivatives investigated in this work.

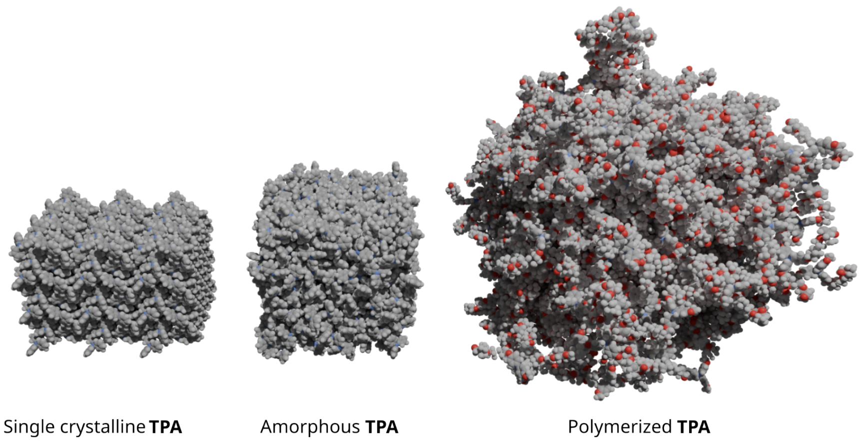
Single crystalline **TPA**
Amorphous **TPA**
Polymerized **TPA**

Figure 1.3: Visualization of the bulk structures of single crystalline and amorphous **TPA** as well as polymerized oxetane-functionalized **TPA-1**.

In addition to the electronic properties, the morphology of the materials is of utmost relevance to the device application. In Fig. 1.3, visualizations of different morphologies as obtained from molecular dynamics simulations are shown. Generally, highly ordered structures such as (semi-)crystalline materials exhibit higher charge mobilities, however, device fabrication can be more complex and a lower thermal stability can occur. As mentioned before, polymeric materials can be more easily processed and exhibit higher stability at the cost of lower mobilities.

Based on these features, many device applications for **TPA**s are conceivable. The insolubility of cross-linked **TPA**s combined with the good hole- and ion-transporting properties makes them attractive for electrochemical applications such as rechargeable batteries or electrochemical transistors (OECT), where the material appears as OMIEC. Both in monomeric or polymeric form they can also be used for hole-transport layers in e.g. OLED, OSC or OFET applications. Generally, chemical modifications can be applied in order to tailor the material to specific application requirements. Fig. 1.4 shows an overview over the possible device applications of **TPA**s.

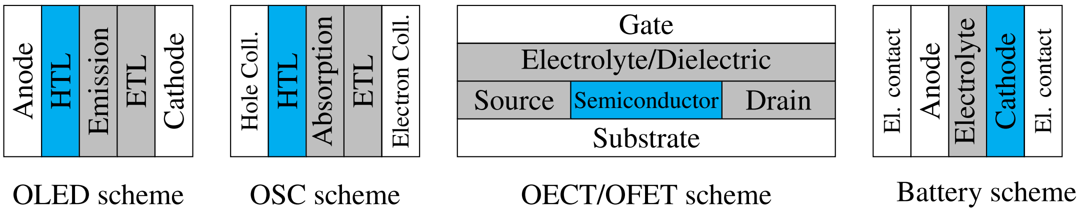

Figure 1.4: Schematic overview of electronic device architectures. The blue areas indicate possible applications for **TPA**s.

Hole Transport Materials: In their function as hole transport materials, **TPA**s need to exhibit a high mobility and should be reasonably processable and stable. In a device architecture as shown in Fig. 1.4, HTL, ETL as well as emissive or absorptive layers are sandwiched in between the current collectors. The energy levels of the individual layers are typically tailored chemically to fit to the neighbouring layers, enabling highly efficient and stable devices by avoiding dark current and degradation. **TPA** based materials are among the most efficient organic hole-transporting materials.

Electrochemical Application: Using **TPA**s as an OMIEC for electrochemical applications has different requirements. Both high electronic and ionic mobilities are desirable, but due to the contact with an electrolyte, insolubility is also of high importance.

Electrochemical Energy Storage: **TPA**s can be used as cathode material in lithium ion batteries, where under discharge operation both charge and ion movement is important for device operation. In addition to high electronic and ionic mobilities and insolubility, for electrochemical energy storage additional energetic requirements dictate the design choices.

The basic characteristics and performance indicators of electrochemical energy storage systems are the cell voltage, capacity, specific energy as well as energy and power density. Ideally, the cell configuration consists of materials that are light and have a high capacity and voltage, optimizing overall performance, however many practical hurdles such as reactivity or difficulties in practical handling restrict the possible combinations. Different electrochemical energy storage technologies therefore vary significantly in their characteristics. They can be designed with e.g. the goal of high power- or energy density as well as high rechargeability or even recyclability, depending on the demands of the application. Nowadays, large research efforts into materials design are directed towards reducing the amount of inactive components to improve energy density or increasing rechargability.

[47] **TPA**s have a relativey high redox potential vs. Li/Li^+ (> 3.5 V) and thus a high cell voltage compared to other materials such as e.g. carbonyl redox polymers. [48] Compared to e.g. directly polymerized variants, cross-linked **TPA**s sacrifice specific capacity and energy density due to the larger monomer mass in exchange for higher cycleability.

1.3 Donor-Acceptor substituted compounds for organic light emitting diodes

A different important class of organic functional materials for device applications are emitter compounds, which can be used in OLEDs. For such applications, the photophysical properties are of central importance. In order to achieve highly efficient emitter materials, multiple aspects are relevant, which can be addressed by molecular design. The central quantity to be maximized is the quantum yield. Due to spin statistics, only 25 % of excitations can be exploited for light emission since emission from the triplet states is quantum mechanically forbidden. However, in systems with small singlet-triplet energy gaps, efficient intersystem crossing and thus triplet upconversion can be observed, leading to TADF (thermally activated delayed fluorescence) and quantum yields of up to 100 %. Such small singlet-triplet gaps can be achieved e.g. by donor-acceptor substitution and orbital separation. [49] Other design considerations include the impact of the molecular design on the emission wavelength and the molecular orientation in an OLED so as to achieve maximum outcoupling efficiency by horizontal alignment of the molecular transition dipole moment, thermal stability, processability and others. [50–52]

Due to the heterogeneous aspects that need to be considered, efficient emitter design amounts to a very complex task. In order to understand the performance of different materials in OLEDs, it is crucial to thoroughly characterize the compounds combining experimental and computational approaches. This thesis includes the excited-state photophysical characterization of TADF emitters, as synthesized in the Meerholz group by Christopher Wallerius. The goal of this investigation was to unravel the effect of the molecular design approach on the photophysical properties of the compounds and rationalize their OLED performance.

1.4 Method development for multiscale modeling approaches

In addition to the multiscale modeling of various organic functional materials, this thesis also encompasses method development related to modeling approaches. Many multiscale modeling approaches rely e.g. on force field parametrization and the accurate determination of charge transport parameters which are often evaluated on the basis of density functional theory or wave function methods. Such methods can be very computationally demanding, introducing the need for efficient yet sufficiently accurate schemes. Constrained DFT (CDFT) has proven to be a useful tool in the earlier mentioned research activities. It has been used for the calculation of reorganization energies, the description of highly dipolar molecules and charge transfer excited states as well as various other works. [53–55] Since CDFT is computationally too expensive for calculations on larger systems, a less computationally demanding method is desirable, providing the motivation to implement a constraint-methodology in the framework of tight-binding DFT methodology (e.g., GFN2-xTB) which is presented in this thesis.

CHAPTER 2

Scope of thesis

This thesis mainly focuses on the multiscale modeling of **TPA**s for organic electronic applications. To understand the structure-property relationships with regard to the hole transport in **TPA**s, the morphology and hole transport in a series of **TPA** derivatives, as shown in Fig 2.1 was modeled. Special attention was given to the relationship between structural complexity, morphology and charge transport for a number of **TPA** derivatives with increasing complexity. By modeling the hole transport in both single crystalline as well as the amorphous morphologies, the limits of ordered versus disordered systems were considered. The results have been published in Publication I. [56]

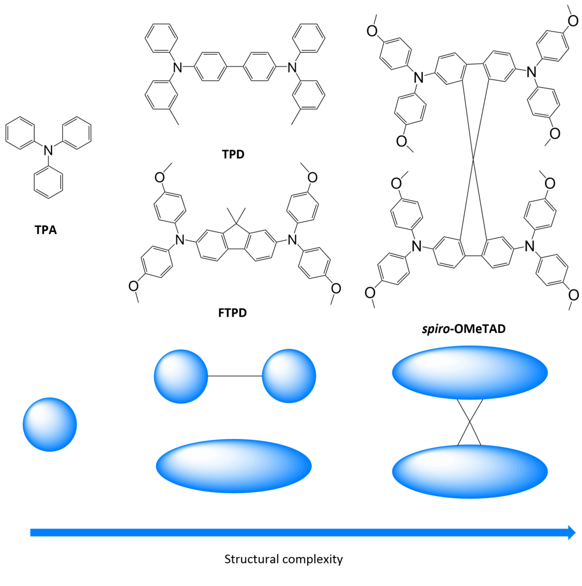

Figure 2.1: **TPA** derivatives with increased structural complexity as investigated in Publication I.

In a second investigation, the coupled hole- and ion transport in polymerized **TPA** systems for OMIEC applications was modeled. Since the experimental morphology of the polymerized **TPA**s is not known due to their insolubility, a heuristic approach was taken to model the polymerization reaction *in silico*. With the polymerized systems at hand, the relation between molecular and bulk structure, glass transition temperature as well as hole- and ion transport properties was investigated as illustrated in Fig. 2.2. In order to investigate the mixed ionic-electronic conduction mechanism in **TPA**s central to OMIEC application, a novel approach based on effective Marcus residence times was devised. Specifically, this approach captures the influence of dynamic disorder on the charge transport. The results have been published in Publication II [57].

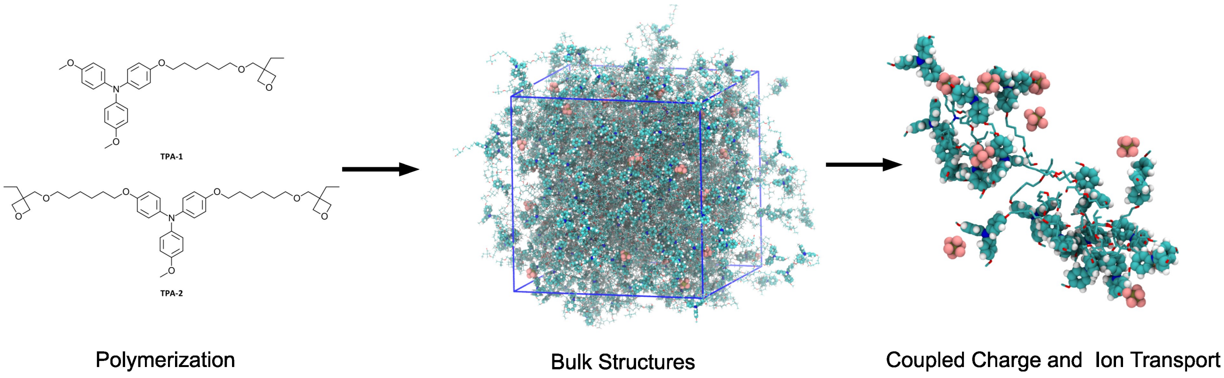

Polymerization

Bulk Structures

Coupled Charge and Ion Transport

Figure 2.2: Investigation into the mixed electronic and ionic transport in cross-linked **TPA**s in Publication II.

In addition to this core investigation, an implementation of the constrained DFT formalism was done in the framework of GFN2-xTB (CxTB). CxTB was implemented to facilitate fast and accurate computation of charge transport parameters as well as various general purpose applications. This implementation is presented and discussed in Manuscript I.

As a further investigation into organic functional materials, the excited state properties, including the reverse intersystem crossing rates of a series of TADF emitters was investigated in order to elucidate the effect of using different donor moieties and bridging units in donor-acceptor substituted emitter compounds.

CHAPTER 3

Theory

3.1 Charge transport

The central process in any (Organic) Electronics application is the charge transport. In the more specific context of Organic Electrochemical applications, two different types of charge transport are of central importance: electronic and ionic charge transport. Both are discussed here first generally on the basis of classical physics using the textbook by Wolfgang Demtröder [58] and then in more detail at the quantum mechanical level.

3.1.1 Classical physics

Without an external field, free charge carriers move diffusively. They are scattered from collisions with e.g. solvent molecules, randomly distributing their direction of travel, leading to an overall zero mean current density $\bar{\mathbf{j}}$

$$\bar{\mathbf{j}} = nq\bar{\mathbf{v}} = \mathbf{0} \tag{3.1}$$

where n is the charge carrier density, q is the elemental charge and $\bar{\mathbf{v}}$ is the average velocity. Applying an electric field $\mathbf{E}$ introduces a force $\mathbf{F}_{el}$

$$\mathbf{F}_{el} = q\mathbf{E} \tag{3.2}$$

acting on the charge carriers with the mass m, which in turn leads to an acceleration $\mathbf{a} = \frac{\mathbf{F}_{el}}{m}$. Due to the acceleration, the charge carriers obtain an additional velocity

$$\Delta\mathbf{v} = \mathbf{a}\tau_s \tag{3.3}$$

which depends on the mean free time τ_s. $\Delta\mathbf{v}$ is small compared to $\mathbf{v}$. The mean additional velocity is the drift velocity $\mathbf{v}_D$

$$\mathbf{v}_D = \langle\Delta\mathbf{v}\rangle \tag{3.4}$$

which generates charge transport along the electric field. Importantly, $\mathbf{v}_D$ is constant despite the acceleration due to the electric field, because scattering leads to a constant changing of the direction of travel of the charge carriers and due to $\mathbf{v}_D \ll \mathbf{v}$, all directions have the same probability. [58]

Ohm's law establishes the relationship between current density $\mathbf{j}$ and the electric field and is given by

$$\mathbf{j} = \sigma_{el}\mathbf{E} \tag{3.5}$$

with the electrical conductivity σ_{el} being a material constant. σ_{el} depends on the charge carrier concentration n and the charge mobility μ and is given by

$$\sigma_{el} = en\mu. \tag{3.6}$$

The mobility μ itself results from the drift velocity $\mathbf{v}_D$ and the electric field $\mathbf{E}$ [58]

$$\mu = \frac{\mathbf{v}_D}{\mathbf{E}}. \tag{3.7}$$

In a diffusive regime, the charge carrier mobility is given by the Einstein-Smoluchowski equation [59, 60]

$$\mu = \frac{Dq}{k_B T} \tag{3.8}$$

where D is the diffusion coefficient, k_B is Boltzmann's constant and T is the temperature. μ is one of the central parameters to characterize the charge transport in any material. The diffusion coefficient is given by

$$D = \lim_{t\to\infty} \frac{MSD}{6t}. \tag{3.9}$$

It is important to note here, that $\mathbf{v}_D$ is not necessarily proportional to $\mathbf{E}$, meaning that μ still depends on $\mathbf{E}$. [13]

3.1.2 Ion transport

For ionic transport in dilute solutions, similar considerations can be made. In absence of an electric field, the ions move diffusively and no net charge transport is found. Applying an electric field, the force acting on the ions is given by eq. 3.2. Considering the ionic charge number z and the elementary charge e, eq. 3.2 can be written as [61]

$$\mathbf{F}_{el} = ze\mathbf{E} \tag{3.10}$$

Stokes law gives the frictional force counteracting the electric field as [61]

$$\mathbf{F}_f = -6\pi\eta\mathbf{r}\mathbf{v} \tag{3.11}$$

where η denotes the solvents viscosity, $\mathbf{r}$ denotes the ion radius and $\mathbf{v}$ denotes the velocity. Constant velocity is found in the equilibrum of electric and frictional forces [61]

$$\mathbf{F}_{el} = \mathbf{F}_f. \tag{3.12}$$

Thus, $\mathbf{v}$ can be obtained as [61]

$$\mathbf{v} = \frac{zeE}{6\pi\eta\mathbf{r}} \tag{3.13}$$

Finally, the mobility μ is calculated from $\mathbf{v}$ and $\mathbf{E}$ [61]

$$\mu = \frac{v}{\mathbf{E}} = \frac{ze}{6\pi\eta\mathbf{r}}. \tag{3.14}$$

μ depends on η and therefore also on the temperature and pressure. The ion radius and concentration also influence μ. [61]

3.1.3 Quantum mechanical charge transport

To describe the charge transport in molecular materials such as organic semiconductors in detail, classical physics is not sufficient. Generally, the sites involved in the charge transfer reaction can be molecules, parts of molecules or polymers. In the molecular orbital picture, hole transport consists of electron transfer at the HOMO (Highest occupied molecular orbital) level, while electron transport is the same phenomenon at the LUMO (Lowest unoccupied molecular orbital) level. [13] As it is quite useful for understanding general concepts of charge transport theory, the general tight-binding, second-quantized one electron Hamiltonian for charge transport is discussed first. It can be written as [62]

$$\hat{H} = \hat{H}_0 + \hat{H}_1 + \hat{H}_2 + \hat{H}_3 + \hat{H}_4 \tag{3.15}$$

with

$$\begin{aligned}
\hat{H}_0 &= \sum_i \epsilon_i a_i^\dagger a_i + \sum_\lambda \hbar\omega_\lambda \left(b_\lambda^\dagger b_\lambda + \frac{1}{2} \right) \\
\hat{H}_1 &= \sum_{i \neq j} J_{ij} a_i^\dagger a_j \\
\hat{H}_2 &= \sum_\lambda \sum_i g_{i\lambda}^2 \hbar\omega_\lambda a_i^\dagger a_i (b_\lambda + b_{-\lambda}^\dagger) \\
\hat{H}_3 &= \sum_{i \neq j} \sum_\lambda f_{ij\lambda}^2 \hbar\omega_\lambda a_i^\dagger a_j (b_\lambda + b_{-\lambda}^\dagger) \\
\hat{H}_4 &= \sum_i \delta\epsilon_i a_i^\dagger a_i + \sum_{i \neq j} \delta J_{ij} a_i^\dagger a_j
\end{aligned} \tag{3.16}$$

where $a_i^\dagger$ and a_i refer to the annihilation and creation operators for electrons or holes on site i, and $b_\lambda^\dagger$ and b_λ refer to the annihilation and creation operators of phonons. ϵ_i is the site energy while J_{ij} is the electronic coupling with the corresponding fluctuations $\delta\epsilon_i$ and δJ_{ij} due to disorder. $g_{i\lambda}$ and $f_{ij\lambda}$ are electron-phonon coupling constants to the respective vibrational mode with frequency ω_λ. $\hat{H}$ does not consider electron correlation and coulombic interactions. [13, 62]

The term $\hat{H}_0$ corresponds to the total energy of the system without electron-phonon coupling. $\hat{H}_1$ contains the electronic coupling term between two sites describing electron transfer. $\hat{H}_2$ and $\hat{H}_3$ on the other hand contain the electron-phonon coupling terms, often also referred to as polaronic effects. While $\hat{H}_2$ modulates the energy of a site due to interaction with a certain mode, the last term, $\hat{H}_3$ modulates the transition probability between two sites. Finally, $\hat{H}_4$ contains the static disorder terms due to e.g. structural and morphological disorder. Diagonalization of such a Hamiltonian yields eigenvalues and eigenstates that correspond to the energies of the various distributions of the charge on the available sites. [13, 62]

Depending on the dominant terms in $\hat{H}$, different charge transport regimes are distinguished. If $\hat{H}_1$ is dominant, the charge transport is band transport which is mostly found in crystalline materials. On the other hand, if $\hat{H}_2$ and $\hat{H}_3$ are dominant, polaronic transport is found. Lastly, if $\hat{H}_4$ is dominant, the transport is called disorder-controlled as is typically the case in amorphous organic materials. Both polaronic and disorder-controlled charge transport are types of hopping transport that are distinctly different from band-like charge transport although intermediate or mixed regimes also exist. [13, 30, 62]

Band transport

In the first case discussed above, that is if $\hat{H}_1$ is dominant, the charge transport is found to be band transport which is typically the case in defect-free crystalline materials. Due to the large J_{ij}, the charge carriers are delocalized and form a Bloch wave that propagates through the system and can be scattered by lattice vibrations. The mobility in this charge transport regime is given by

$$\mu = \frac{\mathrm{e}\tau}{m_{\mathrm{eff}}} \tag{3.17}$$

with τ the mean scattering time and m_{eff} the effective hole or electron mass. Experimentally, band transport can be distinguished from other forms of transport by investigating the temperature dependence of the mobility. For band transport

$$\mu \propto T^{-n}, 0 < n < 3 \tag{3.18}$$

is found, as μ decreases at elevated temperature due to increased scattering. [13]

Hopping transport

If any of the terms $\hat{H}_2$, $\hat{H}_3$ or $\hat{H}_4$ are dominant, the charge carriers become localized and hopping transport is found. For example, $\hat{H}_4$ is often dominant in the case in amorphous organic solids, which show high structural (conformational) and morphological disorder. Such disorder leads to a broad distribution in site energies and consequently a large $\hat{H}_4$ term. The terms $\hat{H}_2$ and $\hat{H}_3$ are large in the case of strong electron-phonon coupling where large geometric variation is connected to charge transfer. Hopping transport is generally characterized by incoherent transfer events. In order for charge transfer to occur, an activation energy barrier has to be overcome. In contrast to band transport, the temperature dependence of the mobility in hopping transport is given by [19]

$$\mu = \mu_0 \exp\left(-\frac{E_a}{k_B T}\right) \tag{3.19}$$

where μ_0 is the prefactor mobility and E_a is an activation energy. Elevated temperature leads to an increased mobility μ by providing the necessary energy to overcome the activation barriers. [13, 19]

In the case of an ordered, i.e. crystalline, organic solid, where strong electron-phonon coupling prevails, $\hat{H}_2$ and $\hat{H}_3$ are dominant. Charge transfer is coupled to intra- and intermolecular vibrational modes, meaning that the charge forms a *polaron*. Polaronic charge transport is described by the

Holstein model. [63, 64] Here, the electronic transfer rate k_{ET} is given as

$$k_{ij} = \frac{J_{ij}^2}{\hbar}\sqrt{\frac{\pi}{2E_{pol}k_BT}}\exp\left(-\frac{E_{pol}}{2k_BT}\right) \tag{3.20}$$

where E_{pol} is the polaron binding energy that corresponds to the energy of geometric reorganization related to the charge transfer event. For weak electron-phonon coupling, the Holstein model predicts decreased mobility with increased temperature, while the inverse is true for strong electron phonon coupling. Thus, the Holstein model correctly captures the temperature dependence trends of charge transport. [13]

In disordered (amorphous) organic solids, the charge transport is often controlled by $\hat{H}_4$, i.e. the broad distribution of site energies, also termed static disorder. In this case, the hopping sites vary in energy and spatial distribution, and the charge transport corresponds to a random walk. The Miller-Abrahams model gives the electron transfer rate for disorder-controlled charge transport as

$$k_{ij} = \nu_0\exp(-2\gamma r_{ij}) \times \begin{cases} \exp[-(\epsilon_j - \epsilon_i)/k_BT] & \epsilon_j > \epsilon_i \\ & \epsilon_j < \epsilon_i \end{cases} \tag{3.21}$$

where r_{ij} is the inter-site distance, γ is the inverse localization radius and ν_0 is the attempt-to-hop frequency. [65]

In many systems, superpositions of different charge transport regimes are realized, meaning that both static and dynamic disorder are important factors that need to be considered. For such systems, Marcus-Theory is a useful approach. In Marcus-Theory, the charge transfer rate is given as

$$k_{ij} = \frac{2\pi}{\hbar}\frac{J_{ij}^2}{\sqrt{4\pi\lambda k_BT}}\exp\left[-\frac{(\Delta E + \lambda)^2}{4\lambda k_BT}\right] \tag{3.22}$$

where λ is the reorganization energy corresponding to the energy of geometric relaxation upon charge transfer and ΔE is the total energy difference between the initial and final states of the charge transfer process. [66–68]

3.2 Charge transport parameters

In the following, the charge transport parameters and their calculation within the framework of the `VOTCA` [21] program package are discussed, as they are of high significance to this work.

3.2.1 Site energy

The total energy difference between two molecules $\Delta E_{ij} = E_i - E_j$ in the Marcus eq. 3.22 is the driving force for the charge transfer between two sites i and j. This term approximates the change in Gibbs free energy ΔG^0 which is found in the original equation of Marcus. [66–68] Multiple different factors contribute to ΔE_{ij}.

Internal energy difference: The internal energy difference corresponds to the differences in the adiabatic ionization potential between sites i and j in the case of hole transport and to the adiabatic electron affinity in the case of electron transport. It can be written as

$$\Delta E_{ij}^{int} = \Delta U_i - \Delta U_j = (U_i^{cC} - U_i^{nN}) - (U_j^{cC} - U_j^{nN}) \tag{3.23}$$

Here, $U_i^{cC(nN)}$ denotes the total energy of site i in the charged state and geometry (cC) and the neutral state and geometry (nN). In the case of one-component systems and only minor conformational changes, ΔE_{ij}^{int} can be neglected in good approximation. [21]

Electric field: In the case of an externally applied electric field, an additional contribution to the site energy differences is given by

$$\Delta E_{ij}^{ext} = q(\mathbf{F}\mathbf{r}_{ij}) \tag{3.24}$$

with $\mathbf{F}$ denoting the electric field, q denoting the charge and $\mathbf{r}_{ij}$ denoting the distance vector between sites i and j. [21]

Electrostatic interaction energy: The atomic partial charges of surrounding molecules constitute an electric field that influences the site energy differences. Such an electrostatic interaction energy difference ΔE_{ij}^{el} can be calculated as

$$E_i^{el} = \frac{1}{4\pi\epsilon_0} \sum_{a_i} \sum_{b_k, k \neq i} \frac{(q_{a_i}^c - q_{a_i}^n) q_{b_k}^n}{\epsilon_s r_{a_i b_k}} \tag{3.25}$$

using the atomic partial charges of the neutral and charged species $q_{a_i}^n$ and $q_{a_i}^c$ as well as the relative static dielectric constant ϵ_s and the interatomic distance $r_{a_i b_k}$ between atoms a_i and b_k belonging to molecule i and the surrounding molecules k. Within `VOTCA`, the molecule for which the site energy difference is calculated is placed in the center of the box in order to minimize edge effects. [21]

Polarization effects: Polarization effects are an important part to consider for calculating the site energies. They screen the electrostatic interactions and lead to an overall more realistic description of the site energy differences. In eq. 3.25, ϵ_s can be used in a simple approach to include electrostatic screening of the site energies. The Clausius-Mosotti-equation can be used to calculate bulk dielectric constants as

$$\epsilon_s = 1 + \frac{12\pi\alpha N/V}{3 - 4\pi\alpha N/V} \tag{3.26}$$

where α is the molecular polarizability, N is the number of molecules and V is the box volume. [69] Such an uniform scaling approach is however incapable of describing microscopic polarization effects. A more accurate description can be achieved by employing a self-consistent approach to obtain the polarization fields. Within `VOTCA` this is achieved by using a polarizable force field based on the `TINKER` implementation of the Thole model. [70, 71] The electric field $\mathbf{F}_{a_i}^0$ for the atom a belonging to molecule i is computed employing no screening $\epsilon_s = 1$. Based on $\mathbf{F}_{a_i}^0$, the initial induced dipoles $\boldsymbol{\mu}_{a_i}^0$ can be computed. They are then iteratively refined using

$$\boldsymbol{\mu}_{a_i}^{k+1} = \omega \mathbf{F}_{a_i}^k \alpha_{a_i} + (1 - \omega)\boldsymbol{\mu}_{a_i}^k \tag{3.27}$$

with α_{a_i} the atomic polarizability and ω a successive overrelaxation factor. Based on the induced dipoles, the new electric fields can be calculated until the procedure converges. [21]

3.2.2 Electronic coupling

The definition of the electronic coupling J_{ij} that enters the Marcus equation 3.22 is given by

$$J_{ij} = \left\langle \Psi_i | \hat{H} | \Psi_j \right\rangle \tag{3.28}$$

where $\hat{H}$ denotes the electronic Hamiltonian of the dimer and Ψ_i and Ψ_j denote the wavefunctions of the initial and final states of the charge transport pair. [21]

In typical approaches to obain J_{ij}, the frozen orbital approximation is employed and the dimer frontier orbitals are developed in terms of the monomer frontier orbitals ϕ^i and ϕ^j. Solving the generalized secular equation

$$(\mathbf{H} - E\mathbf{S})\mathbf{C} = 0 \tag{3.29}$$

as formed from the the Hamiltonian $\mathbf{H}$, the eigenvalues E and the overlap matrix $\mathbf{S}$, the expansion coefficients $\mathbf{C}$ are obtained. [72, 73] $\mathbf{H}$ and $\mathbf{S}$ are given by

$$\mathbf{H} = \begin{pmatrix} e_i & J_{ij} \\ J_{ij} & e_j \end{pmatrix} \tag{3.30}$$

and

$$\mathbf{S} = \begin{pmatrix} 1 & S_{ij} \\ S_{ij} & 1 \end{pmatrix} \tag{3.31}$$

with the matrix elements

$$e_i = \left\langle \phi^i | \hat{H} | \phi^i \right\rangle \tag{3.32}$$

$$e_j = \left\langle \phi^j | \hat{H} | \phi^j \right\rangle \tag{3.33}$$

$$J_{ij} = \left\langle \phi^i | \hat{H} | \phi^j \right\rangle \tag{3.34}$$

$$S_{ij} = \left\langle \phi^i | \phi^j \right\rangle \tag{3.35}$$

The nonorthonormality of the basis set leads to $\mathbf{S} \neq \mathbf{1}$, and makes transformation of $\mathbf{H}$ to an orthonormal form $\mathbf{H}^{eff}$ necessary. This can e.g. be achieved by the Löwdin transformation [72, 73]

$$\mathbf{H}^{eff} = \mathbf{S}^{-\frac{1}{2}} \mathbf{H} \mathbf{S}^{-\frac{1}{2}} \tag{3.36}$$

Thus, one obtains

$$\mathbf{H}^{eff}\mathbf{C} = E\mathbf{C} \tag{3.37}$$

with

$$\mathbf{H}^{eff} = \begin{pmatrix} e_i^{eff} & J_{ij}^{eff} \\ J_{ij}^{eff} & e_j^{eff} \end{pmatrix} = \begin{pmatrix} \epsilon_i & t_{ij} \\ t_{ij} & \epsilon_j \end{pmatrix} \tag{3.38}$$

The elements of $\mathbf{H}^{eff}$ can be written as [72, 73]

$$e_{i(j)}^{eff} = \epsilon_{i(j)} = \frac{1}{2}\frac{1}{1 - S_{ij}^2}\left((e_i + e_j) - 2J_{ij}S_{ij}(e_i - e_j)\sqrt{1 - S_{ij}^2} \right) \tag{3.39}$$

and

$$J_{ij}^{eff} = t_{ij} = \frac{J_{ij} - \frac{1}{2}(e_i + e_j)S_{ij}}{1 - S_{ij}^2} \tag{3.40}$$

The HOMO-HOMO-1 energy splitting ΔE of the dimer is given by [72, 73]

$$\Delta E = \sqrt{(\epsilon_i - \epsilon_j)^2 - (2t_{ij})^2} \tag{3.41}$$

thus, the transfer ingetral can be obtained from the dimer frontier orbital energies via [72, 73]

$$t_{ij} = \frac{1}{2}\sqrt{(\Delta E^2 - (\epsilon_i + \epsilon_j)^2)}. \tag{3.42}$$

Electronic coupling via dimer projection (DIPRO): The dimer projection method (DIPRO) as developed by Baumeier et al. [72] is one approach to approximate J_{ij}. The dimer orbitals of **H** form an orthonormal set. Thus,

$$\mathbf{1} = \sum_A |\psi_A\rangle\langle\psi_A| \tag{3.43}$$

can be inserted into eq. 3.34 to obain

$$J_{ij} = \langle\phi^i \sum_i |\psi_A\rangle\langle\psi_A|\hat{H}| \sum_j |\psi_B\rangle\langle\psi_B|\phi^j\rangle = \sum_{ij} \langle\phi^i|\psi_A\rangle\langle\psi_A|\hat{H}|\psi_B\rangle\langle\psi_B|\phi^j\rangle \tag{3.44}$$

which can be succinctly rewritten as

$$J_{ij} = \sum_i \gamma_A^i \epsilon_i \gamma_B^j = \gamma_A^i \mathrm{diag}(\epsilon_i)\gamma_B^j \tag{3.45}$$

where $\langle\phi^i|\psi_i\rangle = \gamma_i^i$ are the eponymous projections. These projections are then determined by expanding the monomer and dimer orbitals in counterpoise atom-centered basis functions. As has also been shown by Baumeier et al., using a non-counterpoise basis set leads to only negligible errors and can thus be used as an acceptable approximation. [72]

Electronic Coupling via molecular orbital overlap (MOO): A different approximate method for the calculation of J_{ij} is based on the ZINDO-Hamiltonian. Using the ZINDO-approach allows for much faster evaluation of the coupling integrals at the cost of reduced accuracy due to the neglect of polarization effects. [74] In the ZINDO approach, the modifications to $e_{i(j)}$ and J_{ij} due to nonorthonormality vanish. [72]

The MOO method projects the molecular orbitals of the dimers onto the basis of the monomer molecular orbitals. The construction of the Hamiltonian in the monomer basis, requiring only one self-consistent calculation on an isolated monomer. [74]

The ZINDO Hamilton matrix elements are given by [74]

$$\hat{H}_{\mu\nu} = S_{\mu\nu}\frac{(\beta_a + \beta_b)}{2} + P_{\mu\nu}\frac{\gamma_{ab}}{2} \tag{3.46}$$

a and b denote the atomic centers on which μ and ν orbitals are centered, $S_{\mu\nu}$ denote the elements of the overlap matrix, β denote the bonding parameters, $P_{\mu\nu}$ denote the density matrix elements and γ denotes the Mataga–Nashimoto potential. The block-orthogonality of $P_{\mu\nu}$ means that it does not contribute to $\hat{H}_{\mu\nu}$, leaving the determination of $S_{\mu\nu}$ as the only remaining task. [74]

3.2.3 Reorganization energy

The geometric changes upon charge transfer events are quantified by the reorganization energy λ. λ can be split up into an inner and an outer contribution, where the inner part λ_i considers the geometric variation of the charge transfer site, while the outer part λ_o is due to the relaxation of the surrounding environment. [13]

$$\lambda = \lambda_i + \lambda_o \tag{3.47}$$

Adiabatic potential method: In this work, the adiabatic four-point method is used to compute the internal reorganization energies [75]

$$\lambda_i = \left(E^{(1)}(M) - E^{(0)}(M)\right) + \left(E^{(1)}(M^{+\bullet}) - E^{(0)}(M^{+\bullet})\right). \tag{3.48}$$

Here, $E^{(0)}(M)$ and $E^{(0)}(M^{+\bullet})$ denote the energies of the equilibrium geometries of the neutral and charged state, whereas $E^{(1)}(M^{+\bullet})$ and $E^{(1)}(M)$ denote the energies of the neutral and charged equilibrium geometries in the differetly charged state. The procedure is illustrated in Fig. 3.1.

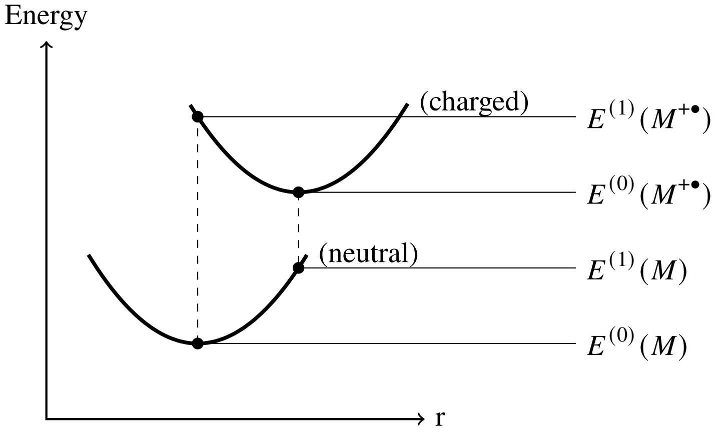

Figure 3.1: Illustration for the calculation of the reorganization energy from the adiabatic potential energy surfaces.

3.3 Static and dynamic disorder

As they are highly relevant factors in this work, the terms static and dynamic disorder are here discussed in more detail. Static disorder refers to a time-independent spread in charge transport parameters (generally the site energies and the electronic coupling) due to various underlying disorder types (e.g morphological, conformational or electrostatic disorder). Dynamic disorder on the other hand refers to time-dependent fluctuations of such parameters due to e.g. molecular motion or vibration. Typically both disoder types are present in a real system but can vary in magnitude. In this work, static disorder is found due to the conformational and morphological disorder and at the electrostatic level due to the inclusion of polarization effects. Other approaches include e.g. embedding methods to describe microscopic polarization. [76, 77] Dynamic disorder is evaluated explicitly on the basis of evaluating the charge transport parameters over the time-evolution of the systems. Both static and dynamic disorder have also been evaluated efficiently on the basis of incorporating machine-learning models into multiscale simulations. [22]

3.4 Thermally activated delayed fluorescence

Thermally activated delayed fluorescence (TADF) is a photophysical phenomenon in which delayed fluorescence is observed due to the thermal upconversion of triplet excitons to singlet excitons. [78–80] A basic state diagram for the relevant photophysical processes is shown in Fig. 3.2.

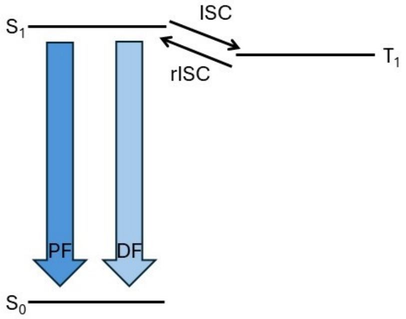

Figure 3.2: State diagram showing the TADF process. Light emission occurs due to prompt fluorescence (PF) and delayed fluorescence (DF). The populations of T_1 and S_1 are determined by intersystem crossing (ISC) and reverse intersystem crossing (ISC), respectively.

The rate of prompt fluorescence k_{PF} is given by [81–83]

$$k_{PF} = \frac{2\pi e^2 n^3 f \omega^2}{\epsilon_0 \mathrm{m}_e c} \tag{3.49}$$

where ω denotes the excitation energy, n denotes the refractive index of the medium, f denotes the oscillator strength, ϵ_0 denotes the dielectric constant, c denotes the speed of light and m_e denotes the electron mass. The fluorescence decay time is given by [81–83]

$$\tau_{PF} = \frac{1}{k_{PF} + k_{IC} + k_{ISC}} \tag{3.50}$$

where k_{PF}, k_{IC} and k_{ISC} denote the rates of prompt fluorescence, internal conversion (IC) and intersystem crossing (ISC). k_{IC} is often negligible for TADF emitters. The TADF rate k_{TADF} depends on k_{PF} and the population of S_1 which is determined by k_{ISC} and k_{rISC} the reverse intersystem crossing rate. If $\mathrm{k}_{rISC} \gg \mathrm{k}_{PF}$, S_1 and T_1 can be modeled as in a thermal equilibrium, and the S_1 population depends only on the adiabatic singlet triplet gap ΔE_{ST} [81–83]

$$k_{TADF} = k_{PF} \cdot \frac{1}{1 + 3\exp(\Delta E_{ST}/k_B T)}. \tag{3.51}$$

This equation corresponds to an upper limit of the TADF rate.

As the most important factor for TADF, k_{rISC} is given by [80]

$$k_{rISC} = \frac{2\pi}{\hbar} \frac{|\hat{H}_{SO}|^2}{\sqrt{4\pi k_B T}} \exp\left[- \frac{E_A}{k_B T} \right] \tag{3.52}$$

where $\hat{H}_{SO}$ is the spin-orbit coupling, λ is the reorganization energy and E_A is the activation energy. The latter is given by

$$E_A = \frac{(\Delta E_{ST} + \lambda)^2}{4\lambda} \tag{3.53}$$

with ΔE_{ST} denoting the adiabatic singlet-triplet gap.

3.5 Methods

3.5.1 Electronic structure theory

The basis of electronic structure theory is the Schrödinger equation

$$\hat{H}\Psi = E\Psi \tag{3.54}$$

where $\hat{H}$ is the molecular Hamiltonian operator, Ψ is the wavefunction and E is the total energy. $\hat{H}$ is defined as

$$\begin{aligned} \hat{H} &= -\sum_{i=1}^{n} \frac{\hbar^2}{2m_e}\nabla_i^2 - \sum_{I=1}^{N} \frac{\hbar^2}{2M_I}\nabla_I^2 - \sum_{i=1}^{n}\sum_{I=1}^{N} \frac{Z_I e^2}{4\pi\varepsilon_0 r_{iI}} + \sum_{I>J} \frac{Z_I Z_J e^2}{4\pi\varepsilon_0 r_{IJ}} + \sum_{i>j} \frac{e^2}{4\pi\varepsilon_0 r_{ij}} && (3.55) \\ &= E_{el}^{kin} + E_{nuc}^{kin} + E_{nuc-el}^{pot} + E_{nuc-nuc}^{pot} + E_{el-el}^{pot} && (3.56) \end{aligned}$$

where the physical meaning of each term is noted below. In eq. 3.55, $\hbar$ is Planck's constant divided by 2π, m_e is the mass of an electron, M_I is the mass of nucleus I, r_{iI} is the distance between electron i and nucleus I, r_{IJ} is the distance between nucleus I and nucleus J, r_{ij} is the distance between electron i and electron j, Z_I is the nuclear charge, e is the elemental charge and ϵ_0 is the dielectric constant of vacuum. In atomic units, eq. 3.55 becomes

$$\hat{H} = -\sum_{i=1}^{n} \frac{1}{2}\nabla_i^2 - \sum_{I=1}^{N} \frac{1}{2M_I}\nabla_I^2 - \sum_{i=1}^{n}\sum_{I=1}^{N} \frac{Z_I}{r_{iI}} + \sum_{I>J} \frac{Z_I Z_J}{r_{IJ}} + \sum_{i>j} \frac{1}{r_{ij}}. \tag{3.57}$$

Due to the slow movement of nuclei compared to electrons, the former are treated as fixed points within the Born-Oppenheimer approximation, which further simplifies eq. 3.57 to

$$\hat{H}_{el} = -\sum_{i=1}^{n} \frac{1}{2}\nabla_i^2 - \sum_{i=1}^{n}\sum_{I=1}^{N} \frac{Z_I}{r_{iI}} + \sum_{i>j} \frac{1}{r_{ij}}. \tag{3.58}$$

Solving the Schrödinger equation yields the wavefunction Ψ which contains information about the quantum mechanical system. Unfortunately, analytical solution of eq. 3.54 is not possible except for very simple systems. Therefore, many approximate methods have been developed. The basis of many later approaches is Hartree-Fock theory and the Self-Consistent field (SCF) procedure, where a mean-field approach is used to obtain a non-correlated approximate wavefunction. [84]

The ansatz for Ψ in wavefunction theory is a Slaterdeterminant Ψ^{SD} given by

$$\Psi^{SD}(1,2,3,...,n) = \frac{1}{\sqrt{n!}} \begin{vmatrix} \chi_1(1) & \chi_2(1) & ... & \chi_n(1) \\ \chi_1(2) & \chi_2(2) & ... & \chi_n(2) \\ \vdots & \vdots & \ddots & \vdots \\ \chi_1(n) & \chi_2(n) & ... & \chi_n(n) \end{vmatrix} \tag{3.59}$$

where $\frac{1}{\sqrt{n!}}$ is the normalization constant, and $\chi_i(i)$ are spin orbitals. Slaterdeterminants fulfill the Pauli principle due to which a many-electron wavefunction must be antisymmetric with respect to the interchange of the spin- or spatial coordinates of two electrons. [84]

Due to the variational principle, which states that the energy of any approximate trial wavefunction is always higher than the energy of the true wavefunction, the orbitals that make up Ψ^{SD} can be systematically varied in order to obtain an optimal Ψ^{SD}. Using an approach of Lagrange minimization and the constraint that the orbitals remain orthonormal, the functional L can be written as

$$L = \left\langle \Psi^{SD} | \hat{H} | \Psi^{SD} \right\rangle - E(\left\langle \Psi^{SD} | \Psi^{SD} \right\rangle - 1) \tag{3.60}$$

with E the lagrangian multiplier. Setting the first variation of L to zero leads to the equation

$$f|\chi_a\rangle = \sum_{b=1}^{N} \epsilon_{ba} |\chi_b\rangle \tag{3.61}$$

for the spin orbitals. However, due to the unitary invariance of the spin orbitals, eq. 3.61 can be rewritten in its canonical form as

$$f|\chi_a\rangle = \epsilon_a |\chi_a\rangle \tag{3.62}$$

which is the Hartree-Fock equation for a single spin orbital. The SCF procedure can be employed to solve the matrix version of eq. 3.62, known as the Roothaan-Hall equation, as given by eq. 3.63.

$$\mathbf{FC} = \mathbf{SC}\epsilon \tag{3.63}$$

Since 3.62 depends on its own solutions, the SCF is an iterative approach. [84]

Improving on this description are Configuration Interaction and Coupled Cluster which include electron correlation by using more than one Slaterdeterminant at increased computational cost.[84]

3.5.2 Density functional theory

Density functional theory (DFT) is another approximate method to solve eq. 3.54 which is based on the electron density instead of the wavefunction. [85]

The one-particle electron density of a system is related to the wavefunction by [85]

$$\rho(\mathbf{r}_1) = n \int ... \int |\Psi(x_1, x_2, ..., x_n)|^2 \mathrm{d}\sigma_1 \mathrm{d}x_2 ... \mathrm{d}x_n \tag{3.64}$$

where n is the number of electrons, x_i is the spatial coordinate and σ_i is the spin coordinate. Based on $\rho(\mathbf{r})$, the number of electrons can be consequently obtained by[85]

$$\int \rho(\mathbf{r})\mathrm{d}\mathbf{r} = n. \tag{3.65}$$

The Hohenberg-Kohn theorems [86] show that the ground-state of a system is fully described by the electron density by showing that the external potential is uniquely defined. $\rho(\mathbf{r})$ contains the number of electrons as well as the number and positions of nuclei via the position and magnitude of the maxima in $\rho(\mathbf{r})$. Furthermore, the variational principle is applicable to the functional of the energy $E_{DFT}[\rho]$. [85]

$E_{DFT}[\rho]$ is given by [85, 87]

$$E_{DFT}[\rho] = T[\rho] - \sum_{I}^{N} Z_I \int \frac{\rho(\mathbf{r})}{\mathbf{R}_I - \mathbf{r}}\mathrm{d}\mathbf{r} + \frac{1}{2}\iint \frac{\rho(\mathbf{r}_i)\rho(\mathbf{r}_j)}{\mathbf{r}_i - \mathbf{r}_j}\mathrm{d}\mathbf{r}_i\mathrm{d}\mathbf{r}_j + K[\rho] \tag{3.66}$$

with $T[\rho]$ being the kinetic energy, the second and third term being the nuclear-electron interaction and coulombic interaction term and $K[\rho]$ being the exchange interaction term. [85] $K[\rho]$ and $T[\rho]$ can not be expressed analytically in terms of the density and thus need to be approximated. In the Kohn-Sham approach, a Slaterdeterminant of spin orbitals is used to approximate the missing terms. [85, 87]

Splitting up the kinetic energy in a correlated $T_c[\rho]$ and a non-interacting part $T_0[\rho]$ gives [85, 87]

$$T[\rho] = T_0[\rho] + T_c[\rho] \tag{3.67}$$

with

$$T_0[\phi] = -\frac{1}{2}\sum_{i=1}^{n} \langle \phi_i | \Delta | \phi_i \rangle. \tag{3.68}$$

Now, all unknown parts of $E_{DFT}[\rho]$ can be summed up in the Exchange-Correlation term $E_{XC}[\rho]$

$$E_{XC}[\rho] = T_c[\rho] + K[\rho]. \tag{3.69}$$

This term is topic of much research and is approximated with different approaches and at many different levels of theory. [85, 87] Finally, to obtain the Kohn-Sham Orbitals, the Kohn-Sham equations are solved analogously to Hartree-Fock with the SCF procedure. They are given by [85, 87]

$$\left(-\frac{1}{2}\nabla_1^2 - \sum_{I=1}^{N} \frac{Z_I}{\mathbf{r}_{I1}} + \int \frac{\rho(\mathbf{r}_2)}{\mathbf{r}_{12}}\mathrm{d}\mathbf{r}_2 + V_{XC}(\mathbf{r}_1)\right)\phi_i(\mathbf{r}_1) = \epsilon_i\phi_i(\mathbf{r}_1) \tag{3.70}$$

where $V_{XC}[\rho]$ is given by [85, 87]

$$V_{XC}[\rho] = \frac{\partial E_{XC}[\rho]}{\partial \rho} \tag{3.71}$$

3.5.3 Excited state methods

Excited state methods are used to treat the electronic excitations in many-particle systems. Multiple approaches exist, e.g. Configuration Interaction Singles (CIS), time-dependent Hartree-Fock (TDHF) or time-dependent density-functional theory (TDDFT). An overview over excited state methods is given here. [88]

CIS

CIS is the simplest scheme to obtain excited states. It uses the Hartree-Fock ground state as a basis, which is obtained by solving eq. 3.63 and consists of a single Slater determinant. As the Hartree-Fock method in a basis of size K yields n occupied and $K-n$ virtual orbitals, the CIS wavefunction Ψ_{CIS} is then expanded as a linear combination of the ground state and all singly substituted Slater determinants Φ_i^a

$$\Psi_{CIS} = \sum_{ia} c_i^a \Phi_i^a(\mathbf{r}) \tag{3.72}$$

where c_i^a denotes the expansion coefficient, i denote the occupied and a denote the virtual orbitals. [88]

Eq.3.72 can be inserted in the time-independent Schrödinger equation eq. 3.54 and left multiplied with $\langle \Phi_j^b |$ to form

$$\sum_{ia} \langle \Phi_j^b | \hat{H} | \Phi_i^a \rangle c_i^a = E_{CIS} \sum_{ia} c_i^a \delta_{ij} \delta_{ab}. \tag{3.73}$$

Using

$$\langle \Phi_j^b | \hat{H} | \Phi_i^a \rangle = (E_0 + \epsilon_a - \epsilon_i)\delta_{ij}\delta_{ab} + (ia||jb) \tag{3.74}$$

where $(ia||jb)$ denotes the antisymmetrized two-electron integrals, ϵ denote the orbital energies, E_0 denotes the ground state energy and δ the Kronecker delta, one obtains for the excitation energies $\omega_{CIS} = E_{CIS} - E_0$

$$\sum_{ia} ((\epsilon_a - \epsilon_i)\delta_{ij}\delta_{ab}) + (ia||jb))c_i^a = \omega_{CIS} \sum_{ia} c_i^a \delta_{ij}\delta_{ab}. \tag{3.75}$$

Eq. 3.75 can be rewritten in matrix form as

$$\mathbf{AX} = \omega \mathbf{X} \tag{3.76}$$

with $A_{ia,jb} = (\epsilon_a - \epsilon_i)\delta_{ij}\delta_{ab}) + (ia||jb)$. Solving

$$(\mathbf{A} - \omega)\mathbf{X} = 0 \tag{3.77}$$

then yields the excitation energies as eigenvalues and the expansion coefficients as eigenvectors. [88] CIS is a conceptually simple size-consistent method that has the advantage of being analytically differentiable, making analytical gradients possible. However, CIS typically overestimates excitation energies since determinants derived from the Hartree-Fock ground state only poorly approximate the excited states because the virtual orbital energies are calculated for the (N+1) system. Furthermore, CIS mostly neglects electron correlation. [84, 88]

TDHF

Time-dependent Hartree-Fock (TDHF) approximates the solution to the time-dependent Schrödinger equation

$$\hat{H}\Psi(\mathbf{r},t) = i\frac{\partial}{\partial t}\Psi(\mathbf{r},t) \tag{3.78}$$

with a single Slater determinant. In eq. 3.78, $\hat{H}(\mathbf{r},t)$ is the time-dependent Hamiltonian, which is supplemented with a time-dependent potential

$$\hat{V}(\mathbf{r},t) = \sum_{i}^{N} \hat{v}_i(\mathbf{r},t). \tag{3.79}$$

This leads to the time-dependent Fock equation

$$\hat{F}\Phi(\mathbf{r},t) = i\frac{\partial}{\partial t}\Phi(\mathbf{r},t) \tag{3.80}$$

which not only contains a time-dependent potential explicitly in the time-dependent Fock operator $\hat{F}(\mathbf{r},t)$ but is also time-dependent implicitly due to the time-dependent orbitals influencing the exchange and coulomb operators. The TDHF equations can be obtained by first-order perturbation theory, i.e. the linear response of the orbitals and the time-dependent Fock operator. They are of the same form as the TDDFT equations which are discussed next. Generally, TDHF has similar properties compared to CIS, however it is known to show triplet instabilities. [88]

TDDFT

TDDFT can be viewed as the time-dependent variant of ground state DFT. [88, 89] The foundation of TDDFT is the Runge-Gross theorem, stating that TDDFT exactly describes the time-evolution of a many-electron system on the basis of the electron density. [90] As such, it is analogous to the first Hohenberg-Kohn theorem. The second Hohenberg-Kohn theorem states that the variational principle holds for DFT. In the case of TDDFT, if the condition

$$\Psi(\mathbf{r},t_0) = \Psi_0(\mathbf{r},t) \tag{3.81}$$

holds for the time-dependent wavefunction, then the exact wave function is the one that leads to a stationary point in the action integral $A[\rho]$ in accordance with Hamiltons principle. $A[\rho]$ can be written as a functional of ρ due to the first Hohenberg-Kohn theorem

$$A[\rho] = \int_{t_0}^{t_1} dt \left\langle \Psi[\rho](\mathbf{r},t) \middle| i\frac{\partial}{\partial t} - \hat{H}(\mathbf{r},t) \middle| \Psi[\rho](\mathbf{r},t) \right\rangle \tag{3.82}$$

and it can be made stationary with respect to the variation of $\rho(\mathbf{r},t)$, such that $A[\rho]$ does not change with small perturbations of the density

$$\frac{\partial A[\rho]}{\partial \rho(\mathbf{r},t)} = 0. \tag{3.83}$$

$A[\rho]$ can be reformulated as

$$A[\rho] = B[\rho] - \int_{t_0}^{t_1} \mathrm{d}^3\mathbf{r}\rho(\mathbf{r},t)v(\mathbf{r},t) \tag{3.84}$$

with $v(\mathbf{r},t) = \hat{V}_{el-nuc}(\mathbf{r}) + \hat{V}(\mathbf{r},t)$ the external potential and $B[\rho]$ the universal functional

$$B[\rho] = \int_{t_0}^{t_1} dt \left\langle \Psi[\rho](\mathbf{r},t) \middle| i\frac{\partial}{\partial t} - \hat{T}(\mathbf{r},t) - \hat{V}_{el-el}(\mathbf{r}) \middle| \Psi[\rho](\mathbf{r},t) \right\rangle. \tag{3.85}$$

Similar to the Kohn-Sham approach described earlier, a non-interacting time-dependent reference system $\rho_S(\mathbf{r},t)$ subject to an external one-particle potential $v_S(\mathbf{r},t)$ is assumed which is equal to the exact electron density $\rho(\mathbf{r},t)$ so that

$$\rho(\mathbf{r},t) = \rho_S(\mathbf{r},t) = \sum_i^N |\phi_i(\mathbf{r},t)|^2. \tag{3.86}$$

This leads to

$$i\frac{\partial}{\partial t}\phi_i(\mathbf{r},t) = \left(-\frac{1}{2}\nabla_i^2 + v_S(\mathbf{r},t) \right)\phi_i(\mathbf{r},t) \tag{3.87}$$

for the determination of $\rho(\mathbf{r},t)$, which is now determined by both eq. 3.86 and eq. 3.87. Using both equations and some further derivation, the time-dependent Kohn-Sham equations are obtained

$$i\frac{\partial}{\partial t}\phi_i(\mathbf{r},t) = \left(-\frac{1}{2}\nabla_i^2 + v(\mathbf{r},t) \int \mathrm{d}^3\mathbf{r}' \frac{\rho(\mathbf{r}',t)}{|\mathbf{r}-\mathbf{r}'|} + \frac{\partial A_{XC}[\rho]}{\partial \rho(\mathbf{r},t)} \right)\phi_i(\mathbf{r},t) \tag{3.88}$$

where

$$A_{XC}[\rho] = B_S[\rho] - \frac{1}{2}\int_{t_0}^{t_1} \mathrm{d}t \int \mathrm{d}^3\mathbf{r} \int \mathrm{d}^3\mathbf{r}' \frac{\rho(\mathbf{r},t)\rho(\mathbf{r}',t)}{|\mathbf{r}-\mathbf{r}'|} - B[\rho] \tag{3.89}$$

and

$$B_S[\rho] = \int_{t_0}^{t_1} dt \left\langle \Psi[\rho](\mathbf{r},t) \middle| i\frac{\partial}{\partial t} - \hat{T}(\mathbf{r},t) \middle| \Psi[\rho](\mathbf{r},t) \right\rangle. \tag{3.90}$$

Omitting the detailed derivation (available e.g. in [88]), the TDDFT equations are obtained in matrix form by using a density matrix based perturbation theory approach. They are given by [88]

$$\begin{bmatrix} \mathbf{A} & \mathbf{B} \\ \mathbf{B}^* & \mathbf{A}^* \end{bmatrix} \begin{bmatrix} \mathbf{X} \\ \mathbf{Y} \end{bmatrix} = \omega \begin{bmatrix} \mathbf{1} & \mathbf{0} \\ \mathbf{0} & \mathbf{-1} \end{bmatrix} \begin{bmatrix} \mathbf{X} \\ \mathbf{Y} \end{bmatrix} \tag{3.91}$$

where $A_{ia,jb} = \delta_{ij}\delta_{ab}(\epsilon_a - \epsilon_i) + (ia||jb)$ and $B_{ia,jb} = (ia||bj)$, while $\mathbf{X}$ and $\mathbf{Y}$ correspond to the excitations and deexcitations with the energies ω. [88] Setting the $\mathbf{B}$ matrix to zero corresponds to the Tamm-Dancoff approximation (TDA) and leads to the CIS expansion in the case of TDHF. The advantage of TDDFT lies in more accurate excitation energies depending on which exchange-correlation functional is used. Additionally, TDDFT shows more favourable computational scaling. However due to the self-interaction error present in standard DFT, TDDFT exhibits large errors e.g. for charge transfer excitations. Such problems can be overcome by using range-separated functionals. [88]

ΔSCF

ΔSCF is an elegant and powerful alternative to TDDFT for certain cases. In the ΔSCF approach, excited states are obtained by converging the SCF procedure to an excited state, i.e. a higher energy self-consistent solution. [91–93] Thus, the excited state is obtained as a ground state of the SCF. The existence of such solutions has been proven [94, 95], however such solutions are difficult to obtain since the SCF algorithm is designed to find the lowest-energy solution. [91–93]

Gilbert et al. introduced the Maximum Overlap Method (MOM) as a systematic approach to obtain higher-energy solutions through the SCF. [91] In each iteration of the SCF procedure, the Fock matrix is rebuilt from the current coefficient matrix. Normally, the lowest energy orbitals are chosen as occupied, following the *aufbau* principle. However in the MOM protocol, the orbitals which have the largest overlap with the span of the old orbitals are chosen. The orbital overlap is given as

$$\mathbf{O} = (\mathbf{C}^{old})^{\dagger}\mathbf{S}\mathbf{C}^{new} \tag{3.92}$$

Therefore, the projection p_j of the jth new orbital onto the old orbitals is given by

$$p_j = \sum_i^n O_{ij} = \sum_\nu^N [\sum_\mu^N (\sum_i^n C_{i\mu}^{old}) S_{\mu\nu}] C_{\nu j}^{new}. \tag{3.93}$$

If the starting orbitals are chosen to represent the desired excited state, the MOM procedure ensures that the occupation scheme always corresponds to the target state. Thus, the excited state is obtained as the ground state solution to the SCF. [91] The related Initial Maximum Overlap Method (IMOM) uses the inital set of orbitals to determine the overlap and thus the occupied orbitals and is therefore more likely to converge to a specific excited state solution.

Corzo et al. later introduced the Projection-based Maximum Overlap Method (PMOM) and the Projection-based Initial Maximum Overlap Method (PIMOM). [92] While relying on the same basic scheme, these methods use a projection operator corresponding to a target density in the basis of either the initial or the current orbitals to determine the orbital occupation. [92] The PMOM/PIMOM schemes define a target density operator P^{target} in the MO space as

$$P^{target} = \sum_i |i^{target}\rangle\langle i^{target}| \tag{3.94}$$

which can be represented at each SCF step as

$$P_{pq}^{target} = \langle p|P^{target}|q\rangle = \sum_i \langle p|i^{target}\rangle\langle i^{target}|q\rangle \tag{3.95}$$

or in AO basis as

$$P_{pq}^{target} = \sum_i \sum_{\mu\nu} \sum_{\lambda\sigma} C_{\mu p} S_{\mu\lambda} C_{\lambda j}^{target} C_{\sigma i}^{target} S_{\sigma\nu} C_{\nu q}. \tag{3.96}$$

Such a modified *aufbau* metric leads to a superior performance when compared to MOM and IMOM, and can robustly access excited states not available via the other methods. [92]

The general advantage of ΔSCF methods compared with TDDFT is its low computational cost and even more importantly that it considers orbital relaxation effects on the excited state energies and geometries. Therefore, ΔSCF has been shown to outperform TDDFT in many aspects, like the prediction of Singlet-Triplet gaps. [96] However at the same time it is limited to single-determinantal systems, limiting it to a certain class of problems. [93]

3.5.4 GFN2-xTB

GFN2-xTB is based on the density functional tight binding (DFTB) method, which assumes that the electron density ρ of a system can be expanded in terms of fluctuations $\delta\rho$ around atomic reference densities ρ_0. [97]

$$E[\rho] = E^{(0)}[\rho_0] + E^{(1)}[\rho_0, \delta\rho] + E^{(2)}[\rho_0, \delta(\rho)^2] + E^{(3)}[\rho_0, \delta(\rho)^3] + ... \tag{3.97}$$

Employing such fixed reference densities, all electronic structure calculations can be done in terms of the density fluctuations. Eq. 3.97 is typically truncated differently, giving rise to various levels of DFTB. [97] In GFN2-xTB, density fluctuations up to the third term are included. Furthermore, in contrast to other implementations, a nonlocal VV10-type correlation is included which is essential for the description of long-range correlation and dispersion effects. The typical assumption that the density fluctuations are only relevant to the valence orbital space is also made for GFN2-xTB. The energy expression of GFN2-xTB is given by

$$E_{GFN2-xTB} = E_{rep} + E_{disp} + E_{EHT} + E_{IES+IXC} + E_{AES} + E_{AXS} + G_{Fermi}. \tag{3.98}$$

The terms in $E_{GFN2-xTB}$ denote the repulsive, dispersive, extended-Hückel-type, isotropic electrostatic, isotropic exchange correlation, anisotropic electrostatic, anisotropic exchange correlation and Fermi energy contributions, which are all expressed in terms of the density and its fluctuations. Employing a core Hamiltonian, the valence orbitals can then expanded in a minimal basis. As before, this leads to a standard eigenvalue problem which can be solved iteratively via the SCF procedure. [98]

3.5.5 Molecular dynamics

Molecular dynamics (MD) simulations describe the time-evolution of a system of atoms or molecules, which is typically done by integrating Newtons classic equation of motion [99]

$$\mathbf{F} = m\mathbf{a} \tag{3.99}$$

or in its differential form

$$-\frac{dV}{d\mathbf{r}} = m\frac{d^2\mathbf{r}}{dt^2} \tag{3.100}$$

where V is the potential at position $\mathbf{r}$. Its negative gradient represents the force $\mathbf{F}$ while the second derivative of the position with respect to the time represents the acceleration $\mathbf{a}$. The time-evolution of the system is given by the change in position of the particles, that is their trajectory. It can be calculated for discrete timesteps Δt as [99]

$$\mathbf{r}_{i+1} = \mathbf{r}_i + \frac{\partial\mathbf{r}}{\partial t}(\Delta t) + \frac{1}{2}\frac{\partial^2\mathbf{r}}{\partial t^2}(\Delta t)^2 + \frac{1}{6}\frac{\partial\mathbf{r}^3}{\partial t^3}(\Delta t)^3 + ... \tag{3.101}$$

which can be expressed as

$$\mathbf{r}_{i+1} = \mathbf{r}_i + \mathbf{v}_i(\Delta t) + \frac{1}{2}\mathbf{a}_i(\Delta t)^2 + \frac{1}{6}\mathbf{b}_i(\Delta t)^3 + ... \tag{3.102}$$

with $\mathbf{v}_i$ denoting the velocities, $\mathbf{a}_i$ denoting the accelerations, $\mathbf{b}_i$ denoting the hyperaccelerations etc. Analogously, the positions at an earlier timestep can be calculated by

$$\mathbf{r}_{i-1} = \mathbf{r}_i - \mathbf{v}_i(\Delta t) + \frac{1}{2}\mathbf{a}_i(\Delta t)^2 - \frac{1}{6}\mathbf{b}_i(\Delta t)^3 + ... \tag{3.103}$$

where $-\Delta t$ has been used instead of Δt. The positions at a later timestep can be calculated by combining eqs. 3.102 and 3.103 via addition to form

$$\mathbf{r}_{i+1} = (2\mathbf{r}_i - \mathbf{r}_{i-1}) + \mathbf{a}_i(\Delta t)^2 + ... \tag{3.104}$$

$\mathbf{a}_i$ can be obtained from the force as

$$\mathbf{a}_i = \frac{\mathbf{F}_i}{m}. \tag{3.105}$$

Here, the terms due to $\mathbf{b}_i$ vanish, making this approach correct up to the third order. This approach is called the Verlet-algorithm and can be used to obtain the trajectory and this the time-evolution of the system. The Verlet-algorithm has two drawbacks, mainly numerical instabilities due to the addition of a relatively small number in Δt to the difference of two relatively large numbers $(2\mathbf{r}_i - \mathbf{r}_{i-1})$ as well as the problem that the velocities do not appear in eq. 3.104, making it more complicated to relate it to the kinetic energy and thus the temperature. The leap-frog algorithm can be used to improve this approach by using a half-step for the timestep [99]

$$\mathbf{r}_{i+1} = \mathbf{r}_i + \mathbf{v}_{i+\frac{1}{2}}\Delta t^2 \tag{3.106}$$

which gives for the velocity

$$\mathbf{v}_{i+1} = \mathbf{v}_i + \frac{1}{2}(\mathbf{a}_i + \mathbf{a}_{i+\frac{1}{2}})\Delta t. \tag{3.107}$$

The outlined procedure constitutes the numerical integration of Newtons equation of motion. What remains to be discussed is how the Forces $\mathbf{F}$ are obtained within a simulation for which multiple approaches and levels of theory exist. In ab initio MD, the forces are generated by electronic structure calculations. In most simulations however, the forces are generated on the basis of classical force fields. Assuming a ball-and-spring model for the molecular geometry, the force field energy E_{FF} can be written as a superposition of multiple contributions as [99]

$$E_{FF} = E_{bond} + E_{angle} + E_{torsion} + E_{nonbonded} \tag{3.108}$$

where E_{bond} denotes the bond stretching term, E_{angle} denotes the angle bending term, $E_{torsion}$ denotes the torsional potential term and $E_{nonbonded}$ denotes the nonbonded, i.e. coulombic and Lennard-Jones terms. Depending on the assumptions behind the force field, different terms and varying functional forms of the terms are present. [99] Here, the OPLS force field is discussed as it is employed throughout this thesis. The OPLS force field is given by [100, 101]

$$E^{OPLS}_{bond} = \sum_{bonds} K_r(r - r_{eq})^2 \tag{3.109}$$

$$E^{OPLS}_{angle} = \sum_{angles} K_\theta(\theta - \theta_{eq})^2 \tag{3.110}$$

$$\begin{aligned} E^{OPLS}_{torsion} = \sum_i \frac{V_1^i}{2}[1 + \cos(\phi_i - f_{i,1})] + \frac{V_2^i}{2}[1 - \cos(2\phi_i - f_{i,2})] \\ + \frac{V_3^i}{2}[1 + \cos(3\phi_i - f_{i,3})] + \frac{V_4^i}{2}[1 - \cos(4\phi_i - f_{i,4})] \end{aligned} \tag{3.111}$$

$$E^{OPLS}_{nonbonded} = \sum_{i>j} f_{ij}(\frac{q_i q_j \mathrm{e}^2}{r_{ij}} + 4\epsilon_{ij}(\frac{\sigma_{ij}^{12}}{r_{ij}^{12}} - \frac{\sigma_{ij}^6}{r_{ij}^6})) \tag{3.112}$$

The K_r, $K_{r,\theta}$ and V^i are the bonding, angular and torsional force constants. In eq. 3.109, r and r_{eq} are the (equilibrium) bond lengths, while in eq. 3.110, θ and θ_{eq} are the (equilibrium) angles. Similarly, in eq. 3.111, the ϕ_i are the torsional angles and the f_i are phase factors. Lastly, in eq. 3.112, q_i are the atomic partial charges, r_{ij} are the interatomic distances and σ_{ij} and ϵ_{ij} are the Lennard-Jones parameters. The standard combining rules of $\sigma_{ij} = (\sigma_{ii}\sigma_{jj})^{\frac{1}{2}}$ and $\epsilon_{ij} = (\epsilon_{ii}\epsilon_{jj})^{\frac{1}{2}}$ are applied, while f_{ij} is a fudge factor to scale 1,4-interactions with $f_{ij} = 0.5$, while $f_{ij} = 1.0$ otherwise. [100, 101]

3.5.6 Kinetic Monte Carlo

Monte Carlo methods are based on the use of random numbers for the numerical solution of problems. In the case of kinetic Monte Carlo (kMC), the problem at hand is the dynamical, or time evolution of a system, making it an alternative to MD simulations. However, while MD approaches simulate the time-evolution explicitly by integrating Newtons equations of motion on the basis of a force-field, kMC simulations instead focus on state-to-state dynamics on the basis of transition rates, thereby simulating the time-evolution of a system as a series of transitions between energetic minima. This allows kMC simulations to achieve trajectories on longer timescales than MD simulations. [13, 99, 102] In the case of disorder-controlled hopping transport, the time-evolution of the system can be expressed in the form of a general master equation for the populations $p_i(t)$ and $p_j(t)$ of sites i and j as [13]

$$\frac{\mathrm{d}p_i(t)}{\mathrm{d}t} = \sum_{j \neq i}[-k_{ij}p_i(t)[1 - p_j(t)] + k_{ji}p_j(t)[1 - p_i(t)]] \tag{3.113}$$

where k_{ij} are the charge transfer rates. In the case of low charge-carrier concentrations, eq. 3.113 reduces to [13]

$$\frac{\mathrm{d}p_i(t)}{\mathrm{d}t} = \sum_j[-k_{ij}p_i(t) + k_{ji}p_j(t)] \tag{3.114}$$

Solutions to eq. 3.114 can be obtained by kMC. In Markovian kinetics, a memoryless process where the probability of exiting state i is independent of the probability of entering state i previously is assumed. The system repeatedly loses its memory while attempting to exit a state, meaning that the probability of survival $p_{survival}(t)$ of a state is the same in each increment of time and can be described by first-order kinetics as [102]

$$p_{survival}(t) = \exp^{-k_{tot}t} \tag{3.115}$$

where the total escape rate k_{tot} is given by

$$k_{tot} = \sum_{j} k_{ij}. \tag{3.116}$$

For each pathway, one obtains analogously

$$p_{ij}(t) = \exp^{-k_{ij}t}. \tag{3.117}$$

A simple approach for a kMC simulation consists of the determination of all possible k_{ij} for the system and drawing a random number r from the interval $(0, 1)$ for each pathway. The escape time for each pathway t_{esc} can then be calculated by

$$t_{esc} = -\left(\frac{1}{k_{ij}}\right)\ln(r). \tag{3.118}$$

Lastly, the pathway with the smallest t_{esc} is chosen for the transfer event and the clock is advanced before repeating the process. [102]

3.6 Computational procedures

3.6.1 Software

In this work, multiple program packages have been used. Quantum chemical and semiempirical calculations have been performed with `Gaussian`, [103] `Orca`, [104] `NWChem`, [105] and `xTB`. [98] Molecular dynamics simulations have been performed with `Gromacs`, [106–108] and `Lammps`. [109, 110] Charge transport simulations have been performed with VOTCA. [21] For DFT calculations in solvents, the PCM model was used. [111, 112]

3.6.2 Force field parametrization

In order to run accurate molecular dynamics simulations, the force field parameters detailed in section 3.5.5 need to be determined. While certain parameters can be taken from the literature, it is often necessary to reparametrize the force field specifically for the compounds under investigation. Often times, due to the interdependence of the parameters, an iterative approach can be necessary. The workflow in Fig. 3.3 shows a typical approach. Based on the DFT optimized geometry of the most stable conformer of a compound, the partial charges and Lennard-Jones parameters can be determined. In this work, mostly the ωB97X-D [113]/6-311G* [114–116] level of theory was used for DFT calculations, while conformer searches were performed using `CREST` [117] at the coupled FF/GFN2-xTB level of theory. Partial charges and Lennard-Jones parameters were determined using CHELPG together with Lennard-Jones parameters from the literature or by using DDEC6 charges and

Lennard-Jones parameters as determined using `Chargemol` [118]. Following the determination of the charges and Lennard-Jones parameters, the Bond, Angle and Dihedral parameters are determined by fitting force field potential energy scans with the force field parameters set to zero to DFT potential energy scans using the corresponding bond- angle- or dihedral functional form prescribed by the force field. For this work, bonding and angle parameters were taken from the literature or from the standard force field parameters, while the dihedral parameters were determined from scratch. Finally, the force field is validated by comparing simulation data to experimental or ab initio data.

3.6.3 Charge transport simulations

Charge hopping transport was simulated in this work based on Marcus theory and kMC using the `VOTCA` [21] program package. The fundamental approach and workflow is shown in Fig. 3.3. The input bulk morphologies can be obtained from experiment (e.g. crystal structures from X-Ray diffraction) or from MD simulations. The input structures are then partitioned into hopping sites, which can be whole molecules or parts of molecules or polymers. For the designated hopping sites, the site energies, electronic couplings and reorganization energies are determined which are then used to obtain the Marcus charge transport rates. Based on the charge transfer rates, the kMC simulations can be run which are then used to calculate the final charge mobility.

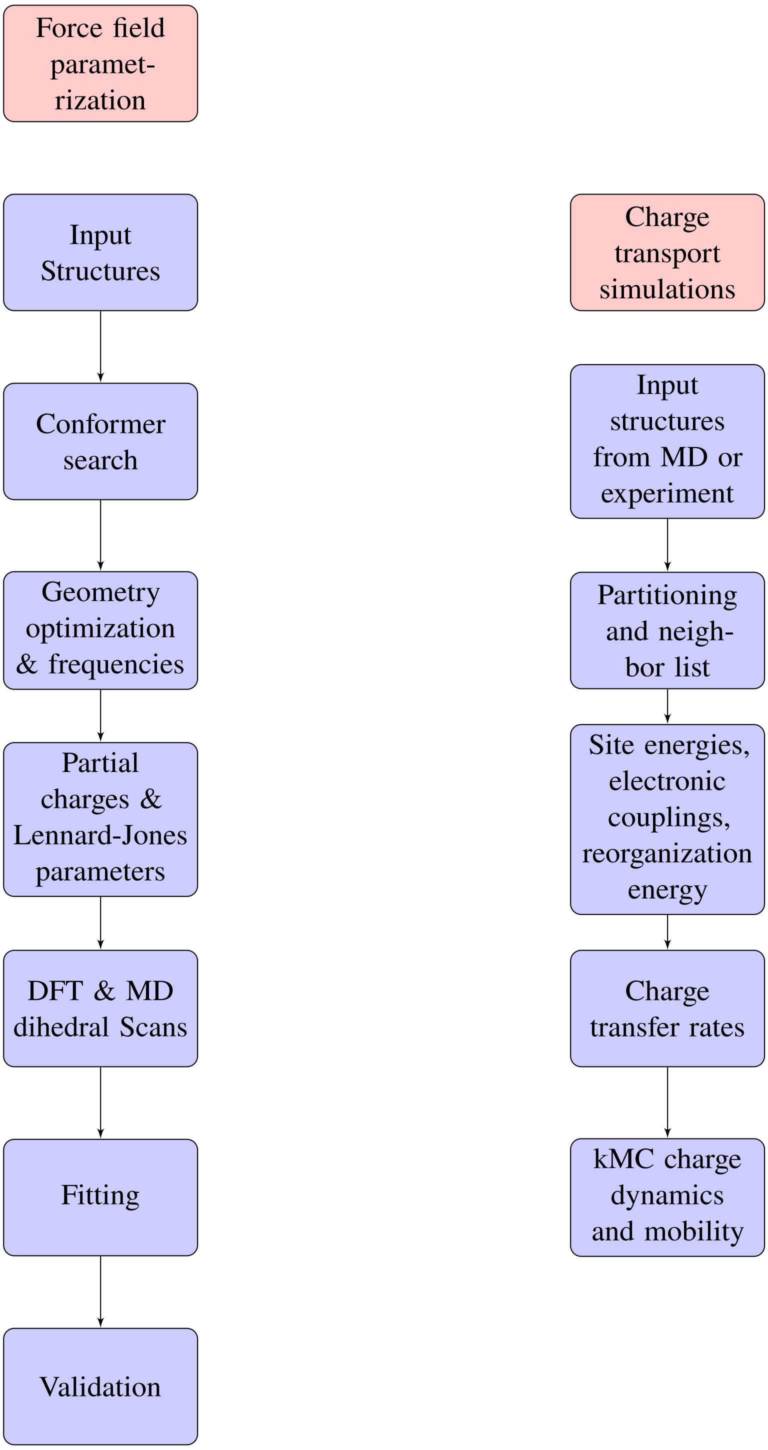

Figure 3.3: Workflow for force field parametrization (left) and for charge transport simulations with `VOTCA` (right).

CHAPTER 4

Charge transport in TPA derivatives

The aim of the first project of this thesis was to derive structure-property relationships for **TPA**-derivatives with regard to hole transport. Understanding the interrelation between structure, morphology and charge transport serves as an important first step for any further research efforts into **TPA**s as hole transport materials for specific device applications. The results of this investigation were published in Publication I. The full publication with all details is given in section 4.6, while the results are summarized here and put into the context of the thesis.

4.1 Structure-property relationships

The versatility of **TPA**s in Organic Electronic applications as summarized in section 1.2 is based on their structural diversity and adaptability to various applications, and on their charge transport properties. Molecular engineering approaches mostly focus on using electroactive substituents, alkyl substitution or differently connecting multiple **TPA**-centers [16]. In order to optimize the material for different applications, clear structure-property relationships are necessary to avoid pure trial-and-error approaches, however such knowledge is very hard to obtain, requiring deep understanding of the complex interrelation between molecular structure, morphology and charge transport. Using an approach based on systematically varying structural and morphological parameters, the hole transport and its relation with bulk- and molecular structural features was investigated aiming at the aftorementioned structure-property-relationships. In Fig. 4.1, the research approach is illustrated.

The bulk structural properties and charge transport of a selected library of **TPA** derivatives, as shown in Fig. 2.1, was investigated. The compounds were specifically chosen to understand the effect of having one or more **TPA** centers as well as the influence of the flexibility of the bridging unit between the **TPA** centers on both the supramolecular packing as well as on the charge transport parameters and finally the charge mobility. The effect of morphological (dis)order was investigated by considering the limit cases of single crystalline vs. amorphous structures for the charge transport simulations. The bulk structures were derived from the experimental crystal structures [119–122] in the crystalline case or generated *in silico* by a simulated thermal annealing procedure via molecular dynamics (MD) simulations in the amorphous case (see A.1 for details on the Force Field parametrization and the thermal annealing approach). Charge transport parameters were computed using a combination of Semiempirical-quantum-mechanical (SQM), DFT and force field methods.

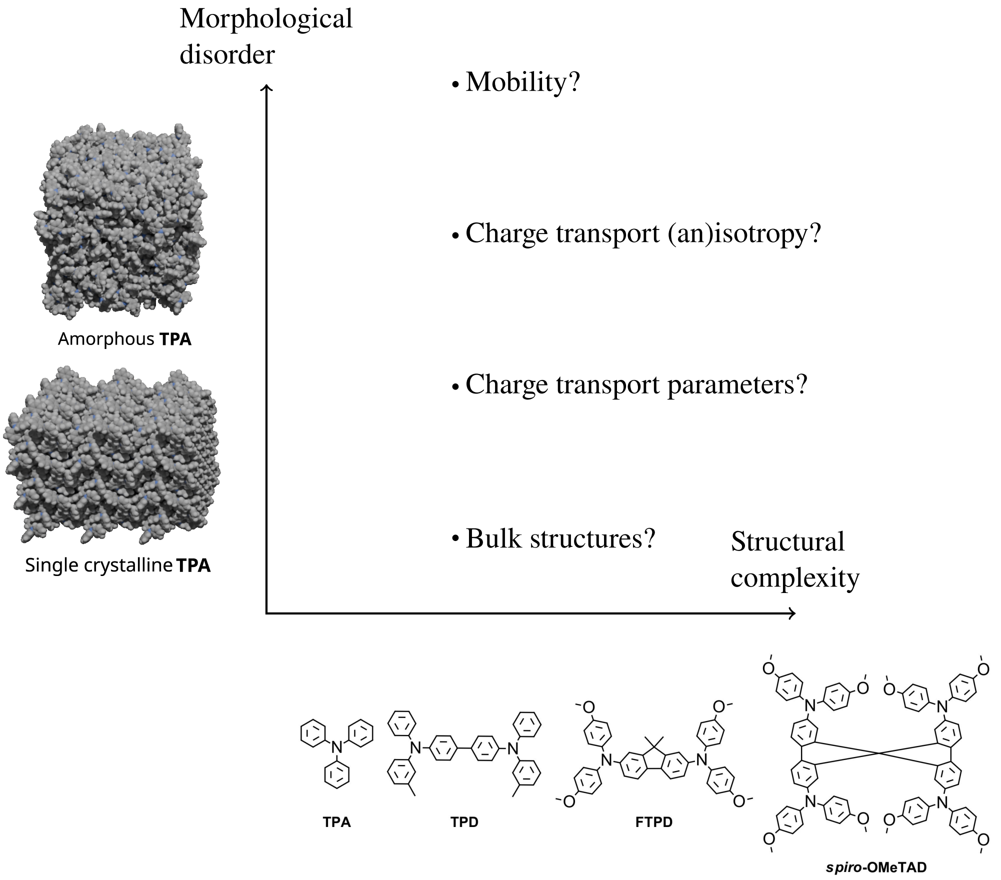

Figure 4.1: Illustration of the research approach in Publication I: Systematic variation of the structural complexity and degree of morphological order to derive structure-property-relationships for **TPA** derivatives.

4.2 Bulk morphologies: crystalline vs amorphous phases

In order to relate the molecular and the bulk structure, the center-of-mass (CoM) radial distribution functions (see Fig. 4.2) of the different compounds in the single crystalline and amorphous phases were analyzed. While the amorphous morphologies were generated via molecular dynamics simulations, the crystal structures were taken from experimental data. [119–122] The small, spherical **TPA** showed smaller CoM distances in both the crystalline and the amorphous phases than the larger and more elongated derivatives **TPD**, **FTPD** and ***spiro*-OMeTAD**. The structurally more flexible **TPD** and **FTPD** compounds show in turn smaller CoM distances in the amorphous phases than the most bulky of the investigated compounds, ***spiro*-OMeTAD**. The size, shape and flexibility of the compounds is thus reflected in the bulk structures and packing.

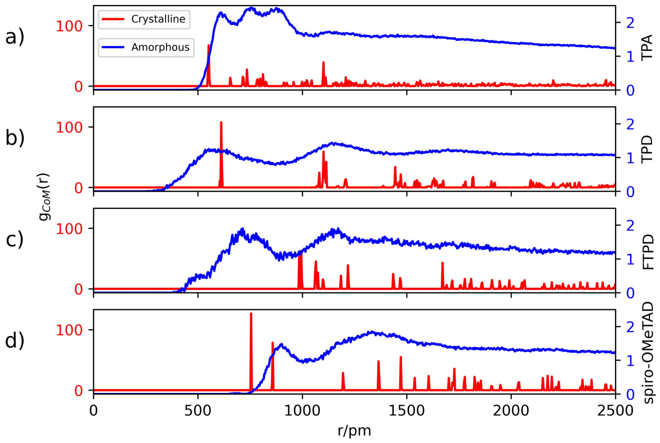

Figure 4.2: Center-of-mass (CoM) radial distributions for **TPA** derivatives in the amorphous and crystalline phases.

4.3 Charge transport parameters

4.3.1 Hole reorganization energy

The hole reorganization energy was calculated using the adiabatic four-point-method at multiple different levels of theory and related with structural features. The reorganization energy strongly influences the final charge mobility and needs to be estimated as accurately as possible. As a feature related mostly to the molecular structure, it is furthermore important to understand the relation between the molecular structure and the reorganization energy, since it is most amenable to molecular engineering. The reorganization energies at different levels of theory are shown in Fig. 4.3.

Since the evaluation of the reorganization energy involves calculations on charged species, it is important to consider the self-interaction error (SIE) and its effect on the reorganization energy when choosing the level of theory, as well as thoroughly analyzing the neutral and charged states. While for **TPA**, all methods yield very similar results, for all other compounds, the reorganization energy varies strongly, indicating complications in the correct estimation of the reorganization energy. Using functionals that include long-range correction such as ωB97X-D or CAM-B3LYP[123] leads to a strongly increased reorganization energy through mitigation of the SIE in the case of the larger compounds showing charge delocalization **TPD**, **FTPD**, and ***spiro*-OMeTAD**. This circumstance is shown clearly by using a constrained DFT (CDFT) [55, 124, 125] approach in conjunction with a range-separated functional such as CAM-B3LYP. By constraining the charge over different areas (see Fig. 4.4) of the compounds such as one ore more **TPA**-subunits, the impact of charge delocalization is shown clearly.

Constraint schemes $c0$ and $c2$ show increased reorganization energies due to the charge delocalization over the two bridging units. Further investigation into the bond length alternation pattern and the dihedral angles defining the geometric conformation of the compounds, as well as using the ωB97X-D functional together with frozen dihedral angles showed that charge delocalization is related to a significant decrease of the central dihedral angles and an equilibration of the bond lengths, consistent with π-electron delocalization and the related resonance stabilization. Such geometric relaxation is not always possible in the sterically congested bulk phase. [25] Thus, the reorganization energy is

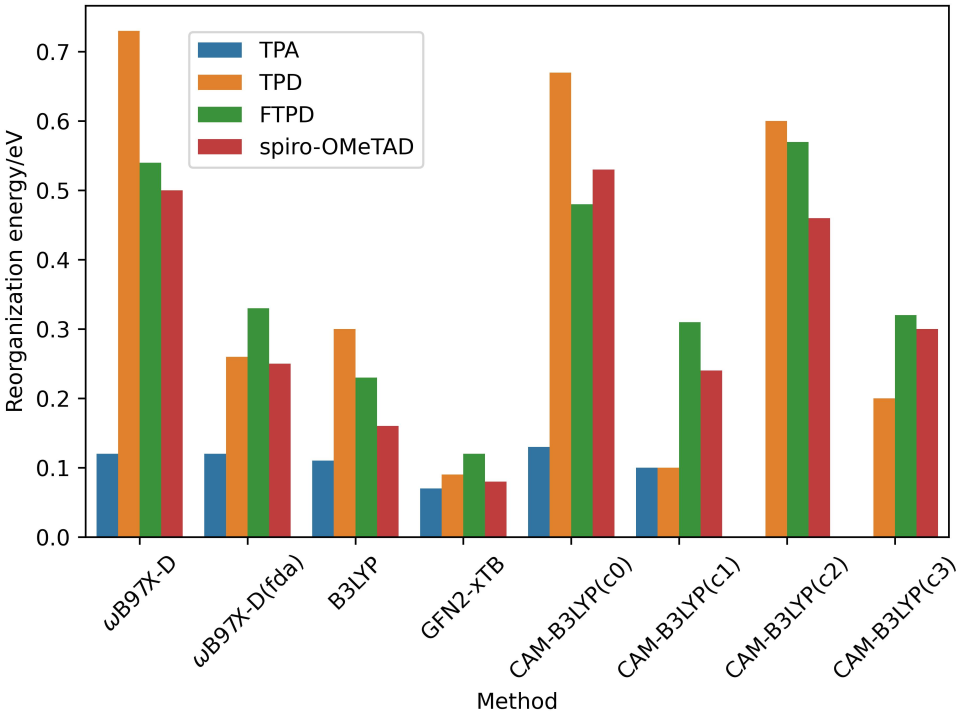

Figure 4.3: Reorganization energies at different levels of theory for **TPA** derivatives.

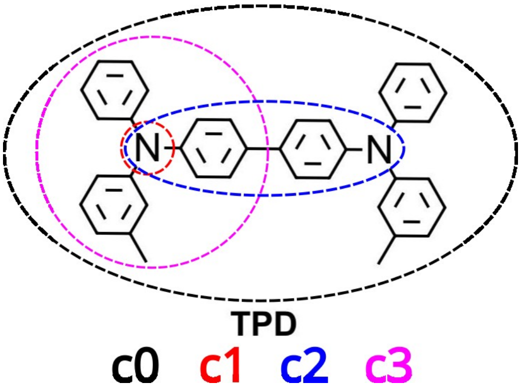

Figure 4.4: CDFT charge partitioning schemes for the calculation of the reorganization energy

most adequatly estimated with constrained scheme $c0$ (no constraint) for **TPA** and $c3$ for the other compounds, which allow for the largest degree of delocalization while at the same time not requiring extensive geometric relaxation.

4.3.2 Site energy differences and electronic coupling

The morphological order is clearly reflected in the site energy differences and the electronic couplings (see Fig. 4.5 and Fig. 4.6), showing Gaussian-like distributions in the amorphous phase and rather discrete distributions in the crystalline phase. The energetic disorder, i.e. site energy difference distribution broadening, as quantified by the standard deviation σ, results from the superposition of electrostatic, dipolar, conformational and morphological disorder, all of which are not necessarily independent of each other. Similarly, the conformational and morphological disorder also strongly impacts the coupling integral distribution, leading to a broadening in the amorphous phase. The dynamic disorder which results from the time-development of the system is not explicitly considered in this investigation. The standard deviation σ of the site energy difference distributions in the amorphous phase is of similar magnitude compared to the reorganization energies, indicating the site energies and thus the energetic disorder as the dominant charge transport parameter in the amorphous phase. In the crystalline phase, the narrower site energy difference distribution indicate the reorganization energy as the dominant charge transport parameter. The electronic couplings are low compared to the reorganization energies and the site energy differences, and mainly influence the charge transport (an)isotropy. While in the amorphous phase, isotropic charge transport is found in all cases, the single crystalline phases show anisotropic charge transport in the case of **TPD**, **FTPD** and ***spiro*-OMeTAD**, as related to the crystal packing (see Fig. 4.7). In **TPD**, the high-coupling pairs are stacked along the crystallographic b-axis, leading to preferred charge transport along this axis. A similar anisotropy is found for the crystallographic a-axis of ***spiro*-OMeTAD**. A rather isotropic charge transport is found in **FTPD** due to the shifted nature of the molecules in the crystal packing.

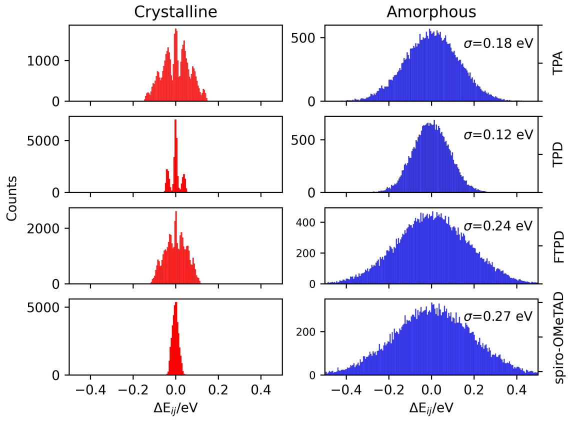

Figure 4.5: Site energy difference distributions in the experimental crystalline (red) and MD-generated amorphous (blue) phases, reporting the standard deviation σ in each panel.

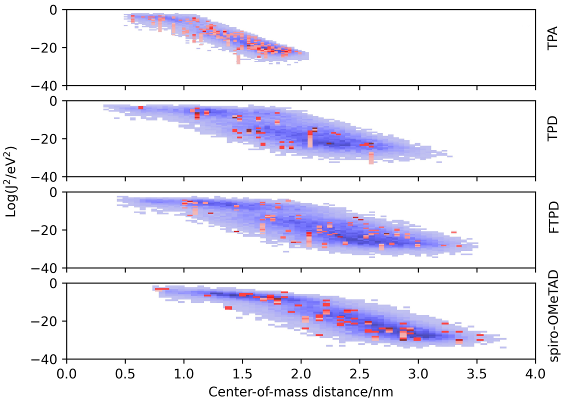

Figure 4.6: Distributions of the electronic couplings in the experimental crystalline (red) and MD-generated amorphous (blue) phases.

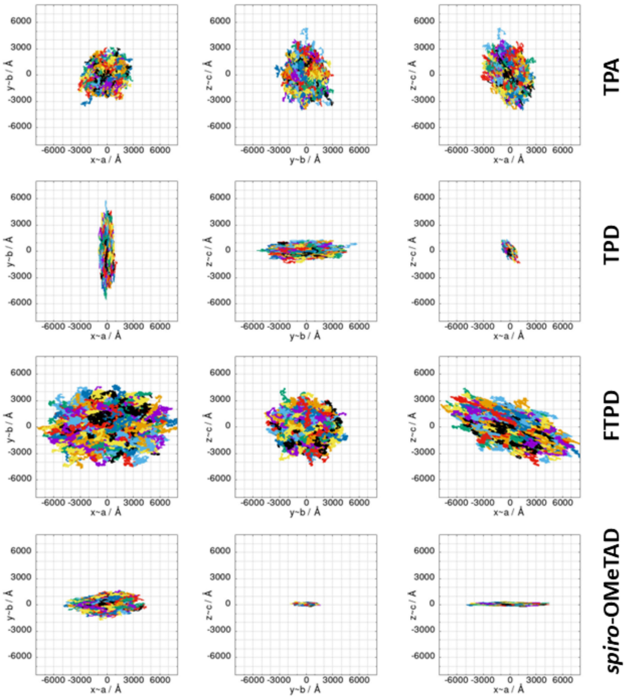

Figure 4.7: Superimposed kinetic Monte Carlo trajectories (1000 trajectories with each 10^5 steps) from the simulations on the single crystal structures as viewed from different planes. Different colors are used for discernibility of the individual trajectories.

4.4 Hole mobility

The hole mobility as derived from the kinetic Monte Carlo simulations results from the interplay of molecular and bulk structural features with the charge transport parameters. Thus, the accurate reproduction of experimental values serves not only to validate the approach but also to finally derive structure-property relations. The hole mobilities together with the experimental values [119, 120, 126, 127] are shown in Fig. 4.8.

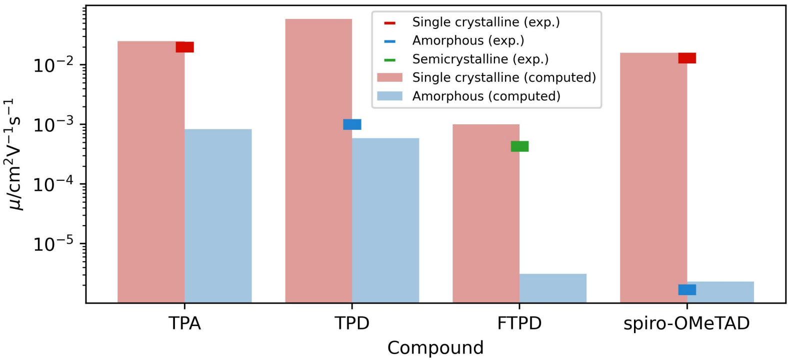

Figure 4.8: Hole mobilities in the amorphous and crystalline phases together with the literature values. [119, 120, 126, 127]

The experimental and computed hole mobilities generally show good agreement, validating the chosen approach. The highest mobility was found as expected in the crystalline systems due to the lower energetic disorder. In the case of **FTPD** and ***spiro*-OMeTAD**, the drop in hole mobility is more pronounced due to the increased static energetic disorder as shown by the broader site energy difference distributions. In the case of the crystalline phases, the hole mobilities are rather similar with the sole exception of **FTPD** due to the reduced values for the electronic coupling. Finally, the anisotropy of the charge transport in the case of single crystalline **TPD** and **FTPD** could allow for even higher mobilities if morphological control can be achieved in a device. In summary, from the point of view of molecular engineering, connecting **TPA**-subunits does not lead to a strongly increased reorganization energy due to the high probability of charge localization, however it strongly influences the crystal structure and thereby influences the charge transport isotropy and the final charge mobility. The difference in mobility in the crystalline and amorphous phases is related to the width of the site energy difference distribution which is markedly larger in **FTPD** and ***spiro*-OMeTAD**, most likely owed to the methoxy substitution. Finally, some factors that were not considered in this work is the dynamic evolution of the charge transport parameters as well as impurities, crystal defects and other circumstances that are relevant to real-world applications. Additionally, it should be noted here that the charge transport in single crystalline **TPA** is not hopping transport but rather multiple-trapping and release. [126] However in order to enable comparability, the compounds need to be described in the same framework and thus for all charge transport simulations, hopping transport was used.

4.5 Conclusion

Several findings reported here are of central importance for the modeling and application of **TPA**s in Organic Electronic applications. The modeling approach has shown to be appropriate by yielding good agreement between experimental and computed hole mobilities. In addition to structural understanding, insight into the fundamental charge transport parameters and processes was obtained. A non-trivial relationship between molecular and bulk structure and the hole reorganization energy was uncovered which is not only highly relevant to molecular design approaches for Organic Electronic applications but also needs to be considered in future modeling investigations. Flexible compounds only lead to increased reorganization energies if full geometric relaxation is probable, however the typical steric hindrance in bulk morphologies makes this less likely. Concerning modeling approaches, the positively charged state of the compounds needs to be modeled carefully, i.e. using approaches like CDFT or optimal tuning of the exchange-correlation functionals. The relative magnitude of the charge transport parameters indicates the reorganization energies and the site energy differences as the dominant charge transport parameters, leading to overall disorder controlled transport in **TPA** derivatives. From a device manufacturing standpoint, crystalline materials under morphological control would be preferable, because they allow for the highest hole mobility.

4.6 Publication I

All simulations and data analyses have been performed by me. I have written the initial manuscript of the publication and revised it together with the co-authors. I have worked on and written about the topic of publication I as a part of my Master's Thesis, however the work was substantially revised and all simulations including the parametrization of the force field and the charge transport simulations were redone for this publication. Only the electronic couplings at the DFT level, the reorganization energy at the ωB97X-D and B3LYP level of theory and the depiction of the electronic coupling pairs in the crystalline phase were used directly in publication I.

Journal of
Materials Chemistry C

ROYAL SOCIETY OF CHEMISTRY

PAPER

View Article Online
View Journal | View Issue

Check for updates

Cite this: *J. Mater. Chem. C*, 2023, 11, 11969

Revealing the interplay between the structural complexity of triphenylamine redox derivatives and their charge transport processes *via* computational modeling†

Robert Herzhoff,[a] Fabrizia Negri,[b] Klaus Meerholz*[a] and Daniele Fazzi*[b]

Triphenylamine derivatives (**TPAs**) are organic functional materials well known for their semiconducting charge transport and redox properties. These features characterize their applications in the field of organic electronics, for instance as hole transport layers for organic light emitting diodes (OLEDs), and perovskite-based solar cells (PSCs), as well as organic cathodes for electrochemical energy storage (EES) devices (*e.g.* organic batteries). Despite a large number of experimental and computational investigations, some structure–property relationships still remain elusive. Here, we explore through a bottom-up computational approach the molecular and solid state structures, as well as the charge transport processes in amorphous and single crystalline phases of four different redox active **TPAs**, characterized by increased molecular structure complexity. The **TPAs** considered feature one-, two- or four redox centers, namely (i) a single **TPA** unit, two **TPAs** linked *via* (ii) a flexible diphenyl bridge (**TPD**) or (iii) a rigid fluorene bridge (**FTPD**), and (iv) four **TPAs** connected *via* a spiro-center (***spiro*-OMeTAD**). A combination of density functional theory, semiempirical and molecular dynamics methods is used to analyse the experimental crystalline structures, to generate the amorphous morphologies, and to calculate the charge transport parameters and hole mobility. Our results show that short- and long-range structural order in condensed phases is strongly influenced by the molecular architecture. Furthermore, charge transport parameters, such as site energies, reorganization energies and coupling integrals, are intimately coupled with the number of redox centers and the way they are connected. The charge transport is differently characterized depending on the degree of morphological disorder, namely reorganization energy-controlled transport in the crystalline phase and site-energy static-disorder controlled transport in the amorphous phase. The computed hole bulk mobilities for both single crystal and amorphous cases are in good agreement with the available experimental literature data.

Received 23rd June 2023,
Accepted 7th August 2023

DOI: 10.1039/d3tc02206d

rsc.li/materials-c

Introduction

Triphenylamines (**TPAs**) are commonly used in various (opto-)electronic devices due to their good hole-transporting properties,[1–4] their high redox potential *vs.* Li/Li$^+$ and cycling stability,[5] and their high glass transition temperature.[6,7] Moreover, they are readily synthetically available, allowing for fine-tuning of their redox, spectroscopic and charge transport properties through the use of electro-active substituents.[8,9] **TPAs** are used as hole transporting layers (HTL) in organic light emitting diodes (OLEDs),[4,10] organic solar cells (OSCs),[11] and perovskite solar cells (PSCs),[12] and as redox-active materials for rechargeable electrochemical energy storage (EES) devices, such as organic batteries and supercapacitors.[9,13] Due to the popularity of such compounds in organic electronics (especially OLED applications), a significant number of experimental publications,[12,14–16] as well as theoretical and computational investigations, have been reported.[17–22] Fundamental charge transport parameters, such as the inner reorganization energy (λ_{int}), have been studied systematically at multiple levels of theory and relevant structural parameters have been identified.[20,23,24] Charge mobilities for various triphenylamine derivatives have been computed in the amorphous phase in good agreement with experimental data.[17] However, some questions concerning the relationships between the molecular structure, bulk morphology, and charge transport properties still remain to be answered. For example, it is not clear how the presence of

---

[a] *Department für Chemie, Universität zu Köln, Institut für Physikalische Chemie, Köln, Nordrhein-Westfalen, Germany. E-mail: klaus.meerholz@uni-koeln.de*
[b] *Università di Bologna, Department of Chemistry 'G. Ciamician', Bologna, Italy. E-mail: daniele.fazzi@unibo.it*

† Electronic supplementary information (ESI) available. See DOI: **https://doi.org/10.1039/d3tc02206d**

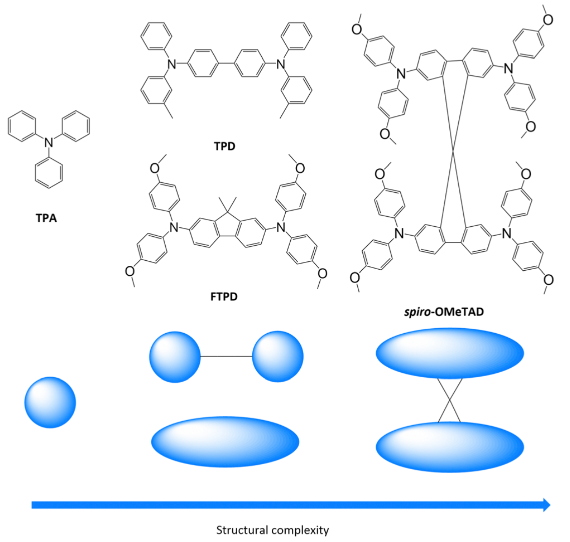

Fig. 1 Triphenylamine derivatives investigated in this work (**TPA**, **TPD**, **FTPD** and ***spiro*-OMeTAD**) with simplified sketches showing their structural complexity.

one-, two- or more redox centers (*i.e.*, triphenylamine units) affects the supramolecular organisation in the solid state, for both crystalline and amorphous phases, and how it impacts the charge transport parameters and the charge mobility, specifically with respect to the mixed-valence nature of multi-**TPA** compounds. Herein, we analyse such aspects as well as the influence of crystal packing and amorphous morphologies on the degree of charge transport isotropy/anisotropy. These issues have not been comprehensively addressed so far, in particular a systematic comparison between the computed charge transport parameters and hole mobilities in single crystalline *vs.* amorphous morphologies.

We focus on a library of four triphenylamine derivatives showing increasing molecular structure complexity, namely triphenylamine (**TPA**), *N*,*N*′-bis-(3-methylphenyl)-*N*,*N*′-diphenylbenzidin (**TPD**), N^2,N^2,N^7,N^7-Tetrakis(4-methoxyphenyl)-9,9-dimethyl-9*H*-fluorene-2,7-diamine (**FTPD**), and N^2,N^2,$N^{2\prime}$,$N^{2\prime}$,N^7,N^7,$N^{7\prime}$,$N^{7\prime}$-Octakis(4-methoxyphenyl)-9,9′-spirobi[fluorene]-2,2′,7,7′-tetraamine (***spiro*-OMeTAD**) (see Fig. 1). Ideally, we would have chosen identical substitution patterns for all cases (*i.e. para*-methoxy substituents on the peripheral aryl substituents, such as MeO-**TPD**); however, we were limited to the compounds for which experimental crystal structures are available in the literature. While **TPA** has one redox center, **TPD** and **FTPD** have two redox centers, as connected either *via* a flexible bridge (**TPD**) or by a rigid (ladder type) one (**FTPD**), and finally ***spiro*-OMeTAD** has four redox centers, consisting of two **FTPD**-subunits that are orthogonally connected *via* a central spiro carbon. Such increasing structural complexity impacts the inter-molecular packing and morphological properties, as well as the charge transport processes in the bulk phase. The goal of our work is to rationalize *via* a bottom-up molecular modeling approach the impact of different molecular structures, as characterized by various internal torsional degrees of freedom and steric demand, on both the morphological and charge-transport properties for both crystalline and amorphous states. To this end, a computational methodology was chosen that focuses on accurately describing the energetic and static disorder as well as those charge transport parameters intimately connected to the molecular structure.

By combining density functional theory (DFT), molecular dynamics (MD), and kinetic Monte-Carlo (KMC) methods we simulated the molecular and bulk properties, encompassing the calculation of the charge transport parameters and charge mobility. For each species, we analysed both single crystalline (experimental (XRD)) and amorphous phases (generated *via* MD simulations), focusing on the impact of the structural complexity as well as the morphological and static energetic disorder on the charge transport properties. We found a subtle interplay between the molecular structure complexity (namely one-, two- and four redox centers differently linked), supramolecular organizations, and charge transport mechanisms. The molecular geometry and shape impact not only the supramolecular organization in the condensed phases but also the reorganization energy and the isotropy of charge carrier diffusion *via* its short- and long-range effects on the crystal packing, as well as the site energy difference distributions in the amorphous phase.

Computational methods

Single molecule equilibrium geometries

The calculations were performed at multiple computational levels. For the DFT calculations, the range separated hybrid functional with Grimme's scheme of dispersion corrections ωB97X-D,[25] the hybrid B3LYP[26–28] and the triple-split polarized Pople basis set 6-311G*[29–31] were used. Constrained-DFT (C-DFT) schemes were applied to localize the charge on specific molecular fragments. C-DFT calculations were performed by using the Coulomb Attenuated Method (CAM-B3LYP[32]) with the 6-311G* basis-set. All molecular geometries optimized at the DFT level showed stable equilibrium structures (no imaginary frequencies found). Geometries were also computed at the semiempirical quantum mechanical tight-binding DFT level (SQM) by using GFN2-*x*TB as proposed by Grimme *et al.*[33,34] The neutral ground state calculations were performed at the restricted DFT level while the singly charged state calculations were performed at the spin-polarized unrestricted (UDFT) level.

Bulk morphologies

The single crystalline morphologies were obtained from experimental XRD-data,[21,22,35,36] while the amorphous morphologies were generated *via* MD simulations, where a simulated annealing procedure was employed for equilibration. Details about the force field parametrization and the MD simulations can be found in the ESI.† For all compounds, systems of 1000 molecules were generated, in the case of the crystalline morphologies by expanding the experimental unit cell as a supercell.

Charge transport parameters

Marcus theory[37,38] provides the rates k_{ij} for the charge transfer between two sites i and j in the low electronic coupling regime as

$$k_{ij} = \frac{2\pi}{\hbar}\frac{J_{ij}^2}{\sqrt{4\pi\lambda k_\mathrm{B}T}}\exp\left[-\frac{(\Delta E_{ij}+\lambda)^2}{4\lambda k_\mathrm{B}T}\right] \tag{1}$$

where J_{ij} is the electronic coupling, λ is the reorganization energy and ΔE_{ij} is the site energy difference.[37,38] The reorganization energy λ consists of an intramolecular (λ_int) and an external (outer) contribution (λ_o)

$$\lambda = \lambda_\mathrm{int} + \lambda_\mathrm{o} \tag{2}$$

In this work, λ_int was calculated at multiple levels of theory by using the adiabatic potential method.[39] λ_int is given by

$$\lambda_\mathrm{int} = (U^\mathrm{nC} - U^\mathrm{nN}) + (U^\mathrm{cN} - U^\mathrm{cC}) \tag{3}$$

In eqn (3), U is the energy, the superscripted lower-case letters stand for the electronic state (neutral or charged) while the superscripted upper-case letters stand for the equilibrium geometry. For the outer reorganization energy λ_o, a constant of 50 meV was assumed.[40–42]

The electronic coupling J_{ij} between two sites i and j is given by[43]

$$J_{ij} = \langle\phi^i|\hat{H}|\phi^j\rangle \tag{4}$$

where $\phi^{i,j}$ are the highest occupied molecular orbitals (HOMOs) of the molecules taking part in the charge transfer reaction and $\hat{H}$ is the electronic Hamiltonian of the dimer. In this work, J_{ij} is calculated using the DIPRO (dimer projection) method[44] at the DFT level or the MOO (molecular orbital overlap) approach[45] at the semiempirical (ZINDO/S) level as implemented in the open-source package VOTCA.[44–46]

The site energy differences (ΔE_{ij}) for the crystalline and amorphous morphologies were calculated based on the static electrostatic interactions and induced dipoles, all based upon the atomic partial charges evaluated at the CHELPG level (ωB97X-D/6-311G*). The site energy E_i is given by[46,47]

$$E_i = \frac{1}{4\pi\varepsilon_0}\sum_{a_i}\sum_{b_{k,k\neq i}}\frac{(q^\mathrm{c}_{a_i} - q^\mathrm{n}_{a_i})q^\mathrm{n}_{b_k}}{\varepsilon_s r_{a_i b_k}} \tag{5}$$

where a_i and b_k are the atomic indices running over the atoms of molecules i and k, $r_{a_i b_k}$ is the distance, q is the atomic partial charge, ε_0 is the dielectric constant of the vacuum and ε_s is the static relative dielectric constant. The sums extend over the atoms of molecule i, for which the site energy is calculated and all atoms $k \neq i$ of the surrounding molecules. To take polarization effects into account, the contribution of induced dipoles is calculated with a self-consistent approach. First, the electric field $\boldsymbol{F}_{a_i}{}^{(0)}$ is calculated for atom a in molecule i based on the atomic partial charges and using $\varepsilon_s = 1$. Subsequently, the induced dipole moments $\boldsymbol{\mu}_{a_i}{}^{(0)}$ can be calculated. The new induced dipoles can be iteratively computed by using $\boldsymbol{\mu}_{a_i}{}^{(k+1)} = \omega\boldsymbol{F}_{a_i}{}^{(k)}\alpha_{a_i} + (1-\omega)\boldsymbol{\mu}_{a_i}{}^{(k)}$ where ω is the successive over-relaxation factor and α_{a_i} is the atomic polarizability. From this, the new electric fields are obtained and the process continues until the difference between the induced dipoles is consistent with the convergence criterion of 10^{-6} Debye. A fixed set of atomic polarizabilities was used (Thole approximation), as implemented in VOTCA.[46,47]

Charge transport simulations

The charge transport simulations (hopping regime) were performed using a kinetic Monte Carlo (KMC) approach, based on the Marcus charge transfer rates calculated *via* eqn (1). The charge transport parameters, such as the coupling and the site energies, were computed separately for the entire system before each KMC run. The KMC simulations were performed under periodic boundary conditions for a single charge at a temperature of 300 K, using 1000 trajectories of 10^5 steps each. The diffusion coefficient (D) was obtained by a linear fit to the mean square displacements and the zero-field mobility was computed *via* the Einstein–Smoluchowski relationship:

$$\mu = \frac{De}{k_\mathrm{B}T} \tag{6}$$

The KMC procedure was repeated for ten snapshots as extracted from the MD production run at a temperature of 300 K. The final hole mobilities are averaged over all KMC trajectories obtained from the ten snapshots.[48] With the charge mobility being a tensor, we refer here to μ as the average value (*i.e.* $\mu_\mathrm{average} = \frac{1}{3}(\mu_{xx} + \mu_{yy} + \mu_{zz})$, with μ_{ii} being the i,i-component of the mobility tensor, $i \in x, y, z$). For those cases where the charge transport presents a pronounced anisotropy, single values of the tensor along specific axes are specified (*vide infra*, Table 3). Charge transport simulations were also performed with an applied electric field of 10^8 V m^{-1}. The results for these last simulations are listed in the ESI.†

Software

DFT calculations were performed by combining the codes GAUSSIAN[49] and ORCA,[50] C-DFT was carried out by using NWChem,[51] while GFN2-*x*TB calculations were done with *x*TB.[33,34] MD simulations were executed with GROMACS,[52–56] using an in-house re-parameterized version of the OPLS-AA force field[57,58] (see the ESI† for details). The evaluation of the electronic couplings was done by using the open-source code VOTCA[46] for both the crystalline and amorphous bulk morphologies. For crystalline morphologies, additionally an in-house DIPRO script interfaced with Gaussian and ORCA was also adopted. Charge transport simulations for crystalline structures were performed (and internally compared for consistency) by using two codes: an in-house code developed by Negri *et al.*[59–61] and the open-source code VOTCA.[46] Charge transport simulations for amorphous morphologies were carried out with VOTCA.

Results and discussion

(1) Bulk morphologies: crystalline *vs.* amorphous phases

The center-of-mass (CoM) radial distribution functions ($g_{\text{CoM}}(r)$) of the simulated amorphous and experimental single crystalline[21,22,35,36] morphologies for each compound, as reported in Fig. 2, show clear differences that can be traced back to the molecular structure and the short-/long-range supramolecular packing.

Generally, in the amorphous phase, $g_{\text{CoM}}(r)$ is a continuous distribution characterized by broad bands reflecting different nearest-neighbours coordination shells and a lack of long-range structural order, while in the crystalline phase, as expected, $g_{\text{CoM}}(r)$ consists of narrow and well-defined peaks, according to the periodic structural order appropriate for crystals. Notably, the different molecular sizes and shapes of the **TPA** derivatives impact $g_{\text{CoM}}(r)$ of both crystalline and amorphous phases.

For **TPA** in the crystal phase, $g_{\text{CoM}}(r)$ shows an intense peak at 551 pm and many small peaks centered at well-defined distances. In the amorphous phase, $g_{\text{CoM}}(r)$ shows three broad bands from 600 pm to 800 pm, followed by a constant distribution at higher distances. The three bands reflect a short-range structural order, showing the formation of multiple coordination shells around each **TPA**. This local structural order, induced by the isotropic molecular structure (sphere-like shape) of **TPA**, is however lost for large distances (r > 1000 pm).

TPD, featuring two redox-centers, is characterized by a more elongated and, therefore, anisotropic molecular structure in contrast to **TPA**. This is also reflected in the herringbone-type packing in the crystalline phase of **TPD** (see the ESI†), leading to larger CoM distances and more defined coordination shells. In the amorphous phase, the $g_{\text{CoM}}(r)$ of **TPD** shows two very broad coordination shells, centered around the crystalline peaks at 600 pm and 1200 pm, with contributions falling off to smaller values than **TPA** (<500 pm). This is caused by a fraction of molecules that can get very close to each other affording very short CoM distances, a feature which is enabled in the amorphous phase by the elongated and flexible structure of **TPD**.

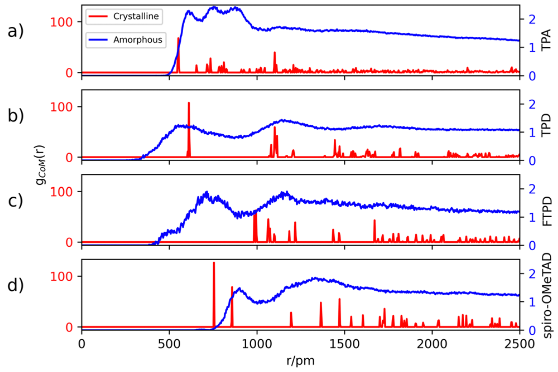

Fig. 2 Center-of-mass (CoM) radial distribution functions $g_{\text{CoM}}(r)$ in the crystalline (red) and amorphous (blue) morphologies. Crystalline structures of **TPA**, **TPD**, **FTPD** and ***spiro*-OMeTAD** are taken from ref. 21, 22, 35, and 36, and the bulk amorphous structures are obtained from MD simulations (see details in the Computational methods section and the ESI†). Labels (a), (b), (c) and (d) refer to **TPA**, **TPD**, **FTPD** and *spiro*-OMeTAD respectively.

FTPD shows an elongated structure similar to **TPD**, however, it is characterised by a more rigid backbone due to the suppression of the inter-ring torsional degree of freedom *via* the fluorene structure. The $g_{\text{CoM}}(r)$ of the crystalline phase of **FTPD** is therefore very different from those of **TPD** and **TPA**, showing the first coordination peak at around 1000 pm. However, similarly to **TPD**, in the amorphous case the first coordination shell of **FTPD** is computed at lower values than the crystalline phase, namely at around 750 pm, showing a broad band falling off below 500 pm, thus indicating close CoM distances between the molecules. These results suggest that molecules with elongated shapes enable short range packing in the amorphous phase, a situation that is however not always observed in the crystal phase. For **FTPD** such short range packing in the amorphous phase stems from cross-like pair configurations (see Fig. S12, ESI†), *i.e.* pairs where the molecules cross along their long axes forming an X-shaped structure. This configuration enables small CoM distances.

For crystalline ***spiro*-OMeTAD**, the coordination shells are located at higher values than **TPA**, **TPD** and **FTPD**, thus showing the very bulky nature of the molecule. In the amorphous phase, a sharp coordination shell around 800 pm, followed by a very broad band centered at 1200 pm, is observed. Only a very small fraction of the molecules gets closer (~650 pm) than in the crystal. Generally, the steric hindrance and the aspect ratio of the molecule prevent close contacts also in the amorphous phase, in contrast to **TPD** and **FTPD**. With respect to other **TPAs**, ***spiro*-OMeTAD** shows the highest CoM distance of the first $g_{\text{CoM}}(r)$ peak in the amorphous phase, which reflects the bulkier nature of ***spiro*-OMeTAD** as compared to the other compounds.

From the structural investigation in solid phases we can draw some partial conclusions based on the molecular structures: (i) as expected, small, sphere-like, one-redox center systems (*e.g.*, **TPA**) show smaller CoM distances in the crystalline phase than the elongated and bulkier derivatives (*e.g.*, **TPD**, **FTPD** and ***spiro*-OMeTAD**), however (ii) elongated two-redox centers derivatives (*e.g.*, **TPD** and **FTPD**), afford short CoM distances in the amorphous phase thanks to their structural flexibility and molecular aspect ratio. Finally, (iii) sterically demanding four-redox centers compounds (*e.g.*, ***spiro*-OMeTAD**) present the largest CoM distances in both crystalline and amorphous phases due to their bulky nature.

(2a) Charge transport parameters: hole reorganization energy

The first charge transport parameter we computed is the internal (intramolecular) reorganization energy λ_{int}. λ_{int} was calculated at multiple levels of theory (Table 1), encompassing DFT, SQM and constrained-DFT (C-DFT), by assuming the charge partitioning schemes as reported in Fig. 3. An additional calculation of λ_{int} using the BLYP35 functional, as previously

Table 1 Calculated (DFT, C-DFT and SQM) internal hole reorganization energies (λ_{int}, eV). Different partitioning schemes for the C-DFT calculations are labeled as c_i (i = 0–3). For the DFT calculations, the 6-311G* basis set was used. In the case of ***spiro*-OMeTAD**, due to the elevated computational costs, for C-DFT schemes c_1–c_3, the geometries optimized at the 6-31G level were used employing single-point calculations at the 6-311G* level. In the frozen dihedral approach (fda), the dihedral angles were fixed during the geometry optimizations of the charged state at their neutral ground state positions

	TPA	TPD	FTPD	*spiro*-OMeTAD
ωB97X-D	0.12	0.73	0.54	0.50
ωB97X-D (fda)	0.12	0.26	0.33	0.25
B3LYP	0.11	0.30	0.23	0.16
GFN2-*x*TB	0.07	0.09	0.12	0.08
CAM-B3LYP, c_0	0.13	0.67	0.48	0.53
CAM-B3LYP, c_1	0.10	0.10	0.31	0.24
CAM-B3LYP, c_2	—	0.60	0.57	0.46
CAM-B3LYP, c_3	—	0.20	0.32	0.30

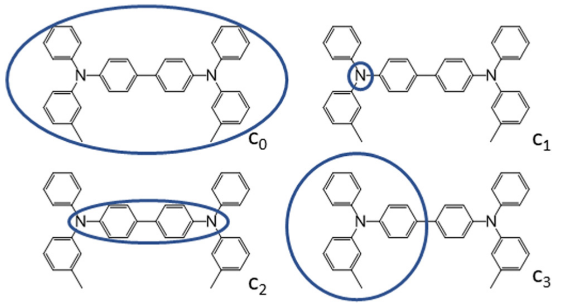

Fig. 3 Charge constraint schemes for **TPD**. The circles indicate the domains where the positive charge is localized. Charge-constrain schemes for **FTPD** and ***spiro*-OMeTAD** are reported in the ESI.†

introduced by Renz *et al.* for the quantum-chemical characterization of mixed-valence systems,[62] can be found in Table S12 of the ESI.†

All methods are largely consistent for **TPA**, leading to hole reorganization energy values around 0.1 eV, very much in accordance with the literature data.[23] Moving to two- (**TPD** and **FTPD**) and four redox units (***spiro*-OMeTAD**) all methods yield very different results. This discrepancy can be traced back to the well-known self-interaction error (SIE), which in the case of B3LYP and GFN2-*x*TB leads to an artificial stabilization of the charged state.[63] When long range corrected schemes are taken into account (*e.g.* CAM-B3LYP, ωB97X-D) the reorganization energy raises up to 0.73 eV for **TPD**. Similar findings have been reported by Li *et al.*[64] and by Blaskovitz *et al.*[24] This result shows that an accurate description of the reorganization energy is not trivial. While the SIE can be mitigated by using a range-separated functional like ωB97X-D, Renz *et al.* reported that mixed-valence systems – very similar to **TPD** – are borderline cases of the Robin-Day classification, with a charged state being on the border between delocalization and partial localization.[62] This circumstance has an additional impact on the final value of the reorganization energy. BLYP35, as introduced by Renz *et al.*, resulted in similar reorganization energy values as B3LYP, showing the lowest for **TPA** and the highest for **TPD**. Here, we suggest an alternative approach to describe the reorganization energy by taking into account both the SIE and the partial localization problem.

To characterize the nature of the charged state, we devised multiple charge-constrain partitioning schemes at the C-DFT level, as reported in Fig. 3 (for the sake of simplicity only **TPD** is shown) and recalculated the reorganization energy accordingly. The partitioning serves to characterize the extreme cases of full delocalization (c_0 and c_2) *versus* full localization (c_1 and c_3). The SIE is mitigated by using the range separated CAM-B3LYP functional.

We compared the unconstrained situation (c_0, normal DFT) to different charge partitioning schemes, namely the charge confined to one nitrogen atom (c_1), to the central bridging unit (c_2), or to one **TPA**-subunit (c_3). Generally, the reorganization energies computed with C-DFT-schemes c_1 and c_3 are similar to those evaluated at the B3LYP level, while the reorganization energies computed with C-DFT-schemes c_0 and c_2 are similar to those calculated at the ωB97X-D level. In C-DFT-schemes c_0 and c_2 the charge is allowed to delocalize across the bridge and since the functional used (CAM-B3LYP) is a range-separated one, similar results as by using ωB97X-D are obtained. For the C-DFT-schemes c_1 and c_3 a lower reorganization energy is obtained than for c_0 and c_2 by avoiding the charge delocalization across the whole molecular backbone. This trend shows that the delocalization of the charge across the bridge connecting the redox centers is the main factor governing the magnitude of the reorganization energies in multi-**TPA** species. Still, what remains to be answered is which kind of scenario (localized or delocalized charged state), is more realistic when modeling charge transfer processes in bulk **TPA**-based materials, which we approach by analysing the charged state geometries.

From Fig. 4 the effects of charge delocalization become clear (data for **FTPD** and ***spiro*-OMeTAD**, respectively, are reported in Fig. S4 and S6 of the ESI†). In the unconstrained/delocalized schemes (*i.e.*, c_0 and c_2 C-DFT, as well as normal DFT at the B3LYP and ωB97X-D levels), significant changes in the bond lengths and dihedral angles occur. Most notably, the central bond (number 5) shortens significantly, and the central dihedral angle *D* becomes planar (quinoid-like structure). In the constrained/localized schemes (*i.e.* c_1, c_3), the bond length changes are much less pronounced and an asymmetric change in the dihedral angles occurs, where only the dihedral angles of the charge-bearing **TPA**-redox subunit change significantly. Thus, a large contribution to the reorganization energy can be related to the variation of the dihedral angles.

This feature was already reported by Friedrich *et al.*[17] Since the steric demands of the surrounding molecules in the bulk phase presumably hinder large dihedral relaxations upon charging, we recalculated the reorganization energy by fixing the dihedral angles at the values they assumed in the neutral state, similar to reports in literature.[17] Very similar reorganization energies as compared to those values obtained by the C-DFT scheme c_3 were computed (see the fda approach in Table 1).

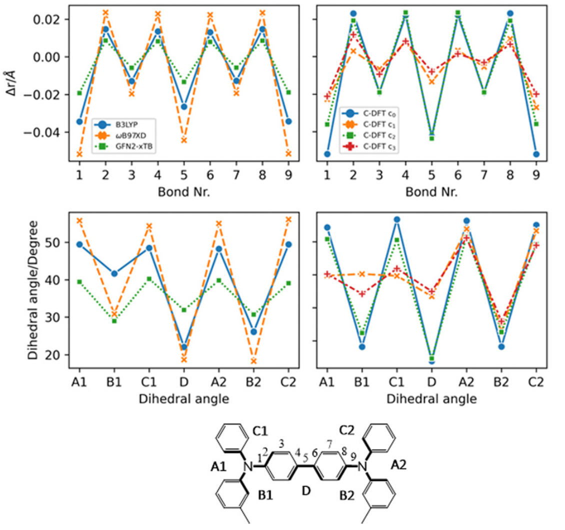

Fig. 4 Geometric parameters of **TPD** in the charged state (+1) by considering different methods (DFT, C-DFT, GFN2-xTB), DFT functionals and various charge constraint (C-DFT) schemes. The two panels on the top show the bond length difference ($\Delta r = r_{\text{charged}} - r_{\text{neutral}}$) patterns by moving from the neutral to the charged state. Top left panel: DFT (B3LYP *vs.* ωB97X-D) *versus* GFN2-xTB data. Top right panel: C-DFT data with different schemes. The two panels on the bottom show the dihedral angles in the charged state. Bottom left panel: DFT (B3LYP *vs.* ωB97X-D) *versus* GFN2-*x*TB data. Bottom right panel: C-DFT data with different charge constraint schemes. See the ESI† (Fig. S4 and S6) for the geometric parameters of the other compounds.

Therefore, either assuming a charge localization (C-DFT) or a frozen dihedral approach leads to the same effects. Constraining the dihedral angles prevents the multi-**TPA** compounds to assume a quinoidal structure upon charging, thus corresponding to a delocalization restraint. In this work we assume for the final calculation of the charge transfer rates and mobility the intramolecular reorganization energy as obtained by C-DFT scheme c_3 for **TPD**, **FTPD** and ***spiro*-OMeTAD** and c_0 (unconstrained) for **TPA.**

Summarizing, by constraining the charge over one **TPA** redox unit (c_3 scheme) as suggested by chemical intuition, the reorganization energy smoothly increases from 0.10 eV for **TPA**, up to 0.20–0.30 eV for the two- (**TPD**, **FTPD**) and four-redox centers (***spiro*-OMeTDAD**) cases. We believe that this trend reflects the dispersion of the hole reorganization energy by moving from one to multiple **TPA** centers, also mimicking the structural constraints as induced in the bulk phase by the surrounding molecules. Globally, our computational analysis shows that the hole reorganization energy in multi-redox **TPA** compounds is intrinsically linked to the degree of charge delocalization across units, and thus the variation of the central bond lengths and dihedral angles upon charging. The computed reorganization energies are however still approximate in nature, with the true reorganization energy lying in between the localized/frozen dihedral energies and the unconstrained calculations (*e.g.*, using the BLYP35 functional), corresponding to a probably partially localized situation.

(2b) Charge transport parameters: site energy differences

The impact of morphological order becomes apparent when analysing the charge transport parameters, like the site energy difference distributions ΔE_{ij} (see eqn (1)) as shown in Fig. 5.

As it can be generally expected, rather discrete ΔE_{ij} distributions are found for single crystalline phases, while the amorphous phases show much wider, Gaussian-like shapes due to the statistical distribution of conformers. The nonequivalent molecular sites of the crystalline phases are reflected in the peaks of the histograms, with each peak being slightly broadened due to the finite numerical accuracy in the calculation of the site energies. The electrostatic disorder, quantified as the standard deviation σ of the site energy difference distributions in the amorphous phase, is of a similar magnitude as the reorganization energies for each compound. This feature leads to the static disorder being the dominating parameter for hopping transport in the amorphous phase. On the other hand, the site-energy difference distributions in the crystalline phases are narrower, causing the reorganization energy to be the dominant parameter for the hopping transport in crystals. Comparable values for the static disorder have been reported by Friedrich *et al.*,[17] Lin *et al.*[20] and Mondal *et al.*[19] Comparing the σ-values, molecules characterized by an increased structural complexity like **FTPD** and ***spiro*-OMeTAD** show increased electrostatic disorder effects in the amorphous phase when compared to **TPA** and **TPD.**

(2c) Charge transport parameters: electronic couplings

The electronic coupling distributions (Fig. 6) as computed for both crystalline and amorphous morphologies, show similar characteristics as the site energy difference distributions, being continuous in the amorphous phase and discrete in the

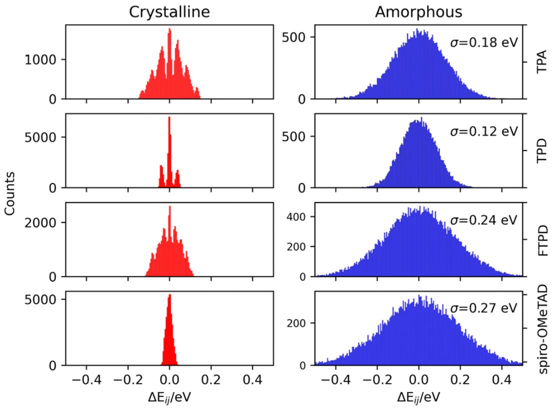

Fig. 5 Histograms of the computed site energy difference distributions (ΔE_{ij}) for the experimental crystalline (left) and MD-generated amorphous (right) phases of **TPA**, **TPD**, **FTPD** and ***spiro*-OMeTAD**. For the amorphous phase the standard deviation (σ) of the site energy difference distributions is reported for each case.

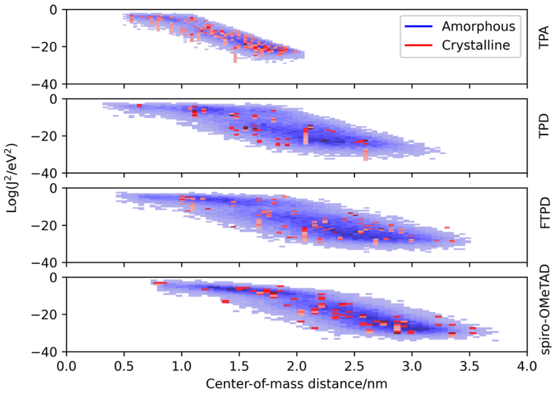

Fig. 6 Coupling integral distributions ($\text{Log}(J_{ij}^2/\text{eV}^2)$) as calculated with the MOO approach (ZINDO/S) *versus* center-of-mass (CoM) distance in experimental crystalline (red) and MD generated amorphous (blue) phases.

crystalline phase. Generally, low values are obtained for the electronic coupling (largest J_{ij} is around 20 meV), clearly supporting the observation of a disorder-controlled nature of the charge transport.

Comparing the molecular classes, we notice that the coupling distribution in the **TPA** crystal is much more narrow than in the **TPD**, **FTPD** and ***spiro*-OMeTAD** crystals, reflecting the smaller size and sphere-like shape (isotropy) of the molecule. For **TPD**, **FTPD** and ***spiro*-OMeTAD**, broader distributions are obtained, and even at large CoM distances (>2 nm) nonzero electronic coupling is found due to the elongated or bulky shape of the molecules. In the amorphous phase, we can observe that there are two trends for the couplings, a horizontal dispersion (from roughly 0.5 to 1.5 nm) and a linear one (from 2.0 to 3.5 nm). In the first range, the couplings are almost independent from the CoM distances, indicating the interplanar distance as the determining factor for the magnitude of the coupling, while at larger CoM distances, the coupling drops approximately linearly, indicating a crossing point at which the CoM distance becomes the dominating factor ruling the strength of the electronic coupling. Considering the logarithmic scale, this linear decrease corresponds to an exponential decrease in a linear scale.

Analysis of the electronic couplings based on the experimental crystal structures

To gain an in-depth understanding about the influence of solid-state packing and molecular orientations on the electronic coupling, the crystal structures of **TPA**, **TPD**, **FTPD** and ***spiro*-OMeTAD** were analysed by calculating the electronic coupling using the DIPRO approach (ωB97X-D/6-311G*) for each unique molecular site and its neighbours, applying a cutoff of 1.5 nm. A detailed listing of the results and the geometric parameters can be found in the ESI† (Tables S2–S9). For **TPA**, **TPD** and **FTPD** three non-equivalent pairs (couplings) can be isolated, named A, B and C in Table 2. For ***spiro*-OMeTAD** only two pairs are identified (A and B).

Table 2 Electronic couplings (J_{ij}, meV) for the pairs shown in Fig. 7. Pair A refers to the pair formed from the black and red monomers, pair B to the pair formed from the black and green monomers and pair C to the pair formed from the black and blue monomers. ***spiro*-OMeTAD** shows only A and B type pairs

	TPA	TPD	FTPD	*spiro*-OMeTAD
A (black-red)	50	36	9.8	39
B (black-green)	40	11	9.3	15
C (black-blue)	36	8	9	

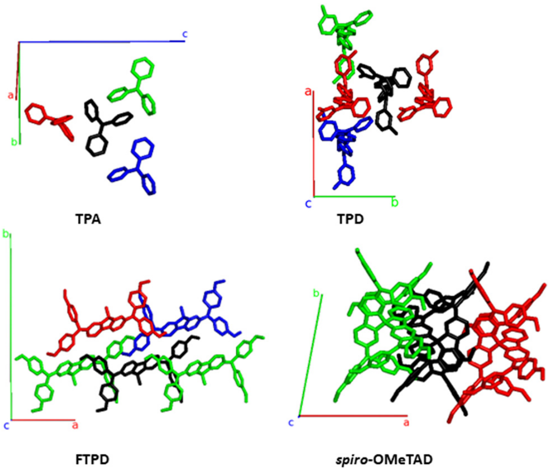

Fig. 7 Structures featuring the largest electronic coupling (see main text) from the **TPA**- **TPD**-, **FTPD**- and ***spiro*-OMeTAD** crystal unit cells, also reporting the crystallographic axes. The central molecule is shown in black. The pair formed by the black and red molecules is, for each compound, the one with the highest electronic coupling, followed by the black-green and black-blue pairs, respectively (see Table 2).

From Fig. 7 and Table 2 we can observe that **TPA** shows the highest electronic couplings amongst the triphenylamine series. Furthermore, the highest **TPA** coupling (50 meV) results from an interdigitation of the amine moieties, see pair A (black-red pair). For **TPA**, all couplings are of the same order of magnitude, thus, an isotropic transport of the charges within the crystal is to be expected. For **TPD** a similar interdigitation motif as for **TPA** is found (pair A), resulting in a high electronic coupling (36 meV). However, in contrast to **TPA**, for **TPD** the other couplings (pairs B and C) are smaller in magnitude than pair A. Because pair A of **TPD** is prevalently aligned with the crystallographic axis *b*, charge transport is expected to occur preferably along this direction in an anisotropic way in the crystal. For the case of **FTPD**, lower couplings ($\sim$10 meV) are observed when compared to the other triphenylamine compounds. This can be due to the shifted orientation of the monomers in the crystal packing, which prevents close contact between the molecular backbones (as reported in the $g_{\text{CoM}}(r)$, Fig. 2) and the interdigitation of the triphenylamine moieties. All **FTPD** couplings are very similar in magnitude, in accordance with ref. 21, making isotropic-like charge transport in the crystal probable. Finally, for ***spiro*-OMeTAD**, one can observe that pair A is more intertwined than the others, leading to higher electronic coupling (39 meV), in accordance with ref. 21, possibly resulting in an anisotropic charge diffusion as for the case of the **TPD** crystal.

Kinetic Monte-Carlo charge transport simulations and zero-field (Brownian) hole mobilities

The computed KMC charge percolation pathways for single crystals, as reported in Fig. 8, show the expected characteristics as anticipated from the analysis of the electronic couplings. While for **TPA**, due to its molecular shape (sphere-like) and solid state packing, isotropic charge transport is found, other compounds show either marked anisotropic charge diffusion (**TPD** and ***spiro*-OMeTAD**) or weak anisotropic charge percolation (**FTPD**) due to different molecular aspect ratios, bridge flexibility, steric hindrance and packing motifs. In **TPD**, the *b* direction is clearly favoured over the *a* and *c* axes (Fig. 7). This preferred direction is readily explained by the orientation of the main charge transport pairs (*i.e.*, those showing the highest J_{ij}) along the *b* axis (Fig. 7 and Table 2), as favoured by the elongated molecular shape and interdigitation of the nearest neighbour **TPA** units. In the charge mobility simulations of single crystal **FTPD**, a weak anisotropy of the charge transport along the *a* axis is observed, due to the similar (small) magnitude of the electronic coupling in all charge transport pairs (~9 meV, Table 2). In the charge hopping pathways of ***spiro*-OMeTAD**, the charge transport takes place mainly along the *a* axis due to the high coupling (39 meV) on the basis of the π–π stacking along this direction (Fig. 7).

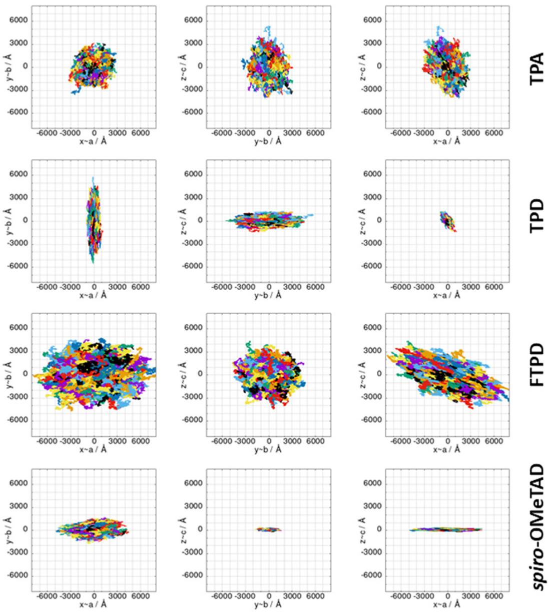

Fig. 8 KMC charge hopping trajectories for all **TPAs** here investigated, evaluated for the experimental single crystal structures, shown from different planes. The colours used in the plots only serve to discern the superimposed trajectories.

Table 3 collects the computed zero-field (Brownian) KMC hole mobilities (that is, $\mu_{\text{average}} = \frac{1}{3}(\mu_{xx} + \mu_{yy} + \mu_{zz})$, with μ_{ii} being the *i,i*-component of the mobility tensor, $i \in x, y, z$) for all species in their crystalline and amorphous phases. In Table 3 are also shown the experimental data available from the literature. A one-to-one comparison between the computed single crystal/amorphous charge mobility and the experimental single crystal/amorphous-films hole mobility was sometimes not possible to do. For instance, for **TPA** only the experimental single crystal hole mobility was found, while no data is available for amorphous films. The only case in which we could find both single crystal and amorphous measured hole mobility is ***spiro*-OMeTAD**. In the ESI† are reported the computed mobilities in the presence of an electric field (Table S10). Furthermore, we report also the μ_{xx}, μ_{yy}, and μ_{zz} components in order to highlight the isotropy *vs.* anisotropy of the charge transport in single crystals.

By moving from the crystalline to the amorphous phase a drop of various orders of magnitude of the charge mobility occurs, as expected due to the impact of morphological (Fig. 2) and energetic (Fig. 5) disorder. This phenomenon is, however, more drastic in the case of **FTPD** and ***spiro*-OMeTAD**, due to the higher σ value of the site energy difference distributions in the amorphous phase (Fig. 5). In the crystalline phase, the computed hole mobilities are generally comparable to each other (~10^{-2} cm^2 V^{-1} s^{-1}), with the only exception of **FTPD**, which has a lower average mobility, probably due to the rather low values of the electronic couplings (around 9 meV), as compared to the other triphenylamines. For those cases in which the experimental single crystal hole mobility is available in the literature, that are **TPA** and ***spiro*-OMeTAD** (Table 3), the computed hole mobilities of single crystals are in very good agreement with the measured one. For **TPD** we could not find experimental data referring to single crystals, while for **FTPD** the experimental values refer to semi-crystalline thin films. Clearly, our simulations on a single crystal do not take into account the presence of defects (*e.g.*, vacancies, dislocations), impurities or grain boundaries, thus overestimating the charge mobility. We note that one cannot trivially infer the magnitude of the charge mobility from the size of the area covered by the superimposed trajectories (Fig. 8) alone when comparing different compounds, since the time it took to complete the trajectories is not visible in the plots and the same number of KMC steps is performed in all cases. The anisotropy of the mobility tensors however can be clearly observed.

Comparing the results from the KMC charge transport simulations in the crystalline and amorphous morphologies (see also the ESI,† Fig. S11 and S14), besides the drop of the hole mobility from two to four orders of magnitude (which is expected for small molecules), one can also observe the loss of directional anisotropy, especially for **TPD** and ***spiro*-OMeTAD**, which show clear preferential charge percolation directions in single crystals. Interestingly, for these anisotropic cases (**TPD** and ***spiro*-OMeTAD**), the highest computed hole mobility (μ_{yy} = 1.6 × 10^{-1} cm^2 V^{-1} s^{-1} for **TPD** and μ_{xx} = 4.3 × 10^{-2} cm^2 V^{-1} s^{-1}

Table 3 Computed Brownian hole mobilities (μ, cm^2 V^{-1} s^{-1}) for single crystal and amorphous phases. Computed Brownian hole mobilites along the *x*, *y* and *z* axes (μ_{xx}, μ_{yy}, μ_{zz}) for each single crystal. Experimental mobilities can refer to single crystal (**TPA**, ***spiro*-OMeTAD**), amorphous (**TPD**, ***spiro*-OMeTAD**) or semicrystalline thin films (**FTPD**), as taken from the literature

	TPA	**TPD**	**FTPD**	***spiro*-OMeTAD**
Computed (single crystal)				
μ_{average}	2.5×10^{-2}	5.9×10^{-2}	1.0×10^{-3}	1.6×10^{-2}
μ_{xx}	2.3×10^{-2}	7.1×10^{-3}	1.8×10^{-3}	4.3×10^{-2}
μ_{yy}	2.2×10^{-2}	1.6×10^{-1}	8.6×10^{-4}	5.3×10^{-3}
μ_{zz}	3.1×10^{-2}	1.1×10^{-2}	4.5×10^{-4}	3.4×10^{-4}
Computed (amorphous)				
μ_{average}	8.3×10^{-4}	5.9×10^{-4}	3.1×10^{-6}	2.3×10^{-6}
Experimental data from literature	2×10^{-2} [65] (single crystal)	1×10^{-3} [1] (amorphous thin film)	4.3×10^{-4} [21] (semicrystalline thin film)	1.30×10^{-3} [22] (single crystal) 1.69×10^{-6} [22] (amorphous thin film)

for ***spiro*-OMeTAD**) can be one or two orders of magnitude larger than the other components of the mobility tensor. This knowledge can pave the way for exploiting morphologically controlled experimental techniques to grow the **TPAs** crystals along with particular directions, in order to enhance the hole mobility.

In the amorphous bulk morphology all triphenylamines show isotropic Brownian charge diffusion. This feature is related to the loss of structural order passing from the crystal to the amorphous phase, as suggested by the radial distribution function analysis (Fig. 2). **TPA** and **TPD** show the highest computed hole mobilities (8.3 and 5.9 × 10^{-4} cm^2 V^{-1} s^{-1}) in the amorphous phase, two orders of magnitudes higher than **FTPD** and ***spiro*-OMeTAD** ($\sim 10^{-6}$ cm^2 V^{-1} s^{-1}). These differences originate from the site energy disorder (Fig. 4), which is lower for **TPA** and **TPD** (σ = 0.18 and 0.12 meV, respectively) with respect to **FTPD** and ***spiro*-OMeTAD** (σ = 0.24 and 0.27 meV, respectively). The broad site energy difference distributions in the amorphous phase of each species lead to charge trapping and low charge transfer rates, thus impacting the final zero-field charge mobility. A good agreement is achieved between the computed charge mobility for the amorphous phase with respect to the available experimental data, as for the cases of **TPD** and ***spiro*-MeOTAD**.

Conclusion

We have presented an in-depth study about the interplay between the structural complexity, the supramolecular packing in the crystalline and amorphous condensed phases, and the charge transport parameters of four triphenylamine derivatives. The influence of the molecular architecture can be observed in the radial distribution function characterising the CoM distances at short- and long-ranges, in both the crystalline and amorphous phases. In the crystal phase, small, sphere-like compounds like **TPA** can get very close to each other, resulting in packed structures, while elongated two-redox center (**TPD**, **FTPD**) or sterically demanding four-redox center (***spiro*-OMeTAD**) compounds show very large CoM distances. In the amorphous phase, however, due to the favourable aspect ratio or backbone flexibility, the elongated two-redox center derivatives can afford shorter CoM distances than **TPA** and ***spiro*-OMeTAD.** Such a different structural order impacts the bulk charge mobility.

From the calculation of the charge transport parameters, we firstly remarked the dependence of the intramolecular reorganization energy on the degree of charge delocalization in multi-redox-center **TPA** species. This charge delocalization is influenced by the flexibility of the molecular structure, namely the bridge connecting the redox centers. We found that reasonable reorganization energies can be computed by adopting a charge partitioning scheme (*via* C-DFT), which localizes the charge on single redox **TPA** centers. This method provides values of the internal reorganization energy very close to those obtained by the well-consolidated frozen dihedral angle approach, where torsional angles are fixed upon charging, thus avoiding the twisting which is reasonably hindered in the bulk phase.

The narrow site-energy distributions in the crystalline phase as computed for all **TPAs** lead to a reorganization energy controlled hopping transport regime in single crystals. In the amorphous phase, however, the charge transport is instead dominated by the static energetic disorder. Indeed, the standard deviation of the site energy difference distributions of amorphous morphologies is larger than for crystals. In particular, the structurally complex compounds like **FTPD** and ***spiro*-OMeTAD** show higher energetic disorder than **TPA** and **TPD**, thus leading to very low (10^{-6} cm^2 V^{-1} s^{-1}) values for the charge mobility in the amorphous phase. A detailed analysis of the crystal structures of **TPAs** with regard to molecular packing and electronic coupling distribution revealed the origin of the charge transport (an)isotropy in the single crystalline phases. In particular, elongated **TPD** or bulky ***spiro*-OMeTAD** show preferential charge diffusion along specific crystal axes, leading to strong anisotropy in hole transport. Our work shows that in crystalline phases the average mobility is very similar for all compounds; however the charge transport anisotropy leads to charge mobility differences for some directions of multiple orders of magnitude for some species, like **TPD** and ***spiro*-OMeTAD**. This characteristic can be potentially exploited to grow crystalline films along particular crystallographic directions, thus achieving the highest charge mobility for that compound. Generally, the computed hole mobilities are in very good agreement with the available experimental data (either measured on single crystal/semi-crystalline films, or amorphous films), corroborating our computational approach.

Author contributions

R. H. and D. F. performed the calculations and the computational analyses. R. H., D. F., K. M. and F. N. conceptualized the work. All authors contributed to rationalizing the data and writing the manuscript.

Conflicts of interest

There are no conflicts of interest to declare.

Acknowledgements

D. F. acknowledges the Deutsche Forschungsgemeinschaft (DFG) for the grant (FA 1502/1-1, years 2018-2021), the Regional Computing Centre (RRZK) of the University of Cologne for providing computing time and resources on the HPC RRZK CHEOPS, and partial funding from the National Recovery and Resilience Plan (NRRP), Mission 04 Component 2, Investment 1.5 – NextGenerationEU, Call for tender n. 3277 dated 30/12/2021, Award Number: 0001052 dated 23/06/2022. K. M., D. F. and R. H. acknowledge the excellence initiative of the University of Cologne, "Quantum Matter and Materials" (QM2), and the DFG Research Training Group 2591 "Template-designed Organic Electronics (TIDE)" for supporting their research.

Notes and references

1 M. Stolka, J. F. Yanus and D. M. Pai, *J. Phys. Chem.*, 1984, **88**, 4707–4714.

2 P. Cias, C. Slugovc and G. Gescheidt, *J. Phys. Chem. A*, 2011, **115**, 14519–14525.

3 C. Adachi, K. Nagai and N. Tamoto, *Appl. Phys. Lett.*, 1995, **66**, 2679–2681.

4 Y. Shirota, *J. Mater. Chem.*, 2005, **15**, 75–93.

5 J. K. Feng, Y. L. Cao, X. P. Ai and H. X. Yang, *J. Power Sources*, 2008, **177**, 199–204.

6 H. Tanaka, S. Tokito, Y. Taga and A. Okada, *Chem. Commun.*, 1996, 2175.

7 S. Tokito, H. Tanaka, K. Noda, A. Okada and Y. Taga, *Appl. Phys. Lett.*, 1997, **70**, 1929–1931.

8 P. Agarwala and D. Kabra, *J. Mater. Chem. A*, 2017, **5**, 1348–1373.

9 P. Blanchard, C. Malacrida, C. Cabanetos, J. Roncali and S. Ludwigs, *Polym. Int.*, 2019, **68**, 589–606.

10 Y. Tao, Q. Wang, C. Yang, C. Zhong, J. Qin and D. Ma, *Adv. Funct. Mater.*, 2010, **20**, 2923–2929.

11 A. Leliège, P. Blanchard, T. Rousseau and J. Roncali, *Org. Lett.*, 2011, **13**, 3098–3101.

12 H. Choi, J. W. Cho, M.-S. Kang and J. Ko, *Chem. Commun.*, 2015, **51**, 9305–9308.

13 N. Goujon, N. Casado, N. Patil, R. Marcilla and D. Mecerreyes, *Prog. Polym. Sci.*, 2021, **122**, 101449.

14 L. Fan, Q. Liu, Z. Xu and B. Lu, *ACS Energy Lett.*, 2017, **2**, 1614–1620.

15 S. Feser and K. Meerholz, *Chem. Mater.*, 2011, **23**, 5001–5005.

16 P. Zacharias, M. C. Gather, M. Rojahn, O. Nuyken and K. Meerholz, *Angew. Chem., Int. Ed.*, 2007, **46**, 4388–4392.

17 P. Friederich, V. Meded, A. Poschlad, T. Neumann, V. Rodin, V. Stehr, F. Symalla, D. Danilov, G. Lüdemann, R. F. Fink, I. Kondov, F. von Wrochem and W. Wenzel, *Adv. Funct. Mater.*, 2016, **26**, 5757–5763.

18 K.-H. Lin, L. Paterson, F. May and D. Andrienko, *npj Comput. Mater.*, 2021, **7**, 1–7.

19 A. Mondal, L. Paterson, J. Cho, K.-H. Lin, B. van der Zee, G.-J. A. H. Wetzelaer, A. Stankevych, A. Vakhnin, J.-J. Kim, A. Kadashchuk, P. W. M. Blom, F. May and D. Andrienko, *Chem. Phys. Rev.*, 2021, **2**, 31304.

20 K.-H. Lin, A. Prlj, L. Yao, N. Drigo, H.-H. Cho, M. K. Nazeeruddin, K. Sivula and C. Corminboeuf, *Chem. Mater.*, 2019, **31**, 6605–6614.

21 L. Fang, A. Zheng, M. Ren, X. Xie and P. Wang, *ACS Appl. Mater. Interfaces*, 2019, **11**, 39001–39009.

22 D. Shi, X. Qin, Y. Li, Y. He, C. Zhong, J. Pan, H. Dong, W. Xu, T. Li, W. Hu, J.-L. Brédas and O. M. Bakr, *Sci. Adv.*, 2016, **2**, e1501491.

23 B. C. Lin, C. P. Cheng and Z. P. M. Lao, *J. Phys. Chem. A*, 2003, **107**, 5241–5251.

24 J. T. Blaskovits, K.-H. Lin, R. Fabregat, I. Swiderska, H. Wu and C. Corminboeuf, *J. Phys. Chem. C*, 2021, **125**, 17355–17362.

25 J.-D. Chai and M. Head-Gordon, *Phys. Chem. Chem. Phys.*, 2008, **10**, 6615–6620.

26 A. D. Becke, *J. Chem. Phys.*, 1993, **98**, 5648–5652.

27 C. Lee, W. Yang and R. G. Parr, *Phys. Rev. B: Condens. Matter Mater. Phys.*, 1988, **37**, 785–789.

28 S. H. Vosko, L. Wilk and M. Nusair, *Can. J. Phys.*, 1980, **58**, 1200–1211.

29 R. Krishnan, J. S. Binkley, R. Seeger and J. A. Pople, *J. Chem. Phys.*, 1980, **72**, 650–654.

30 B. P. Pritchard, D. Altarawy, B. Didier, T. D. Gibson and T. L. Windus, *J. Chem. Inf. Model.*, 2019, **59**, 4814–4820.

31 T. Clark, J. Chandrasekhar, G. W. Spitznagel and P. V. R. Schleyer, *J. Comput. Chem.*, 1983, **4**, 294–301.

32 T. Yanai, D. P. Tew and N. C. Handy, *Chem. Phys. Lett.*, 2004, **393**, 51–57.

33 C. Bannwarth, E. Caldeweyher, S. Ehlert, A. Hansen, P. Pracht, J. Seibert, S. Spicher and S. Grimme, *WIREs Comput. Mol. Sci.*, 2021, **11**, e1493.

34 C. Bannwarth, S. Ehlert and S. Grimme, *J. Chem. Theory Comput.*, 2019, **15**, 1652–1671.

35 K. Ramachandran, A. Raja, N. Lingamurthy, M. S. Pandian, P. Ramasamy and S. Venugopal Rao, *Chem. Phys. Lett.*, 2020, **742**, 137128.

36 Z. Zhang, E. Burkholder and J. Zubieta, *Acta Crystallogr., Sect. C: Cryst. Struct. Commun.*, 2004, **60**, o452–4.

37 R. A. Marcus, *Angew. Chem., Int. Ed. Engl.*, 1993, **32**, 1111–1121.

38 R. A. Marcus and N. Sutin, *Biochim. Biophys. Acta, Bioenerg.*, 1985, **811**, 265–322.

39 S. F. Nelsen, S. C. Blackstock and Y. Kim, *J. Am. Chem. Soc.*, 1987, **109**, 677–682.

40 S. Di Motta, E. Di Donato, F. Negri, G. Orlandi, D. Fazzi and C. Castiglioni, *J. Am. Chem. Soc.*, 2009, **131**, 6591–6598.

41 D. P. McMahon and A. Troisi, *J. Phys. Chem. Lett.*, 2010, **1**, 941–946.

42 J. E. Norton and J.-L. Brédas, *J. Am. Chem. Soc.*, 2008, **130**, 12377–12384.

43 E. F. Valeev, V. Coropceanu, D. A. Da Silva Filho, S. Salman and J.-L. Brédas, *J. Am. Chem. Soc.*, 2006, **128**, 9882–9886.

44 B. Baumeier, J. Kirkpatrick and D. Andrienko, *Phys. Chem. Chem. Phys.*, 2010, **12**, 11103–11113.

45 J. Kirkpatrick, *Int. J. Quantum Chem.*, 2008, **108**, 51–56.

46 V. Rühle, A. Lukyanov, F. May, M. Schrader, T. Vehoff, J. Kirkpatrick, B. Baumeier and D. Andrienko, *J. Chem. Theory Comput.*, 2011, **7**, 3335–3345.

47 J. Kirkpatrick, V. Marcon, K. Kremer, J. Nelson and D. Andrienko, *J. Chem. Phys.*, 2008, **129**, 94506.

48 I. Yavuz, B. N. Martin, J. Park and K. N. Houk, *J. Am. Chem. Soc.*, 2015, **137**, 2856–2866.

49 M. J. Frisch, G. W. Trucks, H. B. Schlegel, G. E. Scuseria, M. A. Robb, J. R. Cheeseman, G. Scalmani, V. Barone, G. A. Petersson, H. Nakatsuji, X. Li, M. Caricato, A. V. Marenich, J. Bloino, B. G. Janesko, R. Gomperts, B. Mennucci, H. P. Hratchian, J. V. Ortiz, A. F. Izmaylov, J. L. Sonnenberg, D. Williams-Young, F. Ding, F. Lipparini, F. Egidi, J. Goings, B. Peng, A. Petrone, T. Henderson, D. Ranasinghe, V. G. Zakrzewski, J. Gao, N. Rega, G. Zheng, W. Liang, M. Hada, M. Ehara, K. Toyota, R. Fukuda, J. Hasegawa, M. Ishida, T. Nakajima, Y. Honda, O. Kitao, H. Nakai, T. Vreven, K. Throssell, J. A. Montgomery, Jr., J. E. Peralta, F. Ogliaro, M. J. Bearpark, J. J. Heyd, E. N. Brothers, K. N. Kudin, V. N. Staroverov, T. A. Keith, R. Kobayashi, J. Normand, K. Raghavachari, A. P. Rendell, J. C. Burant, S. S. Iyengar, J. Tomasi, M. Cossi, J. M. Millam, M. Klene, C. Adamo, R. Cammi, J. W. Ochterski, R. L. Martin, K. Morokuma, O. Farkas, J. B. Foresman and D. J. Fox, *Gaussian*, Gaussian, Inc., Wallingford CT, 2016.

50 F. Neese, F. Wennmohs, U. Becker and C. Riplinger, *J. Chem. Phys.*, 2020, **152**, 224108.

51 E. Aprà, E. J. Bylaska, W. A. de Jong, N. Govind, K. Kowalski, T. P. Straatsma, M. Valiev, H. J. J. van Dam, Y. Alexeev, J. Anchell, V. Anisimov, F. W. Aquino, R. Atta-Fynn, J. Autschbach, N. P. Bauman, J. C. Becca, D. E. Bernholdt, K. Bhaskaran-Nair, S. Bogatko, P. Borowski, J. Boschen, J. Brabec, A. Bruner, E. Cauët, Y. Chen, G. N. Chuev, C. J. Cramer, J. Daily, M. J. O. Deegan, T. H. Dunning, M. Dupuis, K. G. Dyall, G. I. Fann, S. A. Fischer, A. Fonari, H. Früchtl, L. Gagliardi, J. Garza, N. Gawande, S. Ghosh, K. Glaesemann, A. W. Götz, J. Hammond, V. Helms, E. D. Hermes, K. Hirao, S. Hirata, M. Jacquelin, L. Jensen, B. G. Johnson, H. Jónsson, R. A. Kendall, M. Klemm, R. Kobayashi, V. Konkov, S. Krishnamoorthy, M. Krishnan, Z. Lin, R. D. Lins, R. J. Littlefield, A. J. Logsdail, K. Lopata, W. Ma, A. V. Marenich, J. Del Martin Campo, D. Mejia-Rodriguez, J. E. Moore, J. M. Mullin, T. Nakajima, D. R. Nascimento, J. A. Nichols, P. J. Nichols, J. Nieplocha, A. Otero-de-la-Roza, B. Palmer, A. Panyala, T. Pirojsirikul, B. Peng, R. Peverati, J. Pittner, L. Pollack, R. M. Richard, P. Sadayappan, G. C. Schatz, W. A. Shelton, D. W. Silverstein, D. M. A. Smith, T. A. Soares, D. Song, M. Swart, H. L. Taylor, G. S. Thomas, V. Tipparaju, D. G. Truhlar, K. Tsemekhman, T. van Voorhis, Á. Vázquez-Mayagoitia, P. Verma, O. Villa, A. Vishnu, K. D. Vogiatzis, D. Wang, J. H. Weare, M. J. Williamson, T. L. Windus, K. Woliński, A. T. Wong, Q. Wu, C. Yang, Q. Yu, M. Zacharias, Z. Zhang, Y. Zhao and R. J. Harrison, *J. Chem. Phys.*, 2020, **152**, 184102.

52 H. Berendsen, D. van der Spoel and R. van Drunen, *Comput. Phys. Commun.*, 1995, **91**, 43–56.

53 B. Hess, C. Kutzner, D. van der Spoel and E. Lindahl, *J. Chem. Theory Comput.*, 2008, **4**, 435–447.

54 E. Lindahl, B. Hess and D. van der Spoel, *J. Mol. Model.*, 2001, **7**, 306–317.

55 S. Pronk, S. Páll, R. Schulz, P. Larsson, P. Bjelkmar, R. Apostolov, M. R. Shirts, J. C. Smith, P. M. Kasson, D. van der Spoel, B. Hess and E. Lindahl, *Bioinformatics*, 2013, **29**, 845–854.

56 D. van der Spoel, E. Lindahl, B. Hess, G. Groenhof, A. E. Mark and H. J. C. Berendsen, *J. Comput. Chem.*, 2005, **26**, 1701–1718.

57 W. L. Jorgensen, D. S. Maxwell and J. Tirado-Rives, *J. Am. Chem. Soc.*, 1996, **118**, 11225–11236.

58 G. A. Kaminski, R. A. Friesner, J. Tirado-Rives and W. L. Jorgensen, *J. Phys. Chem. B*, 2001, **105**, 6474–6487.

59 E. Di Donato, R. P. Fornari, S. Di Motta, Y. Li, Z. Wang and F. Negri, *J. Phys. Chem. B*, 2010, **114**, 5327–5334.

60 S. Di Motta, M. Siracusa and F. Negri, *J. Phys. Chem. C*, 2011, **115**, 20754–20764.

61 N. Gildemeister, G. Ricci, L. Böhner, J. M. Neudörfl, D. Hertel, F. Würthner, F. Negri, K. Meerholz and D. Fazzi, *J. Mater. Chem. C*, 2021, **9**, 10851–10864.

62 M. Renz, K. Theilacker, C. Lambert and M. Kaupp, *J. Am. Chem. Soc.*, 2009, **131**, 16292–16302.

63 M. Lundberg and P. E. M. Siegbahn, *J. Chem. Phys.*, 2005, **122**, 224103.

64 Y. Li, H. Li, C. Zhong, G. Sini and J.-L. Brédas, *npj Flexible Electron.*, 2017, **1**, 1–8.

65 D. C. Hoesterey and G. M. Letson, *J. Chem. Phys.*, 1964, **41**, 675–679.

CHAPTER 5

Mixed hole and ion transport in cross-linkable TPAs

Oxetane-functionalized **TPAs** have long been used as cross-linkable hole-transport layers for organic electronics applications. [36, 43–45] Due to the insolubility of the cross-linked films, they can also be used for electrochemical applications. The aim of the second investigation was to analyze and understand the structure as well as the coupled electronic and ionic transport in cross-linkable **TPA**s as OMIECs for electrochemical devices. The coupled hole and ion transport in OMIECs is a highly complex phenomenon which is not fully understood due to a missing combined physical model. Such understanding is required for future design of **TPA** based OMIECs. The full publication with all details is given in section 5.7, while the results are summarized here and put into the context of the thesis.

5.1 Mixed hole and ion transport

The research approach of publication II was to obtain a realistic morphology, determine the timescales involved in electronic and ionic transport, statically and dynamically evaluate the energetic landscape based on the site energies and the Marcus transfer rates in order to finally gain a deeper understanding of the coupled electronic and ionic transport. It is noteworthy that the large static disorder (width of the site energy distributions) that can be found in OMIECs contradicts the experimentally found high mobilities, a fact which can only be reconciled by simultaneous high dynamic disorder that allows to remove holes from trapped states. [23, 128] A combined physical model describing the coupled charge and ion transport is missing however. In publication II, a new approach to describe the electronic charge transport in the presence of high static and dynamic disorder based on effective Marcus residence times is presented. Polymerizable **TPA**s as shown in Fig. 5.1 are especially amenable for this investigation since they feature localized sites that allow for the determination of discrete Marcus rates.

5.2 Polymer systems

At first, polymer morphologies of the two polymerizable **TPA**s were generated as accurately as possible in lieu of experimental data via the heuristic protocol `REACTER` [110] that models the chemical reaction *in silico*. The polymerization reaction is shown in Figure 5.2.

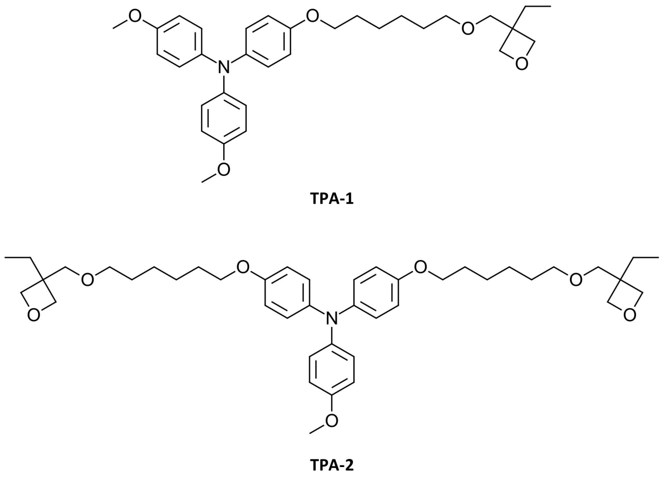
TPA-1

TPA-2

Figure 5.1: Oxetane-functionalized **TPAs**.

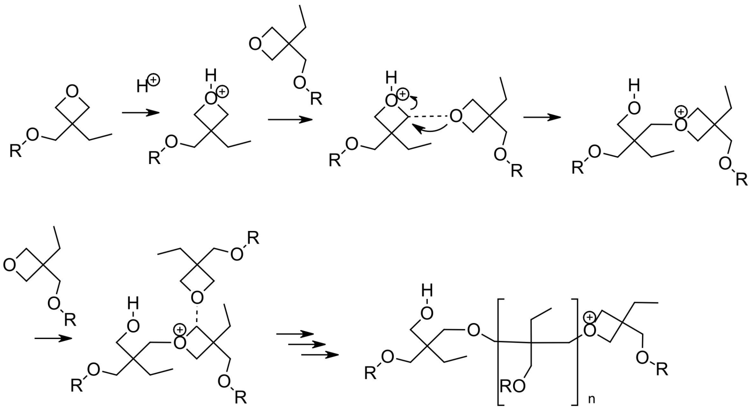

Figure 5.2: Cationic ring-opening polymerization reaction of oxetanes. Electrophilic attack of a proton initiates the reaction, followed by the ring-opening attack of another oxetane ring. The polymeric product is formed by continuous opening of the oxetane rings.

The polymerization reaction is a living polymerization reaction, meaning it has no termination reaction and a relatively narrow distribution of chain lengths can be expected. The high ring-strain of the oxetanes minimizes re-closure of the oxetane rings and allows for high conversion rates.

The polymer systems were generated in step-wise approach. After reparametrizing the OPLS-AA force field (see A.2 for details) equilibrated monomer system were generated by a thermal annealing approach. From the equilibrated monomer systems (512 monomers), the polymerized systems were generated by using `REACTER` and mimicking the experimental procedure by using 5 mol% protons as initiator, however using high temperature (1000 K) and pressure (100 bar) in order to ensure fast reaction completion. It should be noted that **TPA-1** yields linear polymers (**pTPA**) and **TPA-2** yields cross-linked systems (**xTPA**). Investigating on these two systems allows to focus on the limit cases of fully cross-linked versus linear polymers. Fig. 5.3 shows the reaction turnover and the oligomer length distribution in the case of **TPA-1**.

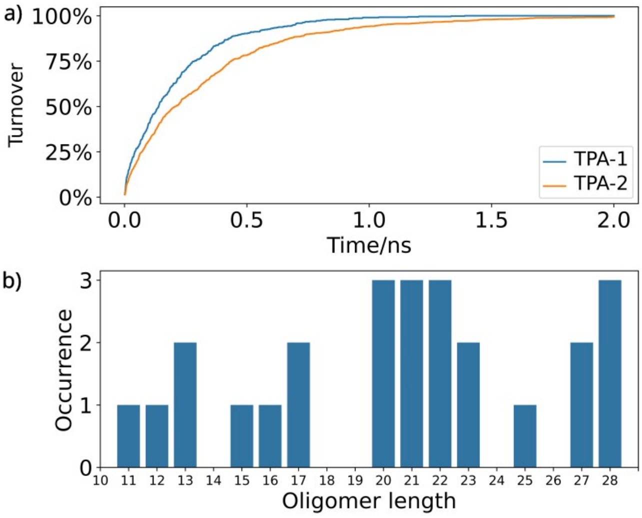

Figure 5.3: MD simulations to generate polymer systems. a) Turnover of the CROP reaction using 512 monomers. b) Distribution of oligomer lengths after full oxetane conversion in **TPA-1**.

After generating the polymerized systems, their glass transition temperature T_g was determined and compared with experimental data in order to validate the modeling approach, which yielded satisfactory agreement (see also Fig. 5.10(a)) Analyzing the bulk structures via the radial distribution functions showed that upon polymerization, the tertiary oxetane carbon and the nitrogen centers move farther apart due to the increased steric congestion limiting conformational freedom in the polymeric phase. An average pore radius in the bulk structures of 1.69 Å for **pTPA** and 1.83 Å for **xTPA** was found, suggesting slow ion diffusion for PF_6^- ions featuring a radius of 2.33–2.88 Å.

5.3 Ion transport

Ion transport simulations were performed by randomly inserting one PF_6^- ion into the systems and generating a MD trajectory for analysis. Investigating the mean square displacement of the PF_6^- ions showed that even after 100 ns, the ion transport had not become diffusive (see Fig. 5.4). Generally, the ion transport takes place in the nano- up to microsecond time scale, being much slower than the typical timescale of electronic transport (ps-range). In the linear polymer system **pTPA**, the ion transport was found to be faster than in the more constrained cross-linked **xTPA**, showing the influence of the polymer mobility.

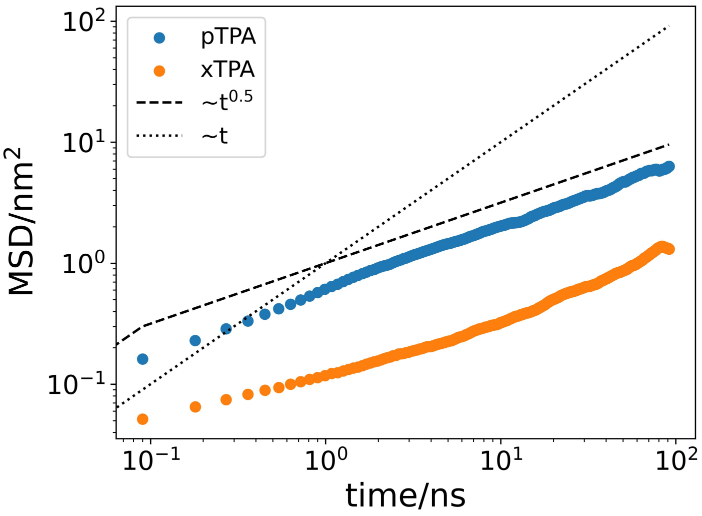

Figure 5.4: Mean square displacement (MSD) of a PF_6^- ion in a log-log plot.

5.4 Static and dynamic site energy landscapes

The static site energy landscape at different doping levels (0%-15%) was assessed as one of the central charge transport parameters. Strong static disorder was found in all systems as shown in Fig. 5.5, indicating deep traps and low mobilities, even vanishing charge transport. However, monitoring the site energy difference fluctuations showed very strong variations consistent with high dynamic disorder that can remove deep traps, as shown in Fig. 5.6. In order to quantify the dynamic disorder, the autocorrelation function (ACF) of the site energy differences was calculated. It is given by

$$ACF = \left\langle \Delta E_{ij}(t_0) \Delta E_{ij}(t_0 + \tau) \right\rangle \tag{5.1}$$

where t_0 is the starting time and τ are the time-lags. A 10 ps MD trajectory, using a sampling rate of one snapshot every 10 fs was used, averaging over 20 close-contact **TPA** pairs and employing a running average over 10 timesteps to exclude high frequency vibrations that would be ill-described by classical MD. Investigating the autocorrelation function (ACF) of the site energy differences showed a decay within ca. 1 ps in all systems as related to fast intramolecular vibrations, occuring on a much faster timescale than the previously investigated ion transport.

Following the strong site energy difference fluctuations, the Marcus rates also strongly change in time, leading to continuously opening and closing charge transfer channels, allowing to overcome trapping. However, since the timescale seperation betweeen site energy fluctuation and the charge transfer events is no longer present in systems with such high dynamic disorder, standard kinetic Monte-Carlo simulations and fixed rates can no longer be used for simulation of the charge mobility.

5.5 Effective Marcus residence times

Due to the circumstances explained in the previous section, a novel approach was developed to describe the coupled charge and ion transport by including the dynamic site energy fluctuations caused by

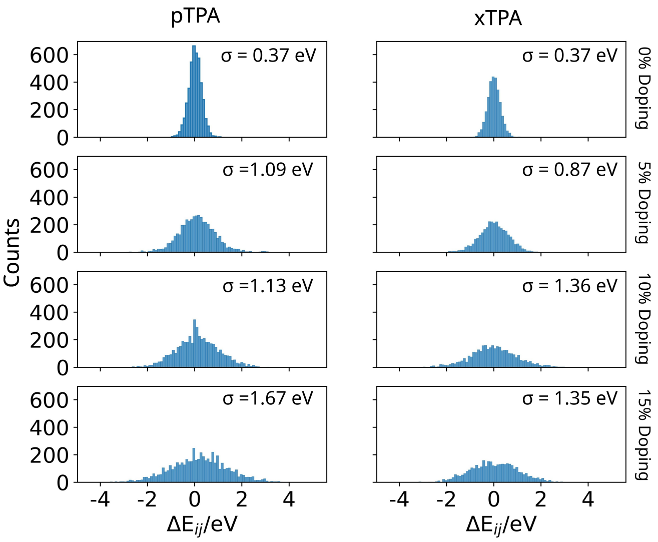

Figure 5.5: Site energy differences at different doping levels.

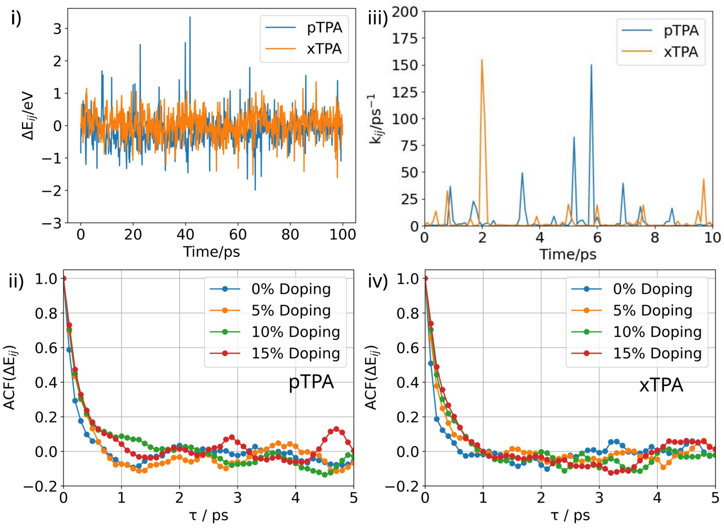

Figure 5.6: Fluctuations of site energy differences and Marcus rates as well as site energy difference autocorrelation functions.

polymer-ion motion. Eq. 5.2 yields the time dependent population P_i at time T of site i due to depopulation to site j. $k_{ij}(t_n)$ are the time-dependent rates at timestep t_n and ΔT are the time steps of 0.1 ps. A time of 100 ps was monitored during this investigation.

$$P_i(T = N\Delta T) = 1 - \sum_{n=1}^{N} k_{ij}(t_n) \mathrm{e}^{-k_{ij}(t_n)t_n} \Delta T \tag{5.2}$$

The effective Marcus residence time $\tau_{i\to j}$ is the time at which P_i=0.5, i.e. the half-time of depopulation. Using the τ as well as the fixed Marcus rates at the first timeframe, the static and effective lifetimes t_i^{static} and $t_i^{effective}$ of the states can be computed using eq. 5.3 and eq. 5.4.

$$t_i^{static} = \left(\frac{1}{\sum_j k_{ij}}\right) \tag{5.3}$$

$$t_i^{effective} = \left(\sum_j \frac{1}{\tau_{i\to j}}\right)^{-1} \tag{5.4}$$

While t_i^{static} describes the liftime of a state if the energy landscape remains unchanged, $t_i^{effective}$ incorporates the site energy fluctuations into the lifetimes. The distributions of t_i^{static} and $t_i^{effective}$ are shown in Fig. 5.7.

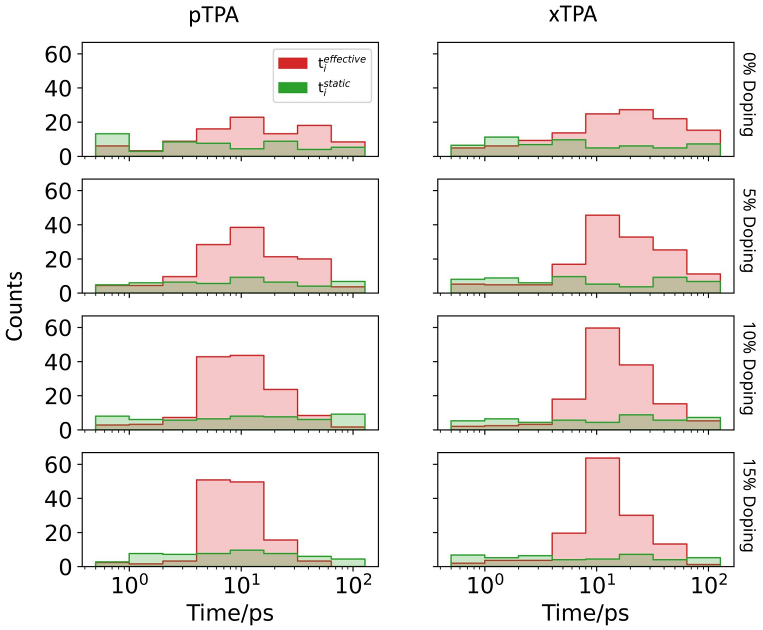

Figure 5.7: Distributions of the static lifetimes t_i^{static} and the effective lifetimes $t_i^{effective}$.

Analyzing t_i^{static} and $t_i^{effective}$ shows that the $t_i^{effective}$ distributions are shifted to much lower values, indicating that the dynamically shifting site energy landscape leads to efficient detrapping, promoting charge transfer despite high static disorder.

In order to obtain further insight into the charge transport and include the three-dimensionality of the charge transport networks developing in time, graph representations of the networks were generated. These networks, as shown in Fig. 5.8, become progressively less dense with increased doping level, showing that even though the detrapping due to the high dynamic disorder promotes rapid charge transfer, the charge transport networks are also transient in time and develop only slowly in the higher doped cases. This additional analysis shows the delicate nature of the coupled electronic and ionic transport in OMIECs.

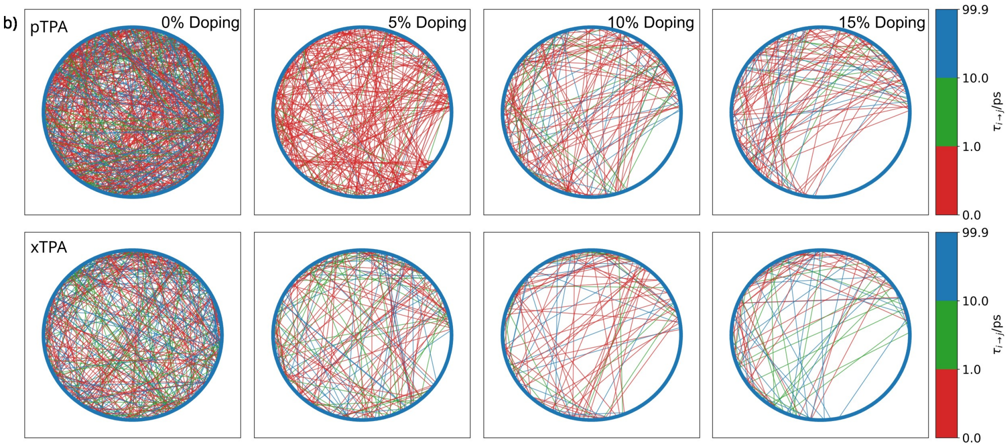

Figure 5.8: Circular graph representations of the effective Marcus residence times at different doping levels.

5.6 Conclusion

In summary, not only the complex polymer structure of oxetane-functionalized and polymerized **TPA**-based OMIECs has been accurately modeled and analyzed in this work, the static and dynamic energy landscapes and the timescales of transport processes were determined as well including a novel approach for the description of charge transport in the presence of high dynamic disorder. The work is based on a realistic approach for generating the systems employing *in silico* polymerization of the monomeric materials. Such an approach generates much more realistic polymer systems than the typically truncated polymer models used in literature, leading to excellent agreement between the experimental and computed glass transition temperatures. Realistic morphologies are also very important to accurately describe the complex polymer-ion dynamics. The investigation revealed slow, and for electrochemical applications most likely rate-determining ion transport. The charge transport occurs on much faster timescales as it is related to the comparably rapid site energy fluctuations. Since such fast site energy fluctuations, i.e. large dynamic disorder leads to likewise fluctuation charge transfer rates, kinetic Monte Carlo and a fixed set of rates can not be used to characterize the charge transport. Therefore, a new approach incorporating dynamic disorder into the charge transport description was devised to model the coupled charge and ion transport central to OMIEC applications based on effective Marcus residence times. This work represents an important step on the way to obtain a deeper understanding of OMIEC materials, both on a structural and on a functional level. The system generation approach can be used in future work to gain more knowledge of the structure-property and structure-function relationships of similar cross-linked systems.

5.7 Publication II

All simulations and data analyses have been performed by me. I have written the initial manuscript of the publication and revised it together with the co-authors. The experimental data has been provided by Laura Plein.

Volume 12
Number 19
7 October 2025
Pages 7621–8218

Materials Horizons

rsc.li/materials-horizons

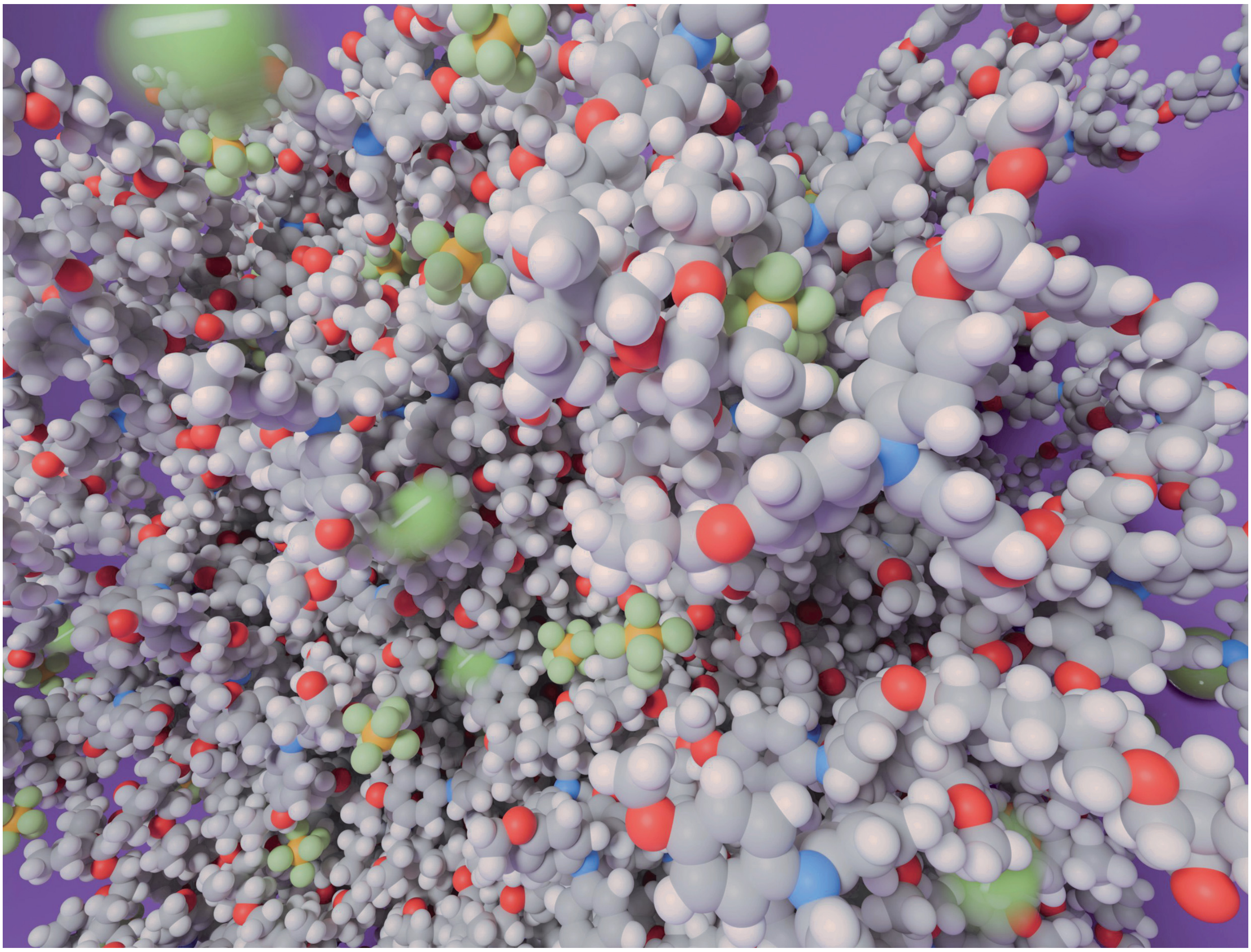

ISSN 2051-6347

ROYAL SOCIETY
OF **CHEMISTRY**

COMMUNICATION
Klaus Meerholz, Daniele Fazzi *et al.*
Dynamics of disorder in mixed ionic–electronic transport in cross-linked non-conjugated redox polymers

Materials
Horizons

ROYAL SOCIETY
OF **CHEMISTRY**

COMMUNICATION

View Article Online
View Journal | View Issue

Check for updates

Cite this: *Mater. Horiz.*, 2025, **12**, 7924

Received 3rd April 2025,
Accepted 7th July 2025

DOI: 10.1039/d5mh00610d

rsc.li/materials-horizons

Dynamics of disorder in mixed ionic–electronic transport in cross-linked non-conjugated redox polymers†

Robert Herzhoff, [a] Laura Plein, [a] Alessandro Troisi, [b] Klaus Meerholz *[a] and Daniele Fazzi *[ac]

The coupled electronic and ionic transport mechanisms in organic mixed ionic–electronic conductors (OMIECs) remain elusive to rationalize. We introduce here an approach to model the entangled hole and ion transport in linear and cross-linked triphenylamine-based (TPA) non-conjugated polymers, studied as redox active materials for organic electrodes. The polymers are created *via* a heuristic method based on molecular dynamics (MD) simulations. Remarkable energetic disorder effects (up to 1.6 eV) are computed in the static limit, for both pristine and doped polymer films, seemingly hindering hole transport. The explicit inclusion of dynamic effects in modelling the energetic disorder leads instead to strong and rapid oscillations of the site-energies, thus enabling a dynamic opening of hole transport channels. To go beyond the static limit for the calculation of the hole transfer rates, encompassing the time-dependence of disorder effects, effective Marcus residence times are introduced for the first time. Distributions of charge escape times are derived for both linear and cross-linked polymers, in their pristine and doped states. Linear polymers show hole escape networks denser than cross-linked ones, suggesting a more efficient hole de-trapping developing as a function of time and disorder effects. Our approach shows that electronic transport in non-conjugated organic electrodes is a highly interdependent phenomenon connected to the bulk morphologies, polymer chain mobility and ion dynamics. A multiscale modelling that captures the dynamics of disorder is therefore indispensable.

New concepts

Dynamic effects, arising from the interplay between electronic charges, ions and molecular motions, govern the transport phenomena in organic mixed ionic–electronic conductors (OMIECs). Rationalizing such complex events, providing a mechanistic understanding at different length-scales, remains challenging due to the structural complexity of organic electrodes. Focusing on cross-linked non-conjugated redox polymers used as organic electrodes, we present a thorough bottom-up approach for modelling the coupled charge- and ion transport. We show how to generate *in silico* cross-linked bulk morphologies, leading to amorphous and porous structures allowing ion penetration and diffusion. We introduce a novel strategy to evaluate both static and dynamic disorder effects in the description of the electronic charge transport, by including the influence of polymer segments and ion motions. Our findings show how deep traps, caused by remarkable static energetic disorder, can be overcome by dynamical effects leading to efficient charge de-trapping and electronic transport. We suggest that the dynamics of disorder are the key to understand the origin of the transport mechanisms in organic electrodes.

Introduction

Organic mixed ionic–electronic conductors (OMIECs) are materials featuring both ionic and electronic conductivities.[1–4] Typical examples include conjugated small molecules (*e.g.*, naphthalene diimide (NDI)-based)[5–8] or polymers (*e.g.*, polythiophenes, poly(2-(4,4′-bis(2-methoxyethoxy)-5′-methyl-[2,2′-bithiophen]-5-yl)-5-methylthieno[3,2-*b*]thiophene) (pgBTTT), poly(3,4 ethylenedioxy-thiophene):polystyrene sulfonate (PEDOT:PSS), poly-(benzimidazobenzophenanthrolin) (BBL), *etc.*),[2,3,8–13] as well as non-conjugated materials like poly(4-glycidyloxy-2,2,6,6-tetramethylpiperidine-1-oxyl) (PTEO)[14] and they represent ideal active systems for a plethora of electrochemical applications, ranging from electrochemical energy storage (EES) devices (*e.g.*, secondary batteries and supercapacitors),[9,15–19] bioelectronics,[20] and optoelectronics,[21] as well as neuromorphic and sensing technologies.[22] Focusing on batteries, organic electrodes can represent an alternative to traditional electrodes commonly based on inorganic materials (*e.g.*, lithium transition metal oxides and nickel–manganese–cobalt-oxides (NMC)) or graphite.[23] Such systems show high energy density; however, they suffer from severe capacity loss due to the degradation of the crystal structure and they are reliant on non-renewable resources.[24] Organic electrodes

---

[a] *Institut für Licht und Materialien, Department für Chemie, Universität zu Köln, Greinstr. 4-6, 50939 Köln, Germany. E-mail: klaus.meerholz@uni-koeln.de, daniele.fazzi@unibo.it*

[b] *University of Liverpool, Department of Chemistry, Liverpool, L69 3BX, UK*

[c] *University of Bologna, Department of Chemistry 'Giacomo Ciamician', via P. Gobetti 85, 40129 Bologna, Italy*

† Electronic supplementary information (ESI) available. See DOI: **https://doi.org/10.1039/d5mh00610d**

can be a sustainable alternative,[25] however, depending on their chemical structure, they feature low specific capacity and energy density.[17] Thus, at the moment, they are rather complementary to the strengths of the inorganic counterparts.

Recent experimental and theoretical contributions from various research groups (*e.g.* Moia *et al.*,[9] Siemons *et al.*,[26] Keene *et al.*,[27,28] Sunny *et al.*,[29] Khot *et al.*,[30] Giovannitti *et al.*,[31] and Tsafati *et al.*[32]) showed that the bulk morphology of conjugated polymer-based OMIECs is highly affected by multiple factors, such as the flexibility of the polymer backbone, the nature of the side chains (*e.g.*, the amount and position of ether groups), and the ability to take in ions and solvent molecules. Changes in the morphology and ion uptake naturally influence the bulk transport properties, but a clear understanding about how ions and charge transport are coupled is still missing. Burke *et al.* and Landi *et al.* have underlined the importance of considering electrostatic disorder effects in modelling the electronic conduction mechanisms in conjugated polymers.[33,34] Their studies revealed that OMIECs are characterised by a large amount of static energetic disorder, represented by a broad distribution of the hopping site energies (ranging from 0.1 to 0.3 eV).[33] In accordance with the charge transfer theories for disordered (amorphous) materials (*e.g.*, Miller–Abrahams[35,36]), charge transport should not occur under high static energetic disorder conditions due to charge trapping in the tail states of the density of states, however this conclusion contradicts the experimental evidence.[37] Despite the large static disorder, charge transport in OMIECs can take place thanks to a favourable energy-level alignment of the hopping sites which develops in time, spontaneously arising from their fluctuations. It is, therefore, the dynamics of the system (*e.g.*, intra- and intermolecular vibrations, polymer segment mobility, and ion motion) which play a central role in organic electrodes and thus need to be included into any atomistic modelling strategy, since a static approach is insufficient to capture the transient nature of the charge transfer events.[33] Despite these findings, the understanding of the interrelated ionic and electronic charge transport in organic electrodes as well as the complex relationship between composition, morphology and transport properties remains limited.[4,28]

In this study, we address the above issues guided by the following questions: (i) what are the time scales characterising transport mechanisms in non-conjugated organic electrodes, that is the dynamics of disorder, (ii) how can we include both nuclear motions, across various time scales, and the charge transfer mechanisms into the charge transport description, and (iii) what are the consequences of different disorder effects (*e.g.*, structural, energetic, *etc.*) impacting the coupled ionic–electronic transport.

To answer the above questions, we model the pristine (*i.e.*, undoped) and doped (*i.e.*, charged‡) bulk morphologies for two redox-active non-conjugated triphenylamine (**TPA**) polymers (so-called redox polymers) *via* molecular dynamics (MD) simulations, encompassing the evaluation of the static and dynamic energy landscape, the rates of the electronic charge transport, and the ion diffusion. The **TPA** monomers, functionalized with one (**TPA-1**) or two (**TPA-2**) oxetane-bearing sidechains, are shown in Fig. 1. They can be polymerized by cationic ring-opening polymerization (CROP), *e.g.* by using a photoacid generator as the proton source after UV-light irradiation, leading to the formation of a linear side-chain polymer (**pTPA**) or a cross-linked polymer network (**xTPA**).[38,39] This approach, successfully exploited in the past for producing hole transport layers for organic light emitting diodes (OLEDs),[40] also allows fabrication of organic cathodes with high cycling stability due to the insolubility of the cross-linked polymer network.[41] Our non-conjugated systems represent a unique platform for an in-depth understanding of the mixed ionic–electronic conduction mechanisms in non-conjugated organic redox materials.[42–45] Indeed, in non-conjugated **TPA**s, the electronic charge (hole) is naturally localized on a particular redox unit (**TPA**), avoiding an undefined degree of charge delocalization (*e.g.*, polaron) over the polymer backbone, as it may occur in π-conjugated systems, in which charge transport may thus follow a different transfer mechanism.[46,47] At the same time, charge localization allows electronic charge mobility by hopping, and cross-linked non-conjugated **TPA**-based polymers have been successfully exploited in the past for organic electronic applications.[38–40]

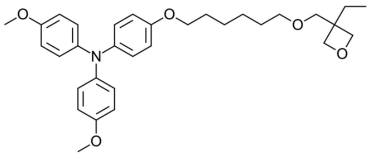

TPA-1

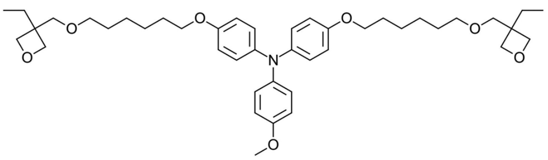

TPA-2

Fig. 1 Chemical structures of triphenylamine compounds with one (**TPA-1**, top) and two oxetane functionalities (**TPA-2**, bottom).

We introduce a novel procedure to model the microstructure of pristine and doped polymerized **TPA**s. For both cases, we compute the hole transport parameters, among which are the site energy differences and their time-dependent fluctuations. Our **TPA** systems show high static site energy disorder ($\sigma \sim 0.4$ eV) already in the pristine state. The energetic disorder increases in the presence of counter ions (hexafluorophosphate anions, PF_6^-), reaching σ values of up to ~1.70 eV. *Via* MD simulations, we demonstrate that the site energies undergo rapid fluctuations in time (ps-timescale) affecting the charge transfer rates. Such fast oscillations of the site energy landscape suggest that the use of a set of fixed charge transfer rates (*e.g.*, Marcus rates) for describing the electronic transport is not meaningful. Therefore, we devise a new approach to explicitly include the dynamics of disorder effects into the hole transport processes, namely to take into account the site energy fluctuations as induced by the molecular vibrations, polymer chains and ion motions. We define an effective Marcus residence time of the charges on individual sites, considered as the average time required by a hole to escape from a trap. Distributions of charge escape times are derived, representing the hole de-trapping process governed by the interplay between the site energy fluctuations, polymer segments and ion movements. Linear polymers show more dense hole escape networks than cross-linked ones, suggesting a more efficient hole de-trapping developing as a function of time and disorder effects.

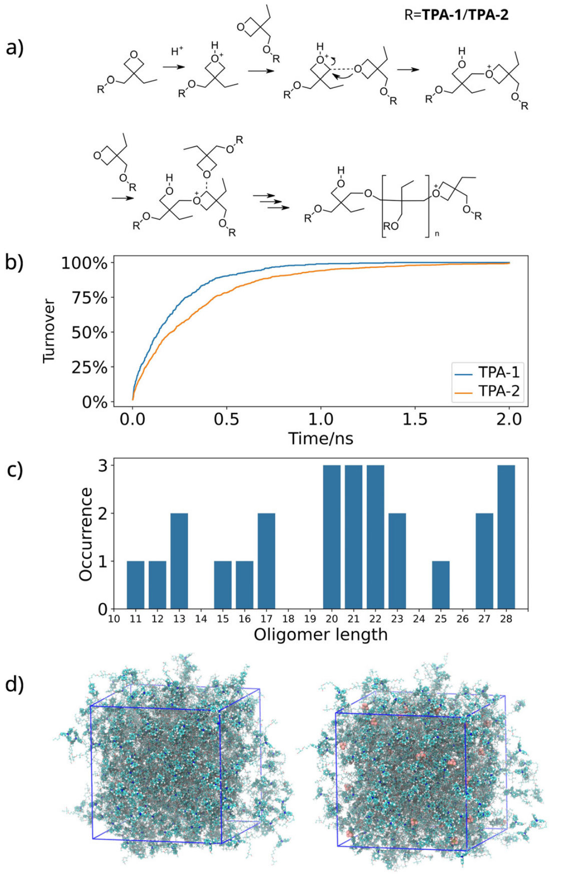

Fig. 2 (a) CROP mechanism.[40] (b)–(d) MD-REACTER simulations using 512 **TPA-1** or **TPA-2** monomers, respectively. (b) Oxetane ring opening turnover. (c) Oligomer length distribution after full oxetane conversion of **TPA-1**. (d) Simulation box for pristine cross-linked **xTPA** (left) and simulation box for **xTPA** with a 10% PF_6^- ion (brown structures) content (right).

Polymerization and bulk morphology generation *via* MD simulations

At the basis of our computational investigation is the creation of reliable bulk morphologies *via* MD simulations. Details about the force field parametrization and the MD simulations are found in the ESI,† while a short overview is given here. Since the polymer structural parameters (*e.g.*, chain lengths, molecular weights, and morphology) are unknown experimentally we adopted a special *in silico* heuristic strategy, explored in the past to determine the morphology of cross-linked polymers.[48] A thermal annealing procedure was used to generate the equilibrated morphologies of the monomers (512 molecules per system) for both **TPA-1** and **TPA-2** species (*i.e.*, unreacted **TPA**s, showing intact oxetane rings (Fig. 1), see the ESI†). Afterwards, MD simulations coupled with the algorithm REACTER[49] (MD-REACTER) were performed to – heuristically – model the ring opening chemical reaction, which leads to the formation of polymers. It is important to mention that the CROP reaction shown in Fig. 2a leads to the formation of a cross-linked network (**xTPA**) in the case of two oxetane functionalities (**TPA-2**), while in the case of **TPA-1**, a linear polymer (**pTPA**) is formed. The initiation step was achieved by randomly placing 25 protons (and 25 chloride ions to ensure charge neutrality) in the monomer simulation boxes, corresponding to *ca.* 5 mol% initiator concentration, and running MD-REACTER simulations at high temperature (1000 K) and pressure (100 bar) to quickly reach complete oxetane conversion (*i.e.*, ring opening). Fig. 2b reports the CROP reaction turnover, showing a faster conversion of **TPA-1** compared to **TPA-2**. While experimentally, a yield of 100% is not achievable because of the limited diffusional mobility of the oxetane groups within the solid thin film, and in the simulation such a high turnover is possible under harsh thermodynamic conditions. Fig. 2c shows the chain length distribution for **pTPA** after 50 ps MD equilibration, and Fig. 2d (left panel) shows an exemplary MD box for the polymer. It should be noted here that the simulated polymer length distributions are limited by the system size of the simulations (*i.e.* 512 monomers) and cannot be directly compared to experimental values.

To better characterize the thermodynamic properties of the linear and cross-linked polymers, we computed the glass transition temperature (T_g) of both **pTPA** and **xTPA** (details in ESI†), by following the MD protocol reported by Lin *et al.* based on cooling the system from 800 K to 300 K and monitoring the density, followed by fitting of the linear regions in the density-temperature plots.[50] Depending on the choice of the fitting range, T_g was predicted to fall in the range between *ca.* 319–333 K (**pTPA**) and 308–328 K (**xTPA**), generally well matching the experimental data (see Fig. S5 in the ESI†) of 297 K (**pTPA**) and 325 K (**xTPA**). The procedure was not able to reproduce the experimental trend in the T_g for **pTPA** and **xTPA** (*i.e.* T_g (**xTPA**) > T_g (**pTPA**)); however, the computed T_g are overall acceptable. To strengthen our modeling approach, we experimentally determined the density of the monomeric systems and compared them to the simulated values, yielding good agreement and matching trends between **TPA-1** and **TPA-2** (see Table S16, ESI†). Furthermore, the T_g values of the 80% polymerized systems were determined, which are generally similar to the T_g values of the fully polymerized systems (see Fig. S9 and Tables S14, S15 in the ESI†). Therefore, the deviations of the simulated and experimental T_g are most likely due to the cooling protocol and force field parameters, rather than the polymer model or the polymerization degree.[51,52] We also note here that the simulated T_g values lie above room temperature, in line with experimental data, meaning that all simulations were performed on solids. The polymer bulk morphologies of **pTPA** and **xTPA** correspond to that of the pristine case (*i.e.*, the absence of PF_6^-) and were used as the starting point for various production runs (*vide infra*).

The morphology and the bulk properties of the doped polymers were obtained by randomly inserting PF_6^- ions in the simulation box at various concentrations, and at the same time creating an equal number of positively charged **TPA** units. We considered different doping levels of 5%, 10% and 15% ion contents relative to the number of monomer units (an example of the MD simulation box at 10% doping is reported in Fig. 2d). For the charge transport analysis, after energy minimization and a further 50 ps MD run of thermal equilibration, both a 10 ps and a 100 ps MD trajectory were generated using sampling rates of one snapshot every 0.01 ps and 0.1 ps, respectively, to generate the data. For the ion diffusion, 300 ns MD trajectories of a singular PF_6^- ion in the bulk polymer morphologies were generated, following a similar procedure as reported by Webb *et al.*[53] The MD simulations were performed by using both LAMMPS[54] (coupled with MD-REACTER), for the generation of the polymerized bulk morphologies and for producing the trajectories for the charge transport analysis and GROMACS[55] (for the ion diffusion study). A reparametrized version of the OPLS-AA[56,57] force field was considered. For visualization and analysis, VMD[58] and TRAVIS[59] were adopted. The code HOLE[60] was used to characterise the dimensions and distribution of pores (voids) of the polymer bulk. Further details are reported in the ESI.† Restart files for all simulations can be found on Github under **https://github.com/rbrthrz/pTPA_xTPA**.

Charge transport parameters

Charge (hole) transport rates k_{ij} between two sites (*i.e.*, **TPA** units) i and j are computed using Marcus theory:[61,62]

$$k_{ij} = \frac{2\pi}{\hbar}\frac{J_{ij}^2}{\sqrt{4\pi\lambda k_B T}}\exp\left[-\frac{\left(\Delta E_{ij}+\lambda\right)^2}{4\lambda k_B T}\right] \quad (1)$$

For the evaluation of the charge transport parameters and rates, the open-source code VOTCA[63] was adopted. In eqn (1), ΔE_{ij} is the site energy difference, λ is the total reorganization energy and J_{ij} is the electronic coupling. J_{ij} is given by:[64]

$$J_{ij} = \langle \phi^i | \hat{H} | \phi^j \rangle \quad (2)$$

where $\phi^{i,j}$ are the highest occupied molecular orbitals (HOMOs) of sites i and j involved in the charge transfer reaction and $\hat{H}$ is the Hamiltonian operator of the dimer. In this work, J_{ij} is approximated with the molecular orbital overlap (MOO) method[65] based on ZINDO/S. The total reorganization energy λ consisting of an inner and an outer contribution is given by:

$$\lambda = \lambda_i + \lambda_o \quad (3)$$

Herein, reorganization energies calculated in a previous investigation[66] based on the adiabatic four point method[67] were used. For λ_o, an estimate of 0.05 eV was assumed, since the explicit calculation of the outer reorganization energy is computationally too demanding. The site energies E_i are given by:[63]

$$E_i = \frac{1}{4\pi\varepsilon_0}\sum_{a_i}\sum_{b_{k,k\neq i}}\frac{\left(q^c_{a_i} - q^n_{a_i}\right)q^n_{b_k}}{\varepsilon_s r_{a_i b_k}} \quad (4)$$

where q is the atomic partial charge, r is the distance, ε_0 is the vacuum dielectric constant and ε_s is dielectric constant of the material. The summation indices a and b run over the atoms of sites i and k, while the superscripts c and n indicate the electronic state (charge (+1), neutral). In this work, ε_s is given by 2.63 (**TPA-1**) and 2.64 (**TPA-2**), as computed from the Clausius–Mossotti eqn (5):

$$\varepsilon_s = 1 + \frac{12\pi\alpha\frac{N}{V}}{3 - 4\pi\alpha\frac{N}{V}} \quad (5)$$

In eqn (5), N is the number of molecules, V is the MD box volume, and α is the molecular polarizability as computed with VOTCA based on the atomic polarizabilities. The description of the site energies can possibly be improved by including distance-dependent screening or even explicit dipole–dipole interactions; however, this was not computationally feasible in the scope of this work. The atomic partial charges used for eqn (4) were calculated at the ωB97X-D[68] level with a triple-split polarized Pople basis set 6-311G*[69–71] and by employing the DDEC6 method, as implemented in the CHARGEMOL program.[72] The required geometry optimizations of **TPA-1** and **TPA-2** monomers were initially conducted *via* conformer searches using the semiempirical quantum mechanical (SQM) tight-binding DFT method GFN2-xTB[73] and CREST.[74] DFT calculations of neutral states were performed at the restricted level, while singly charged states (+1 oxidation state) were performed at the unrestricted spin-polarized level. All equilibrium optimized geometries were confirmed by frequency calculations. DFT and SQM calculations were performed with GAUSSIAN16[75] and xTB.[73] For the computation of the charge transport parameters in the charged cases, within VOTCA the **TPA**-units closest to the PF_6^- ions were set to the monocationic state to balance out the negative charge of the counterions. In this way, the presence of the counterions affects the charge transport by impacting the site energies through their atomic partial charges.

Bulk structural analysis

The bulk morphologies of the monomeric materials (*i.e.*, **TPA-1** and **TPA-2**, before the ring-opening polymerisation) and polymers (*i.e.*, **pTPA** and **xTPA**) were analysed with regard to their structural features. Fig. 3a compares the radial distribution function of the nitrogen centers, $g_{NN}(r)$, which are representative of amorphous morphologies, being unstructured at long range distances. In the case of **xTPA**, a slightly less featured band is observed compared to **TPA-2**, which is related to the more rigid cross-linked network, hindering local ordering of

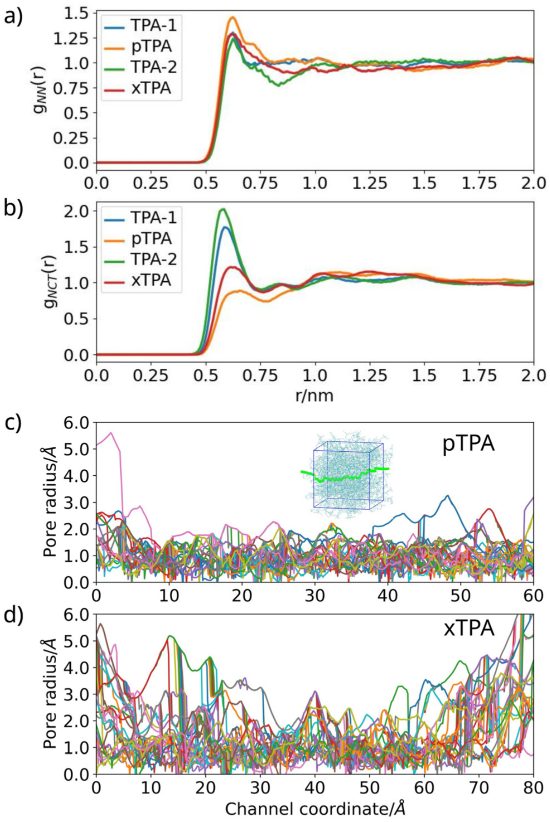

Fig. 3 Radial distribution functions of (a) the nitrogen-centers ($g_{\mathrm{NN}}(r)$) and (b) the nitrogen-centers with respect to the tertiary oxetane carbon ($g_{\mathrm{NCT}}(r)$) in **TPA-1**/**pTPA** (blue/orange) and **TPA-2**/**xTPA** (green/red) systems. Panels (c) and (d) show the overlayed pore radii across the MD box for different trajectories for the polymerized bulk morphologies of **pTPA** and **xTPA**. Different colours represent different trajectories probing the pore size across the simulation box. In light green, an exemplary trajectory across the simulation box is shown (inset).

the repeat units. Interestingly, the nitrogen–nitrogen distances are quite similar for all materials.

In Fig. 3b, the radial distribution function of the nitrogen-centers and the tertiary oxetane carbons $g_{\mathrm{NCT}}(r)$ show a drastic change upon cross-linking. The first band shows as expected a strong decrease upon polymerization. While in the monomeric phase the **TPA** redox-units can assume a coiled conformation, where the oxetane units and the nitrogen-centers can be in close contact, such conformational freedom is not given in polymers. In the latter, the former oxetane units constitute the polymer backbone and their mobility is therefore hindered, limiting coiled configurations and close contact with the nitrogen centers.

Since monomeric (unreacted) **TPA-1** and **TPA-2** cannot be used for OMIECs and battery applications due to their solubility in the electrolyte, both were not included in the following investigations. Fig. 3c and d show the radii of the pores inside the **xTPA** and **pTPA** bulk, respectively. The overlayed void radii were computed with the code HOLE, by using 100 probing trajectories across the bulk of the polymers. Stronger variations in pore radii are encountered in **xTPA** than in **pTPA**, due to the more bundled structure of the polymer network formed by the two-armed system. The void radii vary generally below 2–4 Å in both cases. Such pore radii are of similar magnitude compared to the ion radius of PF_6^- (2.33–2.88 Å[76]). The overall average pore radius for all probing trajectories in **pTPA** is 1.69 Å, while for **xTPA** it is 1.83 Å. This structural feature suggests a generally slow ion diffusion process throughout the materials, as it will be evaluated *via* the MD simulations in the next section.

Ion transport

The PF_6^- ion transport is quantified by analysing the MD trajectory of the ion inserted in the polymer bulk phases.[77,78] The mean square displacement (MSD) of the PF_6^- ion positions is about one order of magnitude less in **xTPA** than in **pTPA** (see Fig. 4). In long MD trajectories, even after 100 ns, the ion transport has not become diffusive yet (*i.e.*, MSD ∼ t), as shown by the significant deviation of the MSD gradient from unity. The computed ion transport is rather in a sub-diffusive regime (*i.e.*, MSD ∼ $t^{0.5}$), implying that during the timescale considered for hole transport (100 ps, *vide infra*), only very short distances are covered by the PF_6^- ions. Sub-diffusive regimes have been well documented in the literature of ion transport in polymer electrolytes.[53,77] Despite the limited displacements of ions, due to strong electrostatic effects even small ion movements can have a significant influence on the site energy differences (ΔE_{ij}) and their time-dependent fluctuations ($\Delta E_{ij}(t)$) (*vide infra*).

Static site energy landscape in pTPA and xTPA polymers

In a first assessment of the hole transport properties, the site energy landscape was investigated. It is commonly accepted

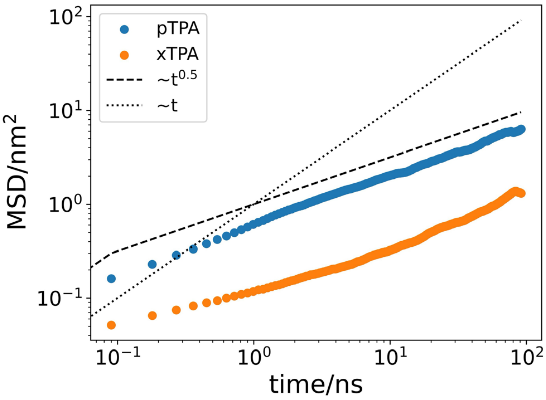

Fig. 4 Log–log plot of the mean square displacement (MSD) of a single PF_6^- ion in **pTPA** (blue) and **xTPA** (orange) bulk phases *vs.* time, as obtained *via* MD simulations. The dotted line shows the linear (diffusive) regime (*i.e.*, MSD ∼ t), while the dashed line shows the sub-diffusive one (*i.e.*, MSD ∼ $t^{0.5}$).

that high energetic disorder (high ΔE_{ij}) leads to charge trapping and low hole transfer rates (see eqn (1)). The static site-energy difference distributions for pristine and doped **pTPA** and **xTPA** are shown in Fig. 5.

High energetic disorder is already present in the undoped (pristine) cases, (σ = 0.37 eV) due to the high conformational disorder (amorphous phases, see the radial distribution functions given in Fig. 3a and b) of the alkyl linkers, combined also with remarkable electrostatic effects as provided by the oxygen atoms of the polymer chains. When the doping level increases (from 5% to 15% doping), the energetic disorder becomes larger due to electrostatic effects provided by the presence of the counterions (PF_6^-). Such high static disorder, with computed σ values ranging from 0.87 eV to 1.67 eV, is usually indicative of non-conductive materials and deep intrinsic traps for the electronic charges (tail states). For comparison, an MD simulated amorphous film of **TPA** monomers without oxetane chains is characterized by a σ value of 0.18 eV, leading to a computed hole mobility of 2.5×10^{-2} cm^2 V^{-1} s^{-1}.[66] In Monte–Carlo simulations based on the Gaussian disorder model, σ values of about 0.1 eV are often reported based on experimental observations.[79–81] However, as anticipated in the Introduction section, the time-dependent oscillations of the site-energies in the presence of alkyl groups and/or ions become crucial for understanding the coupled electronic–ionic transfer in OMIECs, being the key for allowing the energy level alignment[33] thus opening effective charge transport channels, as it will be discussed in the following section.

Dynamics of disorder in pTPA and xTPA polymers

To assess the dynamics of disorder effects, the site energy differences were evaluated over a time of 100 ps (10^3 frames, one snapshot every 100 fs), as shown in Fig. 6a. Large fluctuations can be observed in both cases. This finding prompted us to perform a deeper analysis to quantify the dynamics of disorder by calculating the time autocorrelation function (ACF) of the site energy differences, which is given by:

$$\mathrm{ACF} = \langle \Delta E_{ij}(t_0)\Delta E_{ij}(t_0+\tau)\rangle \tag{6}$$

where t_0 is the starting time and τ is the time-lags. Here, a 10 ps MD trajectory (one snapshot every 10 fs) was used, and the ACF was averaged over 20 close-contact **TPA**-pairs. Furthermore, a running average over 10 timestep (100 fs) at a time was performed to filter out high frequency vibrations that are not well-described by classical MD.

As reported in Fig. 6b and c, the ACF quickly decays to zero – in about 1 ps – for all cases, followed by slower fluctuations that start to emerge on longer timescales. The dynamics underlying this behaviour are characterised by various processes occurring at different timescales, such as fast processes, as induced by bond vibrations (*e.g.*, C–C stretching occurring at 20–40 ps^{-1}), and slow processes, as given by the polymer segment rearrangements and ion motions. Additional fitting of the ACFs with an exponential function was performed and the data are reported in the ESI† (Fig. S10 and S11). For both **pTPA** and

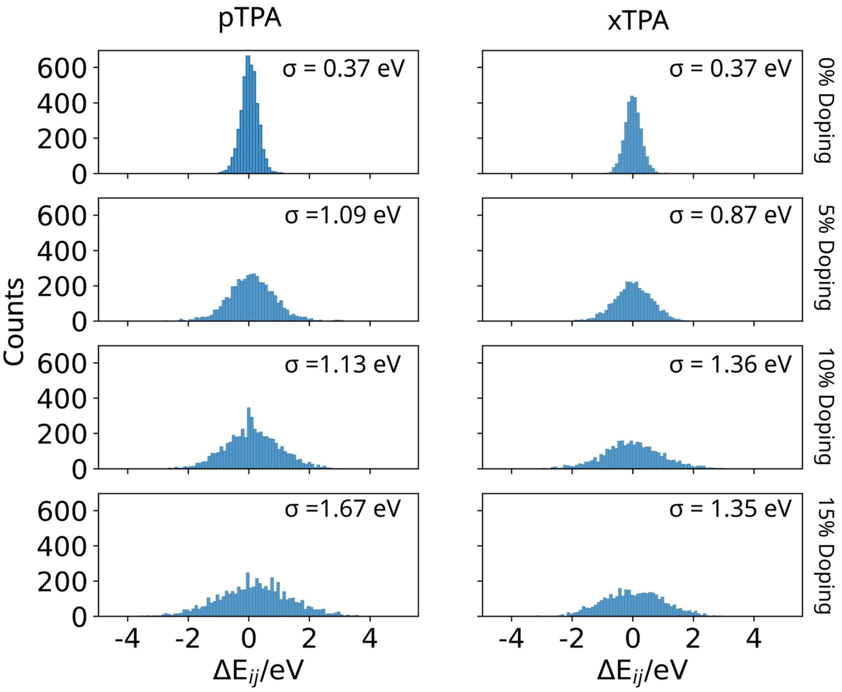

Fig. 5 Site energy difference (ΔE_{ij}) distributions of **pTPA** (left) and **xTPA** (right) polymers with 0%, 5%, 10% and 15% (top to bottom) PF_6^- ion contents (doping level), respectively. The computed σ values are given as insets.

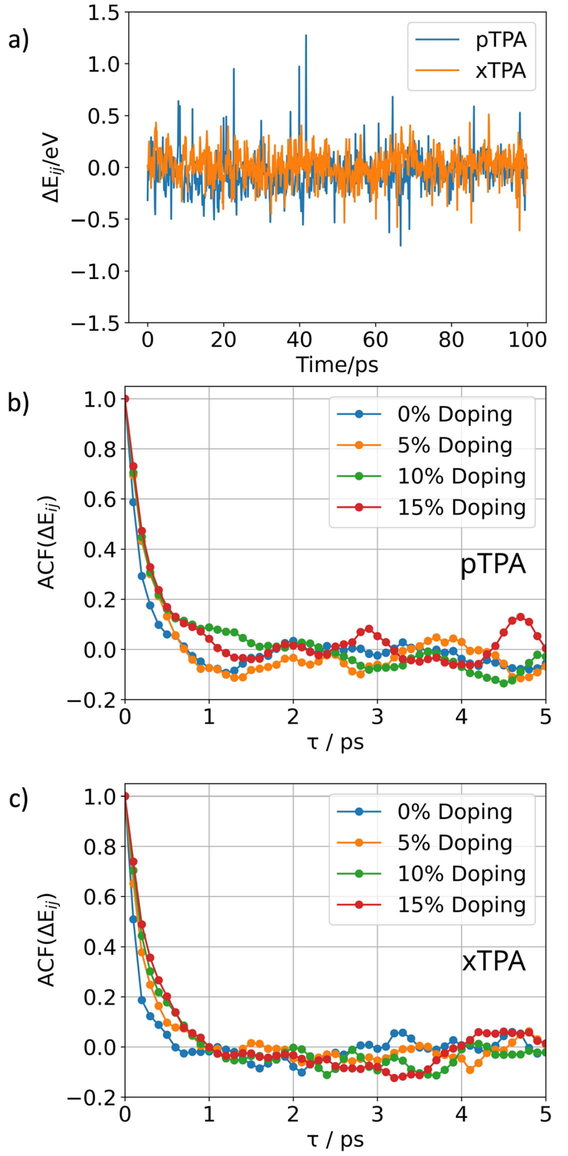

Fig. 6 (a) Site energy difference (ΔE_{ij}) fluctuations of a sample pair in pristine (= undoped) **pTPA** (blue) and **xTPA** (orange). Autocorrelation functions (ACF) of the site energy differences for the pristine (0% doping – blue) and doped (5% – orange, 10% – green and 15% – red, doping levels) cases for (b) **pTPA** and (c) **xTPA**.

xTPA, the pristine case (0% doping) shows a decay time constant ranging from 140 to 180 fs. By increasing the doping level, the time constants increase up to *ca.* 300 fs. Such decay times may be related to low-intermolecular vibrational modes (below 100 cm^{-1}) and for the case of doped systems, to the coupling modes between polymer segments and ions. The large fluctuations of the site energies lead to a temporally changing distribution of Marcus transfer rates spanning over orders of magnitudes (see Fig. 7), which complicate the analysis of the charge transport.

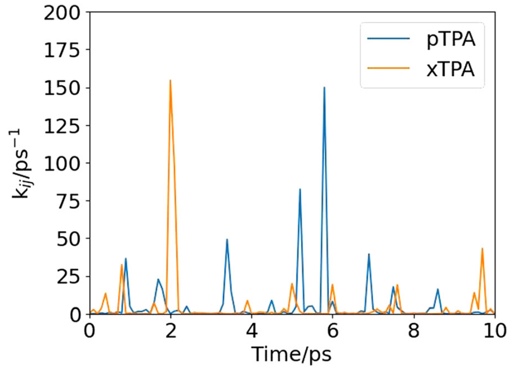

Fig. 7 Computed Marcus hole transfer rates (eqn (1)) for a sample pair as taken from the pristine **pTPA** (blue) and **xTPA** (orange) morphology over a time of 10 ps.

In a system characterised by such strongly fluctuating rates over a short period of time (~10 ps), charge transfer channels open and close quickly and continuously. Therefore, the standard approach of using kinetic Monte Carlo and state-to-state dynamics with a fixed set of rates (k_{ij}) is no longer applicable, because the assumption of a timescale separation of the site energy-fluctuations and the charge transfer events is *de facto* not present. The dynamics of the system become the determining factor influencing the hole transport, which has been conceptualized as a highly interdependent, coupled phenomenon. Due to the high dynamic disorder, the electronic charges (holes) can reside on a site until a favourable energy level alignment occurs and the transfer event can take place.

Effective Marcus residence times

Due to the large fluctuations of the site energy differences, leading to time-dependent transfer rates, a new approach is needed to analyse the electronic transport by taking into account high energetic disorder effects, as well as the polymer segments and ion oscillations. We replace the instantaneous hopping rates (k_{ij}) with the half-time of hopping between sites i and j by integrating the time-dependent $k_{ij}(t)$ over a period of time. For an (i, j) pair, with a time dependent rate $k_{ij}(t)$, we compute the hypothetical time evolution of the charge population ($P_i(t)$) due to hopping from site i to site j (assuming that only the hopping $i \rightarrow j$ can take place). The time-dependent charge population $P_i(t)$ of site i reads as follows:[82]

$$-\frac{\mathrm{d}P_i(t)}{\mathrm{d}t} = k_{ij}(t)\mathrm{e}^{-k_{ij}(t)t} \qquad (7)$$

Rearranging and integrating yields:

$$P_i(T) = P_i(0) - \int_0^T k_{ij}(t)\mathrm{e}^{-k_{ij}(t)t}\mathrm{d}t \qquad (8)$$

where T is the total integration time. The integral on the right-hand side of eqn (8) can be numerically solved by discretizing the total integration time T in N discrete intervals ΔT. Assuming the charge on site i, that is $P_i(0) = 1$, the final expression for the population of site i, $P_i(T)$ reads as follows:

$$P_i(T = N\Delta T) = 1 - \sum_{n=1}^{N} k_{ij}(t_n)\mathrm{e}^{-k_{ij}(t_n)t_n}\Delta T \tag{9}$$

We compute $P_i(T)$ for all triphenylamine pairs of **pTPA** and **xTPA** bulk systems over an integration time (T) of 100 ps, by using a sampling rate of one snapshot every 100 fs, thus resulting in a ΔT of 0.1 ps. We term the half-time of the population decay as the effective Marcus residence time $\tau_{i\to j}$. In the ESI,† an example for the $P_i(T)$ decay is reported. $\tau_{i\to j}$ represents a new descriptor for the electronic charge transport, considering the time-dependent history of the sites and encompassing the intrinsic dynamics of the systems. It can be used to quantify the influence of the dynamics of disorder, going beyond the static picture provided by the Marcus rates k_{ij}.

We calculate the distributions of lifetimes (t_i),[83] defined as the time required by a hole to escape from a given site i to any possible site j. t_i can be computed by considering either the static, instantaneous Marcus rates (k_{ij}, eqn (1)) or the effective Marcus residence times $\tau_{i\to j}$. If t_i is evaluated based on static rates, the lifetime of a carrier is given by:

$$t_i^{\text{static}} = \left(\frac{1}{\sum_j k_{ij}}\right) \tag{10}$$

while if it is based on the effective Marcus residence times $\tau_{i\to j}$ it reads:

$$t_i^{\text{effective}} = \left(\sum_j \frac{1}{\tau_{i\to j}}\right)^{-1} \tag{11}$$

Fig. 8 reports the distributions of lifetimes t_i of a hole for both **pTPA** and **xTPA** in the pristine case and at different doping states (5%, 10% and 15% of $\mathrm{PF_6}^-$). The distribution of $t_i^{\text{effective}}$ is narrower for all cases (pristine and doped states) than those obtained from t_i^{static}, and the latter being more equally distributed. Note that many t_i^{static} are computed at longer time, outside the range considered in the figure, while no effective lifetime is longer than 100 ps, *i.e.* the main effect of including the dynamic disorder is to remove long-lived trap states. While there are no prominent differences between **pTPA** and **xTPA** in the distributions of lifetimes, some variations can be observed by comparing pristine with respect to doped states. The presence of counterions (5% to 15% of $\mathrm{PF_6}^-$) does not hinder the charge transfer events (or, equivalently, the de-trapping of

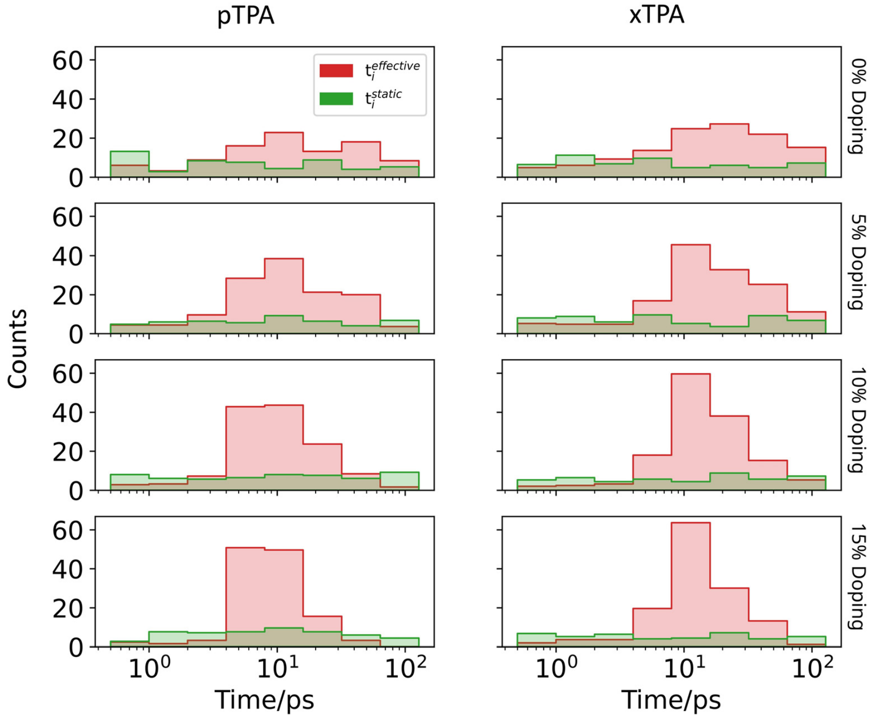

Fig. 8 Distributions of static (t_i^{static}, green) and effective ($t_i^{\text{effective}}$, red) lifetimes for **pTPA** (left) and **xTPA** (right) from pristine (0% doping, top panels) to 5%, 10% and 15% doping (lower panels).

electronic charges) despite the high static disorder (see Fig. 5). Instead, it narrows the lifetime distributions, as evident by moving from 5% to 15% doping (see Fig. 8). Comparing doped **pTPA** and **xTPA** we can further understand the role of the polymer structure. The PF_6^- ions were found to be more mobile in **pTPA** than in **xTPA**, as shown by their higher diffusion (see Fig. 4). This leads to a larger accumulation of shorter $t_i^{\mathrm{effective}}$ in **pTPA** compared to **xTPA**, and thus a more efficient trap removal in linear than cross-linked polymers.

To gain further atomistic insights into the coupled hole and ionic transport, we report the three-dimensional networks of the effective Marcus residence times ($\tau_{i\to j}$) in Fig. 9a and their two-dimensional graph representations in Fig. 9b. We call these visualization hole transport networks and they should not be confused with the (cross-linked) polymer network, as mentioned in the Structural analysis section. Hole transport networks are a convenient representation to understand the topological aspects of the charge transport, and we point the reader to a series of publications where such representations have been introduced and explained in details.[84–88] Each point (node) in these representations constitutes a **TPA** site, and each line (edge) represents an effective Marcus residence time $\tau_{i\to j}$ connecting two sites. Connections between sites represent both a spatial and a time-dependent information: the spatial information concerns which **TPA** sites are involved in the hole transfer process, while the time information regards how much time it takes for a hole to be released from a deep trap. Red lines in Fig. 9a and b represent short $\tau_{i\to j}$, that is depopulation of trap states at early time (0.1 to 1 ps), resulting in a rapid hole transfer process from site i to j despite the high static energetic disorder. Green and blue lines

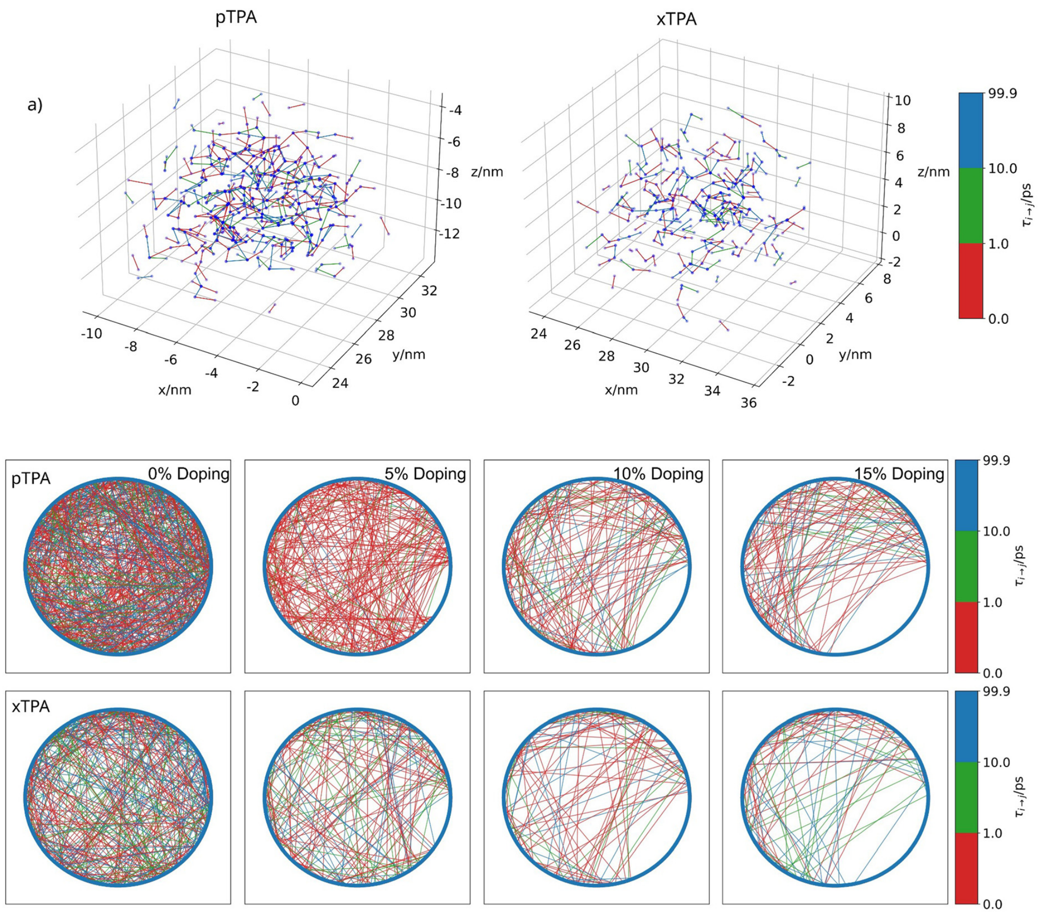

Fig. 9 3D (top) and 2D (bottom) representations of the hole transport networks. (a) Real space representation: nodes are **TPA** units (positioned in real space, *i.e.*, simulation box), while edges (connections between nodes) are effective Marcus residence times $\tau_{i\to j}$ for the pristine case (0% doping) of **pTPA** (left) and **xTPA** (right). A distance cut-off of 6 nm between sites is used to exclude edges crossing the periodic boundary conditions from the plot. (b) 2D representations: nodes are **TPA** units reported as a circular graph, and edges are effective Marcus residence times $\tau_{i\to j}$ computed for 0%, 5%, 10% and 15% doping cases (**pTPA**, top row, and **xTPA**, bottom row). Non-connected nodes have not developed a transfer event within 100 ps or are **TPA** units with fixed positive charges as counterions to the PF_6^- ions that do not take part in the charge transport. Unlike in (a) no cut-off is employed (*i.e.* a full network is shown).

show the same process, however on a longer time scale (up to $\tau_{i\to j}$ = 99.9 ps). Detrapping events taking only place after more than 100 ps (*i.e.* $\tau_{i\to j}$ = 100 ps) are not shown.

In Fig. 9a, we compare pristine **pTPA** (left) and **xTPA** (right), in real space (*i.e.*, MD simulation boxes). Fig. 9b reports the same hole transport networks; however, in an abstract form, that is a circular 2D representation in which the morphological information is removed to better focus on the overall density (*i.e.*, number of lines per area) or connectivity of the hole transport network. Both in the pristine (0%) and in the doped cases (5%, 10%, and 15%), **pTPA** shows a denser hole transport network than **xTPA**, indicating more efficient trap removal (*i.e.*, hole de-trapping events) which can be traced back to a higher ion mobility (Fig. 4) and a lower bulk structural porosity (Fig. 3c and d). The addition of counterions reduces the density of the hole transport network. Such reduction decreases the de-trapping events thus impacting the hole bulk transport which lowers as moving from 5% up to 15% doping. **xTPA** shows hole transport networks which are less dense than that of **pTPA**, reflecting a less efficient trap removal, meaning slower hole de-trapping dynamics (as shown by the green and blue lines in Fig. 9b).

Our analysis captures the fine balance between the dynamics of the trap removal and the dynamics of disorder effects. We stress here that a dynamical approach is essential to understand the complex and coupled ionic–electronic transport motions. Possible charge transport pairs that are not electronically connected initially (*i.e.*, vanishing static k_{ij}, eqn (1)) can instead develop at a later stage a high hole transfer rate through the fluctuations of the system (leading to a decrease of residence time $\tau_{i\to j}$). At the same time, pairs that are connected initially can become disconnected over time. Developing a charge transport analysis which does not consider the time dependency of the transfer rates as well as the density of the hole transport network between all pairs might lead to erroneous conclusions about the physics of the charge transport in highly disordered soft materials.

Conclusions

The coupled electronic and ionic transport in linear (**pTPA**) and cross-linked (**xTPA**) triphenylamine based non-conjugated redox polymers was investigated using a bottom-up multiscale computational approach. The investigated systems are ideal for studying this phenomenon since they feature localized electronic charges (holes), thus legitimizing the evaluation of the charge transfer rates *via* Marcus theory. Polymer chains and bulk formation were modelled by interfacing a heuristic protocol together with extended MD simulations to obtain realistic bulk structures. Morphologies of linear and cross-linked **TPA** polymers show disordered, amorphous structures with short-range coordination between the nearest neighbour redox units. The internal porosity of the polymer films was analysed, yielding larger pore radius variations in cross-linked **xTPA** compared to linear **pTPA** polymers. Insertion of PF_6^- ions was modelled at different doping concentrations, namely 5%, 10% and 15%. Doping causes only minor variations in the polymer bulk morphologies. Energetic disorder effects (site energy differences) were explicitly computed in the static limit leading to broad distributions for both pristine (0.37 eV) and doped polymers, by increasing the ion content up to 1.67 eV. Such large static energetic disorder would hinder any hole transfer process, challenging the experimentally observed electronic and ionic conduction. Dynamic effects are the key to explain the hole release from deep trap states. We computed the dynamics, *i.e.* the time-dependent fluctuations of the site energy differences of pristine and doped polymers, together with their autocorrelation functions. The timescales characterising the decay of the site energy autocorrelation function were found to be around 1 ps, leading to fast and large fluctuations of the hole Marcus transfer rates, opening and closing electronic charge transfer pathways continuously. The dynamics of disorder effects impact the electronic couplings as well, inducing fast fluctuations generally ranging in the order of the fs time-scales. Here, we focused on the analysis of the site energy fluctuations, as they represent the rate-limiting factor since their oscillations and correlation function decay on slower timescales than the electronic couplings. To include the time-dependent disorder effects in a unified electronic transport description, we introduced for the first time an effective Marcus residence time $\tau_{i\to j}$, which considers the temporal history of disorder effects. From $\tau_{i\to j}$, we estimate for each polymer and for both pristine and doped states, distributions of lifetimes, defined as the time required by a hole to escape from a deep trap. We observed that the dynamics of disorder effects can lead to efficient de-trapping and formation of hopping hole transport networks within the polymer bulk. Our study shows the complex and entangled nature of mixed charge- and ion transport in non-conjugated redox soft materials of potential use for organic electrodes. Hole transport cannot be modelled and rationalised in an isolated manner, but has to be analysed considering the spatial and time-dependent interaction between polymer chains, ions and electronic charge carriers.

Author contributions

R. H.: simulations, data curation, conceptualization, and manuscript writing. L. P.: experimental data, T_g and density determination. A. T.: conceptualization and manuscript writing. K. M.: conceptualization and manuscript writing. D. F.: conceptualization, data curation, and manuscript writing.

Conflicts of interest

The authors declare no conflicts of interest.

Data availability

The data supporting this article have been included as part of the ESI.† Technical data (*e.g.*, restart files for all simulations) can be found on Github under https://github.com/rbrthrz/pTPA_xTPA.

Acknowledgements

R. H., L. P., D. F. and K. M. acknowledge the DFG Research Training Group 2591 "Template-designed Organic Electronics (TIDE)" for supporting their research. They also acknowledge the Regional Computing Centre (RRZK) of the University of Cologne for providing computing time and resources on the HPC RRZK CHEOPS. K. M. acknowledges the DFG Priority Programme "Polymer Based Batteries" (SPP 2248) with the grant "SYNERGISTIC" (ME1246-43). D. F. acknowledges the Global Faculty Program of the University of Cologne within the focus area "Quantum Matter and Materials (QM2)", the National Recovery and Resilience Plan (NRRP), the Mission 04 Component 2 Investment 1.5 – NextGenerationEU, Call for tender no. 3277 dated 30/12/2021, Award Number: 0001052 dated 23/06/2022, and the National Project funded by the European Union – Next Generation EU, Project title "Modelling and design of organic conjugated redox materials for energy-saving applications: a bottom-up strategy", code MUR 2022 WKTH9E – CUP J53D23008810006. A. T. acknowledges the support from the European Research Council (grant no. 101020369).

References

‡ In this work, the terms doping level and charging level both refer to the number of positively charged **TPA** units and an equal number of PF_6^- counterions, and can be used interchangeably.

1 P. Gkoupidenis, Y. Zhang, H. Kleemann, H. Ling, F. Santoro, S. Fabiano, A. Salleo and Y. van de Burgt, *Nat. Rev. Mater.*, 2024, **9**, 134–149.
2 B. D. Paulsen, K. Tybrandt, E. Stavrinidou and J. Rivnay, *Nat. Mater.*, 2020, **19**, 13–26.
3 J. Rivnay, S. Inal, A. Salleo, R. M. Owens, M. Berggren and G. G. Malliaras, *Nat. Rev. Mater.*, 2018, **3**, 1–14.
4 S. Fabiano, L. Flagg, T. C. Hidalgo Castillo, S. Inal, L. G. Kaake, L. V. Kayser, S. T. Keene, S. Ludwigs, C. Muller, B. M. Savoie, B. Lüssem, J. L. Lutkenhaus, M. Matta, D. Meli, S. N. Patel, B. D. Paulsen, J. Rivnay and J. Surgailis, *J. Mater. Chem. C*, 2023, **11**, 14527–14539.
5 S. Kang, J. Fan, J. B. P. Soares and M. Gupta, *RSC Adv.*, 2023, **13**, 5096–5106.
6 C. J. Kousseff, R. Halaksa, Z. S. Parr and C. B. Nielsen, *Chem. Rev.*, 2022, **122**, 4397–4419.
7 S. Yu, H.-Y. Wu, V. Lemaur, C. J. Kousseff, D. Beljonne, S. Fabiano and C. B. Nielsen, *Angew. Chem.*, 2024, **136**, e202410626.
8 N. A. Kukhta, A. Marks and C. K. Luscombe, *Chem. Rev.*, 2022, **122**, 4325–4355.
9 D. Moia, A. Giovannitti, A. A. Szumska, I. P. Maria, E. Rezasoltani, M. Sachs, M. Schnurr, P. R. F. Barnes, I. McCulloch and J. Nelson, *Energy Environ. Sci.*, 2019, **12**, 1349–1357.
10 Y. Wang, S. Wustoni, J. Surgailis, Y. Zhong, A. Koklu and S. Inal, *Nat. Rev. Mater.*, 2024, **9**, 249–265.
11 C. B. Nielsen, A. Giovannitti, D.-T. Sbircea, E. Bandiello, M. R. Niazi, D. A. Hanifi, M. Sessolo, A. Amassian, G. G. Malliaras, J. Rivnay and I. McCulloch, *J. Am. Chem. Soc.*, 2016, **138**, 10252–10259.
12 A. Giovannitti, D.-T. Sbircea, S. Inal, C. B. Nielsen, E. Bandiello, D. A. Hanifi, M. Sessolo, G. G. Malliaras, I. McCulloch and J. Rivnay, *Proc. Natl. Acad. Sci. U. S. A.*, 2016, **113**, 12017–12022.
13 R. Kroon, D. Kiefer, D. Stegerer, L. Yu, M. Sommer and C. Müller, *Adv. Mater.*, 2017, **29**, 1700930.
14 I. Yu, D. Jeon, B. Boudouris and Y. Joo, *Macromolecules*, 2020, **53**, 4435–4441.
15 S. Muench, A. Wild, C. Friebe, B. Häupler, T. Janoschka and U. S. Schubert, *Chem. Rev.*, 2016, **116**, 9438–9484.
16 Y. Chen and C. Wang, *Acc. Chem. Res.*, 2020, **53**, 2636–2647.
17 J. Kim, Y. Kim, J. Yoo, G. Kwon, Y. Ko and K. Kang, *Nat. Rev. Mater.*, 2023, **8**, 54–70.
18 T. B. Schon, B. T. McAllister, P.-F. Li and D. S. Seferos, *Chem. Soc. Rev.*, 2016, **45**, 6345–6404.
19 P. Poizot, J. Gaubicher, S. Renault, L. Dubois, Y. Liang and Y. Yao, *Chem. Rev.*, 2020, **120**, 6490–6557.
20 K. A. Ludwig, J. D. Uram, J. Yang, D. C. Martin and D. R. Kipke, *J. Neural Eng.*, 2006, **3**, 59–70.
21 Q. Pei, G. Yu, C. Zhang, Y. Yang and A. J. Heeger, *Science*, 1995, **269**, 1086–1088.
22 J. Jang, J. Ha and J. Cho, *Adv. Mater.*, 2007, **19**, 1772–1775.
23 M. Winter, B. Barnett and K. Xu, *Chem. Rev.*, 2018, **118**, 11433–11456.
24 M. S. Whittingham, *Chem. Rev.*, 2014, **114**, 11414–11443.
25 C. Friebe, A. Lex-Balducci and U. S. Schubert, *ChemSusChem*, 2019, **12**, 4093–4115.
26 N. Siemons, D. Pearce, C. Cendra, H. Yu, S. M. Tuladhar, R. K. Hallani, R. Sheelamanthula, G. S. LeCroy, L. Siemons, A. J. P. White, I. McCulloch, A. Salleo, J. M. Frost, A. Giovannitti and J. Nelson, *Adv. Mater.*, 2022, **34**, e2204258.
27 S. T. Keene, V. Gueskine, M. Berggren, G. G. Malliaras, K. Tybrandt and I. Zozoulenko, *Phys. Chem. Chem. Phys.*, 2022, **24**, 19144–19163.
28 S. T. Keene, J. E. M. Laulainen, R. Pandya, M. Moser, C. Schnedermann, P. A. Midgley, I. McCulloch, A. Rao and G. G. Malliaras, *Nat. Mater.*, 2023, **22**, 1121–1127.
29 S. Sunny, S. Shah, M. Garg, I. Zozoulenko and S. Ghosh, *Macromolecules*, 2024, **57**, 5155–5165.
30 A. Khot and B. M. Savoie, *J. Polym. Sci.*, 2022, **60**, 610–620.
31 A. Giovannitti, I. P. Maria, D. Hanifi, M. J. Donahue, D. Bryant, K. J. Barth, B. E. Makdah, A. Savva, D. Moia, M. Zetek, P. R. F. Barnes, O. G. Reid, S. Inal, G. Rumbles, G. G. Malliaras, J. Nelson, J. Rivnay and I. McCulloch, *Chem. Mater.*, 2018, **30**, 2945–2953.
32 Y. Tsarfati, K. C. Bustillo, B. H. Savitzky, L. Balhorn, T. J. Quill, A. Marks, J. Donohue, S. E. Zeltmann, C. J. Takacs, A. Giovannitti, I. McCulloch, C. Ophus, A. M. Minor and A. Salleo, *Nat. Mater.*, 2025, **24**, 101–108.

33 C. Burke, A. Landi and A. Troisi, *Mater. Horiz.*, 2024, **11**, 5313–5319.

34 A. Landi, M. Reisjalali, J. D. Elliott, M. Matta, P. Carbone and A. Troisi, *J. Mater. Chem. C*, 2023, **11**, 8062–8073.

35 S. D. Baranovskii, *Phys. Status Solidi B*, 2014, **251**, 487–525.

36 S. D. Baranovskii, *Phys. Status Solidi A*, 2018, **215**, 1700676.

37 S. Inal, G. G. Malliaras and J. Rivnay, *Nat. Commun.*, 2017, **8**, 1767.

38 E. Bacher, M. Bayerl, P. Rudati, N. Reckefuss, C. D. Müller, K. Meerholz and O. Nuyken, *Macromolecules*, 2005, **38**, 1640–1647.

39 S. Jungermann, N. Riegel, D. Müller, K. Meerholz and O. Nuyken, *Macromolecules*, 2006, **39**, 8911–8919.

40 S. Feser and K. Meerholz, *Chem. Mater.*, 2011, **23**, 5001–5005.

41 L. Plein, L. Höfer, R. Herzhoff, D. Fazzi and K. Meerholz, *In Preparation*.

42 K. Yamamoto, D. Suemasa, K. Masuda, K. Aita and T. Endo, *ACS Appl. Mater. Interfaces*, 2018, **10**, 6346–6353.

43 L. Fan, Q. Liu, Z. Xu and B. Lu, *ACS Energy Lett.*, 2017, **2**, 1614–1620.

44 F. A. Obrezkov, A. F. Shestakov, V. F. Traven, K. J. Stevenson and P. A. Troshin, *J. Mater. Chem. A*, 2019, **7**, 11430–11437.

45 J. K. Feng, Y. L. Cao, X. P. Ai and H. X. Yang, *J. Power Sources*, 2008, **177**, 199–204.

46 D. Fazzi, S. Fabiano, T.-P. Ruoko, K. Meerholz and F. Negri, *J. Mater. Chem. C*, 2019, **7**, 12876–12885.

47 G. LeCroy, R. Ghosh, V. Untilova, L. Guio, K. H. Stone, M. Brinkmann, C. Luscombe, F. C. Spano and A. Salleo, *Mater. Horiz.*, 2024, **11**, 545–553.

48 S. H. Choi, J. H. Kim, J. Ahn, T. Kim, Y. Jung, D. Won, J. Bang, K. R. Pyun, S. Jeong, H. Kim, Y. G. Kim and S. H. Ko, *Nat. Mater.*, 2024, **23**, 834–843.

49 J. R. Gissinger, B. D. Jensen and K. E. Wise, *Macromolecules*, 2020, **53**, 9953–9961.

50 K.-H. Lin, L. Paterson, F. May and D. Andrienko, *Npj Comput. Mater.*, 2021, **7**, 1–7.

51 M. Klajmon, V. Aulich, J. Ludík and C. Červinka, *Ind. Eng. Chem. Res.*, 2023, **62**, 21437–21448.

52 K. S. Khare and F. R. Phelan, *Macromolecules*, 2018, **51**, 564–575.

53 M. A. Webb, Y. Jung, D. M. Pesko, B. M. Savoie, U. Yamamoto, G. W. Coates, N. P. Balsara, Z.-G. Wang and T. F. Miller, *ACS Cent. Sci.*, 2015, **1**, 198–205.

54 A. P. Thompson, H. M. Aktulga, R. Berger, D. S. Bolintineanu, W. M. Brown, P. S. Crozier, P. J. in't Veld, A. Kohlmeyer, S. G. Moore, T. D. Nguyen, R. Shan, M. J. Stevens, J. Tranchida, C. Trott and S. J. Plimpton, *Comput. Phys. Commun.*, 2022, **271**, 108171.

55 D. van der Spoel, E. Lindahl, B. Hess, G. Groenhof, A. E. Mark and H. J. C. Berendsen, *J. Comput. Chem.*, 2005, **26**, 1701–1718.

56 W. L. Jorgensen, D. S. Maxwell and J. Tirado-Rives, *J. Am. Chem. Soc.*, 1996, **118**, 11225–11236.

57 G. A. Kaminski, R. A. Friesner, J. Tirado-Rives and W. L. Jorgensen, *J. Phys. Chem. B*, 2001, **105**, 6474–6487.

58 W. Humphrey, A. Dalke and K. Schulten, *J. Mol. Graphics*, 1996, **14**(33–38), 27.

59 M. Brehm and B. Kirchner, *J. Chem. Inf. Model.*, 2011, **51**, 2007–2023.

60 O. S. Smart, J. G. Neduvelil, X. Wang, B. A. Wallace and M. S. Sansom, *J. Mol. Graphics*, 1996, **14**(354–360), 376.

61 R. A. Marcus and N. Sutin, *Biochim. Biophys. Acta, Bioenerg.*, 1985, **811**, 265–322.

62 R. A. Marcus, *Angew. Chem., Int. Ed. Engl.*, 1993, **32**, 1111–1121.

63 V. Rühle, A. Lukyanov, F. May, M. Schrader, T. Vehoff, J. Kirkpatrick, B. Baumeier and D. Andrienko, *J. Chem. Theory Comput.*, 2011, **7**, 3335–3345.

64 E. F. Valeev, V. Coropceanu, D. A. da Silva Filho, S. Salman and J.-L. Brédas, *J. Am. Chem. Soc.*, 2006, **128**, 9882–9886.

65 J. Kirkpatrick, *Int. J. Quantum Chem.*, 2008, **108**, 51–56.

66 R. Herzhoff, F. Negri, K. Meerholz and D. Fazzi, *J. Mater. Chem. C*, 2023, **11**, 11969–11979.

67 S. F. Nelsen, S. C. Blackstock and Y. Kim, *J. Am. Chem. Soc.*, 1987, **109**, 677–682.

68 J.-D. Chai and M. Head-Gordon, *Phys. Chem. Chem. Phys.*, 2008, **10**, 6615–6620.

69 T. Clark, J. Chandrasekhar, G. W. Spitznagel and P. V. R. Schleyer, *J. Comput. Chem.*, 1983, **4**, 294–301.

70 B. P. Pritchard, D. Altarawy, B. Didier, T. D. Gibson and T. L. Windus, *J. Chem. Inf. Model.*, 2019, **59**, 4814–4820.

71 R. Krishnan, J. S. Binkley, R. Seeger and J. A. Pople, *J. Chem. Phys.*, 1980, **72**, 650–654.

72 T. A. Manz and N. G. Limas, *RSC Adv.*, 2016, **6**, 47771–47801.

73 C. Bannwarth, S. Ehlert and S. Grimme, *J. Chem. Theory Comput.*, 2019, **15**, 1652–1671.

74 P. Pracht, S. Grimme, C. Bannwarth, F. Bohle, S. Ehlert, G. Feldmann, J. Gorges, M. Müller, T. Neudecker, C. Plett, S. Spicher, P. Steinbach, P. A. Wesołowski and F. Zeller, *J. Chem. Phys.*, 2024, **160**, 114110.

75 M. J. Frisch, G. W. Trucks, H. B. Schlegel, G. E. Scuseria, M. A. Robb, J. R. Cheeseman, G. Scalmani, V. Barone, G. A. Petersson, H. Nakatsuji, X. Li, M. Caricato, A. V. Marenich, J. Bloino, B. G. Janesko, R. Gomperts, B. Mennucci, H. P. Hratchian, J. V. Ortiz, A. F. Izmaylov, J. L. Sonnenberg, D. Williams-Young, F. Ding, F. Lipparini, F. Egidi, J. Goings, B. Peng, A. Petrone, T. Henderson, D. Ranasinghe, V. G. Zakrzewski, J. Gao, N. Rega, G. Zheng, W. Liang, M. Hada, M. Ehara, K. Toyota, R. Fukuda, J. Hasegawa, M. Ishida, T. Nakajima, Y. Honda, O. Kitao, H. Nakai, T. Vreven, K. Throssell, J. A. Montgomery, Jr., J. E. Peralta, F. Ogliaro, M. J. Bearpark, J. J. Heyd, E. N. Brothers, K. N. Kudin, V. N. Staroverov, T. A. Keith, R. Kobayashi, J. Normand, K. Raghavachari, A. P. Rendell, J. C. Burant, S. S. Iyengar, J. Tomasi, M. Cossi, J. M. Millam, M. Klene, C. Adamo, R. Cammi, J. W. Ochterski, R. L. Martin, K. Morokuma, O. Farkas, J. B. Foresman and D. J. Fox, *Gaussian16*, Gaussian, Inc., Wallingford CT, *2016*.

76 A. L. Rohl and D. M. P. Mingos, *J. Chem. Soc., Dalton Trans.*, 1992, 3541.

77 D. Diddens, E. Paillard and A. Heuer, *J. Electrochem. Soc.*, 2017, **164**, E3225–E3231.

78 D. Diddens and A. Heuer, *ACS Macro Lett.*, 2013, **2**, 322–326.

79 H. Bässler, *Phys. Status Solidi B*, 1993, **175**, 15–56.

80 F.-J. Kahle, A. Rudnick, S. Wedler, R. Saxena, R. Ammenhäuser, U. Scherf, S. Bagnich, H. Bässler and A. Köhler, *Adv. Energy Mater.*, 2022, **12**, 2103063.

81 T. Meier, H. Bässler and A. Köhler, *Adv. Opt. Mater.*, 2021, **9**, 2100115.

82 A. F. Voter, K. E. Sickafus, E. A. Kotomin and B. P. Uberuaga, *Radiation Effects in Solids*, 2007, pp. 1–23.

83 C. Poelking, E. Cho, A. Malafeev, V. Ivanov, K. Kremer, C. Risko, J.-L. Brédas and D. Andrienko, *J. Phys. Chem. C*, 2013, **117**, 1633–1640.

84 N. Gildemeister, S. Geller, R. Herzhoff, F. Negri, K. Meerholz and D. Fazzi, *Mater. Adv.*, 2024, **5**, 8475–8489.

85 T. Vehoff, B. Baumeier, A. Troisi and D. Andrienko, *J. Am. Chem. Soc.*, 2010, **132**, 11702–11708.

86 N. E. Jackson, L. X. Chen and M. A. Ratner, *Proc. Natl. Acad. Sci. U. S. A.*, 2016, **113**, 8595–8600.

87 B. M. Savoie, K. L. Kohlstedt, N. E. Jackson, L. X. Chen, M. La Olvera de Cruz, G. C. Schatz, T. J. Marks and M. A. Ratner, *Proc. Natl. Acad. Sci. U. S. A.*, 2014, **111**, 10055–10060.

88 N. E. Jackson, B. M. Savoie, L. X. Chen and M. A. Ratner, *J. Phys. Chem. Lett.*, 2015, **6**, 1018–1021.

5.8 Outlook and continuation of research into TPA-based OMIEC materials

As a follow-up investigation after the initial study into the structure and the coupled charge- and ion transport in **TPA**-based polymers, the Master's Thesis of Agustín López Cabrera focused on the structure, ion transport and electrolyte swelling effects in a series of **TPA**s with varying alkyl-linker lengths. Some results of this Master's Thesis are included and discussed here as they are relevant to the topic of this Thesis. Additionally, the Master's Thesis was supervised by me and is based on my earlier work.

The **TPA** series investigated are shown in Fig. 5.9. For completeness, the **TPA** derivatives investigated in my earlier work are included there as well in the same nomenclature.

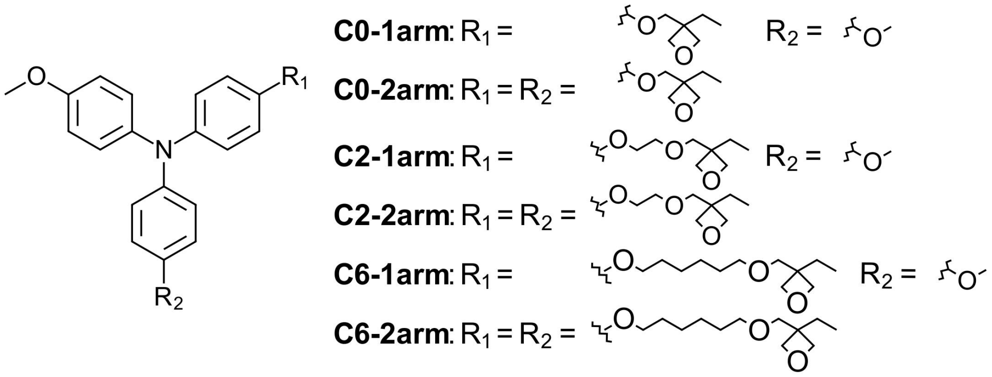

Figure 5.9: **TPA** derivatives investigated in the Master's Thesis of Agustín López Cabrera.

These systems were chosen to complement the **pTPA** and **xTPA** systems, featuring C6-arms, that were investigated prior by me. The approach was to investigate the impact of the side-chain length and the cross-linking degree on the structure, ion transport and swelling behaviour in order to understand if side chain engineering can be used to control structural and thereby functional properties of the materials.

After force field reparametrization, an analogous procedure as reported before and in more detail in publication II was used to generate equilibrated monomer systems via thermal annealing and then polymerized systems using the REACTER approach. The polymerized systems are named **pC0-1arm**, **pC0-2arm**, **pC2-1arm** and **pC2-2arm**.

5.8.1 Glass transition temperature

The T_g simulated in the Master's Thesis of Agustín López Cabrera (**pC0-1arm**, **pC0-2arm**, **pC2-1arm** and **pC2-2arm** systems) are shown in Fig. 5.10(a) together with the T_g of **pTPA** (**pC6-2arm**) and **xTPA** (**pC6-2arm**) as determined in the context of publication II. As before, the experimental T_g have been determined by Laura Plein.

Considering the errors present in both the experimental and the computational approach, the trend over all T_g is generally reproduced to a satisfactory degree, except for the case of **xTPA** (**pC6-2arm**). Fig. 5.10(b) shows a correlation plot of the experimental and simulated data together. From the data, no clear trends as to the structure-property relationships can be deducted. In the case of the C0 systems,

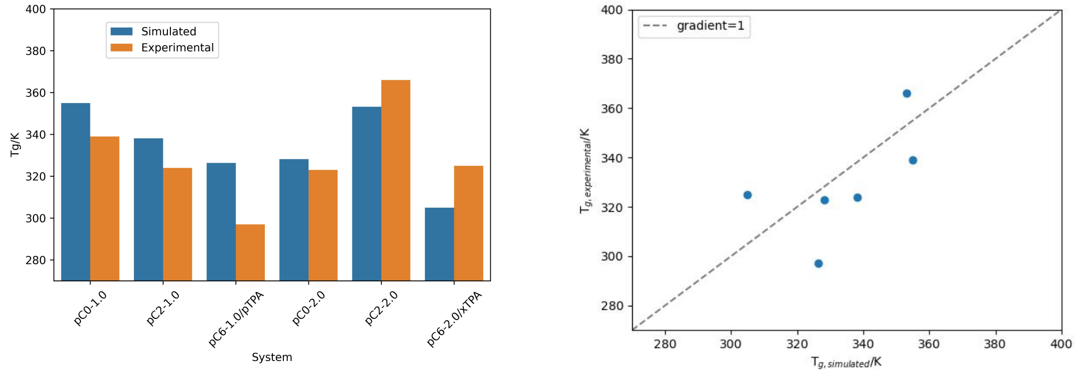

(a)

(b)

Figure 5.10: a) Simulated and experimental glass transition temperatures of polymerized **TPA** systems. b) Correlation plot of simulated and experimental data. The dashed line indicates a gradient of one.

going from a linear to a cross-linked system, the T_g decreases, while for the C2 systems, the opposite is true. In the case of the **pTPA**(**pC6-1arm**) and **xTPA**(**pC6-2arm**) cross-linking decreases the T_g in the experimental data, while the simulated data does not reproduce this trend. As was pointed out by Agustín López Cabrera in his thesis, the T_g behaviour is rooted in the complex relation between monomer stiffness, side-chain length and flexibility as well as the number of side chains and the degree of cross-linking and can not be explained by a single factor. While the C0 systems are packed less densely in the cross-linked state due to the short arm lengths, leading to a lower T_g, this effect is not as strong in the longer-armed systems, leading to a higher T_g in the cross-linked state. Thus, it does not seem to be the case that the structure and related properties can be easily controlled by varying the side chain lengths or the cross-linking degree. It should be noted here, that in the Master's Thesis of Agustín López Cabrera, the effect of different network densities on the T_g have been investigated as well by generating mixed polymer systems from both one- and two-armed monomers. For the C2 systems, a monotonous increase in the T_g was found, while a more complex behaviour was found for the C0-systems, where the T_g first runs through a maximum and then decreases again, falling below the initial value of the linear system. This shows again the complex relationship between monomer structure, polymer structure and finally system properties.

5.8.2 Ion diffusion and swelling

As is shown in publication II, the ion transport in the polymer systems was found to be very slow, being subdiffusive on the nanosecond timescale. Comparing linear and cross-linked systems, the ion transport was faster in the linear systems due to higher segmental mobility. Analogous findings were obtained in the Master's Thesis of Agustín López Cabrera, noting here that a different ion, $TFSI^-$ (bis(trifluoromethane)sulfonimide) was used.

In a further step, electrolyte swelling was introduced. In a preliminary investigation, varying the volume swelling due to solvent (diethyl carbonate (DEC), dimethyl carbonate (DMC), and ethylene carbonate (EC) in a 1:1:1 volume ratio) uptake between 0 % and 40 %, much higher ion displacement was found and the diffusive regime was reached. This shows the drastic effect of solvent swelling on the ion transport properties and finally the electrochemical performance of the materials. Since the experimental degree of swelling is not known, the effect of swelling on the ion transport can not be quantitatively ascertained. However it is clear that the electrolyte swelling needs to be included in further efforts into modeling **TPA**s as OMIEC materials.

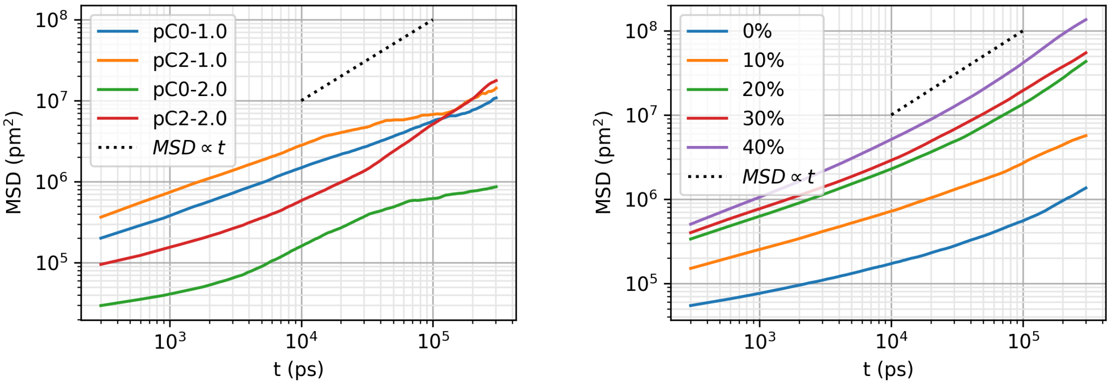

Figure 5.11: a) TSFI$^-$ ion diffusion in dry polymer networks. b) TSFI$^-$ ion diffusion in polymer networks showing 0 %-40 % volume swelling due to solvent uptake. Here, a system consisting of 216 monomers and 11 TSFI$^-$-ions were used corresponding to a doping degree of 5 %. These figures are taken from the Master's Thesis of Agustín López Cabrera.

CHAPTER 6

Constrained GFN2-xTB

Constrained DFT (CDFT) has proven as a valuable tool in the research efforts presented so far, and has additionally found wide application in charge transport research. [54, 129, 130] This provided the motivation to implement a charge and spin constraint methodology within the framework of GFN2-xTB in order to provide efficient and accurate access to charge and spin constrained states. The full manuscript with all details is given in section 6.5, while the results are summarized here and put into the context of the thesis.

6.1 Constrained DFT

Constrained DFT (CDFT) was originally proposed by Dederichs et al. [131] to investigate Cerium impurities. Since then, the method has found wide application and further development by many groups. [55, 124, 125, 129, 132, 133] CDFT is a method that can be used to address specific problems in quantum chemistry. By employing a user-defined constraint on the electronic density, problems due to the self-interaction- or overdelocalization error can be overcome. Furthermore, CDFT enables access to diabatic states and charge-transfer excited states. [124] As an example, CDFT is able to accurately describe the charge-transfer excitation energies in Zinc-Bacteriochlorin as a function of the intermolecular separation, yielding the expected distance dependence, which was not possible using traditional TDDFT methods. [55, 134] In the research presented in this thesis, CDFT has been used extensively in the description of hole reorganization energies. It has also found application in related works. [53] Since semiempirical methods like GFN2-xTB are much less computationally expensive compared to DFT, the implementation of a constraining methodology could enable much faster access to the structures of e.g. highly dipolar molecules or to properties like the reorganization energy.

6.2 Implementation

The implementation presented herein is based on the original work by Dederichs and later van Voorhis et al. [124, 131] The electronic ground state energy $E(N)$ of a constrained system with N electrons in a certain space can be written as

$$E(N) = \min[E[\rho(\mathbf{r})] + V(\int \mathrm{d}^3\mathrm{r} - N)] \tag{6.1}$$

with $E[\rho(\mathbf{r})]$ denoting the DFT functional, V denoting the lagrangian multiplier and $\rho(\mathbf{r})$ denoting the electron density. Eq. 6.1 can be rewritten as the constrained functional W as

$$W[\rho, V; N] = E[\rho(\mathbf{r})] + V(\sum_{\sigma} \int w_k^{\sigma} \rho^{\sigma}(\mathbf{r}) \mathrm{d}^3\mathrm{r} - N) \tag{6.2}$$

where σ denotes the spin variable and w_k^{σ} is a weight function. To obtain the constrained ground state, minimization of 6.2 is required, leading in the Kohn-Sham framework to the well-known eigenvalue problem

$$(-\frac{1}{2}\nabla^2 + v_n(\mathbf{r}) + \int \frac{\rho(\mathbf{r}')}{|\mathbf{r} - \mathbf{r}'|} \mathrm{d}^3\mathrm{r} + v_{XC}^{\sigma}(\mathbf{r}) + \sum_k V_k w_k^{\sigma}(\mathbf{r}))\phi_{i\sigma} = \epsilon_{i\sigma}\phi_{i\sigma} \tag{6.3}$$

with $-\frac{1}{2}\nabla^2$ denoting the kinetic energy term, $v_n(\mathbf{r})$ denoting the nuclear-electronic potential, $\int \frac{\rho(\mathbf{r}')}{|\mathbf{r}-\mathbf{r}'|}\mathrm{d}^3\mathbf{r}$ denoting the coulomb potential, $v_{XC}^{\sigma}(\mathbf{r})$ denoting the exchange correlation potential, $\phi_{i\sigma}$ denoting the orbitals, $\epsilon_{i\sigma}$ denoting the eigenvalues and $\sum_k V_k w_k^{\sigma}(\mathbf{r})$ denoting the additional constraining potential. As was introduced by van Voorhis et al. [124], eg. 6.3 can be solved by a nested-loop approach. In the outer loop, eg. 6.3 is made stationary w.r.t. the orbitals $\phi_{i\sigma}$ by performing the SCF procedure. In the inner loop, at every step eg. 6.3 is made stationary w.r.t the lagrangian multiplier V_k. The first derivative is given by

$$\frac{\mathrm{d}W}{\mathrm{d}V_k} = \sum_{\sigma} \sum_{i}^{N_{\sigma}} \left(\frac{\partial W}{\partial \phi_{i\sigma}^*} \frac{\partial \phi_{i\sigma}^*}{\partial V_k} + cc \right) + \frac{\partial W}{\partial V_k} \tag{6.4}$$

$$= \sum_{\sigma} \int w_k^{\sigma} \rho^{\sigma}(\mathbf{r}) \mathrm{d}^3\mathrm{r} \tag{6.5}$$

$$= 0 \tag{6.6}$$

where cc denotes the complex conjugate and $\frac{\partial W}{\partial \phi_{i\sigma}^*}$ at SCF convergence has been used. It has been shown [124, 131] that

$$\frac{\partial^2 W}{\partial V_k V_l} = \sum_{\sigma} \sum_{i}^{N_{\sigma}} \int w_k^{\sigma} \phi_{i\sigma}^*(\mathbf{r}) \frac{\partial \phi_{i\sigma}^*(\mathbf{r})}{\partial [V_l w_l^{\sigma}(\mathbf{r})]} w_l^{\sigma}(\mathbf{r}) \mathrm{d}^3 r \mathrm{d}^3 r' + cc \tag{6.7}$$

$$= \sum_{\sigma} \sum_{i}^{N_{\sigma}} \int w_k^{\sigma} \phi_{i\sigma}^*(\mathbf{r}) \tag{6.8}$$

$$\times \sum_{a \neq b} \frac{\phi_{a\sigma}^*(\mathbf{r})\phi_{i\sigma}(\mathbf{r})}{\epsilon_{i\sigma} - \epsilon_{a\sigma}} \phi_{a\sigma}^*(\mathbf{r}) w_l^{\sigma}(\mathbf{r}) \mathrm{d}^3 r \mathrm{d}^3 r' + cc \tag{6.9}$$

$$= \sum_{\sigma} \sum_{\sigma}^{N_{\sigma}} \sum_{a > N_{N_{\sigma}}} \frac{\langle \phi_{i\sigma} | w_k^{\sigma} | \phi_{a\sigma} \rangle \langle \phi_{a\sigma} | w_l^{\sigma} | \phi_{i\sigma} \rangle}{\epsilon_{i\sigma} - \epsilon_{a\sigma}} \tag{6.10}$$

For all V_k, the Hessian is

$$\sum_{k,j}^{m} V_k \frac{\partial^2 W}{\partial V_k V_l} = 2 \sum_{\sigma} \sum_{\sigma}^{N_\sigma} \sum_{a>N_{N_\sigma}} \frac{\left\langle \phi_{i\sigma} \right| \sum_k^m V_k w_k^\sigma \left| \phi_{a\sigma} \right\rangle^2}{\epsilon_{i\sigma} - \epsilon_{a\sigma}} \leq 0 \tag{6.11}$$

Since in Kohn-Sham theory, the lowest energy orbitals are chosen to be occupied, $\epsilon_{i\sigma} - \epsilon_{a\sigma} < 0$ is true and the overall term is negative. Therefore, a unique stationary point in $W(V)$ exists which is always a maximum which can be easily located with Newtons algorithm. Once the stationary point has been located, the inner loop terminates and the orbitals are given back to the outer loop performing the SCF procedure.

Within CxTB, Mulliken charges are used to define the constraint. The Mulliken charge q_A on an atom A is given by [84]

$$q_A = Z_A - \sum_{\mu \in A} (\mathbf{PS})_{\mu\mu} \tag{6.12}$$

where Z_A denotes the nuclear charge, **P** and **S** denote the density and overlap matrices and μ denotes the orbital index. The number of electrons N_A is thus given by

$$N_A = \sum_{\mu \in A} (\mathbf{PS})_{\mu\mu}. \tag{6.13}$$

A weight function $w^M_{c\mu\nu}$ for the constraint area C can be defined as [55]

$$w^M_{c\mu\nu} = \begin{cases} S_{\mu\nu} & \text{if } \mu \text{ and } \nu \in C \\ \frac{1}{2} S_{\mu\nu} & \text{if } \mu \text{ or } \nu \in C \\ 0 & \text{if } \mu \text{ and } \nu \notin C \end{cases} \tag{6.14}$$

with which eq. 6.13 can be rewritten as [55]

$$N_C = \sum_{\mu \in C} \mathrm{Tr}(\mathbf{P} w^M_c). \tag{6.15}$$

With this charge definition at hand, the implementation approach for CxTB is complete.

6.3 Test calculations

CxTB was tested on literature known cases, namely highly dipolar merocyanines and the mixed-valence compound tetrathiafulvalene-diquinone, to show its performance (see manuscript I). As an example, the bond length alternation patterns of two merocyanines were calculated and compared with experimental and computational reference data (see Fig. 6.1). Merocyanines are strongly dipolar compounds that show a vanishing bond length alternation pattern in the limit case between zwitterionic and polyenic forms, termed the cyanine limit. The experimental XRD bond length alternation pattern has been reproduced by Gildemeister et al. [53] by using CDFT and a charge separation of ± 0.6 q, indicating that an intermediate charge separation corresponds to the cyanine limit. Using the same charge separation scheme in CxTB leads to excellent agreement with the experimental and computational reference data.

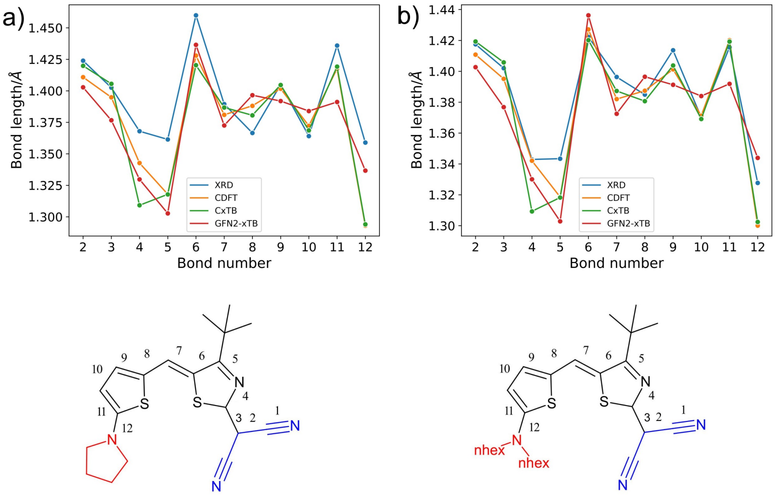

TG008 HB238

Figure 6.1: Bond length alternation patterns at different levels of theory.

6.4 Conclusion

Constrained xTB (CxTB) was successfully implemented and tested on merocyanine geometries and a charge separated mixed-valence compound (see manuscript I). The implementation allows for both charge and spin constraints. The experimental bond length alternation pattern of two merocyanine compounds as well as the geometric asymmetry of the tetrathiafulvalene-diquinone radical anion were reproduced with high accuracy. Simultaneously, a large speedup compared to CDFT was achieved even though a numerical gradient was used in the geometry optimizations. The implementation of an analytical gradient in the future would further improve computation times for geometry optimizations and enable larger-scale calculations, e.g. the calculation of outer-sphere reorganization energies. Accurate and efficient evaluation of the outer-sphere reorganization energy could enable more accurate charge transport simulations.

6.5 Manuscript I

The implementation and testing of CxTB has been performed by me. I have written the initial manuscript and revised it together with the co-authors.

Mulliken population based implementation of charge- and spin-constraints in GFN2-xTB

Robert Herzhoff,[a] Stefan Grimme,[b] Andreas Hansen,[b] Klaus Meerholz,[a] Daniele Fazzi [a,c]

[a] Institut für Licht und Materialien, Department für Chemie, Universität zu Köln, Greinstr. 4-6, 50939 Köln, Germany.

[a] Mulliken Center for Theoretical Chemistry, Universität Bonn, Beringstr. 4, 53115 Bonn, Germany.

[c] Università di Bologna, Dipartimento di Chimica 'Giacomo Ciamician', Via F. Selmi, 2, 40126 Bologna, Italy.

Abstract

A Mulliken population based implementation of charge- and spin constraints in the framework of GFN2-xTB is presented. The implementation is based on constrained DFT. Since GFN2-xTB uses a minimal basis set, the efficient Mulliken population scheme can be used for charge definition without a drawback. The method was tested on two separate literature-known examples, namely zwitterionic merocyanines and the mixed valence compound tetrathiafulvalene-diquinone, providing accurate geometries at reduced computational cost compared to constrained DFT. Implementation of an analytical gradient in the future can enable faster access to geometries and larger-scale systems.

Introduction

Constraint methods such as constrained DFT (CDFT) [1], CDFT-CI, [2] and constrained DFTB+ [3] have proven to be a useful tool for describing electronically intricate systems such as highly polar molecules [4] charge-transfer (CT) [5–7] states, mixed-valence systems [8] and chemical reaction barriers [9]. They offer a direct route to diabatic states [5] and can also be used to mitigate the self-interaction error (SIE) [5]. Since its inception in the 1970s by Dederichs et al. to study cerium impurities [1], CDFT has undergone much development, particularly by van Voorhis and coworkers, [2,10] Frauenheim and coworkers, [3] Pavanello and Coworkers [11], Blumberger and coworkers [12] and others, extending it for example to DFTB and coupling it with molecular dynamics simulations so as to enable the investigation of larger more complex systems. CDFT has also been instrumental to overcome errors present in classical DFT. It has been used to accurately describe the charge transfer excitation energies in Zinc-Bacteriochlorin as a function of the intramolecular separation overcoming a prominent failure of TDDFT. [6] It has further been used to describe the hole reorganization energies of highly polar molecules, for which standard DFT methods were not adequate. [4] Here, we present an implementation of the constraint formalism to GFN2-xTB [13]. GFN2-xTB is a fast, reliable and broadly parametrized semiempirical method, allowing access to much larger systems than DFT. This makes a constrained GFN2-xTB (CxTB) implementation interesting for studying systems such as (multiply) charged polymers or quantities such as the outer reorganization energy which are too computationally demanding for classical CDFT. We tested our method on some literature-known examples to explore the methods capabilities in terms of geometries and energies, yielding promising results.

GFN2-xTB

The theory behind GFN2-xTB is described in detail in the original publication. [13,14] The method is based on density functional tight binding, and as are all tight-binding methods, GFN2-xTB is an approximation to Kohn-Sham DFT. In tight-binding methods, the density of a system is expanded in terms of fluctuations around a reference density, which is truncated after different terms giving rise to various levels of approximation. The GFN2-xTB energy expression contains terms from repulsive, dispersive, extended-Hückel-type, isotropic electrostatic, isotropic exchange correlation, anisotropic electrostatic, anisotropic exchange correlation and Fermi energy contributions. The method has the following features:

- GFN2-xTB uses a minimal valence basis set of atom centered, contracted Gaussian functions.
- GFN2-xTB contains element specific parametrization up to Rn.
- GFN2-xTB includes electrostatic interactions and exchange-correlation effects up to second order in the multipole expansion as well as the D4 dispersion model in a self-consistent formulation.

The method allows robust and fast access to large systems and is used here as the basis of CxTB to take advantage of the efficiency of xTB to describe larger and more complex systems than possible with CDFT.

Constrained DFT

The original formulation of constrained DFT by Dederichs et. al [1] is the basis of the CxTB method presented in this work and will be briefly reviewed in the following passage, adopting the notation from van Voorhis et al. [10] Consider the electronic ground state of a system with the additional constraint that a certain number of electrons N occupy a certain volume. Using the Lagrangian multiplier V, the energy E(N) can be written as

$$E(N) = \min\left[E[\rho(\vec{r})] + V\left(\int d^3r\rho(\vec{r}) - N\right)\right] \qquad (1)$$

with $E[\rho(\vec{r})]$ the DFT functional and $\rho(\vec{r})$the electron density. In principle, many different constraints are conceivable, such as constraints on specific orbitals or magnetization constraints. Using the spin variable σ, eq. (1) can be written as a new functional W

$$W[\rho, V; N] = E[\rho(\vec{r})] + V(\sum_{\sigma} \int w_k^{\sigma}(\vec{r})\rho^{\sigma}(\vec{r})d^3r - N) \quad (2)$$

where the spin-dependent weight function $w_k^{\sigma}(\vec{r})$ is used to define the constraint of interest. Minimization of (2) with respect to $\rho(\vec{r})$ yields the classic Kohn-Sham equations with an additional potential

$$(-\frac{1}{2}\nabla^2 + v_n(\vec{r}) + \int \frac{\rho(\vec{r}')}{|\vec{r} - \vec{r}'|} d^3r' + v_{XC}^{\sigma}(\vec{r}) + \sum_k V_k w_k^{\sigma}(\vec{r})\,)\,\varphi_{i\sigma} = \varepsilon_{i\sigma}\varphi_{i\sigma} \quad (3)$$

The CxTB implementation presented herein is based on the nested-loop approach by van Voorhis et. al. [5], which is detailed in the following. Eq. (3) must be made stationary with respect to the orbitals $\varphi_{i\sigma}$ and with respect to the lagrangian multiplier V_k. The first condition is met by performing the SCF. Trying to make eq. (3) stationary with respect to the lagrangian multipliers leads to [5,10]

$$\frac{dW}{dV_k} = \sum_{\sigma} \sum_{i}^{N_\sigma} \left(\frac{\partial W}{\partial \varphi_{i\sigma}^*} \frac{\partial \varphi_{i\sigma}^*}{\partial V_k} + cc \right) + \frac{\partial W}{\partial V_k} \quad (4)$$

$$= \sum_{\sigma} \int w_k^{\sigma}(\vec{r})\rho(\vec{r})^{\sigma} d^3r - N \quad (5)$$

$$= 0 \quad (6)$$

where cc is the complex conjugate, and the SCF convergence condition of $\frac{\partial W}{\partial \varphi_{i\sigma}^*} = 0$ is used. Importantly, van Voorhis and coworkers have shown [5,10] that the second derivative of W with respect to V is given by

$$\frac{\partial^2 W}{\partial V_k V_l} = 2 \sum_{\sigma} \sum_{\sigma}^{N_\sigma} \sum_{a > N_\sigma} \frac{\langle \varphi_{i\sigma} | w_k^{\sigma} | \varphi_{a\sigma} \rangle \langle \varphi_{a\sigma} | w_l^{\sigma} | \varphi_{i\sigma} \rangle}{\varepsilon_{i\sigma} - \varepsilon_{a\sigma}} \quad (7)$$

For any V_k, the Hessian is given by [10]

$$\sum_{k,j}^{m} V_k \frac{\partial^2 W}{\partial V_k V_l} V_l = 2 \sum_{\sigma} \sum_{\sigma}^{N_\sigma} \sum_{a > N_\sigma} \frac{\langle \varphi_{i\sigma} | \sum_k^m V_k \, w_k^{\sigma} | \varphi_{a\sigma} \rangle^2}{\varepsilon_{i\sigma} - \varepsilon_{a\sigma}} \leq 0 \quad (8)$$

which is nonpositive definite because in Kohn-Sham theory the lowest energy orbitals are chosen to be occupied orbitals $\varepsilon_{i\sigma}$, leading to $\varepsilon_{i\sigma} - \varepsilon_{a\sigma} < 0$. Since the numerator of eq. (8) is positve, the overall term is negative. This means there is a unique stationary point in W(V) which is also a maximum. Employing van Voorhis' nested-loop algorithm, a regular SCF constitutes the outer loop. Upon convergence, the inner loop starts, and Newton's algorithm is used to locate the stationary point of W(V) for the current set of orbitals given by the SCF, thereby fulfilling the constraint. This way, both the SCF condition and also the constraint are fulfilled, leading to a converged set of orbitals which also fulfill the charge constraint.

Charge scheme

Constraints can generally be formulated in terms of real space charge schemes using e.g. the Becke [15] or Hirshfeld [16] population analyses relying on the electronic density $\rho^{\sigma}(\vec{r})$ and the weight function $w_k^{\sigma}(\vec{r})$ or in terms of the one-particle density matrix using e.g. the Löwdin [17] or Mulliken [18] population analyses. In this work, Mulliken charges are used. In order to make the constraint and the weight function appearing in equations (1) - (8) less anonymous, their forms due to the choice of the Mulliken populations is discussed in the following. Mulliken charges on Atom A are given by [18]

$$q_A = Z_A - \sum_{\mu \in A} (\boldsymbol{PS})_{\mu\mu} \tag{9}$$

with q_A the Mulliken charges, Z_A the nuclear charges, $\boldsymbol{P}$ the density matrix, $\boldsymbol{S}$ the overlap matrix and μ the orbital index. Similarly, the number of electrons is given by

$$N_A = \sum_{\mu \in A} (\boldsymbol{PS})_{\mu\mu}. \tag{10}$$

Following van Voorhis et al., a weight function for a constraint area C (Mulliken weight matrix $w_{c\mu\nu}^{M}$) can be defined as [6]

$$w_{c\mu\nu}^{M} = \begin{cases} S_{\mu\nu}\ if\ \mu\ and\ \nu \in C \\ \frac{1}{2} S_{\mu\nu}\ if\ \mu\ or\ \nu \in C \\ 0\ if\ \mu\ and\ \nu \ni C \end{cases} \tag{11}$$

which allows (10) to be rewritten as

$$N_C = \sum_{\mu \in C} Tr(\boldsymbol{P} w_c^{M}) \tag{12}$$

With these equations and charge prescriptions at hand, the nested-loop aproach for CxTB is fully described. The outer loop is solved via a general SCF approach. $\int w_k^{\sigma}(\vec{r})\rho^{\sigma}(\vec{r})d^3r)$ is given by (12) and with the first and second derivatives of W at hand (eq.(5) and eq.(7)), Newtons algorithm can be used to maximise W, fulfilling the constraint in the inner cycle.

Results and Discussion

Validation of charge scheme

In typical CDFT implementations, the usage of Mulliken populations for charge definition is discouraged, due to their principal ability to become negative. [19] Mulliken charges have shown unreliability for example concerning energy separation when considering increasingly charge-separated states. [6] However, the usage of a minimal-valence basis set in CxTB mitigates this problem. In Fig. 1, the energy of a dinitrogen molecule (bond length 1.12 Å) with increasing charge separation is shown.

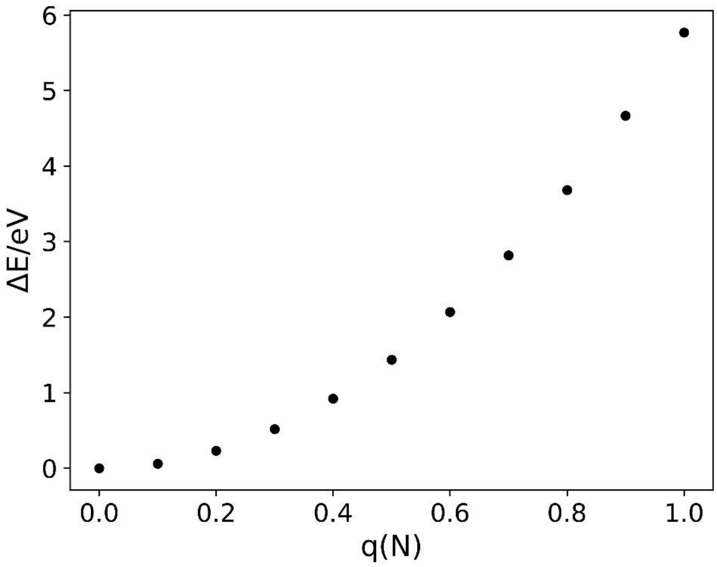

Fig. 1: Energies of a N_2-molecule with increasing charge separation using Mulliken charges.

At a charge separation of 1.0 q, an energy difference of close to 6 eV is obtained, which is much higher and more realistic than the energies obtained from CDFT calculations using Mulliken charges [6]. Here, one of the advantages of CxTB becomes clear, because the simple Mulliken scheme can be used to define constraints without sacrificing accuracy.

Merocyanines

Using CxTB, complex systems such as highly dipolar, zwitterionic molecules or mixed valence compounds can be investigated. We will demonstrate the ability of CxTB to describe such systems with high accuracy with some examples. As a first test case, the geometry, more precisely the bond length alternation pattern of prototypocal merocyanine molecules is investigated. Merocyanines are highly dipolar compounds that have found wide use in organic electronic applications such as solar cells and transistors, mainly owed to their ability to self-assemble based on their dipolar interactions leading to efficient charge-transport. Due to their modular Donor-Acceptor structure and chemical tunability, a large library of merocyanines exist. [4] The structure of a typical merocyanine investigated here together with its two resonance structures is shown in Fig. 2.

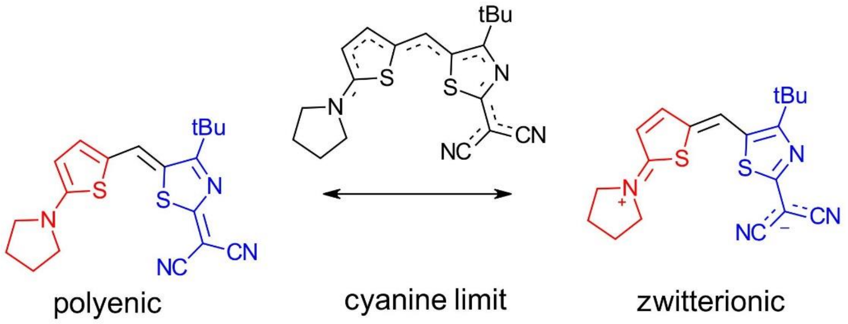

Fig. 2: A typical merocyanine in the polyenic and zwitterionic, charge separated form. Red indicates the Donor part of the molecule while blue indicates the Acceptor part. In the cyanine limit, the bond length alternation is minimized.

Varying the chemical structure of the Donor- and Acceptor parts, the compounds tend more to one of the resonance forms which are mainly characterized by their bond-length alternation pattern, while in the cyanine limit, the bond-length alternation is minimized. Gildemeister et al. have used CDFT to reproduce the experimental (i.e. XRD) bond-length alternation pattern by varying the amount of partial charge on the Donor- and Acceptor units in merocyanines. [4] They have found that using a charge separation $\delta^{D/A}$ of $\pm\ 0.6$ q led to a good agreement with the experimental data, showing that the cyanine limit indeed corresponds to a close-to intermediate charge separation in the molecule, as can be expected by assuming that the polyenic form corresponds to a charge separation $\delta^{D/A}$ of $\pm\ 0.0$ and the zwitterionic form corresponds to a charge separation $\delta^{D/A}$ of $\pm\ 1.0$. In Fig. 3, we compare CDFT, CxTB and experimental bond length alternation patterns, comparing the CxTB geometries to the CDFT calculations of Gildemeister et al. and experimental data. With the sole exception of bond number four, the CxTB geometry very closely reproduces the CDFT and thus the XRD data at much reduced computational cost (see Fig. 5). The CxTB geometries have been optimized using a numerical gradient, confirming the equilibrium structures by a frequency calculation (no imaginary frequencies found).

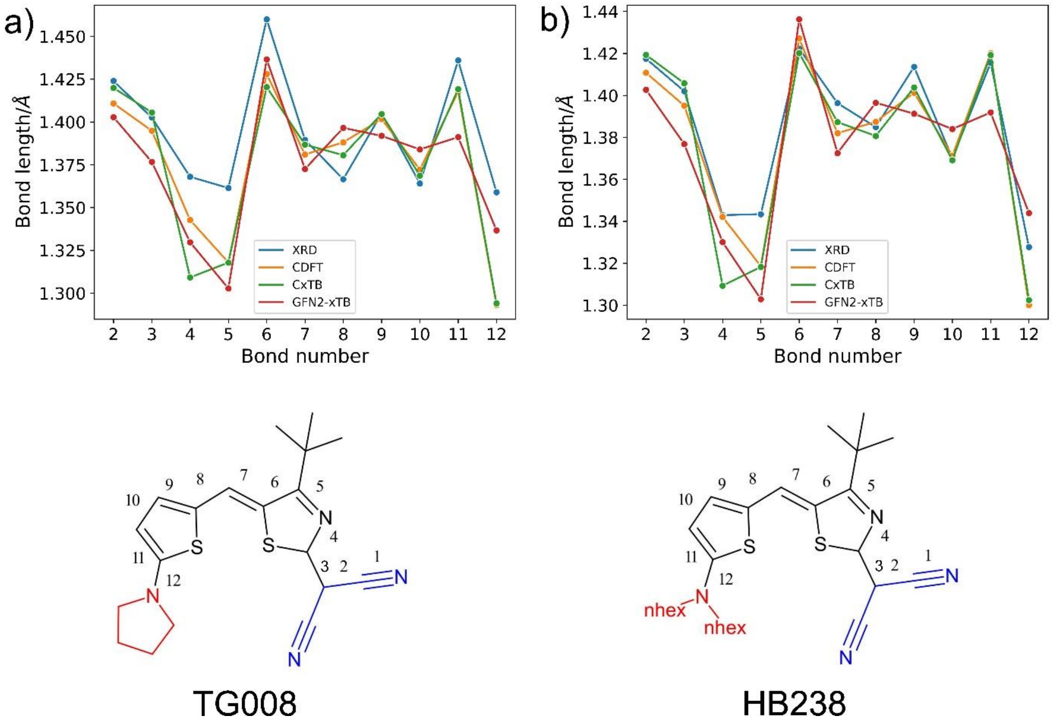

Fig. 3: Bond length alternation patterns of two closely related merocyanines comparing experimental, CDFT (CAM-B3LYP/6-311G), GFN2-xTB and CxTB data. For the calculations, partial charges of* $\delta^{D/A}$ *of* $\pm\ 0.6\ q$ *were used. The CDFT and XRD data is obtained from the authors of* [4].

Tetrathiafulvalene-diquinone radical dianion

As a second example, we investigate the Tetrathiafulvalene-diquinone (QTTFQ$^-$) radical anion (see Fig. 4). QTTFQ$^-$ is a symmetric mixed valence compound, meaning it contains two identical moieties in different oxidation states. The intramolecular charge transfer between the quinone units has been observed by Electron Spin Resonance (ESR). [20] By constraining a charge of -1 and an excess electron on one of the quinone moieties, the charge separated state can be modeled. The bond lengths are summarized in Tab. 1.

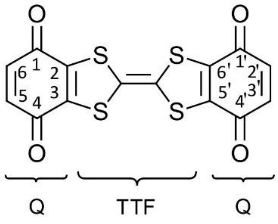

Fig. 4: Chemical structure of the Tetrathiafulvalene-diquinone (QTTFQ) molecule.

Tab. 1: Bond lengths (Å) of the neutral and reduced QTTFQ molecule and of the neutral and reduced quinone molecule. For the bond numbering see Fig.4.

Bonds	*QTTFQ*$^-$ *(xTB)*	*QTTFQ*$^-$ *(*CxTB, neutral Q)	*QTTFQ*$^-$ (CxTB anionic Q)	QTTFQ (xTB)	Q *(*xTB)	Q$^-$ *(*xTB)
O–C1	1.231	1.229	1.258	1.214	1.214	1.258
C1–C2	1.454	1.457	1.460	1.468	1.477	1.44
C2–C3	1.361	1.362	1.389	1.357	1.334	1.359
C1–C6	1.457	1.458	1.454	1.475	1.477	1.44
C5–C6	1.347	1.346	1.375	1.336	1.334	1.359

From Tab. 1, the asymmetry of the QTTFQ radical anion as obtained by CxTB calculations becomes clear. In an unconstrained calculation both quinone moieties have the same bond length pattern, not showing the expected asymmetry, however in the constrained calculations, the charged and uncharged moieties can be distinguished. While the differences are not extremely large, the neutral quinone unit in QTTFQ$^-$ resembles more the neutral quinone molecule, the anionic quinone unit resembles more the anionic quinone molecule. While not as concise as the CDFT results presented in [21], the low computation cost of the calculation is of great advantage when studying larger systems. A numerical gradient has been used for the geometry optimizations and the equilibrium structures were confirmed by a frequency calculation (no imaginary frequencies found).

Timings

In Fig. 5, the timings of CDFT and CxTB are compared. To that end, the CDFT calculations were done with the same computational setup, only differing in the CPU type (4 cores, 4 GB of memory, Intel(R) Xeon(R) W-2145 for CDFT, Intel(R) Xeon(R) W-2245 for CxTB). The calculations on the merocyanines were done at the CAM-B3LYP [22] /6-311G* [23] level of theory, while the calculations on the QTTFQ$^-$ anion were done at the B3LYP/6-31G [24] level of theory in order to correspond to the approach presented in literature. All CDFT calculations were done with NWChem. [25]

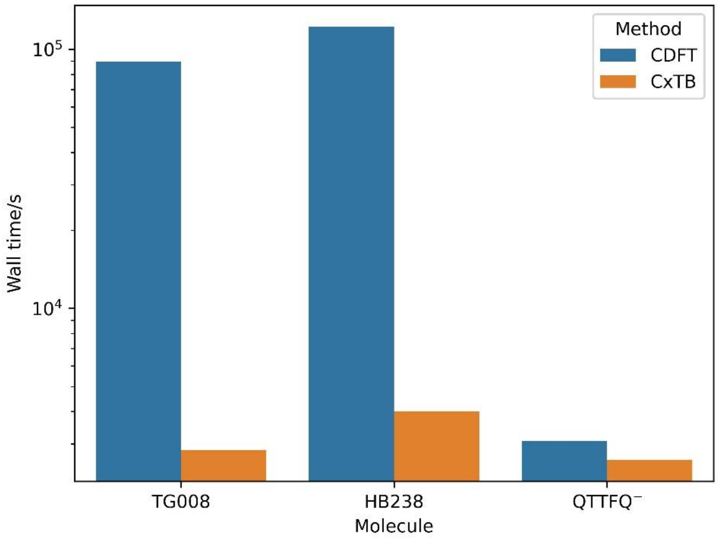

Fig. 5: Wall times comparing CDFT and CxTB. Calculations were performed on 4 cores using 4GB of memory.

As is clear from Fig. 5, CxTB provides a large computational speedup compared to CDFT, even when using a numerical gradient, especially if more complex systems are used in combination with more expensive exchange-correlation funtionals. Therefore, the method can be very useful in larger scale applications such as screening approaches, supramolecular clusters, ONIOM or QM/MM approaches.

Conclusion

A novel implementation of a constraint formalism allowing to fix charge as well as spin on molecular fragments in the framework of GFN2-xTB has been presented and tested on two different literature known examples. The geometries of highly dipolar merocyanines as well as the mixed-valence compound tetrathiafulvalene-diquinone were investigated. CxTB was able to accurately reproduce both experimental as well as theoretical data from CDFT calculations at relatively low cost even though a numerical gradient was used for geometry optimizations. A future implementation of an analytical gradient would allow for the computation of complex quantities such as the outer shell reorganization energy for charge transport simulations or calculations on multi-molecule systems. CxTB and Ctblite are available on github under https://github.com/rbrthrz/CxTB and https://github.com/rbrthrz/Ctblite.

References

[1] P. H. Dederichs, S. Blügel, R. Zeller, H. Akai, *Phys. Rev. Lett.* **1984**, *26*, 2512.

[2] Q. Wu, C.-L. Cheng, T. van Voorhis, *J Chem Phys* **2007**, *16*, 164119.

[3] B. Hourahine, B. Aradi, T. Frauenheim, *J. Phys.: Conf. Ser.* **2010**, 12005.

[4] N. Gildemeister, G. Ricci, L. Böhner, J. M. Neudörfl, D. Hertel, F. Würthner, F. Negri, K. Meerholz, D. Fazzi, *J. Mater. Chem. C* **2021**, *33*, 10851.

[5] Q. Wu, T. van Voorhis, *Phys. Rev. A* **2005**, *2*.

[6] Q. Wu, T. van Voorhis, *J Chem Theory Comput* **2006**, *3*, 765.

[7] S. Difley, T. van Voorhis, *J Chem Theory Comput* **2011**, *3*, 594.

[8] R. Herzhoff, F. Negri, K. Meerholz, D. Fazzi, *J. Mater. Chem. C* **2023**, *35*, 11969.

[9] Q. Wu, B. Kaduk, T. van Voorhis, *J Chem Phys* **2009**, *3*, 34109.

[10] B. Kaduk, T. Kowalczyk, T. van Voorhis, *Chem Rev* **2012**, *1*, 321.

[11] P. Ramos, M. Pavanello, *Phys Chem Chem Phys* **2016**, *31*, 21172.

[12] a) A. Kubas, F. Hoffmann, A. Heck, H. Oberhofer, M. Elstner, J. Blumberger, *J Chem Phys* **2014**, *10*, 104105; b) H. Oberhofer, J. Blumberger, *J Chem Phys* **2009**, 6, 64101.

[13] C. Bannwarth, S. Ehlert, S. Grimme, *J Chem Theory Comput* **2019**, *3*, 1652.

[14] C. Bannwarth, E. Caldeweyher, S. Ehlert, A. Hansen, P. Pracht, J. Seibert, S. Spicher, S. Grimme, *Wiley Interdisciplinary Reviews: Computational Molecular Science* **2021**, *2*, e1493.

[15] A. D. Becke, *J. Chem. Phys.* **1988**, *4*, 2547.

[16] F. L. Hirshfeld, *Theoret. Chim. Acta* **1977**, *2*, 129.

[17] P.-O. Löwdin, *J. Chem. Phys.* **1950**, *3*, 365.

[18] R. S. Mulliken, *J. Chem. Phys.* **1955**, *10*, 1833.

[19] A. E. Reed, R. B. Weinstock, F. Weinhold, *J. Chem. Phys.* **1985**, *2*, 735.

[20] N. Gautier, F. Dumur, V. Lloveras, J. Vidal-Gancedo, J. Veciana, C. Rovira, P. Hudhomme, *Angewandte Chemie* **2003**, *24*, 2871.

[21] Q. Wu, T. van Voorhis, *J Phys Chem A* **2006**, *29*, 9212.

[22] T. Yanai, D. P. Tew, N. C. Handy, *Chemical Physics Letters* **2004**, *1-3*, 51.

[23] a) R. Krishnan, J. S. Binkley, R. Seeger, J. A. Pople, *J. Chem. Phys.* **1980**, *1*, 650; b) B. P. Pritchard, D. Altarawy, B. Didier, T. D. Gibson, T. L. Windus, *Journal of Chemical Information and Modeling* **2019**, *11*, 4814; c) T. Clark, J. Chandrasekhar, G. W. Spitznagel, P. V. R. Schleyer, *J Comput Chem* **1983**, *3*, 294.

[24] a) A. D. Becke, *J. Chem. Phys.* **1993**, *7*, 5648; b) C. Lee, W. Yang, R. G. Parr, *Phys. Rev. B* **1988**, *2*, 785; c) S. H. Vosko, L. Wilk, M. Nusair, *Can. J. Phys.* **1980**, *8*, 1200.

[25] E. Aprà, E. J. Bylaska, W. A. de Jong, N. Govind, K. Kowalski, T. P. Straatsma, M. Valiev, H. J. J. van Dam, Y. Alexeev, J. Anchell, V. Anisimov, F. W. Aquino, R. Atta-Fynn, J. Autschbach, N. P. Bauman, J. C. Becca, D. E. Bernholdt, K. Bhaskaran-Nair, S. Bogatko, P. Borowski, J. Boschen, J. Brabec, A. Bruner, E. Cauët, Y. Chen, G. N. Chuev, C. J. Cramer, J. Daily, M. J. O. Deegan, T. H. Dunning, M. Dupuis, K. G. Dyall, G. I. Fann, S. A. Fischer, A. Fonari, H. Früchtl, L. Gagliardi, J. Garza, N. Gawande, S. Ghosh, K. Glaesemann, A. W. Götz, J. Hammond, V. Helms, E. D. Hermes, K. Hirao, S. Hirata, M. Jacquelin, L. Jensen, B. G. Johnson, H. Jónsson, R. A. Kendall, M. Klemm, R. Kobayashi, V. Konkov, S. Krishnamoorthy, M. Krishnan, Z. Lin, R. D. Lins, R. J. Littlefield, A. J. Logsdail, K. Lopata, W. Ma, A. V. Marenich, J. Del Martin Campo, D. Mejia-Rodriguez, J. E. Moore, J. M. Mullin, T. Nakajima, D. R. Nascimento, J. A. Nichols, P. J. Nichols, J. Nieplocha, A. Otero-de-la-Roza, B. Palmer, A. Panyala, T. Pirojsirikul, B. Peng, R. Peverati, J. Pittner, L. Pollack, R. M. Richard, P. Sadayappan, G. C. Schatz, W. A. Shelton, D. W. Silverstein, D. M. A. Smith, T. A. Soares, D. Song, M. Swart, H. L. Taylor, G. S. Thomas, V. Tipparaju, D. G. Truhlar, K. Tsemekhman, T. van Voorhis, Á. Vázquez-Mayagoitia, P. Verma, O. Villa, A. Vishnu, K. D. Vogiatzis, D. Wang, J. H. Weare, M. J. Williamson, T. L. Windus, K. Woliński, A. T. Wong, Q. Wu, C. Yang, Q. Yu, M. Zacharias, Z. Zhang, Y. Zhao, R. J. Harrison, *J Chem Phys* **2020**, *18*, 184102.

CHAPTER 7

Excited state characterization of TADF emitters

In order to design efficient luminescent materials for OLED applications, a high quantum yield is one of the key molecular design targets. Donor-acceptor compounds have shown excellent quantum yields up to 100% due to thermally activated delayed fluorescence (TADF). [78, 79] The efficiency of TADF and the magnitude of the final quantum yield is intimately tied to excited state characteristics and the relative photophysical rates, especially the reverse intersystem crossing rate k_{rISC} determining the thermal upconversion process. In this work, the effect of the molecular design on such photophysical properties is investigated. The molecules in question are shown in Fig. 7.1.

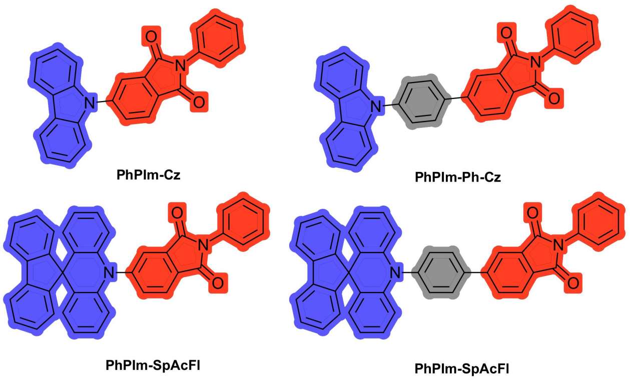

Figure 7.1: TADF emitters as synthesized by Christopher Wallerius. The blue color indicates the donor moiety while the red color indicates the acceptor moiety. The phenyl bridge is colored grey.

The compounds consist of a N-phenyl phthalimide acceptor and either a carbazole or a spiro[acridine-9,9'-fluorene] donor. Two of the compounds additionally contain a phenyl-bridging unit. Thus, the effect of varying the donor unit and the effect of having an additional bridging unit can be assessed. The compounds were synthesized and characterized by Christopher Wallerius. As the most important parameter for TADF, k_{rISC} is given by [80]

$$k_{rISC} = \frac{2\pi}{\hbar} \frac{|\hat{H}_{SO}|^2}{\sqrt{4\pi k_B T}} \exp\left[-\frac{E_A}{k_B T} \right] \tag{7.1}$$

where $\hat{H}_{SO}$ is the spin-orbit coupling, λ is the reorganization energy and E_A is the activation energy. The latter is given by [80]

$$E_A = \frac{(\Delta E_{ST} + \lambda)^2}{4\lambda} \tag{7.2}$$

with ΔE_{ST} denoting the adiabatic singlet-triplet gap. The aim of this project is to rationalize the relation between molecular design and photophysical properties, more specifically k_{rISC}, by a quantum chemical modeling approach in order to enable rational design. As is clear from eq. 7.1 and 7.2, the key parameters to optimize in terms of molecular design are ΔE_{ST}, λ, and the $\hat{H}_{SO}$ to guarantee a high k_{rISC}. Often times, minimization of ΔE_{ST} and maximization of $\hat{H}_{SO}$ are attempted, e.g. by spatially separating HOMO and LUMO orbitals or by including heavy elements, however, it is often times not possible to achieve all design targets at once. Here, the k_{rISC} are computed on the basis of a ΔSCF approach so as to ascertain the efficacy of the molecular design on improving the k_{rISC} rates.

7.1 Computational approach

The optimally tuned range-separated hybrid functional OT-ωB97M-V [135] and the def2-SVP [136] basis set were used as OT-ωB97M-V has shown outstanding performance and accuracy in combination with ΔSCF to calculate the ΔE_{ST} for TADF emitters as shown by Froitzheim et al. [96]. Optimally tuning the range separation parameter reduces the self-interaction error and leads to improved description of Charge-Transfer excited states. The ground state structures for the tuning procedure were generated by geometry optimization in the gas phase using ωB97M-V/def2-SVP with the standard range-separation parameter of 0.3. The optimal tuning procedure was then based on minimizing the expression [137]

$$J(\omega) = \sum_{i=0}^{1} [\epsilon_{HOMO}(N+i) + IP(N+1)]^2 \tag{7.3}$$

where N denotes the number of electrons of the neutral system and IP denotes the vertical ionization potential. The optimal range-separation parameters are summarized in Tab. 7.1. The optimal tuning was performed in the gas phase to obtain general purpose range separated parameters that can be used for different solvents.

Table 7.1: Range separation parameters for OT-ωB97M-V.

	Range separation parameter
PhPIm-Cz	0.180
PhPIm-Ph-Cz	0.170
PhPIm-SpAcFl	0.161
PhPIm-Ph-SpAcFl	0.157

Since ΔSCF requires knowledge of the involved excited states and their orbital occupation scheme, the vertical excitations of the emitters were computed with TDA-DFT. The TDA-DFT calculations yield the orbital occupation schemes for the following ΔSCF calculations. For the subsequent procudure, the two lowest-lying Singlet and Triplet excited states accessible via ΔSCF (i.e. consisting of one dominant orbital transition) and their corresponding orbital occupation schemes as obtained from

TDA-DFT were chosen, and the scheme by Aizawa et al. was followed for the calculation of k$_{rISC}$ [80]. At first, the vertical excitations (absorption) were computed, followed by the geometric relaxation into their respective minima. Here, only the lowest-lying excited state was relaxed. Subsequently, ΔE_{ST}, λ and $\hat{H}_{SO}$ were computed to obtain k_{rISC}. The adiabatic ΔE_{ST} corresponds to the energy difference between the S$_1$ and T$_1$ states. λ was computed as the energy difference between the T$_1$ electronic energies at the equilibrium T$_1$ and S$_1$ geometries. The $\hat{H}_{SO}$ have been calculated using the Breit–Pauli spin–orbit Hamiltonian. The fluorescence oscillator strength was obtained from another TDA-DFT calculation on the ΔSCF optimized S$_1$ structure. The emission wavelength was obtained as the energy difference between the ΔSCF S$_1$ structure and the ground state S$_0$ structure. All calculations assumed PMMA (ϵ_0=3.3, n=1.49) as dielectric medium and all minimum geometries were confirmed by frequency calculations (no imaginary frequencies found).

7.2 Excited state characterization and photophysical properties

Tab. 7.2 summarizes the results of the TDA-DFT calculations, while Fig. 7.2 shows the natural transition orbitals (NTOs). In the case of **PhPLm-SpAcFl**, the S$_1$ and T$_1$ states are comprised of a single HOMO-LUMO transition, whereas in the case of **PhPLm-Ph-SpAcFl**, the S$_1$ and T$_1$ states are only described by 60-74% by a single orbital transition. Similarly, in **PhPLm-Ph-Cz** and **PhPLm-Cz** more than one configuration contributes to the S$_1$ and T$_1$ states, however a dominant transition can be identified. In all cases, the most dominant configuration (highest contribution to the CI expansion) was chosen for the ΔSCF calculations. The charge transfer character was assigned based on visualizing the NTOs.

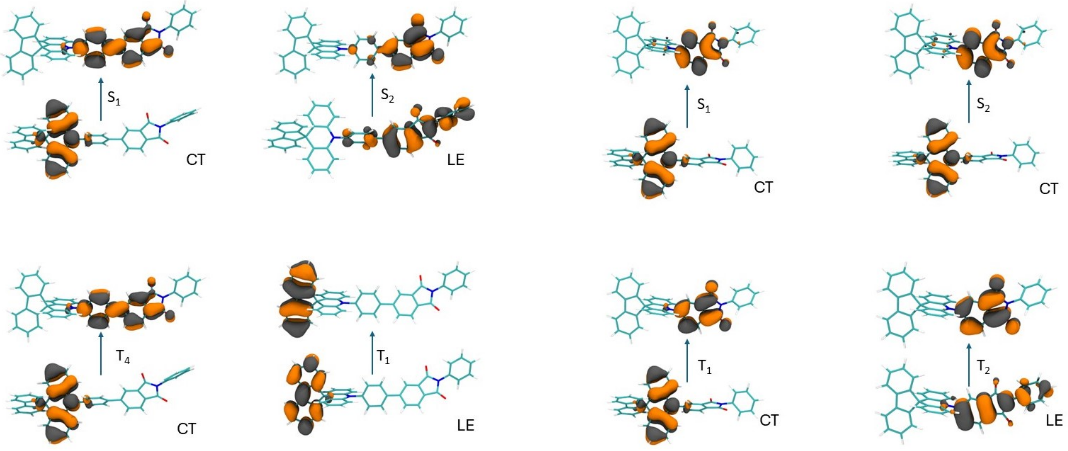

(a) **PhPIm-Ph-SpAcFl**

(b) **PhPIm-SpAcFl**

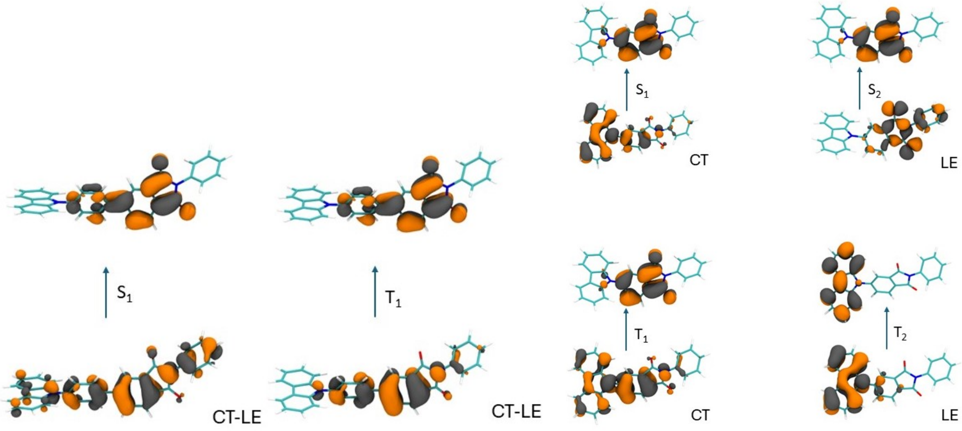

(c) **PhPIm-Ph-Cz**

(d) **PhPIm-Cz**

Figure 7.2: Natural transition orbitals of a) **PhPIm-Ph-SpAcFl** b) **PhPIm-SpAcFl** c) **PhPIm-Ph-Cz** d) **PhPIm-Cz** as obtained from TDA-DFT calculations.

Table 7.2: Photophysical properties from TDA-DFT calculations.

	State	Energy/eV	Assignment	f	CI contribution (%)
PhPIm-Ph-SpAcFl	S_1	3.711	^{1}CT	0.00054	H→L (60) H→L+1 (15) H→L+4 (20)
	S_2	3.940	^{1}LE	0.10141	H-3→L (87)
	T_1	3.300	^{3}LE	-	H-3→L (74)
	T_4	3.706	^{3}CT	-	H→L (57) H→L+1 (15) H→L+4 (19)
PhPIm-SpAcFl	S_1	3.127	^{1}CT	0.00012	H→L (94)
	S_3	4.034	^{1}LE	0.00206	H-3 →L (82)
	T_1	3.132	^{3}CT	-	H→L (93)
	T_2	3.536	^{3}LE	-	H-3→L (58) H-9→L (12) H-10→L (10)
PhPIm-Ph-Cz	S_1	3.919	CT/LE	0.34173	H→L (29) H-2→L (56)
	T_1	3.289	CT/LE	-	H-2→L (46)
PhPIm-Cz	S_1	3.677	^{1}CT	0.17781	H→L (86)
	S_2	4.158	^{1}LE	0.00172	H-5→L (24) H-2→L (25) H-6→L (30)
	T_1	3.254	^{3}CT	-	H→L (61) H-5→L (14)
	T_2	3.684	^{3}LE	-	H→L+2 (89)

Fig. 7.3 shows the vertical and adiabatic excitation energies as well as HOMO and LUMO energy levels and orbital visualization from the ΔSCF calculations. Judging from the frontier orbital visualizations, orbital separation was achieved in all cases due to the orthogonal donor-acceptor design. In all cases, the locally excited states show higher vertical excitation energies than the charge-transfer excited states. In the case of **PhPIm-Ph-SpAcFl**, a comparatively low locally excited T_2 is found. For **PhPIm-Ph-SpAcFl** and **PhPIm-SpAcFl** a much smaller ΔE_{ST} is found compared to the other two compounds. The strong charge transfer character in **PhPIm-Ph-SpAcFl** and **PhPIm-SpAcFl** is also reflected in the large dipole moments of the excited states, as shown in Tab. 7.3.

Tab. 7.4 summarizes the main results of the investigation. **PhPIm-Ph-SpAcFl** and **PhPIm-SpAcFl** show much higher k_{rISC} than **PhPIm-Ph-Cz** and **PhPIm-Cz**. This can be explained by the much smaller ΔE_{ST} due to the orbital separation combined with the orthogonal position of the donor unit leading to low orbital interaction. The relatively small λ due to the rigidity of the compounds further increases k_{rISC}. **PhPIm-Ph-Cz** and **PhPIm-Cz** show a much larger ΔE_{ST} and λ, leading to a smaller k_{rISC}. $\hat{H}_{SO}$ is similarly small in all cases. Notably, the oscillator strength is also very low in all cases due to the coupling between charge transfer states and a nonpolar ground state, reducing the emission

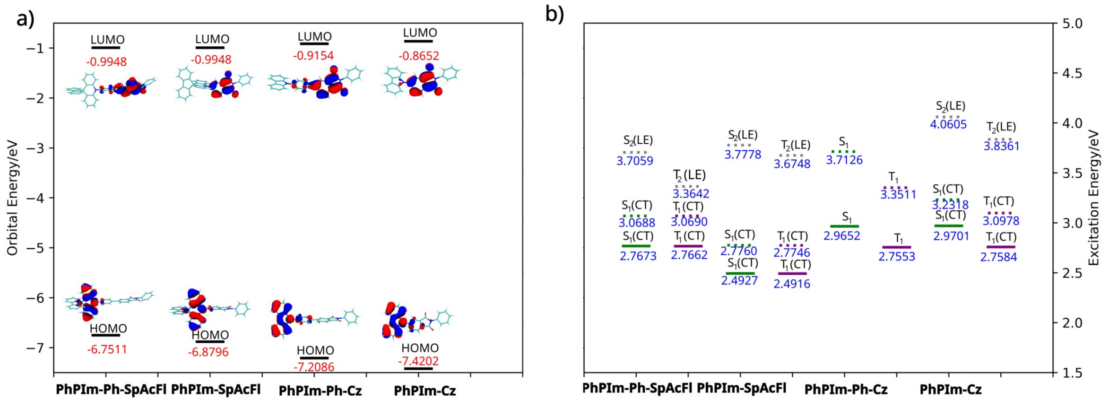

Figure 7.3: a) Frontier molecular orbitals and b) vertical (dashed lines) and adiabatic (solid lines) excitation energies as obtained from ΔSCF. Singlet states are given by green lines while triplet states are given by purple lines. The second excited states are given by grey lines.

Table 7.3: Dipole moments from ΔSCF calculations for the S_1 and T_1 states as well as the ground state (GS).

	D(GS)/Debye	D(S_1)/Debye	D(T_1)/Debye
PhPIm-Ph-SpAcFl	1.74	39.92	36.64
PhPIm-SpAcFl	1.58	24.26	24.19
PhPIm-Ph-Cz	1.69	8.37	11.87
PhPIm-Cz	1.63	20.51	13.91

efficiency.

Comparison with the experimental data (see Tab. 7.5) shows good qualitative agreement. Smaller ΔE_{ST} values are found for **PhPIm-Ph-SpAcFl** and **PhPIm-SpAcFl**, leading to an increased k_{rISC} when compared to **PhPIm-Ph-Cz** and **PhPIm-Cz**. The experimental emission wavelengths are reproduced very well. The theoretical k_{rISC} are overestimated in the case of **PhPIm-Ph-SpAcFl** and **PhPIm-SpAcFl** which might be explained by the smaller theoretical ΔE_{ST}.

Temperature-dependent measurements of the prompt and delayed fluoresence of the compounds by Christopher Wallerius showed the presence of thermally activated delayed fluorescence in **PhPIm-Cz**, **PhPIm-SpAcFl** and **PhPIm-Ph-SpAcFl**, while **PhPIm-Ph-Cz** exhibits mainly prompt fluorescence, consistent with the low k_{rISC}. In the case of **PhPIm-SpAcFl**, rapid onset of the delayed fluorescence (6-10 μs) is observed as can be expected for the nearly degenerate S_1 and T_1 states in a three-level system. In **PhPIm-Ph-SpAcFl**, slower onset (85 μs) of the delayed fluorescence is observed, which can be explained by the presence of a lower-lying locally excited T_2 state, introducing an additional ^{3}CT-^{3}LE-^{1}CT pathway. As such, the TADF process in **PhPIm-Ph-SpAcFl** is best described by a four-level system. Concerning the quantum yields, **PhPIm-Ph-Cz** and **PhPIm-Cz** show lower yields compared to **PhPIm-Ph-SpAcFl** and **PhPIm-SpAcFl**, which can be expected due to the lower k_{rISC}. The lower quantum yield in **PhPIm-SpAcFl** compared to **PhPIm-Ph-SpAcFl** could result from the lower oscillator strength, slowing the emission rate and allowing e.g. for more triplet-triplet annihilation.

Table 7.4: Photophysical data from ΔSCF and TDA-DFT calculations.

	ΔE_{ST}^{theo}/eV	$\hat{H}_{SO}$/eV	λ/eV	Em.^{theo}/eV	f($S_1 \rightarrow S_0$)	k_{rISC}^{theo}/s^{-1}
PhPIm-Ph-SpAcFl	$1.15 \cdot 10^{-3}$	$1.45 \cdot 10^{-5}$	$1.66 \cdot 10^{-3}$	2.48	$6.97 \cdot 10^{-4}$	$8.36 \cdot 10^{7}$
PhPIm-SpAcFl	$1.05 \cdot 10^{-3}$	$1.27 \cdot 10^{-5}$	$1.06 \cdot 10^{-4}$	2.21	$1.41 \cdot 10^{-4}$	$2.33 \cdot 10^{8}$
PhPIm-Ph-Cz	$2.10 \cdot 10^{-1}$	$1.64 \cdot 10^{-5}$	$1.69 \cdot 10^{-1}$	2.19	$9.21 \cdot 10^{-3}$	$2.96 \cdot 10^{3}$
PhPIm-Cz	$2.12 \cdot 10^{-1}$	$4.62 \cdot 10^{-5}$	$6.82 \cdot 10^{-2}$	2.70	$1.09 \cdot 10^{-1}$	$2.05 \cdot 10^{3}$

Table 7.5: Experimental photophysical data from Christopher Wallerius. Singlet–triplet energy gaps ΔE_{ST}^{exp} were obtained from the TRES fluorescence onset and phosphorescence spectra recorded at 77 K or 4 K. Em.^{exp} were obtained as photoluminescence maxima at 300 K from steady-state spectra using an excitation wavelength of 312 nm. k_{rISC}^{exp}/s^{-1} were obtained using the steady-state approximation method described by Dias et al. [138]. The absolute photoluminescence quantum yields Φ_{PL} were measured under nitrogen using an integrating sphere. They are reported as the average of at least three measurements.

	ΔE_{ST}^{exp}/eV	Em.^{exp}/eV	k_{rISC}^{exp}/s^{-1}	Φ_{PL}/%
PhPIm-Ph-SpAcFl	$1.17 \cdot 10^{-1}$	2.48	$2.76 \cdot 10^{4}$	74.0
PhPIm-SpAcFl	$0.51 \cdot 10^{-2}$	2.30	$2.20 \cdot 10^{5}$	43.0
PhPIm-Ph-Cz	$3.41 \cdot 10^{-1}$	2.65	$< 1.0 \cdot 10^{3}$	42.0
PhPIm-Cz	$1.40 \cdot 10^{-1}$	2.58	$1.09 \cdot 10^{4}$	69.0

7.3 Conclusion

In this investigation, TDA-DFT and ΔSCF have been used successfully in combination to calculate the photophysical properties and k_{rISC} of a library of emitter molecules in order to rationalize the impact of molecular design on TADF performance. Using donor-acceptor molecular scaffolds leads to orbital separation as expected, which is increased by inserting a phenyl bridging unit. The ΔE_{ST} however seems to be more influenced by the structure of the donor unit. The compounds with a spiro[acridine-9,9'-fluorene] donor show much reduced ΔE_{ST} and λ, leading to higher k_{rISC} compared to the compounds bearing a carbazole donor moiety. This can be explained by the orthogonality of the orbitals comprising the S_1 and T_1 states due to the molecular geometry. The higher rigidity of the spiro[acridine-9,9'-fluorene] substituents also lowers the λ, leading to a higher k_{rISC}. Taking into account the experimental data, different emission pathways were found for the compounds. While for **PhPIm-Cz** and **PhPIm-SpAcFl**, a three-level system can be assumed, **PhPIm-Ph-SpAcFl** can be more accurately be described as a four-level system due to the presence of a low-lying T_2 state. In order to further increase the performance of the promising spiro[acridine-9,9'-fluorene] substituted emitter compounds, further substitution with electroactive moieties could be attempted. The good agreement between the experimental and theoretical data validates the computational approach.

CHAPTER 8

Conclusion and outlook

Organic functional materials are a diverse group of compounds that are used in various applications such as organic light-emitting diodes (OLED), organic solar cells (OSC), organic field effect transistors (OFET) or organic batteries. As such, research efforts into organic functional materials constitute a broad and complex field spanning multiple disciplines and research aspects like synthesis, device fabrication, theoretical modeling, or theoretical method development.

This thesis presents the results of a multi-faceted research project into organic functional materials, covering several of the abovementioned aspects. Multiscale modeling was used to investigate both hole and ion transport phenomena in **TPA**-based materials. As a highly important aspect of research into not only charge transport but also general quantum chemistry, a translation of the constrained DFT methodology in the framework of constrained xTB was implemented aiming at robust and accurate access to charge transport properties. Finally, the complex photophysical properties of TADF emitters were investigated.

The charge transport in **TPA** derivatives was generally modeled in a bottom-up multiscale fashion as hopping transport using kMC based on Marcus theory, involving multiple levels of theory for the calculation of the charge transport parameters and the generation of bulk (polymer) morphologies. Ion transport was modeled directly via MD simulations. The coupled electronic and ionic transport in **TPA** polymers was investigated employing a novel approach encompassing both static as well as dynamic disorder.

In the **first investigation**, the charge transport in a library of **TPA** derivatives of increasing structural complexity was investigated. The goal was to understand the impact of structural complexity on the charge transport from the molecular level up to the bulk level. In order to probe the effect of structural (dis)order, the charge transport was simulated for single crystalline as well as the amorphous morphologies, representing the limiting cases of perfect order and disorder.

Unsurprisingly, a strong relation between the molecular structure and the bulk morphology was found. Smaller, spherical compounds tend to pack more densely in the crystalline phase, however the more elongated derivatives afford shorter center-of-mass distances in the amorphous phase. Very sterically demanding compounds generally present the largest center-of-mass distances in the crystalline as well as amorphous phases.

The hole reorganization energy showed a complex dependency on the molecular structure. While the small and structurally simple **TPA** showed a relatively low reorganization energy due to the localized nature of the monocationic state, the larger, more complex compounds afforded a very high reorganization energy in the case of a delocalized monocationic state, hindering charge transport. The dihedral relaxation required for full delocalization is however rather improbable in the bulk phase, making a localization of the positive charge over both nitrogen centers less likely. Employing CDFT, a realistic value for the hole reorganization energy based on localizing the charge over one **TPA** center was obtained, mimicking bulk phase effects.

The site energies and the electronic coupling distributions showed the expected behaviour due to morphological order, being rather discrete in the crystalline phases and continuous in the amorphous phase. Further broadening of the site energy difference distributions in the amorphous phase was found for **FTPD** and ***spiro*-OMeTAD** most likely due to the methoxy substituents, increasing the polarization contribution to the static disorder. **Electrostatic disorder effects** on the site energies were considered by way of induced dipoles.

In the crystalline phase, for **TPD** and ***spiro*-OMeTAD**, a strong **anisotropy** of the charge transport was found, which was related to the anisotropic electronic coupling strengths in the single crystalline phase.

Finally, the simulated hole mobilities were found to be in excellent agreement with the experimental data. In a single crystalline morphology, the charge transport is dominated by the electronic coupling and the reorganization energy, while in the amorphous phase, site energy differences and the reorganization energy are the dominant factors. In terms of design rules, the reorganization energy should be minimized by using more rigid, localized compounds. Electronic couplings can be enhanced by increased π - π stacking, while non-polar compounds could show reduced electrostatic disorder. Engineering the molecular structure to influence bulk structural features is however a highly complex task, since even small changes in the molecular structure can drastically change the bulk phases, as already visible in the radial distribution functions of the crystalline phase of the relatively similar **TPD** and **FTPD**.

The **second investigation** was focused around polymerized **TPA**s for OMIEC applications, specifically aiming at closing the knowledge gap on the **coupled electronic and ionic transport**. Since the polymer morphology is central to charge- and ion transport processes, a realistic morphology is required. Because experimental data is not available due to the insolubility of the investigated systems, the polymerization reaction was modeled heuristically via molecular dynamics to obtain realistic polymer systems.

The analysis of the bulk structures showed characteristic differences in the pore radii of linear and cross-linked polymer systems, the latter affording larger pore radii. Generally, the average pore radii are smaller than the radius of the PF_6^--ion investigated in this work, suggesting slow ion diffusion. The average nitrogen-oxetane distance increases upon polymerization due to the more limited side-chain flexibility in the polymer phase.

As anticipated from the small pore radii, relatively **slow PF_6^--ion diffusion** was found in all polymerized systems. In the timescales investigated in this work (100 ns), the ion diffusion stayed in the subdiffusive regime, being much slower than the typical timescales of charge transport (ps-timescale). As expected, the cross-linked system (**xTPA**) showed slower ion diffusion than the linear polymerized system (**pTPA**), indicating the segmental mobility of the polymer system as very important to the ion diffusion.

The site energy landscape in the pristine and doped systems (0% to 15% PF_6^- ion content) showed very **strong static and dynamic disorder**. While the strong static disorder (σ-values of site energy difference distributions between 0.37 eV and 1.67 eV) is normally indicative of deep traps and negligible charge transport, the fast dynamics, as characterized by strong site energy fluctuations can limit trap lifetime and enable charge transport.

Based on the strongly fluctuating site energies, **time-dependent Marcus rates** were found. Therefore, standard kMC simulations with a fixed set of rates are do no longer make sense in the investigated systems, and a new approach is necessary. By numerically integrating the time-dependent Marcus rates over a timeframe of 100 ps, the population decay due to charge transfer events is obtained for each site in the bulk system. Defining the half-time of population decay as the **effective Marcus residence time**, a new descriptor which encompasses the dynamic disorder effects on the charge transport is obtained. The effective Marcus residence times can be used to characterize the coupled charge- and ion transport in OMIEC systems. While charge transport networks are formed in all investigated systems, they are less dense in the higher doped systems, showing that even though trap states can be overcome, it takes a significantly longer time. The effective Marcus residence times can be used to obtain lifetime distributions. Comparing such effective lifetime distributions with static lifetime distributions, the effective lifetimes are shifted to shorter values, again indicating trap removal as a consequence of dynamic disorder.

Considering the results of the first investigation in combination with the results of the second investigation, multiple conclusions can be drawn specifically for polymerized and cross-linked **TPA**s. The first investigation into non-polymerized materials suggested a fine balance between molecular and bulk structural charge transport parameters, meaning that compounds can be meaningfully chosen and tailored for specific applications. While this is true for applications using the monomeric materials, the investigation into the charge transport in the second investigation showed that the charge transport in polymerized or cross-linked bulk structures is completely dominated by the dynamic disorder even in pristine, undoped systems. The highly flexible oxetane-bearing alkyl linker units, even in the non-polymerized state, induce high static and dynamic disorder which dominates the charge transport, leading to the complex hole transfer mechanisms described earlier. Therefore, the choice of the **TPA**-core for the polymer systems can be made irrespective of charge transport efficiency considerations, allowing focus on e.g. energy-level alignment in OSC, e.g. specific capacity in battery materials or general processability.

The **third project** in this thesis was the implementation of a charge constraining methodology in the framework of GFN2-xTB. CxTB was implemented successfully and tested on literature known compounds. The purpose of this implementation is to enable efficient yet accurate calculations with charge or spin constraints which is useful in various scenarios, e.g. for the calculation of charge transport parameters or the investigation of charge transfer excited states. As one test case, the experimental bond length alternation pattern of two merocyanine compounds was reproduced with high accuracy at much reduced computational cost compared to CDFT calculations. In another example, CxTB was able to successfully describe the geometric asymmetry in the tetrathiafulvene-diquinone radical anion which is a mixed-valence compound showing charge localization on one of its identical quinone moieties.

The **fourth part** of this thesis is concerned with an investigation into the excited state characteristics of novel donor-acceptor emitter compounds revealed a strong influence of the spiro[acridine-9,9'-fluorene] donor group on the photophysical properties by lowering the adiabatic singlet triplet gap and the reorganization energy when compared to carbazole substituted compounds. This was found by employing a combined TDA-DFT and ΔSCF approach, which is promising for further investigations.

As an **outlook**, multiple lines of research are possible. With regard to the investigation in the **TPA**-based materials, using longer trajectories would allow for the evaluation of the effective Marcus residence times on longer timeframes, perhaps enabling the computation of a charge mobility via dynamic Monte Carlo. Similarly, the PF_6^- ion mobility can be obtained using longer MD trajectories for the computation of the mean square displacement of the ions. Longer timeframes were not investigated in this thesis due to the high computational cost. The **TPA**-based polymer systems can fulfil a special role in OMIEC research since it is possible to compute Marcus rates for them due to the localized nature of the hole in the polymer, which was especially important for the presented work. This effect can be exploited further for investigating the effect of side-chain mobility on charge- and ion transport. Different degrees of cross-linking showing varying side-chain mobility in the polymeric phase can be generated by using monomeric systems comprised of both mono- and di-functionalized molecules for the polymer generation procedure. Using such partially cross-linked systems, the effect of the cross-linking degree on the morphology and the coupled electronic and ionic transport could be ascertained. Since the cross-linking degree is an experimentally controllable variable, such an investigation could be carried out in parallel with an experimental investigation and compared.

For electrochemical applications, the swelling of the polymeric systems due to the contact with an electrolyte is a highly important factor, influencing the charge- and ion transport. In this work, only the limiting case of a dry polymer was considered, however in future work, the swelling should be investigated and taken into account. The first step into such future investigations was already outlined by the Master's Thesis of Agustín López Cabrera, which was discussed in the context of this thesis.

The CxTB implementation could be used for e.g. the evaluation of the outer reorganization energies in charge transport simulations which can have a strong influence on the charge mobility. In order to improve the implementation, an analytical gradient could be implemented for faster geometry optimizations.

The performance of the investigated donor-emitter substituted TADF emitters could be further improved by using electroactive substituents, influencing e.g. the singlet-triplet gap. Enhancement of the spin-orbit-coupling could be attempted through inclusion of heavy atoms. In terms of computer-aided design, the combined TDA-DFT and ΔSCF approach presented in this thesis could be used for screening applications for potential emitter compounds.

To conclude, it can be stated that multiscale modeling is an indispensable tool for further research into organic functional materials. The relation between molecular and bulk structure as well as functional properties such as charge- and ion mobilities remains highly complex and very challenging to predict from the molecular structure. This is even more true in cases where the dynamic properties of the system are highly relevant. Multiscale modeling has proven to be the key methodology to bridge such knowledge gaps.

CHAPTER 9

Publications and conferences

Publications:

I. R. Herzhoff, F. Negri, K. Meerholz, D. Fazzi, *J. Mater. Chem. C* **2023**, *11*, 11969-11979.

II. R. Herzhoff, L. Plein, A. Troisi, K. Meerholz, D. Fazzi, *Mater. Horiz.* **2025**, *23*, 7924-7936.

Manuscripts:

III. R. Herzhoff, S. Grimme, A. Hansen, K. Meerholz, D. Fazzi, *Unpublished Manuscript* **2025**.

Other Publications (not part of this thesis):

IV. N. Gildemeister, S. Geller, R. Herzhoff, F. Negri, K. Meerholz, D. Fazzi, *Mater. Adv.* **2024**, *5*, 8475-8489.

V. T. Lippold, J. Kosolapova, N. Flosbach, R. Herzhoff, A. Griesbeck, M. Wickleder *Chem. Commun.* **2025**, *61*, 4792-4795.

VI. T. Lippold, A. Griesbeck, R. Herzhoff, M. Wickleder, L. Straub, N. Flosbach *Photochem* **2023**, *3*, 373-389.

Conferences:

I. **CECAM Virtual Winter School** 2022, Single Figure Presentation "Modelling redox and charge transport properties in triphenylamine derivatives as potential candidates for organic battery applications"

II. **EuChemS CompChem** 2023, Thessaloniki (Greece), Poster: "Revealing the interplay between the structural complexity of triphenylamine redox derivatives and their charge transport processes via computational modeling"

III. **TIDE International Research Conference** 2024, Cologne (Germany), Poster: "Atomistic Modeling of Organic Electrodes for Electrochemical Devices"

IV. **ICSM- International Conference on Science and Technology of Synthetic Electronic Materials** 2024, Dresden (Germany), Talk: "Modeling mixed electronic and ion transport in bulk crosslinked triphenylamines"

V. **MRS Fall Meeting & Exhibit** 2025, Boston (USA), Poster: "Dynamics of Disorder in Mixed Ionic-Electronic Transport in Cross-Linked Non-Conjugated Redox Polymers"

APPENDIX A

Appendix

A.1 Supporting Information Publication I

Electronic Supplementary Material (ESI) for Journal of Materials Chemistry C.

Revealing the interplay between the structural complexity of triphenylamine redox derivatives and their charge transport processes via computational modeling

Robert Herzhoff,[a] Fabrizia Negri,[b] Klaus Meerholz,[a] Daniele Fazzi [b]

[a]Institut für Physikalische Chemie, Department für Chemie, Universität zu Köln, Greinstr. 4-6, 50939 Köln, Germany.

[b]Università di Bologna, Dipartimento di Chimica 'Giacomo Ciamician', Via F. Selmi, 2, 40126 Bologna, Italy.

Supporting Information

Table of Contents

Force field parametrization 2

Amorphous morphology simulation 4

Charged state geometric parameters 4

Electronic coupling and geometric data 8

Kinetic Monte-Carlo charge transport simulations (zero-field) in the amorphous phase 12

Charge mobilities with an applied electric field 13

Computed dielectric constants 13

Low CoM distance pair in the amorphous phase of FTPD 14

BLYP35/6-311G* hole reorganization energies 14

Electronic coupling distribution (extended) 15

Computed and experimental hole mobility 16

References 17

Force field parametrization

In this work, the OPLS-AA [1,2] force field parameters for **TPA**, **TPD**, **FTPD** and ***spiro*-OMeTAD** were refined using *ab initio* methods. The procedure is detailed for **TPA** in the following. From the structure optimized at the DFT (ωB97X-D/6-311G*) level, the equilibrium bond distances and dihedral angles were obtained, while the charges were calculated via CHELPG. The force field parameters for the three *identical and correlated* dihedral angles in **TPA** were then determined via the following procedure. One dihedral angle was scanned at the DFT (ωB97X-D/6-311G*) level while the others were allowed to relax. The same scan was repeated at the MD level with the dihedral angle parameters set to zero. Here, the two dihedral angles that were not being scanned were fixed at their QM determined minimum position. The resulting energies of the DFT and MD scan were subtracted from each other, and the resulting potential profile was fitted with the Ryckaert-Bellemans function

$$V_{rb}(\varphi) = \sum_{n=0}^{5} V_n cos^n \varphi \qquad (1)$$

where φ is the dihedral angle, yielding the desired dihedral angle parameters V_n (see Table S1). The procedure was repeated analogously for **TPD**, **FTPD** and ***spiro*-OMeTAD**. In Figure S1, the defined atom types for **TPA**, **TPD** and **FTPD** are shown. The atom types and angles for ***spiro*-OMeTAD** largely correspond to those of **FTPD**, which is why only the central spiro-bifluorene core is shown.

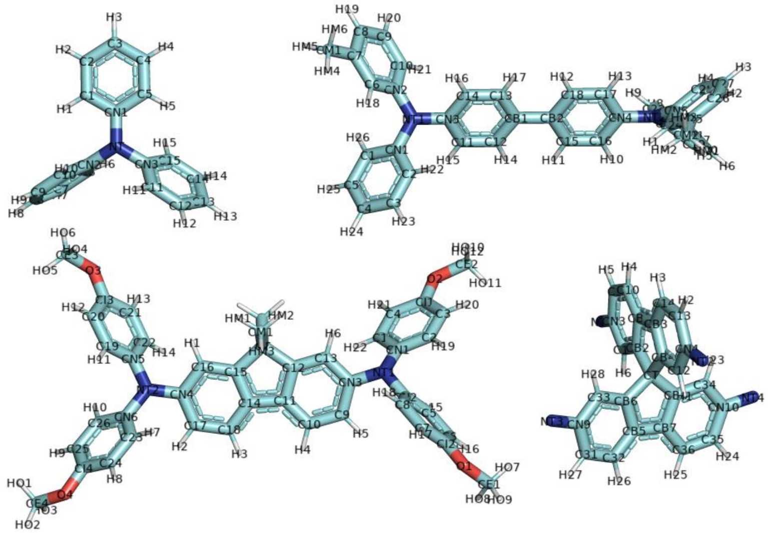

Figure S1: Atom types for **TPA**, **TPD**, and **FTPD**. The atom types and angles for **spiro-OMeTAD** mostly correspond to those of **FTPD**, which is why only the central spiro-bifluorene core is shown.

In Figure S2 the dihedral angle profiles of **TPA**, **TPD** and **FTPD** at the DFT, initial and refined MD level are shown together with the dihedral angle distribution in the amorphous bulk phases. For ***spiro*-OMeTAD**, the dihedral parameters of **FTPD** were used directly, and only the dihedral angle distribution is shown. The Ryckaert-Bellemans parameters of the dihedral angles are given in Table S1.

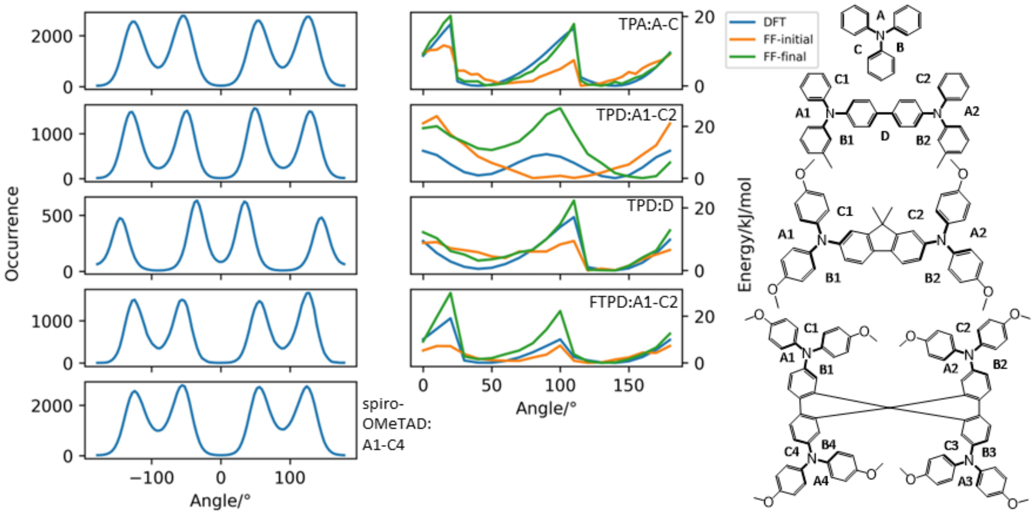

Figure S2: Left panels: dihedral angle distribution in the amorphous bulk phase. Right panels: dihedral angle potential energy profiles at the DFT (ωB97X-D/6-311G*) level and from the initial and final force field. Dihedral angles are indicated in the chemical structures on the right side.

Table S1: Ryckaert-Bellemans parameters $(V_n, \frac{kJ}{mol})$ for the dihedral angles in **TPA**, **TPD** and **FTPD**. For ***spiro*-OMeTAD**, the **FTPD** values were used. **A-C** refers to the dihedral angles between atoms CN-NT-CN-C, **D** refers to the dihedral angle between atoms C-CB-CB-C and **E** refers to the dihedral angle between the atoms C-CI-O-CE.

	V_0	V_1	V_2	V_3	V_4	V_5
TPA:A-C	4.271	0.000	-8.499	0.000	4.469	0.000
TPD:A1-C2	0.152	-14.59	-18.08	23.43	14.22	-11.62
TPD:D	8.589	0.463	-32.30	-11.63	13.86	8.602
FTPD:A1-C2	1.850	-0.350	-10.27	-0.837	9.705	1.867
FTPD:E	4.405	1.665	1.995	-7.289	-10.85	4.864

Amorphous morphology simulation

With the refined force field parameters at hand, amorphous morphologies were simulated with a thermal annealing approach, similar to reports in literature. [3] First, 125 molecules were placed randomly in a box by PACKMOL. [4] Subsequently, an energy minimization was performed using a steepest descent algorithm. The system was then equilibrated in the NVT ensemble at 700 K for 1 ns, followed by NVT equilibration at 300 K for 1 ns. Lastly, NPT equilibration at 300 K was performed until convergence of the density. The system was then extended in a 2x2x2 supercell containing 1000 molecules, and the previous procedure was repeated, extending the last NPT run until the density converged. All molecular dynamics simulations were performed in periodic boundary conditions using the GROMACS [5–9] program package. For temperature control, velocity rescaling with an additional stochastic term was applied (τ_T = 0.2 ps), while for the pressure, isotropic coupling with a Berendsen barostat was applied (p_{ref} = 1.01325 bar, τ_T = 0.5 ps, compressibility = $4.5 \cdot 10^{-5}$ bar^{-1}). A 1 fs timestep was used in all simulations as well as a 10 Å cut-off radius for the van-der-Waals and Coulombic interactions. The PME method with a 0.12 nm Fourier spacing was used for electrostatic interactions.

Charged state geometric parameters

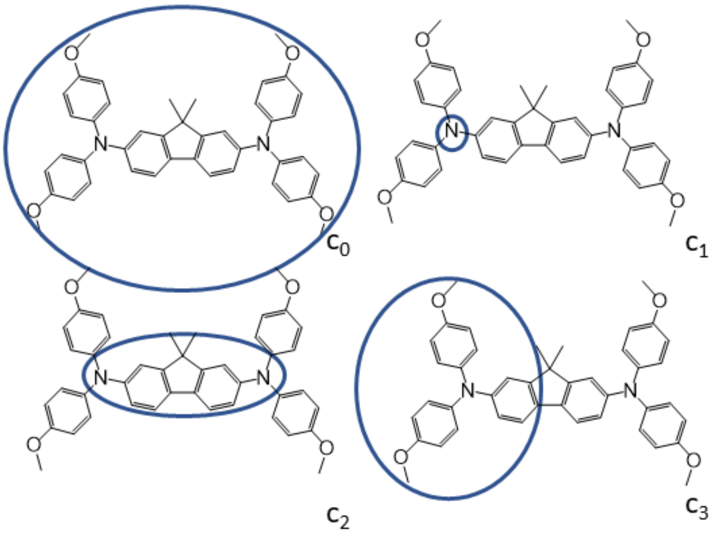

Figure S3: Charge constrain schemes for **FTPD**. The circles indicate the area where the positive charge is localized.

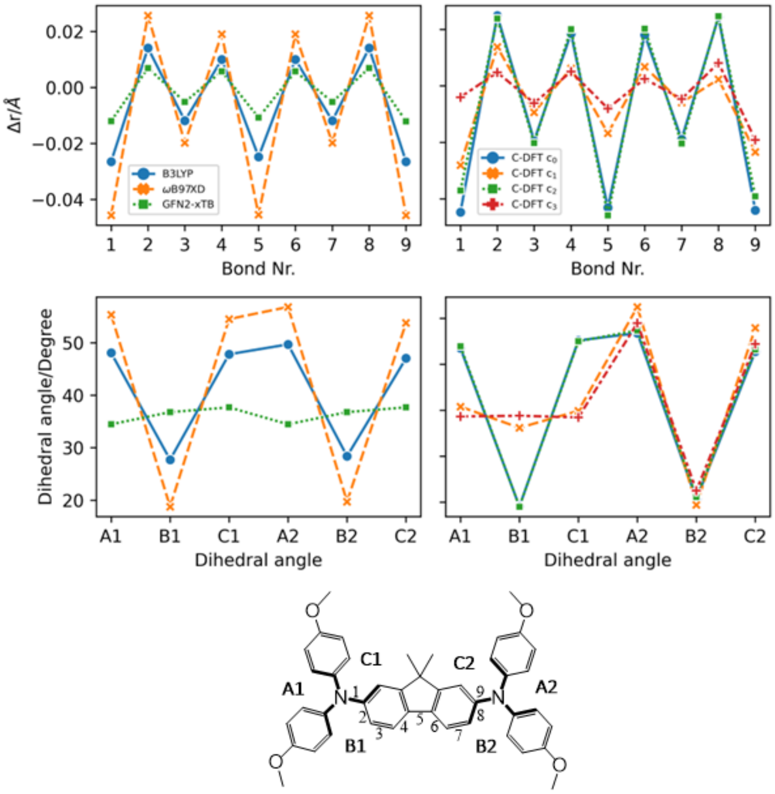

Figure S4: Geometric parameters of **FTPD** in the charged state (+1) by considering different methods (DFT, C-DFT, GFN2-xTB), DFT functionals and various charge constraint (C-DFT) schemes. The two panels on the top show the bond length difference ($\Delta r = r_{charged} - r_{neutral}$) patterns by moving from the neutral to the charged state. Top left panel: DFT (B3LYP, ωB97X-D) and GFN2-xTB data. Top right panel: C-DFT data with different schemes. The two panels on the bottom show the dihedral angles in the charged state. Bottom left panel: DFT (B3LYP, ωB97X-D) and GFN2-xTB data. Bottom right panel: C-DFT data with different charge constraint schemes.

Localizing the charge on one half of the molecule has different effects on **FTPD** when compared with **TPD** (Figure 4). The rigid bridge of **FTPD** leads to a larger reorganization energy in constrain scheme c_3 because the entire bridge reacts to the charged state reorganization instead of just one phenyl unit. On the other hand, the discrepancy between the methods is not as large for **FTPD** because the rigid fluorene unit cannot assume a staggered conformation preventing the delocalization like **TPD**. The bond length alternation patterns also show the impact of the charge delocalization mainly in the bond length of bond 5, which corresponds to the central bond of the bridging unit in both **TPD** and **FTPD**. This bond is significantly shortened if the charge is allowed to delocalize over the central bridging unit due to π-conjugation.

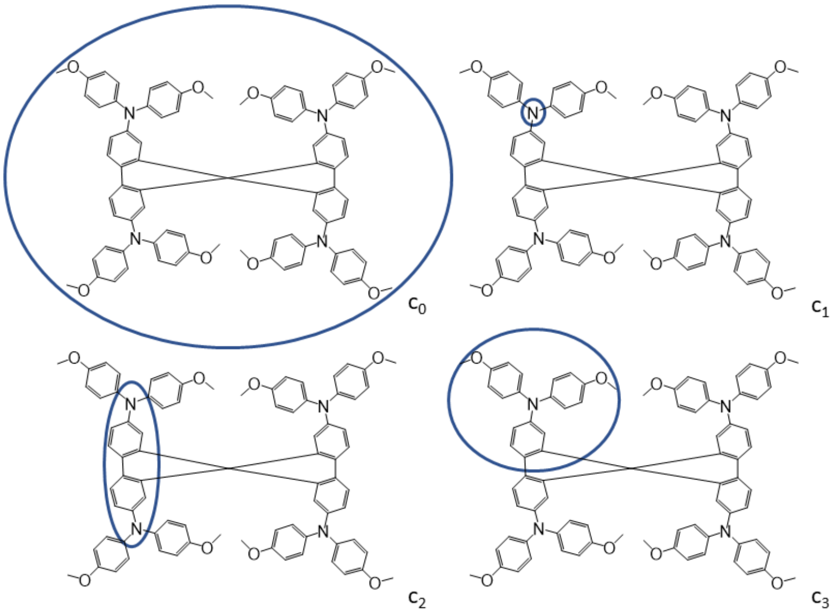

Figure S5: Charge constrain schemes for ***spiro*-OMeTAD**. The circles indicate the area where the positive charge is localized.

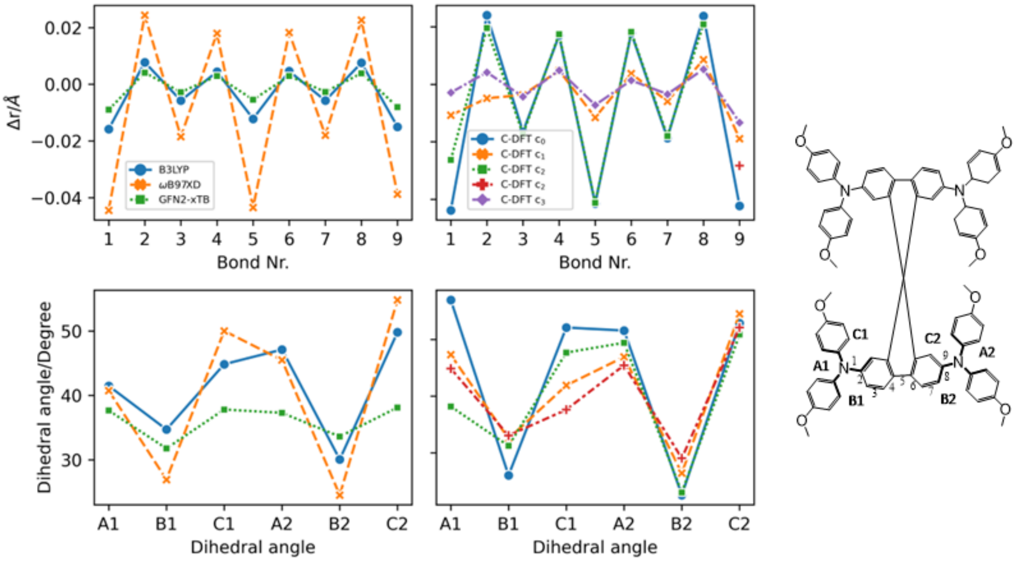

Figure S6: Geometric parameters of ***spiro*-OMeTAD** in the charged state (+1) by considering different methods (DFT, C-DFT, GFN2-xTB), DFT functionals and various charge constraint (C-DFT) schemes. The two panels on the top show the bond length difference ($\Delta r = r_{charged} - r_{neutral}$) patterns by moving from the neutral to the charged state. Top left panel: DFT (B3LYP vs. ωB97X-D) versus GFN2-xTB data. Top right panel: C-DFT data with different schemes. The two panels on the bottom show the dihedral angles in the charged state. Bottom left panel: DFT (B3LYP vs. ωB97X-D) versus GFN2-xTB data. Bottom right panel: C-DFT data with different charge constraint schemes.

For ***spiro*-OMeTAD**, the observations with regard to the bond length alternation patterns and the changes in the dihedral angles are largely consistent with **FTPD**, even though the asymmetric changes in dihedral angles due to charge localization are less pronounced due to the steric demands of the overall bulkier structure.

Electronic coupling and geometric data

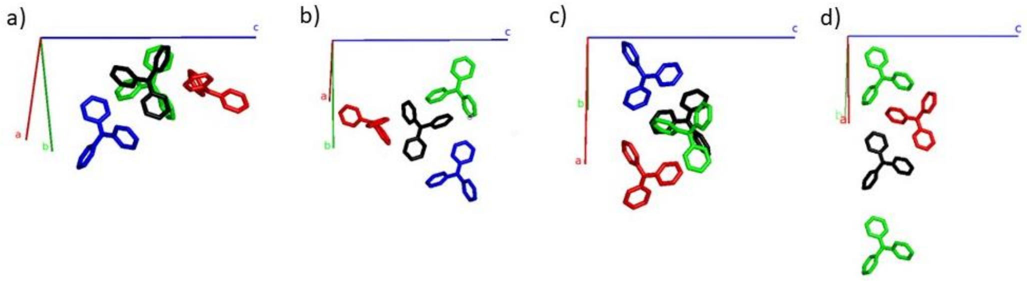

Figure S7: Selected pairs with large electronic coupling for the four unique monomers of the **TPA** unit cell with the crystallographic axes. The four unique centers are shown in black and the neighbours forming the different pairs with the black centers are shown in red, green or blue. The pair formed with the red neighbour has the highest electronic coupling, followed by the green and blue neighbour.

Table S2: Electronic coupling and geometric data for the pairs shown in **Fig. S7(a).** Pair A refers to the pair formed from the black and red monomers, pair B to the pair formed from the black and green monomers and pair C to the pair formed from the black and blue monomers.

	J_{ij}/meV	ΔCoM/Å	ΔCoM x/Å	ΔCoM y/Å	ΔCoM z/Å
A(red)	50	6.56	1.13	0.16	6.46
B(green)	37	5.49	-3.73	4.03	-0.20
C(blue)	34	7.36	5.24	2.72	-4.39

Table S3: Electronic coupling, transfer rates and geometric data for the pairs shown in **Fig. S7(b).**

	J_{ij}/meV	ΔCoM/Å	ΔCoM x/Å	ΔCoM y/Å	ΔCoM z/Å
A(red)	50	6.56	-1.13	0.16	-6.46
B(green)	40	7.15	-5.05	-2.55	4.37
C(blue)	36	7.36	2.7	5.27	4.37

Table S4: Electronic coupling, transfer rates and geometric data for the pairs shown in **Fig. S7(c).**

	J_{ij}/meV	ΔCoM/Å	ΔCoM x/Å	ΔCoM y/Å	ΔCoM z/Å
A(red)	40	7.15	5.05	2.55	-4.37
B(green)	37	5.49	3.73	-4.03	0.2
C(blue)	36	7.36	-2.7	-5.27	-4.37

Table S5: Electronic coupling and geometric data for the pairs shown in **Fig. S7(d).**

	J_{ij}/meV	ΔCoM/Å	ΔCoM x/Å	ΔCoM y/Å	ΔCoM z/Å
A(red)	34	7.36	-5.24	-2.72	4.39
B(green)	10	11.01	-7.75	-7.82	0
C(blue)	10	11.01	7.75	7.82	0

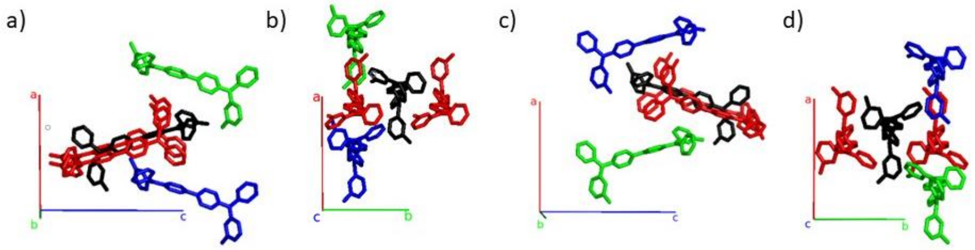

Figure S8: Selected pairs with large electronic coupling for the two unique monomers of the **TPD** unit cell with the crystallographic axes. The two unique centers are shown in black and the neighbours forming the different pairs with the black centers are shown in red, green or blue. The pair formed with the red neighbour has the highest electronic coupling, followed by the green and blue neighbour.

Table S6: Electronic coupling and geometric data for the pairs shown in **Fig. S8(a)/(b).** Pair A refers to the pair formed from the black and red monomers, pair B to the pair formed from the black and green monomers and pair C to the pair formed from the black and blue monomers.

	J_{ij}/meV	ΔCoM/Å	ΔCoM x/Å	ΔCoM y/Å	ΔCoM z/Å
A1(red)	36	6.13	-0.83	-5.51	-2.56
A2(red)	36	6.13	-0.83	5.51	-2.56
B(green)	11	11.06	7.22	-5.43	6.39
C(blue)	8	11.06	-7.22	-5.43	6.39

Table S7: Electronic coupling and geometric data for the pairs shown in **Fig. S8(c)/(d).**

	J_{ij}/meV	ΔCoM/Å	ΔCoM x/Å	ΔCoM y/Å	ΔCoM z/Å
A1(red)	35	6.12	-1.02	-5.51	2.47
A2(red)	35	6.12	-1.02	5.51	2.47
B(green)	11	11.06	-7.22	5.43	-6.39
C(blue)	8	11.06	7.22	5.43	-6.39

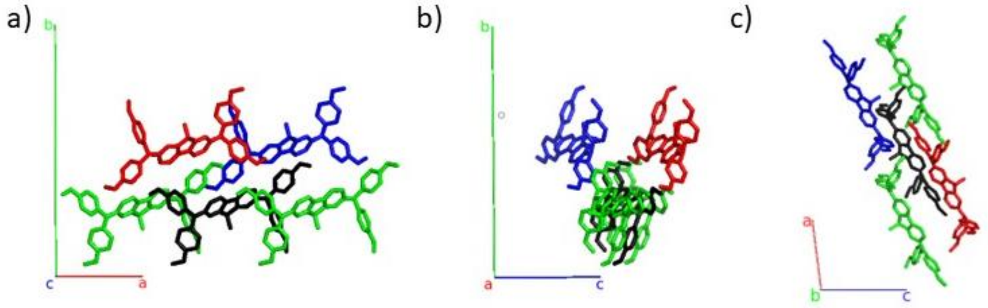

Figure S9: Selected pairs with large electronic coupling for the unique monomer of the **FTPD** unit cell with the crystallographic axes. The unique center is shown in black and the neighbours forming the different pairs with the black centers are shown in red, green or blue. The pair formed with the red neighbour has the highest electronic coupling, followed by the green and blue neighbour.

Table S8: Electronic coupling and geometric data for the pairs shown in **Fig. S9(a)/(b)/(c).**

	J_{ij}/meV	ΔCoM/Å	ΔCoM x/Å	ΔCoM y/Å	ΔCoM z/Å
A(red)	9.8	11.00	-5.25	7.77	5.75
B1(green)	9.3	9.96	-9.96	0	0
B2(green)	9.3	9.96	9.96	0	0
C(blue)	9.0	11.85	6.3	7.77	-6.34

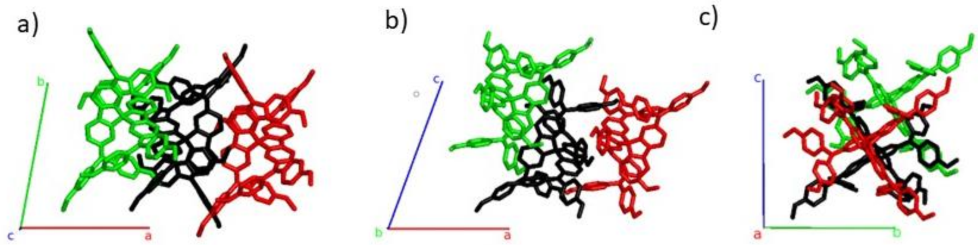

Figure S10: Selected pairs with large electronic coupling for the unique monomer of the ***spiro*-OMeTAD** unit cell with the crystallographic axes. The unique center is shown in black and the neighbours forming the different pairs with the black centers are shown in red, green or blue. The pair formed with the red neighbour has the highest electronic coupling, followed by the green neighbour.

Table S9: Electronic coupling and geometric data for the pairs shown in **Fig. S10 (a)/(b)/(c).**

	J_{ij}/meV	ΔCoM/Å	ΔCoM x/Å	ΔCoM y/Å	ΔCoM z/Å
A(red)	39	8.58	7.44	0.545	4.24
B(green)	15	7.55	-6.22	0.545	4.24

Kinetic Monte-Carlo charge transport simulations (zero-field) in the amorphous phase

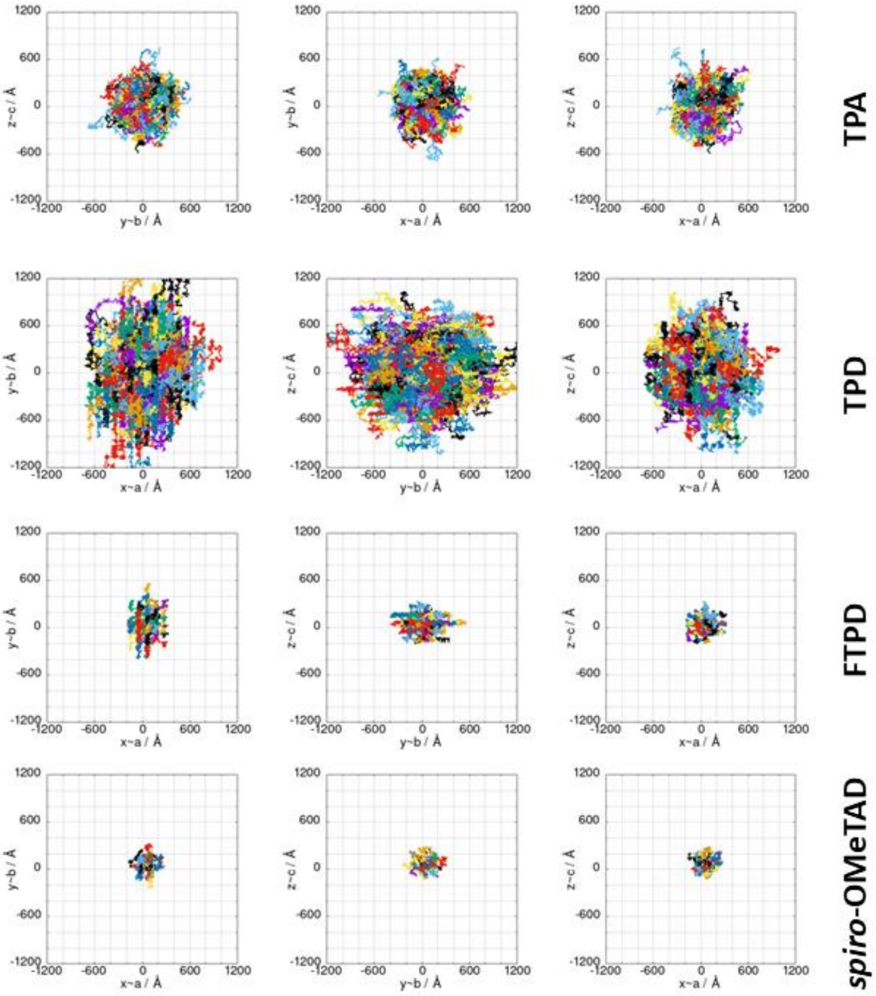

Figure S11: KMC trajectories computed in amorphous phases (zero-field) shown from different planes. The colors used in the plots only serve to discern the superimposed trajectories.

Charge mobilities with an applied electric field

Table S10: Mobilities (μ, $\frac{cm^2}{Vs}$) in the crystalline and amorphous phases in x- y- and z- directions with an electric field of $10^8\,\frac{\mathrm{V}}{\mathrm{m}}$. For these simulations, in the amorphous case, just one snapshot of the MD-simulated systems was used.

	TPA	**TPD**	**FTPD**	***spiro*-OMeTAD**
Crystalline, μ_x	$4.68 \cdot 10^{-2}$	$3.88 \cdot 10^{-3}$	$6.07 \cdot 10^{-3}$	$3.98 \cdot 10^{-2}$
Crystalline, μ_y	$4.82 \cdot 10^{-2}$	$2.97 \cdot 10^{-1}$	$2.53 \cdot 10^{-3}$	$4.04 \cdot 10^{-3}$
Crystalline, μ_z	$3.57 \cdot 10^{-2}$	$1.25 \cdot 10^{-2}$	$3.42 \cdot 10^{-4}$	$8.04 \cdot 10^{-4}$
Amorphous, μ_x	$8.61 \cdot 10^{-3}$	$5.98 \cdot 10^{-3}$	$1.48 \cdot 10^{-4}$	$4.17 \cdot 10^{-5}$
Amorphous, μ_y	$8.71 \cdot 10^{-3}$	$5.72 \cdot 10^{-3}$	$1.34 \cdot 10^{-4}$	$3.93 \cdot 10^{-5}$
Amorphous, μ_z	$7.81 \cdot 10^{-3}$	$5.70 \cdot 10^{-3}$	$8.41 \cdot 10^{-5}$	$5.08 \cdot 10^{-6}$
Experimental	$2 \cdot 10^{-2}$ [10] (single crystal)	$1 \cdot 10^{-3}$ [11] (amorphous thin film)	$4.3 \cdot 10^{-4}$ [12] (semicrystalline thin film)	$1.30 \cdot 10^{-3}$ [13] (single crystal) $1.69 \cdot 10^{-6}$ [13] (amorphous thin film)

Computed dielectric constants

The dielectric constants ε_s were computed based on the Clausius-Mosotti relation [14]

$$\varepsilon_s = 1 + \frac{12\pi\alpha\frac{N}{V}}{3 - 4\pi\alpha\frac{N}{V}} \tag{2}$$

with α being the molecular polarizability volume, N being the number of particles and V being the volume of the simulation boxes.

Table S11: Computed dielectric constants.

	TPA	TPD	FTPD	*spiro*-OMeTAD
ε_s(amorphous)	2.19	1.87	1.99	2.09
ε_s(crystal)	2.42	2.49	2.50	2.70

Low CoM distance pair in the amorphous phase of FTPD

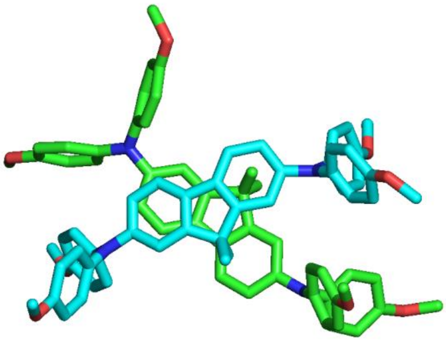

Figure S12: Pair with low CoM distance in the amorphous phase of **FTPD**, taken from the MD-production run. The crossed conformation of the long molecular axes of the pair leads to lower CoM distance values compared to the crystalline phase.

BLYP35/6-311G* hole reorganization energies

Table S12: Internal hole reorganization energy (λ_{int}, eV) calculated at the BLYP35/6-311G* level. In these calculations, imaginary frequencies were encountered which is why they were not used in further simulations, however are still reported here for reference.

	TPA	TPD	FTPD	*spiro*-OMeTAD
BLYP35	0.13	0.46	0.34	0.31

Electronic coupling distribution (extended)

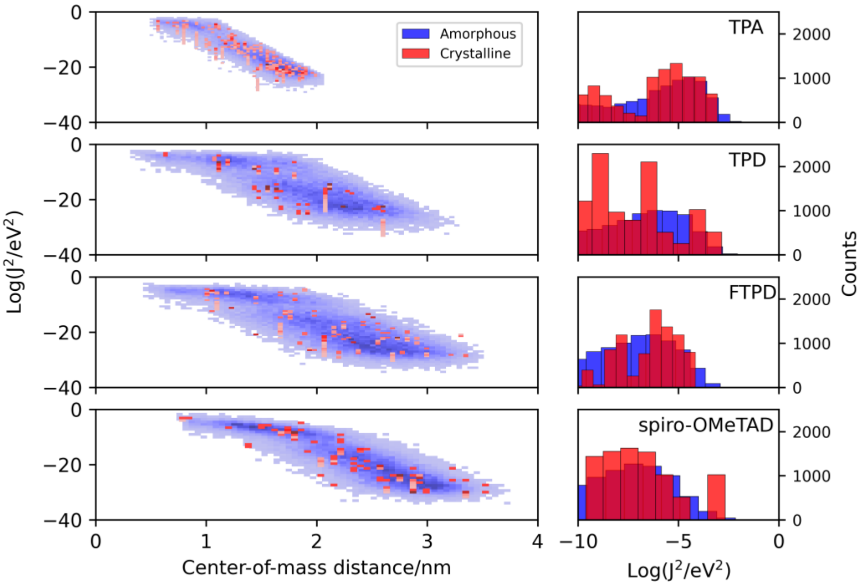

Figure S13: Coupling integral distributions (Log(J_{ij}^2/eV^2)) as calculated with the MOO approach versus center-of-mass (CoM) distance in experimental crystalline (red) and MD generated amorphous (blue) phases, left panels. The right panel shows the coupling integral histograms up to -10 Log(J^2/eV^2), i.e., up to 10^{-5} eV, for both amorphous (blue) and crystalline (red) phases.

Computed and experimental hole mobility

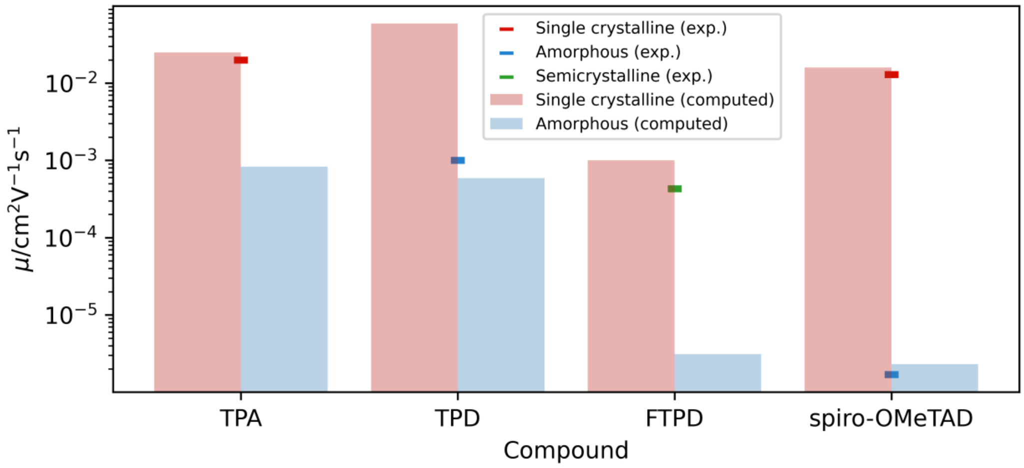

Figure S14: Computed (average) and experimental[10,11,12,13] hole mobility in the crystalline and amorphous phases.

References

1 W. L. Jorgensen, D. S. Maxwell and J. Tirado-Rives, *J. Am. Chem. Soc.*, 1996, **118**, 11225–11236.

2 G. A. Kaminski, R. A. Friesner, J. Tirado-Rives and W. L. Jorgensen, *J. Phys. Chem. B*, 2001, **105**, 6474–6487.

3 K.-H. Lin, A. Prlj, L. Yao, N. Drigo, H.-H. Cho, M. K. Nazeeruddin, K. Sivula and C. Corminboeuf, *Chem. Mater.*, 2019, **31**, 6605–6614.

4 L. Martínez, R. Andrade, E. G. Birgin and J. M. Martínez, *J. Comput. Chem.*, 2009, **30**, 2157–2164.

5 H. Berendsen, D. van der Spoel and R. van Drunen, *Comput. Phys. Commun.*, 1995, **91**, 43–56.

6 B. Hess, C. Kutzner, D. van der Spoel and E. Lindahl, *J. Chem. Theory Comput.*, 2008, **4**, 435–447.

7 E. Lindahl, B. Hess and D. van der Spoel, *J. Mol. Model.*, 2001, **7**, 306–317.

8 S. Pronk, S. Páll, R. Schulz, P. Larsson, P. Bjelkmar, R. Apostolov, M. R. Shirts, J. C. Smith, P. M. Kasson, D. van der Spoel, B. Hess and E. Lindahl, *Bioinformatics*, 2013, **29**, 845–854.

9 D. van der Spoel, E. Lindahl, B. Hess, G. Groenhof, A. E. Mark and H. J. C. Berendsen, *J. Comput. Chem.*, 2005, **26**, 1701–1718.

10 D. C. Hoesterey and G. M. Letson, *J. Chem. Phys.*, 1964, **41**, 675–679.

11 M. Stolka, J. F. Yanus and D. M. Pai, *J. Phys. Chem.*, 1984, **88**, 4707–4714.

12 L. Fang, A. Zheng, M. Ren, X. Xie and P. Wang, *ACS Appl. Mater. Interfaces*, 2019, **11**, 39001–39009.

13 D. Shi, X. Qin, Y. Li, Y. He, C. Zhong, J. Pan, H. Dong, W. Xu, T. Li, W. Hu, J.-L. Brédas and O. M. Bakr, *Sci. Adv.*, 2016, **2**, e1501491.

14 R. P. Feynman, R. B. Leighton and M. Sands, *Lectures on Physics: Commemorative Issue*, Addison Wesley, Reading, MA, 2nd edn., 1971.

A.2 Supporting Information Publication II

Dynamics of disorder in mixed ionic-electronic transport in cross-linked non-conjugated redox polymers

Robert Herzhoff[a], Laura Plein[a], Alessandro Troisi [b], Klaus Meerholz[a*], Daniele Fazzi [a,c*]

[a] Institut für Licht und Materialien, Department für Chemie, Universität zu Köln, Greinstr. 4-6, 50939 Köln, Germany.

[b] University of Liverpool, Department of Chemistry, Liverpool, L69 3BX, United Kingdom

[c] Università di Bologna, Dipartimento di Chimica 'Giacomo Ciamician', Via F. Selmi, 2, 40126 Bologna, Italy.

E-mail: klaus.meerholz@uni-koeln.de, daniele.fazzi@unibo.it

Supporting Information

Table of Contents

Force field parametrization 2

Polymerized and cross-linked morphology generation 13

Experimental glass transition temperature T_g 15

Simulated glass transition temperature T_g 16

Density 19

Exponential fit to autocorrelation functions of the site energy differences 20

Effective Marcus residence time 21

Effective Marcus residence time – hole transport networks 22

References 23

Force field parametrization

For all molecular dynamics simulations presented in this work, the OPLS-AA [1,2] force field was used. Force field parameters were reparametrized for **TPA-1** and **TPA-2** using *ab inito* and semiempirical methods. Due to the large conformational degree of freedom of the alkyl-substituted molecular structures, at first a conformer search was performed using CREST [3] at the GFN2-xTB/GFNFF [4,5] composite level of theory, optimizing and sampling the conformers at the GFN-FF level followed by a GFN2-xTB single-point calculation. Based on the lowest energy conformer, a DFT geometry optimization was performed at the ωB97X-D [6] / 6-311G* [7–9] level of theory in the neutral and monocationic states. Atomic partial charges were computed based on the DDEC6 method at the same level of theory, using the code Chargemol [10]. The charges of the same atom types were then averaged in order to preserve symmetry. While Bonding- and Angle parameters were taken directly from the OPLS-AA force field, the Lennard Jones parameters were obtained by a fitting procedure proposed by Cole et. al [11], similarly as before, averaging the parameters of the same atom types. The dihedral parameters for the central dihedral angles of the triphenylamine core were reparametrized at the DFT level, while all other dihedral parameters were taken directly from the force field. In order to reparametrize the central dihedral angles, a relaxed dihedral scan of an isolated Triphenylamine molecule was performed at the DFT (ωB97X-D/6-311G*) level. This scan was repeated at the MD level with all dihedral parameters set to zero, fixing the not-scanned dihedral angles. The same MD parameters (vide infra) as for the **TPA-1** and **TPA-2** were used in addition to DDEC6-charges computed at the ωB97X-D/6-311G* level of theory. Subtracting the resulting potential energies, the difference profile was fitted with the OPLS-dihedral function

$$V_{opls}(\varphi) = \frac{1}{2}V_1\big(1 + cos(\varphi)\big) + \frac{1}{2}V_2\big(1 - cos(2\varphi)\big) + \frac{1}{2}V_3\big(1 + cos(3\varphi)\big) + \frac{1}{2}V_4(1 - cos(4\varphi)) \quad (1)$$

with φ the dihedral angle, to obtain the desired dihedral angle parameters V_i (see Table S1). In Fig. S1, the DFT determined dihedral potential is shown together with the unparametrized and parametrized dihedral potential for both the neutral and charged states.

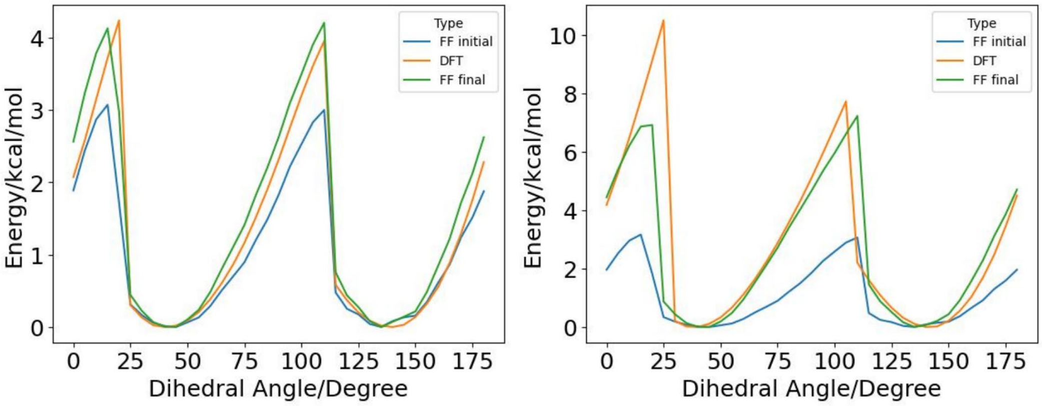

Fig. S1: Dihedral potential for the central C-CN-NT-CN dihedral angle of (DFT, initial force field and reparametrized force field) of **TPA** in the neutral (left panel) and monocationic state (right panel).

The dihedral parameters obtained from this procedure were then transferred to the **TPA-1** and **TPA-2** - systems. Fig. S2 shows the MD atom types of **TPA**, while Fig S3. shows the MD atom types of **TPA-1** and **TPA-2**. Tab. S1-S11 show the atom types, charges, Lennard-Jones parameters as well as the Bonding, Angle and Dihedral parameters.

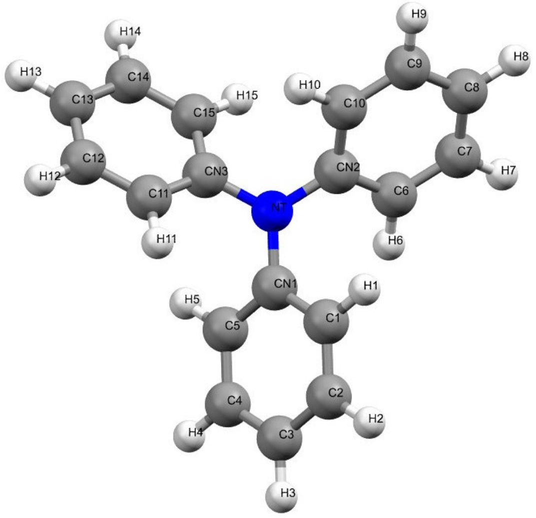

Fig. S2: MD atom types for **TPA.**

Tab. S1: MD atom types and charges for neutral (left, charge(0)) and monocationic (right, charge(+)) **TPA** .

Atom type	*Charge(0)*	*Atom type*	*Charge(0)*	*Atom type*	*Charge(+)*	*Atom type*	*Charge(+)*
NT	-0.219070	C14	-0.086907	NT	-0.010300	C14	-0.079210
CN1	0.200469	C15	-0.200127	CN1	0.150422	C15	-0.153239
C1	-0.200094	H1	0.125745	C1	-0.155964	H1	0.142072
C2	-0.087519	H2	0.109278	C2	-0.075635	H2	0.137575
C3	-0.131260	H3	0.109320	C3	-0.044943	H3	0.135044
C4	-0.087227	H4	0.108112	C4	-0.075251	H4	0.136036
C5	-0.199721	H5	0.125819	C5	-0.150017	H5	0.137404
CN2	0.202661	H6	0.126321	CN2	0.150739	H6	0.138686
C6	-0.202660	H7	0.109166	C6	-0.153633	H7	0.135547
C7	-0.085164	H8	0.109799	C7	-0.073757	H8	0.133935
C8	-0.134260	H9	0.108384	C8	-0.042902	H9	0.136145
C9	-0.085867	H10	0.125205	C9	-0.076569	H10	0.140814
C10	-0.200200	H11	0.125256	C10	-0.152384	H11	0.137472
CN3	0.198975	H12	0.109851	CN3	0.149909	H12	0.135106
C11	-0.198705	H13	0.109238	C11	-0.150550	H13	0.134551
C12	-0.087326	H14	0.109380	C12	-0.074171	H14	0.139333
C13	-0.133242	H15	0.126370	C13	-0.043353	H15	0.141089

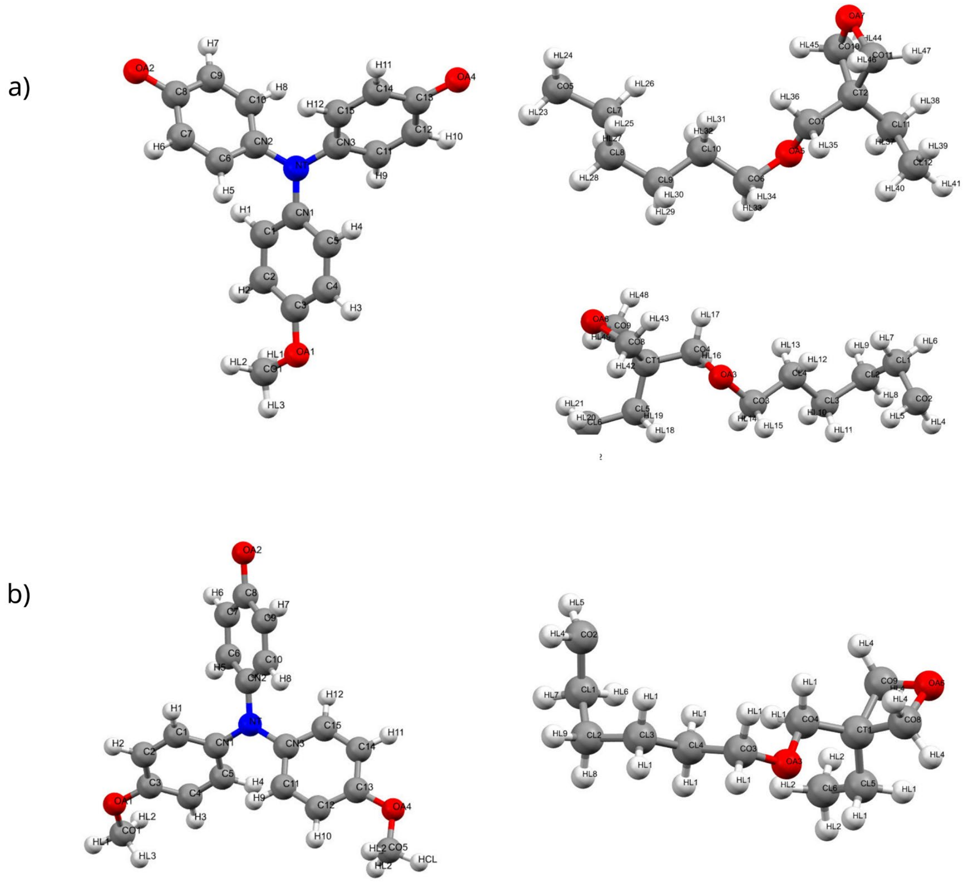

Fig. S3: MD atom types for a) **TPA-2** and b) **TPA-1.**

Tab. S2: MD atom types and charges for PF_6^- .

Atom type	*Charge*
PT	1.919856
F1	-0.486705
F2	-0.486384
F3	-0.486245
F4	-0.486723
F5	-0.486864
F6	-0.486935

Tab. S3: MD atom types and charges for neutral **TPA-1.**

Atom type	*Charge*	*Atom type*	*Charge*	*Atom type*	*Charge*	*Atom type*	*Charge*
NT	-0.220941	H3	0.125421	CT1	0.054441	HL16	0.079823
CN1	0.173523	H4	0.125421	CL5	-0.196136	HL17	0.079823
C1	-0.194220	H5	0.125421	CL6	-0.196136	HL18	0.079823
C2	-0.194220	H6	0.125421	OA4	-0.252942	HL19	0.079823
C3	0.258230	H7	0.125421	CO5	-0.025216	HL20	0.079823
C4	-0.194220	H8	0.125421	HCL7	0.079823	HL21	0.079823
C5	-0.194220	H9	0.125421	HL1	0.079823	HL22	0.079823
CN2	0.173523	H10	0.125421	HL2	0.079823	HL23	0.079823
C6	-0.194220	H11	0.125421	HL3	0.079823	HL24	0.079823
C7	-0.194220	H12	0.125421	HL4	0.079823	CO8	-0.025216
C8	0.258230	OA1	-0.252942	HL5	0.079823	CO9	-0.025216
C9	-0.194220	CO1	-0.025216	HL6	0.079823	OA6	-0.252942
C10	-0.194220	OA2	-0.252942	HL7	0.079823	HL42	0.079823
CN3	0.173523	CO2	-0.025216	HL8	0.079823	HL43	0.079823
C11	-0.194220	CL1	-0.196136	HL9	0.079823	HL48	0.079823
C12	-0.194220	CL2	-0.196136	HL10	0.079823	HL49	0.079823
C13	0.258230	CL3	-0.196136	HL11	0.079823		
C14	-0.194220	CL4	-0.196136	HL12	0.079823		
C15	-0.194220	CO3	-0.025216	HL13	0.079823		
H1	0.125421	OA3	-0.252942	HL14	0.079823		
H2	0.125421	CO4	-0.025216	HL15	0.079823		

Tab. S4: MD atom types and charges for monocationic **TPA-1.**

Atom type	*Charge*	*Atom type*	*Charge*	*Atom type*	*Charge*	*Atom type*	*Charge*
NT	-0.034492	H3	0.140832	CT1	0.050013	HL16	0.089254
CN1	0.128804	H4	0.140832	CL5	-0.198639	HL17	0.089254
C1	-0.174491	H5	0.140832	CL6	-0.198639	HL18	0.089254
C2	-0.174491	H6	0.140832	OA4	-0.228875	HL19	0.089254
C3	0.319902	H7	0.140832	CO5	-0.029984	HL20	0.089254
C4	-0.174491	H8	0.140832	HCL7	0.089254	HL21	0.089254
C5	-0.174491	H9	0.140832	HL1	0.089254	HL22	0.089254
CN2	0.128804	H10	0.140832	HL2	0.089254	HL23	0.089254
C6	-0.174491	H11	0.140832	HL3	0.089254	HL24	0.089254
C7	-0.174491	H12	0.140832	HL4	0.089254	CO8	-0.029984
C8	0.319902	OA1	-0.228875	HL5	0.089254	CO9	-0.029984
C9	-0.174491	CO1	-0.029984	HL6	0.089254	OA6	-0.228875
C10	-0.174491	OA2	-0.228875	HL7	0.089254	HL42	0.089254
CN3	0.128804	CO2	-0.029984	HL8	0.089254	HL43	0.089254
C11	-0.174491	CL1	-0.198639	HL9	0.089254	HL48	0.089254
C12	-0.174491	CL2	-0.198639	HL10	0.089254	HL49	0.089254
C13	0.319902	CL3	-0.198639	HL11	0.089254		
C14	-0.174491	CL4	-0.198639	HL12	0.089254		
C15	-0.174491	CO3	-0.029984	HL13	0.089254		
H1	0.140832	OA3	-0.228875	HL14	0.089254		
H2	0.140832	CO4	-0.029984	HL15	0.089254		

Tab. S5: MD atom types and charges for neutral **TPA-2.**

Atom type	*Charge*	*Atom type*	*Charge*	*Atom type*	*Charge*	*Atom type*	*Charge*
NT	-0.214982	H10	0.123379	CL12	-0.196341	HL28	0.077918
CN1	0.168853	H11	0.123379	HL1	0.077918	HL29	0.077918
C1	-0.197589	H12	0.123379	HL2	0.077918	HL30	0.077918
C2	-0.197589	OA1	-0.265242	HL3	0.077918	HL31	0.077918
C3	0.264764	CO1	0.008501	HL4	0.077918	HL32	0.077918
C4	-0.197589	OA2	-0.265242	HL5	0.077918	HL33	0.077918
C5	-0.197589	CO2	0.008501	HL6	0.077918	HL34	0.077918
CN2	0.168853	CL1	-0.196341	HL7	0.077918	HL35	0.077918
C6	-0.197589	CL2	-0.196341	HL8	0.077918	HL36	0.077918
C7	-0.197589	CL3	-0.196341	HL9	0.077918	HL37	0.077918
C8	0.264764	CL4	-0.196341	HL10	0.077918	HL38	0.077918
C9	-0.197589	CO3	0.008501	HL11	0.077918	HL39	0.077918
C10	-0.197589	OA3	-0.265242	HL12	0.077918	HL40	0.077918
CN3	0.168853	CO4	0.008501	HL13	0.077918	HL41	0.077918
C11	-0.197589	CT1	0.052972	HL14	0.077918	CO8	0.008501
C12	-0.197589	CL5	-0.196341	HL15	0.077918	CO9	0.008501
C13	0.264764	CL6	-0.196341	HL16	0.077918	OA6	-0.265242
C14	-0.197589	OA4	-0.265242	HL17	0.077918	HL42	0.077918
C15	-0.197589	CO5	0.008501	HL18	0.077918	HL43	0.077918
H1	0.123379	CL7	-0.196341	HL19	0.077918	HL44	0.077918
H2	0.123379	CL8	-0.196341	HL20	0.077918	HL45	0.077918
H3	0.123379	CL9	-0.196341	HL21	0.077918	CO10	0.008501
H4	0.123379	CL10	-0.196341	HL22	0.077918	CO11	0.008501
H5	0.123379	CO6	0.008501	HL23	0.077918	OA7	-0.265242
H6	0.123379	OA5	-0.265242	HL24	0.077918	HL46	0.077918
H7	0.123379	CO7	0.008501	HL25	0.077918	HL47	0.077918
H8	0.123379	CT2	0.052972	HL26	0.077918	HL48	0.077918
H9	0.123379	CL11	-0.196341	HL27	0.077918	HL49	0.077918

Tab. S6: MD atom types and charges for monocationic **TPA-2.**

Atom type	*Charge*	*Atom type*	*Charge*	*Atom type*	*Charge*	*Atom type*	*Charge*
NT	-0.037849	H10	0.139322	CL12	-0.197597	HL28	0.083227
CN1	0.131871	H11	0.139322	HL1	0.083227	HL29	0.083227
C1	-0.174307	H12	0.139322	HL2	0.083227	HL30	0.083227
C2	-0.174307	OA1	-0.252132	HL3	0.083227	HL31	0.083227
C3	0.320431	CO1	0.004526	HL4	0.083227	HL32	0.083227
C4	-0.174307	OA2	-0.252132	HL5	0.083227	HL33	0.083227
C5	-0.174307	CO2	0.004526	HL6	0.083227	HL34	0.083227
CN2	0.131871	CL1	-0.197597	HL7	0.083227	HL35	0.083227
C6	-0.174307	CL2	-0.197597	HL8	0.083227	HL36	0.083227
C7	-0.174307	CL3	-0.197597	HL9	0.083227	HL37	0.083227
C8	0.320431	CL4	-0.197597	HL10	0.083227	HL38	0.083227
C9	-0.174307	CO3	0.004526	HL11	0.083227	HL39	0.083227
C10	-0.174307	OA3	-0.252132	HL12	0.083227	HL40	0.083227
CN3	0.131871	CO4	0.004526	HL13	0.083227	HL41	0.083227
C11	-0.174307	CT1	0.054471	HL14	0.083227	CO8	0.004526
C12	-0.174307	CL5	-0.197597	HL15	0.083227	CO9	0.004526
C13	0.320431	CL6	-0.197597	HL16	0.083227	OA6	-0.252132
C14	-0.174307	OA4	-0.252132	HL17	0.083227	HL42	0.083227
C15	-0.174307	CO5	0.004526	HL18	0.083227	HL43	0.083227
H1	0.139322	CL7	-0.197597	HL19	0.083227	HL44	0.083227
H2	0.139322	CL8	-0.197597	HL20	0.083227	HL45	0.083227
H3	0.139322	CL9	-0.197597	HL21	0.083227	CO10	0.004526
H4	0.139322	CL10	-0.197597	HL22	0.083227	CO11	0.004526
H5	0.139322	CO6	0.004526	HL23	0.083227	OA7	-0.252132
H6	0.139322	OA5	-0.252132	HL24	0.083227	HL46	0.083227
H7	0.139322	CO7	0.004526	HL25	0.083227	HL47	0.083227
H8	0.139322	CT2	0.054471	HL26	0.083227	HL48	0.083227
H9	0.139322	CL11	-0.197597	HL27	0.083227	HL49	0.083227

Tab. S7: Lennard-Jones parameters ε($\frac{k\mathrm{cal}}{\mathrm{mol}}$) and σ (Å) for **TPA-1** and **TPA-2**, PF_6^- and Cl^-

Atom type	*ε*	*σ*
NT	0.101	3.131
CN	0.062	3.515
C	0.062	3.515
H	0.036	2.266
OA	0.100	2.889
CO	0.062	3.471
CL	0.062	3.471
CT	0.062	3.471
HL	0.036	2.317
P[12]	0.200	3.74
F[12]	0.061	3.1181
Cl	0.71	4.02

Tab. S8: Bond force constant ($\frac{k\mathrm{cal}}{\mathrm{mol}}$) and equilibrium length (Å) for **TPA-1** and **TPA-2**, PF_6^-

Bond type	*Force constant*	*Bond length*
C-C (alkane)	268.0	1.529
O-C (alkane)	320.0	1.41
C-H (alkane)	340.0	1.09
C-O (aromatic)	450.0	1.364
N-C (aromatic)	481.0	1.34
C-C (aromatic)	469.0	1.4
C-H (aromatic)	367.0	1.08
P-F[12]	370.46	1.606

Tab. S9: Angle force constant ($\frac{kcal}{mol}$) and equilibrium position (Degree) for **TPA-1** and **TPA-2**, PF_6^-

Angle type	*Force constant*	*Angle*
C-C-C (alkane)	58.35	112.7
C-C-O (alkane)	50.0	109.5
H-(CO)-H (methoxy)	33.0	107.8
O-C-H (methoxy)	35.0	109.5
C-C-H (alkane)	37.5	110.7
C-O-C (alkane)	60.0	109.5
C(aromatic)-O-C	75.0	111.0
C-N-C (aromatic)	50.0	116.0
C-C-C (aromatic)	63.0	120.0
C-C-O (aromatic)	70.0	120.0
N-C-C (aromatic)	70.0	120.0
C-C-H (aromatic)	35.0	120.0
F-P-F[12]	139.22	90.0

Tab. S10: Dihedral parameters ($\frac{kcal}{mol}$) for **TPA-1** and **TPA-2**.

Dihedral type	V_1	V_2	V_3	V_4
OCCC, CCCC (alkane)	1.3	-0.05	0.2	0.0
CCCH,HCCH$_{alk}$,CCOC$_{arom}$	0.0	0.0	0.3	0.0
OCCH$_{alk}$	0.0	0.0	0.468	0.0
CCOC$_{alk}$	0.65	-0.25	0.67	0.0
COCH$_{alk/arom}$	0.0	0.0	0.76	0.0
NCCC,CCCO,HCCO, NCCH,CCCC,CCCH,HCCH (arom)	0.0	7.25	0.0	0.0
C CN NT CN (neutral)	0.082	0.106	0.108	-0.143
C CN NT CN (charged)	0.750	0.118	0.485	-0.565

Tab. S11: Improper dihedral parameters ($\frac{k\mathrm{cal}}{\mathrm{mol}}$) for **TPA-1** and **TPA-2**.

Dihedral type	*Force constant*	*Improper dihedral angles/°*
Aromatic ring atoms	1.1	180.0

Polymerized and cross-linked morphology generation

In all simulations, the same basic force field settings were used. Further, the Nosé-Hoover thermostat [13,14] and barostat [15,16] were used. The simulations were run in periodic boundary conditions with a 10.0 Å cut-off radius for the van-der-Waals and coulombic interactions. For electrostatic interactions, the PPPM method was used with a 0.0001 $\frac{k\text{cal}}{\text{mol}}$ accuracy.

In order to generate the polymerized/cross-linked systems, at first, equilibrated monomeric systems were generated. Initial MD box configurations of 512 molecules were generated with Moltemplate [17,18] for **TPA-1** and **TPA-2**. Afterwards, the systems were equilibrated using a thermal annealing protocol. Firstly, a high pressure NPT run (300 K, 100 bar, 100 ps, Tdamp=100 fs, Pdamp=1000 fs) was performed to quickly contract the box. After relaxing the box in the NPT sample again to ambient conditions (300 K, 1 bar, 100 ps, Tdamp=100 fs, Pdamp=1000 fs), the system was thermally annealed in NVT ensemble going from 1000 K to 300 K in 100 K steps, with 125 ps per step (Tdamp=100 fs). Finally, a 1 ns NPT run at 300 K and 1 bar (Tdamp=100 fs, Pdamp=1000fs) was performed.

To polymerize the equilibrated systems, REACTER [19] was used. Here, the oxetane moieties were identified as the relevant reaction sites. The topological templates and the individual reaction steps defined for the simulation are shown in Fig. S3 together with the fundamental reaction equation.

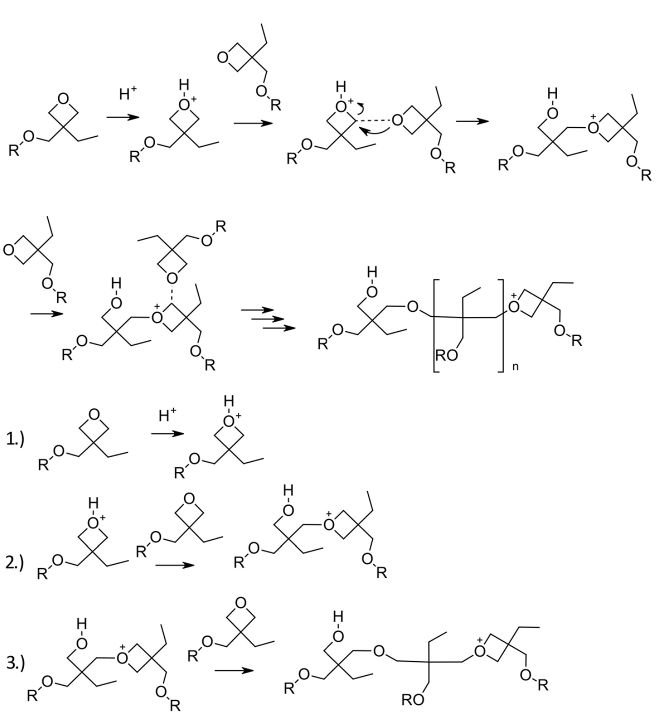

Fig. S3: Crosslinking reaction [20] and individual reaction steps. The oxetane moieties were used as topological templates for identifying reaction sites.

For this work, only the final polymerized/cross-linked system was of interest, therefore, back reactions were excluded from the simulation and high pressure and temperature was used to quickly generate the final systems. Firstly, 25 protons were placed randomly inside the simulation box, while charge equilibration was ensured by adding 25 chloride ions. The reaction was then simulated at 1000 K and 100 bar (Tdamp=100 fs, Pdamp=1000 fs) in the NPT ensemble (Nosé-Hoover thermostat and barostat), for 2 ns. Reaction progress was monitored by tracking the number of opened oxetane-rings, as shown in Fig. 2 of the main text. Before any further simulations, the systems were relaxed back to ambient conditions by a 50 ps NPT run at 300K and 1 bar (Tdamp=100 fs, Pdamp=1000fs). For the case of **pTPA**, the radius of gyration was computed and is shown in Fig. S4. All production runs were performed in NVT ensemble 300K and 1bar (Tdamp=100 fs, Pdamp=1000 fs), and they were either 100 ps or 10 ps long (sampling rate of one snapshot every 0.1 ps or 0.01 ps, respectively).

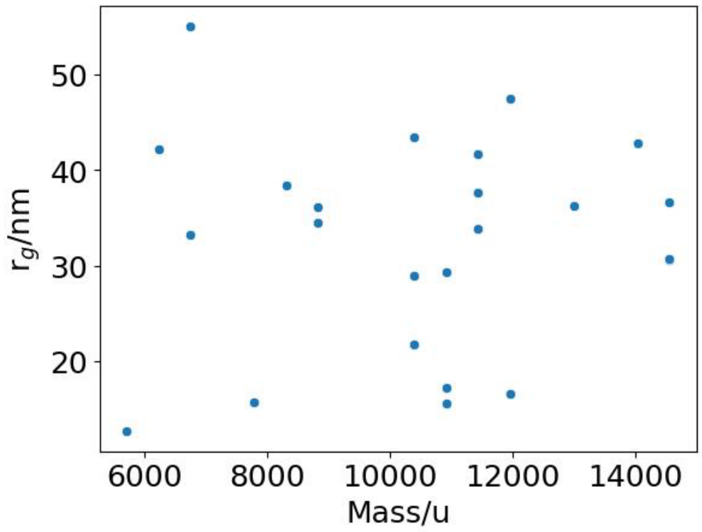

Fig. S4: Radius of gyration vs. mass of the polymeric **pTPA** system.

Experimental glass transition temperature T_g

The glass transition temperatures (T_g) of **pTPA** and **xTPA** were determined experimentally by Differential Scanning Calorimetry (DSC) on a Mettler Toledo DSC821. The samples were prepared by drop casting a solution of the **TPA-1** or **TPA-2** monomer and 2 wt% 4-Octyloxydiphenyliodoniumhexafluorantimonat (OPPI) in THF into the 4 µL aluminium sample pan. The samples were illuminated with UV-light (254nm) for 30 min to obtain the corresponding cross-linked **pTPA** and **xTPA** polymers. The samples were dried at 363 K for 12 h and were sealed subsequently. The DSC measurements were performed at 253 K – 333 K for **pTPA** and 273 K – 373 K for **xTPA** with a heating and cooling rate of 10 K min^{-1} under nitrogen flow. The T_g values were determined with the Mettler Toledo STARe Evaluation Software Version 16.30 and the data were plotted by OriginPro 2023. For **pTPA**, a T_g of 297 K was obtained, while for **xTPA** a T_g of 325 K was obtained.

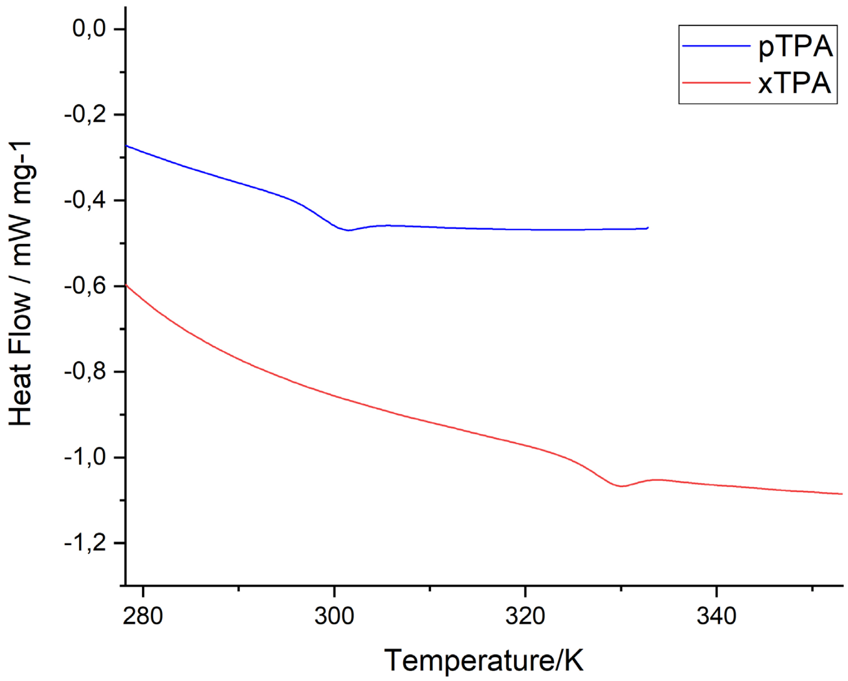

Fig. S5: Differential scanning calorimetry (DSC) of **pTPA** and **xTPA**. The data of the second heating cycle with 10 K min^{-1} is shown.

Simulated glass transition temperature T_g

In order to confirm the structures generated *in silico* by REACTER, the glass transition temperature T_g was computed via MD. The cross-linked structures were heated up to 800 K and the cooled down to 0 K with a cooling rate of 0.08 $\frac{K}{\mathrm{ps}}$ (Tdamp=100 fs, Pdamp=1000 fs) in the NPT ensemble (Nosé-Hoover thermostat and barostat). Density-temperature plots were used to extract the value of T_g by considering different fitting ranges with an approach proposed by Lin et al, [21] in order to minimize arbitrariness and human bias in the fitting procedure. For different fitting ranges, R^2-T plots were generated using the method of Lin et al. with the plotting and analysis scripts based on the material provided by the authors on their gitlab page (https://gitlab.mpcdf.mpg.de/materials/tg) in a modified form. The plots are shown in Fig. S6.

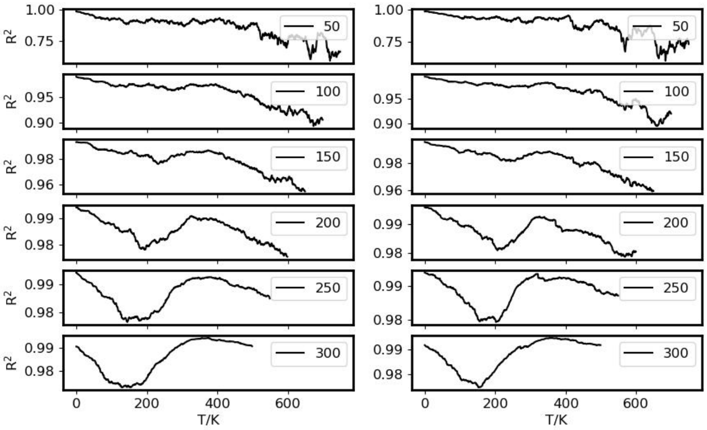

Fig. S6: R^2-T plots for different fitting ranges (50 K-200 K) for **pTPA** (left column) and **xTPA** (right column).

From the plots shown in Fig. S6, valid fitting ranges can be extracted by considering the ranges in which R^2 shows a significant valley, because in this case the non-linear regions of the underlying density-temperature plots are included in the fit. Fig. S7 shows the density-temperature plots with the linear fits using different fitting ranges.

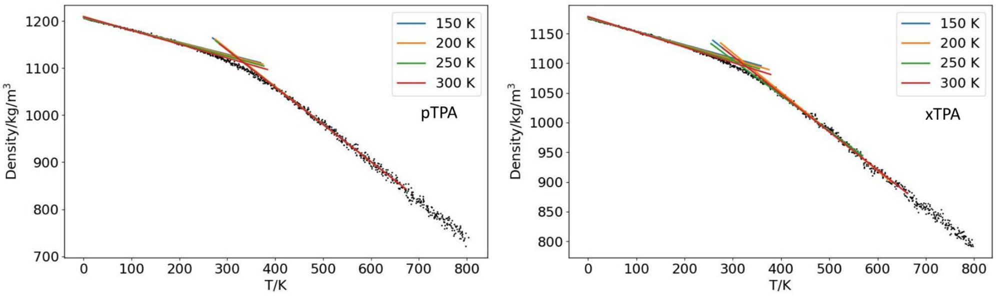

Fig. S7: Temperature-density plots to determine T_g for **pTPA** (left panel) and **xTPA** (right panel) using different fitting ranges as shown in the plot.

Tab. S12 and Tab. S13 show the extracted T_g values. In both **xTPA** and **pTPA**, the extracted T_g values show overall satisfying agreement with the experimental data. For **pTPA**, a slightly higher simulated T_g was obtained, possibly caused by a larger oligomer length in the simulated system.

Tab. S12: Extracted T_g values for **pTPA** using multiple fitting ranges.

Fitting ranges/K	*T_g/K*
1.0 - 151.0 & 407.0 - 557.0	319.53
3.0 -203.0 & 406.0 - 606.0	324.52
0.0 - 250.0 & 379.0 - 629.0	326.33
0.0 - 300.0 & 373.0 - 673.0	334.0

Tab. S13: Extracted T_g values for **xTPA** using multiple fitting ranges.

Fitting ranges/K	*T_g/K*
0.0 - 150.0 & 417.0 - 567.0	308.75
0.0 - 200.0 & 429.0- 629.0	324.85
0.0 - 250.0 & 319.0 - 569.0	304.96
0.0 - 300.0 & 362.0 - 662.0	328.69

In addition to the fully polymerized systems, the T_g values of 80 % polymerized systems were determined using the same procedure as described above. The results shown below are similar to the 100 polymerized systems.

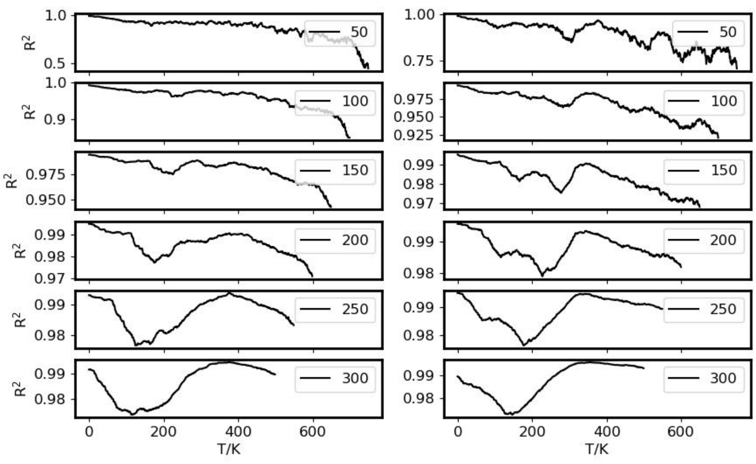

Fig. S8: R^2-T plots for different fitting ranges (50 K-200 K) for 80 % polymerized **pTPA** (left column) and 80 % polymerized **xTPA** (right column).

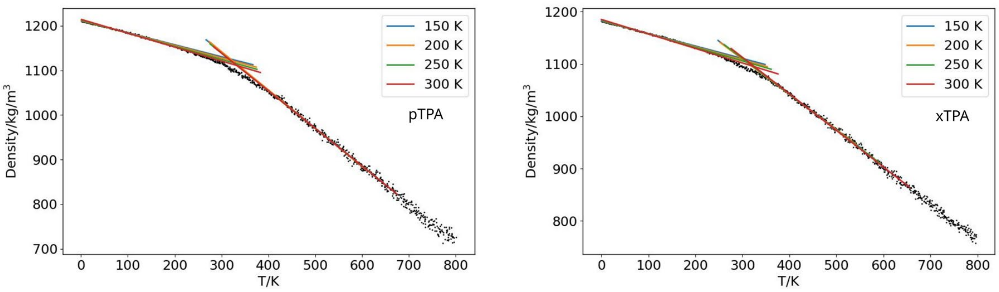

Fig. S9: Temperature-density plots to determine T$_g$ for 80 % polymerized **pTPA** (left panel) and 80 % polymerized **xTPA** (right panel) using different fitting ranges as shown in the plot.

Tab. S14: Extracted T$_g$ values for 80 % polymerized **pTPA** using multiple fitting ranges.

Fitting ranges/K	*T_g/K*
1.0 - 151.0 & 407.0 - 557.0	*317.10*
1.0 -201.0 & 407.0 - 607.0	*324.13*
1.0 - 251.0 & 378.0 - 628.0	*325.59*
1.0 - 301.0 & 373.0 - 675.0	*332.87*

Tab. S15: Extracted T$_g$ values for 80 % polymerized **xTPA** using multiple fitting ranges.

Fitting ranges/K	*T_g/K*
0.0 - 150.0 & 401.0 – 551.0	*298.21*
5.0 - 205.0 & 343.0- 543.0	*302.83*
2.0 - 252.0 & 343.0 - 593.0	*311.23*
0.0 - 300.0 & 355.0 - 655.0	*325.74*

Density

The densities of the **TPA-1** and **TPA-2** monomers were determined with pycnometer (V = 5.013 mL) measurements. The measurements were performed under ambient conditions, the temperature and atmospheric pressure at the date of measurement are given in Tab. S16. For each weight measurement, three weights were determined and the mean value was calculated; the density measurement was repeated three times for each substance and a mean value with its standard deviation is given, see Tab. S16.

First, the empty, clean, and dry pycnometer (m_0) was weighed. Then, it was filled with distilled water and weighed again (m_1). Next, the corresponding substance with a known weight (m_2) was placed into the pycnometer, which was then filled with distilled water and weighed again (m_3). With these measurements, the density of the **TPA** samples ρ_{TPA} could be calculated by using eq. (2) and by taking the density of water at the given temperature and atmospheric pressure[22] into account.

$$\rho_{TPA} = \frac{(m_2 - m_0)}{(m_1 - m_0) - (m_3 - m_2)} \cdot \rho_{H2O} \qquad (2)$$

Tab. S16: Overview of the ambient conditions of the density measurement and the resulting density of the **TPA-1** and **TPA-2** monomers, together with the simulated densities.

Sample	P [MPa]	T [K]	ρ_{H2O} (T,P) [g/cm^3]	ρ_{Sample} [g/cm^3]	$\rho_{simulation}$ [g/cm^3]
TPA-1	0.1023	295.15	0.99778	0.998	1.103
TPA-2	0.1021	297.15	0.99731	0.997	1.070

Exponential fit to autocorrelation functions of the site energy differences

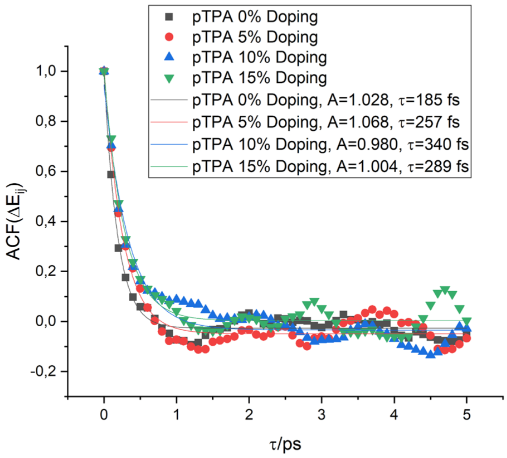

Fig. S10: Fit of an exponential function of the form $f(x) = \mathrm{A} \cdot \mathrm{e}^{-\frac{x}{\tau}} + \mathrm{y}_0$ to the autocorrelation function of the site energy differences ($\Delta\mathrm{E}_{ij}$) of **pTPA**. The extracted pre-exponential factors A and time constants τ are shown in the figure inset.

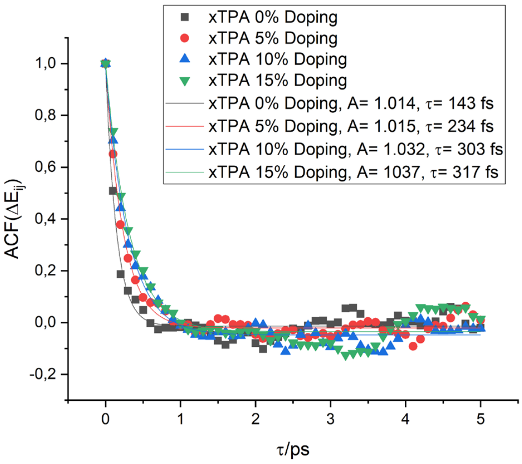

Fig. S11: Fit of an exponential function of the form $f(x) = \mathrm{A} \cdot \mathrm{e}^{-\frac{\mathrm{x}}{\tau}} + \mathrm{y}_0$ to the autocorrelation function of the site energy differences (ΔE_{ij}) of **xTPA**. The extracted preexponential factors A and time constants τ are shown in the figure.

Effective Marcus residence time

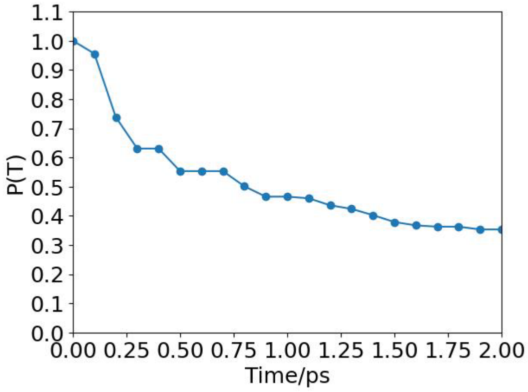

Fig. S12: Plot illustrating the procedure to obtain the *effective Marcus residence times*. P(T) was computed by numerical integration as defined in the main text. The effective Marcus residence time was chosen as the time until 50% occupation (P(T)=0.5) was reached. This procedure was repeated for every pair in the bulk system within a 1.5 nm cutoff.

Effective Marcus residence time – hole transport networks

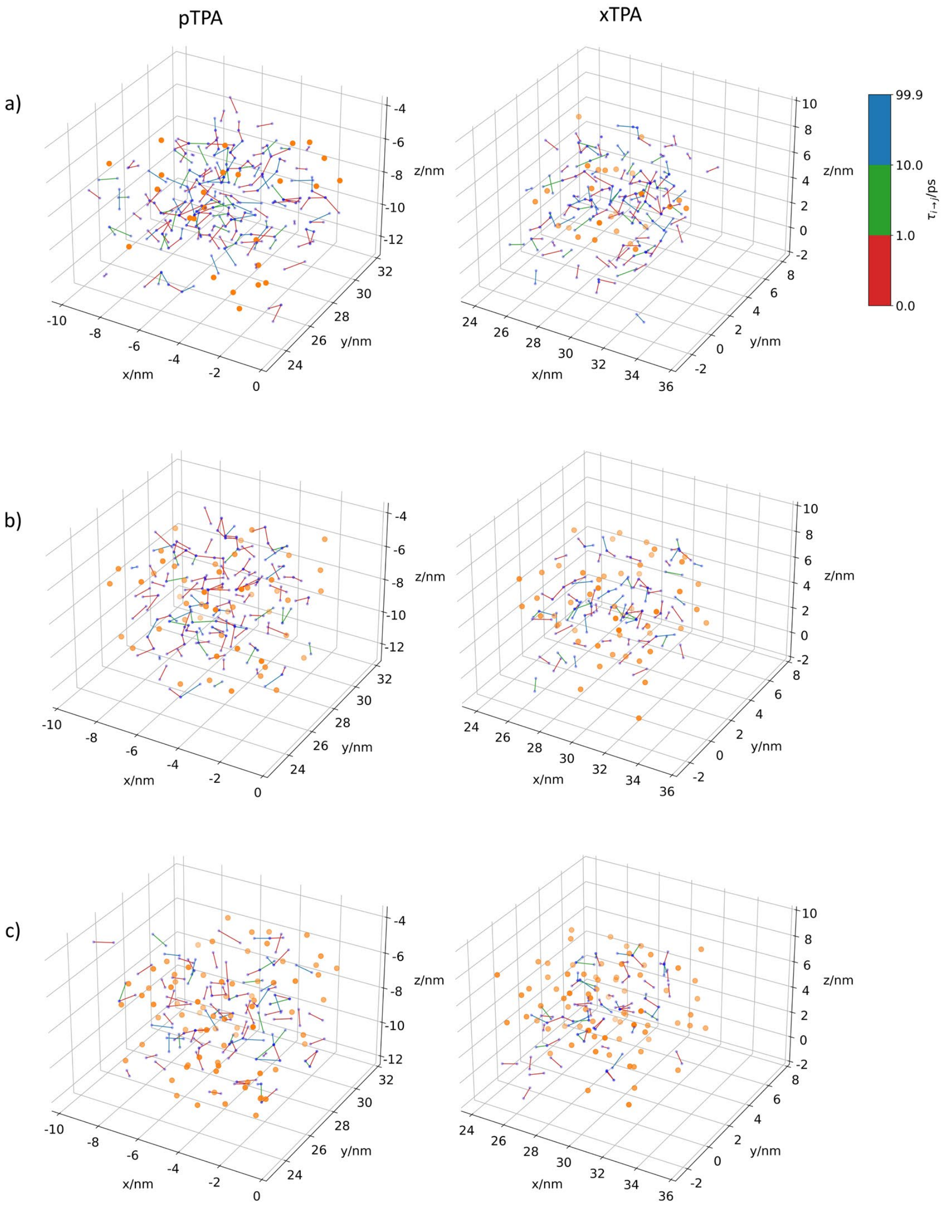

Fig. S13: *Effective Marcus residence time* $\tau_{i\rightarrow j}$ networks for the 5%, (panel a)) as well as 10% (panel b)) and 15% (panel c)) doped cases. The left panels show the networks for **pTPA** while the right panels show **xTPA**. Blue nodes represent **TPA** positions while orange nodes represent ion positions. Connections crossing the periodic boundaries are omitted for clarity.

References

1 W. L. Jorgensen, D. S. Maxwell and J. Tirado-Rives, *J. Am. Chem. Soc.*, 1996, **118**, 11225–11236.

2 G. A. Kaminski, R. A. Friesner, J. Tirado-Rives and W. L. Jorgensen, *J. Phys. Chem. B*, 2001, **105**, 6474–6487.

3 P. Pracht, S. Grimme, C. Bannwarth, F. Bohle, S. Ehlert, G. Feldmann, J. Gorges, M. Müller, T. Neudecker, C. Plett, S. Spicher, P. Steinbach, P. A. Wesołowski and F. Zeller, *J. Chem. Phys.*, 2024, **160**.

4 C. Bannwarth, S. Ehlert and S. Grimme, *J. Chem. Theory Comput.*, 2019, **15**, 1652–1671.

5 S. Spicher and S. Grimme, *Angew. Chem. Int. Ed.*, 2020, **59**, 15665–15673.

6 J.-D. Chai and M. Head-Gordon, *Phys. Chem. Chem. Phys.*, 2008, **10**, 6615–6620.

7 R. Krishnan, J. S. Binkley, R. Seeger and J. A. Pople, *J. Chem. Phys.*, 1980, **72**, 650–654.

8 B. P. Pritchard, D. Altarawy, B. Didier, T. D. Gibson and T. L. Windus, *J. Chem. Inf. Model.*, 2019, **59**, 4814–4820.

9 T. Clark, J. Chandrasekhar, G. W. Spitznagel and P. V. R. Schleyer, *J. Comput. Chem.*, 1983, **4**, 294–301.

10 T. A. Manz and N. G. Limas, *RSC Adv.*, 2016, **6**, 47771–47801.

11 D. J. Cole, J. Z. Vilseck, J. Tirado-Rives, M. C. Payne and W. L. Jorgensen, *J. Chem. Theory Comput.*, 2016, **12**, 2312–2323.

12 B. Doherty, X. Zhong, S. Gathiaka, B. Li and O. Acevedo, *J. Chem. Theory Comput.*, 2017, **13**, 6131–6145.

13 W. G. Hoover, *Phys. Rev. A*, 1985, **31**, 1695–1697.

14 S. Nosé, *J. Chem. Phys.*, 1984, **81**, 511–519.

15 W. G. Hoover, *Phys. Rev. A*, 1986, **34**, 2499–2500.

16 G. J. Martyna, D. J. Tobias and M. L. Klein, *J. Chem. Phys.*, 1994, **101**, 4177–4189.

17 A. I. Jewett, Z. Zhuang and J.-E. Shea, *Biophys. J.*, 2013, **104**, 169a.

18 A. I. Jewett, D. Stelter, J. Lambert, S. M. Saladi, O. M. Roscioni, M. Ricci, L. Autin, M. Maritan, S. M. Bashusqeh, T. Keyes, R. T. Dame, J.-E. Shea, G. J. Jensen and D. S. Goodsell, *J. Mol. Biol.*, 2021, **433**, 166841.

19 J. R. Gissinger, B. D. Jensen and K. E. Wise, *Macromol.*, 2020, **53**, 9953–9961.

20 S. Feser and K. Meerholz, *Chem. Mater.*, 2011, **23**, 5001–5005.

21 K.-H. Lin, L. Paterson, F. May and D. Andrienko, *Npj Comput. Mater.*, 2021, **7**, 1–7.

22 M. L. Huber, R. A. Perkins, D. G. Friend, J. V. Sengers, M. J. Assael, I. N. Metaxa, K. Miyagawa, R. Hellmann and E. Vogel, *J. Phys. Chem. Ref. Data*, 2012, **41**.

Bibliography

[1] P. H. Abelson, A. L. Hammond, *Science* **1977**, *195*, 1087–1091.

[2] M. Lundstrom, *Science* **2003**, *299*, 210–211.

[3] A. J. Heeger, *Angew. Chem. Int. Ed.* **2001**, *40*, 2591–2611.

[4] C. K. Chiang, C. R. Fincher Jr, Y. W. Park, A. J. Heeger, H. Shirakawa, E. J. Louis, S. C. Gau, A. G. MacDiarmid, *Physi. Rev. Lett.* **1977**, *39*, 1098.

[5] C. W. Tang, S. Van Slyke, *App. Phys. Lett* **1987**, *51*, 913.

[6] M. C. Gather, A. Köhnen, K. Meerholz, *Adv. Mater.* **2011**, *23*, 233–248.

[7] S. Muench, A. Wild, C. Friebe, B. Haupler, T. Janoschka, U. S. Schubert, *Chem. Rev.* **2016**, *116*, 9438–9484.

[8] Y. van De Burgt, A. Melianas, S. T. Keene, G. Malliaras, A. Salleo, *Nat. Electron.* **2018**, *1*, 386–397.

[9] D. Larcher, J.-M. Tarascon, *Nat. Chem.* **2015**, *7*, 19–29.

[10] M. Armand, J.-M. Tarascon, *Nature* **2008**, *451*, 652–657.

[11] D. Corzo, D. Rosas-Villalva, C. Amruth, G. Tostado-Blázquez, E. B. Alexandre, L. H. Hernandez, J. Han, H. Xu, M. Babics, S. De Wolf, D. Baran, *Nat. Energy* **2023**, *8*, 62–73.

[12] B. Underwood, H. Saiedian, *Security and Privacy* **2021**, *4*, e142.

[13] A. Köhler, H. Bässler, *Electronic processes in organic semiconductors: An introduction*, John Wiley & Sons, **2015**.

[14] H. Klauk, *Organic electronics: materials, manufacturing, and applications*, John Wiley & Sons, **2006**.

[15] N. A. Kukhta, A. Marks, C. K. Luscombe, *Chem. Rev.* **2021**, *122*, 4325–4355.

[16] P. Agarwala, D. Kabra, *J. of Mater.s Chem. A* **2017**, *5*, 1348–1373.

[17] P. Blanchard, C. Malacrida, C. Cabanetos, J. Roncali, S. Ludwigs, *Polym. Int.* **2019**, *68*, 589–606.

[18] G. Chen, J. Wang, W.-C. Chen, Y. Gong, N. Zhuang, H. Liang, L. Xing, Y. Liu, S. Ji, H.-L. Zhang et al., *Adv. Funct. Mater.* **2023**, *33*, 2211893.

[19] V. Coropceanu, J. Cornil, D. A. da Silva Filho, Y. Olivier, R. Silbey, J.-L. Brédas, *2007* **2007**, *107*, 926–952.

[20] C. Schober, K. Reuter, H. Oberhofer, *J. Phys. Chem. Lett.* **2016**, *7*, 3973–3977.

[21] V. Rühle, A. Lukyanov, F. May, M. Schrader, T. Vehoff, J. Kirkpatrick, B. Baumeier, D. Andrienko, *J. Chem. Theory Comput.* **2011**, *7*, 3335–3345.

[22] P. Reiser, M. Konrad, A. Fediai, S. Léon, W. Wenzel, P. Friederich, *J. Chem. Theory Comput.* **2021**, *17*, 3750–3759.

[23] C. Burke, A. Landi, A. Troisi, *Mater. Horiz.* **2024**, *11*, 5313–5319.

[24] T. Vehoff, Y. S. Chung, K. Johnston, A. Troisi, D. Y. Yoon, D. Andrienko, *J. Phys. Chem. C* **2010**, *114*, 10592–10597.

[25] P. Friederich, V. Meded, A. Poschlad, T. Neumann, V. Rodin, V. Stehr, F. Symalla, D. Danilov, G. Lüdemann, R. F. Fink, W. Wenzel, *Adv. Funct. Mater.* **2016**, *26*, 5757–5763.

[26] N. E. Jackson, L. X. Chen, M. A. Ratner, *Proc. Natl. Acad. Sci. U.S.A.* **2016**, *113*, 8595–8600.

[27] R. Noriega, A. Salleo, A. J. Spakowitz, *Proc. Natl. Acad. Sci. U.S.A.* **2013**, *110*, 16315–16320.

[28] S. Ghosh, S. Giannini, K. Lively, J. Blumberger, *Faraday Discuss.* **2020**, *221*, 501–525.

[29] O. G. Ziogos, S. Giannini, M. Ellis, J. Blumberger, *J. Mater. Chem. C* **2020**, *8*, 1054–1064.

[30] S. Giannini, J. Blumberger, *Acc. Chem. Res.* **2022**, *55*, 819–830.

[31] A. V. Nenashev, J. O. Oelerich, S. D. Baranovskii, *J. Phys.: Condens. Matter* **2015**, *27*, 093201.

[32] W. F. Pasveer, J. Cottaar, C. Tanase, R. Coehoorn, P. A. Bobbert, P. W. M. Blom, D. M. de Leeuw, M. A. J. Michels, *Phys. Rev. Lett.* **2005**, *94*, 206601.

[33] S. D. Baranovskii, A. V. Nenashev, D. Hertel, K. Meerholz, F. Gebhard, *Phys. Rev. Appl.* **2024**, *22*, 014019.

[34] Y. Shirota, *J. Mater. Chem.* **2000**, *10*, 1–25.

[35] P. Cias, C. Slugovc, G. Gescheidt, *J. Phys. Chem. A* **2011**, *115*, 14519–14525.

[36] S. Feser, K. Meerholz, *Chem. Mater.* **2011**, *23*, 5001–5005.

[37] L. Fan, Q. Liu, Z. Xu, B. Lu, *ACS Energy Lett.* **2017**, *2*, 1614–1620.

[38] K. Yamamoto, D. Suemasa, K. Masuda, K. Aita, T. Endo, *ACS Appl. Mater. Interfaces.* **2018**, *10*, 6346–6353.

[39] E. T. Seo, R. F. Nelson, J. M. Fritsch, L. S. Marcoux, D. W. Leedy, R. N. Adams, *J. Am. Chem. Soc.* **1966**, *88*, 3498–3503.

[40] R. R. Nelson, R. N. Adams, *J. Am. Chem. Soc.* **1968**, *90*, 3925–3930.

[41] O. Yurchenko, D. Freytag, L. zur Borg, R. Zentel, J. Heinze, S. Ludwigs, *J. Phys. Chem. B* **2012**, *116*, 30–39.

[42] A. Smie, A. Synowczyk, J. Heinze, R. Alle, P. Tschuncky, G. Götz, P. Bäuerle, *J. Electroanal. Chem.* **1998**, *452*, 87–95.

[43] P. Zacharias, M. C. Gather, M. Rojahn, O. Nuyken, K. Meerholz, *Angew. Chem. Int. Ed.* **2007**, *46*, 4388–4392.

[44] M. S. Bayerl, T. Braig, O. Nuyken, D. C. Müller, M. Groß, K. Meerholz, *Macromol. Rapid Commun.* **1999**, *20*, 224–228.

[45] D. C. Müller, T. Braig, H.-G. Nothofer, M. Arnoldi, M. Gross, U. Scherf, O. Nuyken, K. Meerholz, *ChemPhysChem* **2000**, *1*, 207–211.

[46] O. Nuyken, R. Böhner, C. Erdmann, *Macromol. Symp.* **1996**, *107*, 125–138.

[47] D. Linden, T. B. Reddy, *Handbook of Batteries*, 3rd ed., McGraw-Hill Companies, New York, **2002**.

[48] N. Goujon, N. Casado, N. Patil, R. Marcilla, D. Mecerreyes, *Prog. Polym. Sci.* **2021**, *122*, 101449.

[49] T. Chen, L. Zheng, J. Yuan, Z. An, R. Chen, Y. Tao, H. Li, X. Xie, W. Huang, *Sci. Rep.* **2015**, *5*, 10923.

[50] S. L. Tao, Z. K. Peng, X. H. Zhang, P. F. Wang, C.-S. Lee, S.-T. Lee, *Adv. Funct. Mater.* **2005**, *15*, 1716–1721.

[51] A. Graf, P. Liehm, C. Murawski, S. Hofmann, K. Leo, M. C. Gather, *J. Mater. Chem. C* **2014**, *2*, 10298–10304.

[52] F. Tenopala-Carmona, O. S. Lee, E. Crovini, A. M. Neferu, C. Murawski, Y. Olivier, E. Zysman-Colman, M. C. Gather, *Adv. Mater.* **2021**, *33*, 2100677.

[53] N. Gildemeister, G. Ricci, L. Böhner, J. M. Neudörfl, D. Hertel, F. Würthner, F. Negri, K. Meerholz, D. Fazzi, *J. Mater. Chem. C* **2021**, *9*, 10851–10864.

[54] M. B. Goldey, N. P. Brawand, M. Voros, G. Galli, *J. Chem. Theory Comput.* **2017**, *13*, 2581–2590.

[55] Q. Wu, T. Van Voorhis, *J. Chem. Theory Comput.* **2006**, *2*, 765–774.

[56] R. Herzhoff, F. Negri, K. Meerholz, D. Fazzi, *J. Mater. Chem. C* **2023**, *11*, 11969–11979.

[57] R. Herzhoff, L. Plein, A. Troisi, K. Meerholz, D. Fazzi, *Mater. Horiz.* **2025**.

[58] W. Demtröder, *Experimentalphysik 2, Elektrizität und Optik*, 7th ed., Springer-Verlag, **2017**.

[59] A. Einstein, *Ann. Phys.* **1905**, *4*, 549–560.

[60] M. Von Smoluchowski, *Ann. Phys.* **1906**, *326*, 756–780.

[61] H. Baumgärtel, *Electrochemistry: a guide for newcomers*, Walter de Gruyter GmbH & Co KG, **2019**.

[62] M. Pope, C. E. Swenberg, *Electronic processes in organic crystals and polymers*, Oxford University Press, **1999**.

[63] T. Holstein, *Ann. Phys.* **1959**, *8*, 325–342.

[64] T. Holstein, *Ann. Phys.* **1959**, *8*, 343–389.

[65] A. Miller, E. Abrahams, *Phys. Rev.* **1960**, *120*, 745.

[66] R. A. Marcus, *J. Chem. Phys.* **1956**, *24*, 966–978.

[67] R. A. Marcus, *J. Chem. Phys.* **1963**, *67*, 853–857.

[68] R. A. Marcus, N. Sutin, *Biochim. Biophys. Acta - Bioenerg..* **1985**, *811*, 265–322.

[69] R. P. Feynman, R. B. Leighton, M. Sands, *Lectures on Physics: Commemorative Issue*, Addison Wesley: Reading, MA, **1971**.

[70] B. T. Thole, *Chem. Phys.* **1981**, *59*, 341–350.

[71] P. Ren, J. W. Ponder, *J. Phys. Chem. B* **2003**, *107*, 5933–5947.

[72] B. Baumeier, J. Kirkpatrick, D. Andrienko, *Phys. Chem. Chem. Phys* **2010**, *12*, 11103–11113.

[73] E. F. Valeev, V. Coropceanu, D. A. da Silva Filho, S. Salman, J.-L. Brédas, *J. Am. Chem. Soc.* **2006**, *128*, 9882–9886.

[74] J. Kirkpatrick, *Int. J. Quantum Chem.* **2008**, *108*, 51–56.

[75] S. F. Nelsen, S. C. Blackstock, Y. Kim, *J. Am. Chem. Soc.* **1987**, *109*, 677–682.

[76] J. Armleder, T. Strunk, F. Symalla, P. Friederich, J. Enrique Olivares Peña, T. Neumann, W. Wenzel, A. Fediai, *J. Chem. Theory Comput.* **2021**, *17*, 3727–3738.

[77] P. Friederich, F. Symalla, V. Meded, T. Neumann, W. Wenzel, *J. Chem. Theory Comput.* **2014**, *10*, 3720–3725.

[78] H. Nakanotani, K. Masui, J. Nishide, T. Shibata, C. Adachi, *Nature* **2013**, *3*, 2127.

[79] Y. Olivier, M. Moral, L. Muccioli, J.-C. Sancho-García, *J. Chem. Mater. C* **2017**, *5*, 5718–5729.

[80] N. Aizawa, Y. Harabuchi, S. Maeda, Y.-J. Pu, *Nature* **2020**, *11*, 3909.

[81] J.-M. Mewes, *Phys. Chem. Chem. Phys.* **2018**, *20*, 12454–12469.

[82] R. Gómez-Bombarelli, J. Aguilera-Iparraguirre, T. D. Hirzel, D. Duvenaud, D. Maclaurin, M. A. Blood-Forsythe, H. S. Chae, M. Einzinger, D.-G. Ha, T. Wu et al., *Nat. mater.* **2016**, *15*, 1120–1127.

[83] R. C. Hilborn, *ArXive* **2002**.

[84] A. Szabo, N. S. Ostlund, *Modern Quantum Chemistry: Introduction to Advanced Electronic Structure Theory*, First, revised, Dover Publications, **2012**.

[85] R. G. Parr, W. Yang, *Density-functional theory of atoms and molecules. International Series of Monographs on Chemistry*, *Vol. 3*, **1994**, pp. 14312–14321.

[86] W. Kohn, L. J. Sham, *Phys. Rev.* **1965**, *140*, A1133.

[87] J. Reinhold, *Quantentheorie der Moleküle: Eine Einführung*, 4th ed., Springer-Verlag, Heidelberg, **2012**.

[88] A. Dreuw, M. Head-Gordon, *Chem. Rev.* **2005**, *105*, 4009–4037.

[89] J. Schirmer, *Phys. Chem. Chem. Phys.* **2025**, *27*, 4992–5005.

[90] E. Runge, E. K. U. Gross, *Phys. Rev. Let..* **1984**, *52*, 997.

[91] A. T. B. Gilbert, N. A. Besley, P. M. W. Gill, *J. Phys. Chem. A* **2008**, *112*, 13164–13171.

[92] H. H. Corzo, A. Abou Taka, A. Pribram-Jones, H. P. Hratchian, *J. Comput. Chem.* **2022**, *43*, 382–390.

[93] D. Hait, M. Head-Gordon, *J. Phys. Chem. Lett.* **2021**, *12*, 4517–4529.

[94] P.-L. Lions, *P. Commun. Math. Phys.* **1987**, *109*, 33.

[95] R. E. Stanton, *J. Chem. Phys.* **1968**, *48*, 257–262.

[96] T. Froitzheim, L. Kunze, S. Grimme, J. M. Herbert, J.-M. Mewes, *J. Phys. Chem. A* **2024**, *128*, 6324–6335.

[97] P. Koskinen, V. Mäkinen, *Comput. Mater. Sci.* **2009**, *47*, 237–253.

[98] C. Bannwarth, S. Ehlert, S. Grimme, *J. Chem. Theory Comput.* **2019**, *15*, 1652–1671.

[99] F. Jensen, *Introduction to computational chemistry*, 3rd ed., John wiley & sons, **2017**.

[100] W. L. Jorgensen, J. Tirado-Rives, *J. Am. Chem. Soc.* **1988**, *110*, 1657–1666.

[101] W. L. Jorgensen, D. S. Maxwell, J. Tirado-Rives, *J. Am. Chem. Soc.* **1996**, *118*, 11225–11236.

[102] A. F. Voter in *Radiation effects in solids*, Springer, **2007**, pp. 1–23.

[103] M. J. Frisch, G. W. Trucks, H. B. Schlegel, G. E. Scuseria, M. A. Robb, J. R. Cheeseman, G. Scalmani, V. P. G. A. Barone, G. A. Petersson, H. J. W. C. Nakatsuji et al., *Gaussian Inc. Wallingford CT* **2016**, *1*, 572.

[104] F. Neese, F. Wennmohs, U. Becker, C. Riplinger, *J. Chem. Phys.* **2020**, *152*.

[105] E. Apra, E. J. Bylaska, W. A. De Jong, N. Govind, K. Kowalski, T. P. Straatsma, M. Valiev, H. J. J. van Dam, Y. Alexeev, J. Anchell et al., *J. Chem. Phys.* **2020**, *152*.

[106] H. J. C. Berendsen, D. van der Spoel, R. van Drunen, *Comput. Phys. Commun.* **1995**, *91*, 43–56.

[107] B. Hess, C. Kutzner, D. Van Der Spoel, E. Lindahl, *J. Chem. Theory Comput.* **2008**, *4*, 435–447.

[108] S. Pronk, S. Páll, R. Schulz, P. Larsson, P. Bjelkmar, R. Apostolov, M. R. Shirts, J. C. Smith, P. M. Kasson, D. Van Der Spoel et al., *Bioinform.* **2013**, *29*, 845–854.

[109] A. P. Thompson, H. M. Aktulga, R. Berger, D. S. Bolintineanu, W. M. Brown, P. S. Crozier, *Comput. Phys. Commun.* **2022**, *271*, 108171.

[110] J. R. Gissinger, B. D. Jensen, K. E. Wise, *Macromol.* **2020**, *53*, 9953–9961.

[111] J. Andzelm, C. Kölmel, A. Klamt, *J. Chem. Phys* **1995**, *103*, 9312–9320.

[112] S. Miertuš, E. Scrocco, J. Tomasi, *Chem. Phys* **1981**, *55*, 117–129.

[113] J.-D. Chai, M. Head-Gordon, *Phys. Chem. Chem. Phys.* **2008**, *10*, 6615–6620.

[114] R. Krishnan, J. S. Binkley, R. Seeger, J. A. Pople, *J. Chem. Phys.* **1980**, *72*, 650–654.

[115] B. P. Pritchard, D. Altarawy, B. Didier, T. D. Gibson, T. L. Windus, *J. Chem. Inf. Model.* **2019**, *59*, 4814–4820.

[116] T. Clark, J. Chandrasekhar, G. W. Spitznagel, P. V. R. Schleyer, *J. Comput. Chem.* **1983**, *4*, 294–301.

[117] P. Pracht, S. Grimme, C. Bannwarth, F. Bohle, S. Ehlert, G. Feldmann, J. Gorges, M. Müller, T. Neudecker, C. Plett et al., *J. Chem. Phys.* **2024**, *160*.

[118] T. A. Manz, N. G. Limas, *RSC Adv.* **2016**, *6*, 47771–47801.

[119] L. Fang, A. Zheng, M. Ren, X. Xie, P. Wang, *ACS Appl. Mater. Interfaces.* **2019**, *11*, 39001–39009.

[120] D. Shi, X. Qin, Y. Li, Y. He, C. Zhong, J. Pan, H. Dong, W. Xu, T. Li, W. Hu, J.-L. Brédas, O. M. Bakr, *Sci Adv.* **2016**, *2*, e1501491.

[121] K. Ramachandran, A. Raja, N. Lingamurthy, M. S. Pandian, P. Ramasamy, S. V. Rao, *Chem. Phys. Lett.* **2020**, *742*, 137128.

[122] Z. Zhang, E. Burkholder, J. Zubieta, *Cryst. Struct. Commun.* **2004**, *60*, o452–o454.

[123] T. Yanai, D. P. Tew, N. C. Handy, *Chem. Phys. Lett.* **2004**, *393*, 51–57.

[124] B. Kaduk, T. Kowalczyk, T. Van Voorhis, *Chem. Rev.* **2012**, *112*, 321–370.

[125] Q. Wu, T. Van Voorhis, *J. Phys. Chem. A* **2006**, *110*, 9212–9218.

[126] D. C. Hoesterey, G. M. Letson, *J. Phys. Chem.* **1964**, *41*, 675–679.

[127] M. Stolka, J. F. Yanus, D. M. Pai, *J. Phys. Chem.* **1984**, *88*, 4707–4714.

[128] S. Inal, G. G. Malliaras, J. Rivnay, *Nat. Commun.* **2017**, *8*, 1767.

[129] Q. Wu, T. Van Voorhis, *J. Chem. Phys.* **2006**, *125*.

[130] C. S. Ahart, K. M. Rosso, J. Blumberger, *J. Chem. Theory Comput.* **2022**, *18*, 4438–4446.

[131] P. H. Dederichs, S. Blügel, R. Zeller, H. Akai, *Phys. Rev. Lett.* **1984**, *53*, 2512.

[132] P. Ramos, M. Pavanello, *J. Chem. Phys* **2018**, *148*.

[133] H. Oberhofer, J. Blumberger, *J. Chem. Phys* **2009**, *131*.

[134] A. Dreuw, M. Head-Gordon, *J. Am. Chem. Soc.* **2004**, *126*, 4007–4016.

[135] N. Mardirossian, M. Head-Gordon, *J. Chem. Phys.* **2016**, *144*.

[136] F. Weigend, R. Ahlrichs, *Phys. Chem. Chem. Phys.* **2005**, *7*, 3297–3305.

[137] L. Kunze, A. Hansen, S. Grimme, J.-M. Mewes, *J. Phys. Chem. Lett.* **2021**, *12*, 8470–8480.

[138] F. B. Dias, T. J. Penfold, A. P. Monkman, *Method Appl. Fluoresc.* **2017**, *5*, 012001.